UCLA
UCLA Electronic Theses and Dissertations

Title

Asymmetric Drift-Orbit Bifurcation: Models and Observations

Permalink

https://escholarship.org/uc/item/0594q70q

ISBN

9798277444436

Author

Kamaletdinov, Sergei

Publication Date

2026-03-18

Peer reviewed|Thesis/dissertation

eScholarship.org Powered by the California Digital Library
University of California

University of California
Los Angeles

Asymmetric Drift-Orbit Bifurcation: Models and Observations

A dissertation submitted in partial satisfaction
of the requirements for the degree
Doctor of Philosophy in Geophysics and Space Physics

by

Sergei Railevich Kamaletdinov

2026

© Copyright by
Sergei Railevich Kamaletdinov
2026

Abstract of the Dissertation

Asymmetric Drift-Orbit Bifurcation:
Models and Observations

by

Sergei Railevich Kamaletdinov
Doctor of Philosophy in Geophysics and Space Physics
University of California, Los Angeles, 2026
Professor Vassilis Angelopoulos, Chair

Understanding the dynamics of energetic electron fluxes in Earth's radiation belts remains one of the key challenges in Heliophysics. The two most studied mechanisms contributing to these dynamics are (1) wave–particle resonant interactions, which can accelerate and pitch-angle scatter electrons, and (2) radial diffusion driven by ultra-low-frequency (ULF) waves. Yet, observations often reveal behaviors that cannot be fully explained by these two processes. In particular, they necessitate considering radial transport mechanisms that go beyond classical diffusion. Radial transport can arise even in the absence of waves, solely due to the topology of magnetic field lines. This mechanism is known as Drift-Orbit Bifurcation (DOB), which occurs on the dayside, where solar wind compression splits the equatorial magnetic field minimum into two off-equatorial minima, violating the second adiabatic invariant and enabling radial transport. This mechanism has been investigated for magnetic field configurations exhibiting north–south symmetry relative to the geomagnetic equator and east–west symmetry relative to the noon meridian. Although asymmetric magnetic field configurations occur in nature as a rule rather than an exception, studies quantifying the radial transport associated with these asymmetries—either through case studies or statistical analyses—are still lacking.

This thesis presents a quantitative investigation of the role of magnetospheric asymmetry

in drift-orbit bifurcation. Specifically, it addresses three key questions: (1) the importance of east–west and north–south magnetic field asymmetries in the scattering and radial transport of electrons undergoing drift-orbit bifurcation, (2) the radial transport arising from this asymmetric drift-orbit bifurcation, and (3) the energy range of electrons for which the effects of such transport are comparable to ULF-driven diffusion. To address these questions, we combine (1) empirical magnetospheric magnetic field models driven by realistic solar wind conditions, (2) observations from the THEMIS spacecraft, and (3) the theoretical framework of adiabatic invariant destruction during separatrix crossings. Including realistic magnetospheric asymmetries, driven by a nonzero IMF B_y and dipole tilt, leads to larger jumps in adiabatic invariants and enhances radial transport driven by drift-orbit bifurcation. The developed theoretical framework explains these large jumps as the so-called *geometric* jumps of adiabatic invariants, known in the theory of Hamiltonian systems with an asymmetric separatrix in phase space. Using empirical magnetic field models, these jumps are quantified under various solar wind conditions. Approximating these jumps via a model (lower-dimensional) Hamiltonian system, we study its long-term dynamics and find distinctly fast, non-diffusive transport occurring on timescales comparable to or shorter than those driven by ULF waves for electrons with energies above 0.1–1 MeV. Combining THEMIS observations of dayside magnetopause–outer radiation belt crossings with guiding center simulations under realistic (asymmetric) magnetic field configurations, we show that these large jumps can explain isolated enhancements in energetic electron fluxes occurring near the magnetopause. These findings establish the critical role of magnetic field asymmetry in particle radial transport, advancing our understanding of the mechanisms controlling energetic electron dynamics in the dayside magnetosphere.

The dissertation of Sergei Railevich Kamaletdinov is approved.

Anton Vladimirovich Artemyev

Eduardo Paulo Da Costa Alves

Hao Cao

Marco C.M. Velli

Vassilis Angelopoulos, Committee Chair

University of California, Los Angeles

2026

— Мы сами знаем, что она не имеет решения, — сказал Хунта, немедленно ощетиниваясь. — Мы хотим знать, как её решать.

— Как-то ты странно рассуждаешь, Кристо... Как же искать решение, когда его нет? Бессмыслица какая-то...

— Извини, Теодор, но это ты очень странно рассуждаешь. Бессмыслица — искать решение, если оно и так есть. Речь идёт о том, как поступать с задачей, которая решения не имеет. Это глубоко принципиальный вопрос, который, как я вижу, тебе, прикладнику, к сожалению, не доступен.

-Аркадий и Борис Стругацкие: «Понедельник начинается в субботу»

— 'We know it has no solution,' said Junta, instantly bristling. 'What we want to know is how to go about solving it'.

— That's a strange way of thinking, Cristo... How can you look for a solution when there is none? That makes no sense...

- Sorry, Theodore, but it's you who's thinking strangely. What does not make sense is searching for a solution when there already is one. What we're talking about here is how to deal with a problem that has no solution. This is a deeply fundamental question — and unfortunately, as I see, a practical mind like yours is unable to comprehend it.

-Arkady and Boris Strugatsky, «Monday Begins on Saturday»

Table of Contents

1 Introduction **1**

1.1 Inner Magnetosphere Processes 5

1.2 Charged Particle in Electromagnetic Field 8

1.2.1 Guiding-Center Approximation and the First Adiabatic Invariant . . 9

1.2.2 Bounce Motion and the Second Adiabatic Invariant 13

1.2.3 Cross-Field Drift and the Third Adiabatic Invariant 17

1.2.4 Hamiltonian Description of the Guiding-Center Motion 18

1.3 Adiabatic Invariant 20

1.3.1 Improved Adiabatic Invariant 23

1.3.2 Jumps of Adiabatic Invariant: Separatrix Crossing 25

1.4 Source and loss processes 31

1.4.1 Radial Transport and Diffusion 36

1.4.2 Drift-Orbit Bifurcation 40

1.5 Thesis Organization 48

2 Asymmetric Drift-Orbit Bifurcation and Geometric Jumps of Adiabatic Invariant **50**

2.1 Magnetospheric Asymmetry and IMF B_y 51

2.1.1 Solar Wind Conditions at 1 AU: ARTEMIS dataset 51

2.1.2 Drift Orbit 52

2.1.3 Separatrix 55

2.1.4 Magnetic Field Model . . . 59
2.2 Violation of Adiabaticity . . . 61
2.2.1 Model Hamiltonian . . . 61
2.2.2 Evolution of the Adiabatic Invariant . . . 63
2.2.3 Geometric Jumps . . . 67
2.2.4 Non-conservative Hamiltonian . . . 69
2.2.5 Mapping . . . 72
2.3 Radial Transport due to Geometric Jumps . . . 73
2.4 Discussion and Summary . . . 76

3 Energetic Electron Enhancements Near the Dayside Magnetopause: Outward Radial Transport Due to Asymmetric Drift-Orbit Bifurcation . . . 86
3.1 Observations . . . 87
3.2 Simulations . . . 90
3.2.1 Magnetic Field Model . . . 90
3.2.2 Guiding Center Test-Particle Simulations . . . 92
3.3 Discussion and Summary . . . 95

4 Long-Term Dynamics and Non-Diffusive Radial Transport Driven by Geometric Jumps . . . 104
4.1 Model . . . 105
4.1.1 Hamiltonian with $1\frac{1}{2}$ degrees of freedom . . . 105
4.1.2 Mapping . . . 109
4.1.3 Stationary Distribution and Convergence . . . 111

4.2 Comparison with Radial Diffusion . . . 113
4.2.1 Equivalent Radial Diffusion . . . 113
4.2.2 Comparison with ULF-driven Diffusion . . . 114
4.3 Summary . . . 115

5 Summary and Future Directions . . . 124
5.1 Research Summary . . . 124
5.2 Future Work . . . 127
5.2.1 Statistical Study of Energetic Electron Enhancements Near the Dayside Magnetopause . . . 128
5.2.2 Estimation of the Equivalent Radial Diffusion Rate in a Realistic Magnetic Field Model . . . 129
5.2.3 Role of Temporal Variation in Solar Wind Parameters in Asymmetric Drift-Orbit Bifurcation . . . 130

References . . . 133

List of Figures

1.1 Schematic representation of the Sputnik-2 and Explorer-3 orbits. The red and blue shaded regions indicate the approximate radial locations of the inner (proton) and outer (electron) radiation belts, respectively. For the outer radiation belt, its (inner edge) polar projection along the dipole magnetic field lines is also shown. 2

1.2 Energy flow in the magnetosphere. By Hiroshi Hasegawa, Naritoshi Kitamura, retrieved from `www.isas.jaxa.jp` 6

1.3 Schematic representation of a separatrix and a saddle point. 25

1.4 Three periodic motions in the inner magnetosphere: (a) actual motion of a 1 MeV electron with an artificial mass of 20× the electron mass (for visualization), (b) gyro-motion around the field line, (c) bounce motion along the field line between the mirror points, and (d) drift motion of the gyrocenter. From [Ukhorskiy and Sitnov, 2013] 32

1.5 Typical time scales (frequencies) of three periodic motions in the inner magnetosphere. From [Schulz and Lanzerotti, 1974] 34

1.6 Test-particle simulation of electron radial transport driven by Ultra-Low-Frequency waves. The four upper panels show the electron radial distribution $F(L,t)$ at four moments in time. The lower panels show histograms of L at these same moments. Panel (B) shows $\langle \Delta L^2 \rangle$ calculated over an electron ensemble: a diffusive trend $\langle \Delta L^2 \rangle \propto D_{LL} t$ is observed. From [Ukhorskiy and Sitnov, 2013] 36

1.7 Schematic view of DOB [magnetic field lines from [Tsyganenko and Sitnov, 2005]]. From [Kamaletdinov et al., 2025b] 41

2.1 Distribution of the solar wind parameters collected during 12 years of ARTEMIS observations at 1 AU [Angelopoulos, 2011]: (a) Probability density function (PDF) of the solar wind ram pressure, P_{dyn}, (b) PDF of the magnitude of the solar wind magnetic field, IMF B, (c) PDF (angular diagram) of the angle $\varphi_{\rm IMF} = atan({\rm IMF}B_z/{\rm IMF}B_y)$. 52

2.2 Configuration of the inner magnetosphere based on the TS04 model [Tsyganenko and Sitnov, 2005] with solar wind parameters, $P_{dyn} = 4$ nPa, IMF $B = 5$ nT and $\varphi_{\rm IMF} = 160°$: (a) drift orbit of an equatorially mirroring particle (gray) started at $r_0 \approx 6.8$ R_E at the midnight ($L_B = 7.3$), black line shows position of the magnetopause, blue dots show magnetic local time (MLT) sectors of $0, 10, 14$, (b) magnetic field strength along the field line at MLT $= 0$, red line shows $\varphi_{\rm IMF} = 20°$ and green line shows $\varphi_{\rm IMF} = 160°$, (c) magnetic field strength along the field line at MLT $= 10$, (d) magnetic field strength along the field line at MLT $= 14$. 56

2.3 A schematic of the separatrix in a double-well potential: a) typical W-shape magnetic field strength profile $B(s)$ (effective potential, see Hamiltonian (2.9)), b) associated phase space of (s, P) with phase trajectories (gray) given by Hamiltonian (2.9). 80

2.4 Comparison of magnetic field strength profiles along the drift orbit (Fig. 2.2 with $\phi_{\rm IMF} = 225°$, TS04 [Tsyganenko and Sitnov, 2005]) with the model (Eq. 2.7) at $L_B = 7.3$. a) Magnetic field along the field lines at three MLTs along the the drift orbit (Fig. 2.2), b) Magnetic field along the field lines at the same MLTs yielded by Eq. 2.7, c) TS04-based MLT profiles of the phase areas (apart from a factor p) enclosed inside the main pocket (S_m), adjacent pocket (S_a), and the total area inside the separatrix $S = S_m + S_a$, d) same MLT profiles of S, S_m and S_a yielded by Eq. 2.7. 81

2.5 Test-particle simulation according to Hamiltonian (2.13) with $\varepsilon = 10^{-3}$ and initial conditions, $s(0) = 0$ and $P(0) = \cos\alpha_{eq}$ with $\alpha_{eq} = 66°$: a) test-particle trajectory, $\mathcal{S}(\varepsilon t)$, as a function of slow time (gray), two mirror points,$s_{1,2}$ (blue and red), computed as $H(s_{1,2}, 0; \varepsilon t) = H(s(\varepsilon t), P(\varepsilon t); \varepsilon t)$ from Hamiltonian (2.13), b) phase trajectory of the test-particle in (s, P) for 4 intervals of slow time; $\varepsilon t < 1$ (blue), $\varepsilon t \in [10, 11]$ (green), $\varepsilon t \in [11, 12]$ (violet), and $\varepsilon t > 20$ (dark red), c) adiabatic invariant as a function of slow time, $\mathcal{I}(\varepsilon t)$ (red), total area inside the separatrix, $\mathcal{S}(\varepsilon t)$ (black), phase-area inside the adjacent pocket, $\mathcal{S}_a(\varepsilon t)$ (blue), blue-dashed lines show results of Mapping (2.18), gray lines signify particle trapping and detrapping. Note that $\mathcal{S}$ and $\mathcal{S}_a$ are smaller by a factor of $\sin\alpha_{eq} \approx 0.91$ compared to S and S_a, as shown in Fig. 2.4d. See details in Section 2.2.4. 82

2.6 Evolution of the adiabatic invariant, comparison between test-particle simulations governed by Hamiltonian (2.13) with $\varepsilon = 10^{-4}$ and the result of Mapping (2.18) for different initial values of the adiabatic invariant ($\mathcal{I}$ defined via Eq. 2.10), a) $\mathcal{I}_0 = 0.48$, b) $\mathcal{I}_0 = 0.07$ c) $\mathcal{I}_0 = 1.37$ reflecting different equatorial pitch angles, a) $\alpha_{eq} = 76°$, b) $\alpha_{eq} = 85°$, c) $\alpha_{eq} = 66°$. Panel (d) shows distribution of $\Delta\mathcal{I}(\mathcal{I}_0)$ for $\mathcal{I}_0 \in [0, 3.4]$ from test-particle simulations (red) and results of Mapping (2.18), assuming trapping in the main (green) and adjacent (blue) pockets. Panel (e) shows geometric jumps in terms of $I = J_{||}/p$ obtained by applying Mapping (2.18) to TS04 profiles of the phase-areas shown in Fig. 2.4c. 83

2.7 Radial transport due to asymmetric drift-orbit bifurcation as estimated in the TS04 magnetic field model (P_{dyn} = 4 nPa, IMF B = 5 nT, $\varphi_{\rm IMF}$ = 225°, zero tilt). Panel (a) shows jumps (red/blue) from the drift orbit with $L_B = 7.3$ in L_B–I space. Adiabatic invariant jumps, $\Delta_{m,a}I$, are computed via Mapping (2.23) and converted to radial displacements, $\Delta_{m,a}L$, using transport characteristics (B_m = const, gray). Black lines mark bifurcation boundaries. Panel (b) shows equatorial pitch-angle ranges, α_{eq} (MLT= 6), subject to bifurcation vs. L_B. Red/blue curves correspond to maximum positive/negative jumps, Δ_+I and $\Delta_-I < 0$. Panel (c) shows corresponding radial jumps $\Delta_\pm L$ (Eq. 2.26). The top axis gives $r_{\rm MLT=6}$. 84

2.8 Magnitude of the radial displacement (Eqs. 2.25 and 2.26) from different drift orbits as a function of the solar wind parameters; a) IMF $B = 5$ nT, $P_{\rm dyn} = 4$ nPa, and $\varphi_{\rm IMF} \in [0, 360°]$, b) IMF $B = 5$ nT, $\varphi_{\rm IMF} = 180°$, and $P_{\rm dyn} \in [1, 6]$ nPa, c) $P_{\rm dyn} = 4$ nPa, $\varphi_{\rm IMF} = 180°$, and IMF $B \in [1, 8]$ nT 85

3.1 Crossings of the dayside magnetopause and the outer radiation belt by THEMIS-A and THEMIS-D spacecraft on October 1, 2018, from 8 to 16 UT. Concurrent measurements of the solar wind conditions are provided by THEMIS-C of the ARTEMIS mission. (a) Spacecraft trajectories in the GSM xy-plane. (b) Magnetic field in the GSM system of coordinates measured by THEMIS-A. (c) SST-based omnidirectional electron fluxes measured by THEMIS-A, energy channels from 30 keV to ∼ 700 keV. (d) spacecraft position in terms of MLT-sector, L_B (see Eq. 2.1), and L_{IGRF} (≈ dipole L-shell) parameters. (e,f,g) Data in the same format obtained by THEMIS-D. (h) Solar wind dynamic pressure. (i) Interplanetary Magnetic Field in the GSM system. 98

3.2 The magnetic field model, $\boldsymbol{B} = \boldsymbol{B}_{\rm int} + \boldsymbol{B}_{\rm ext}$. (a) Magnetic field lines of $\boldsymbol{B}_{\rm int}$ (with $\theta = 1°$, Eq. 3.1) and $\boldsymbol{B}_{\rm ext}$ (with $D = 12\mathrm{R_E}$ and $\phi = 4°$, Eqs. 3.2-3.3). Color indicates the magnetic field strength in nT. (b) Magnetic field lines of $\boldsymbol{B}_{\rm int} + \boldsymbol{B}_{\rm ext}$ in the $y = 0$ plane, with color indicating the field strength in nT. MLT profiles of the phase space areas enclosed within the separatrix, $S = 2\int_{s_1^*}^{s_2^*} \sqrt{1 - B(s)/B_{\rm max}} ds$, along the drift orbit with $L_B = 7.5$ (see Chapter 2): (c) using the TS04 [Tsyganenko and Sitnov, 2005] magnetic field with $P_{dyn} = 2.55$ nPa, IMF $B_z = 1.6$ nT, and $B_y = 5.1$ nT, reflecting the solar wind conditions at 12:31 UT; (d) model-based magnetic field. Magnetic field strength profile along the field line at (e) MLT = 0, (f) MLT = 12. Here, $s = 0$ is the position of the equatorially mirroring particle, $B_{\rm max} = B(s^*)$ is the local maximum of the magnetic field strength, and $s^*_{1,2}$ satisfy $B(s_{1,2}) = B_{\rm max}$. . . 99

3.3 Three types of bifurcated trajectories calculated with Eqs. 3.5 in the magnetic field model $\boldsymbol{B} = \boldsymbol{B}_{\rm int} + \boldsymbol{B}_{\rm ext}$ with parameters from Fig. 3.2. The left column shows the guiding-center trajectory in three dimensions (Earth in the center; the dayside is shown in grey), while the right column shows the evolution of the second adiabatic invariant, $I = \oint \sqrt{1 - B(s)/B_m} ds$. In both columns, color indicates the value of I. Note the remarkable similarity to Fig. 2.6 from Chapter 2, obtained using the mapping in the [Tsyganenko and Sitnov, 2005] model. 100

3.4 Simulation of electron transport driven by asymmetric drift-orbit bifurcation. An ensemble of $\approx 35,000$ electrons (energy: 51 keV) is used. The magnetic field is given by $\boldsymbol{B}(\boldsymbol{r},t) = \boldsymbol{B}_{\text{int}}(\boldsymbol{r}) + \boldsymbol{B}_{\text{ext}}(\boldsymbol{r},t)$, with $\phi(t) = 4^\circ \cdot \tanh(t/\tau)$ and $D(t) = 22\text{R}_\text{E} - 10\text{R}_\text{E} \cdot \tanh(t/\tau)$ with $\tau = 1$ hour (see Eqs. 3.1-3.4). (a) Change of ϕ-angle (blue) and the first bifurcated drift orbit over time. (b) Distribution of electron equatorial foot points at $t = 0$. (c) Distribution of electron equatorial foot points at $t = 4.5$ hours. (d) Radial distribution (in L_B) of electron crossings in the MLT = 0 sector. (e) Radial distribution of electron crossings in the MLT = 15 sector. The gray line shows the result accumulated at $t < 1$ hour, while the black line represents the accumulation at $t \in [4,5]$ hours. 101

3.5 Radial transport of electrons driven by asymmetric drift-orbit bifurcation in a *static* magnetic magnetic field configuration identical to the final ($t \gg 1$ hour) configuration from Fig. 3.4: the ensemble setting: 35,000 nearly equatorially mirroring electrons (initial equatorial pitch-angle is 85° with energy of 51 keV). The magnetic field is given by $\boldsymbol{B}(\boldsymbol{r}) = \boldsymbol{B}_{\text{int}}(\boldsymbol{r}) + \boldsymbol{B}_{\text{ext}}(\boldsymbol{r})$, with $\phi = 4^\circ$ and $D = 12\text{R}_\text{E}$. (a) ϕ-angle (blue) and the first bifurcated drift orbit. (b) Distribution of electron equatorial foot points at $t = 0$. (c) Distribution of electron equatorial foot points at $t = 2.5$ hr. (d) Radial distribution (in L_B) of electron crossings in the MLT = 0 sector. (e) Radial distribution of electron crossings in the MLT = 15 sector. The gray line shows the initial distribution, while the black line represents the accumulation of particle crossing the respective MLT-sector at $t \in [2,3]$ hr. 102

3.6 Evolution of the (normalized) second adiabatic invariant, $I = \oint \sqrt{1 - B(s)/B_m} ds$, during one complete drift period for particles of three different energies: 50, 500, and 10,000 keV. Results are shown for an East–West symmetric magnetic field configuration (red lines: $\theta = 0°$, $\phi = 0°$) and an East–West asymmetric configuration (blue lines: $\theta = 0°$, $\phi = 2°$). All particles are initialized at midnight at the radial distances of $L_B = 7.5$. 103

4.1 Hamiltonian (4.1.2) for (a) $\eta = -3/20$ and (b) $\eta = -(3/20)(1/4 + \sin^3 \varphi)$. Panels: (1) potential $U(x, \varphi)$ at different φ, (2) separatrix in the phase-space of (x, p), (3) phase-space areas enclosed within two pockets [$S^{\pm}$, Eq. 4.4] and within the separatrix (S). 107

4.2 Comparison of the separatrix phase-space areas from the empirical magnetic field model [Tsyganenko and Sitnov, 2005], as calculated in Chapter 1 (see Fig. 2.4), and the separatrix phase-space areas of Hamiltonian (4.1.2) as given by Eq. 4.4. (a) Azimuthal profile of the phase-space area enclosed within the separatrix based on the empirical magnetic field model, reproduced from Fig. 2.4. (b) Epoch analysis (gray lines) of the geometric jumps $\Delta S(I_0)$ for $L \in [6.5, 8.0]$, normalized to the maximum separatrix area at each respective L; the black line shows the averaged profile. (c) Azimuthal profile of the phase-space area enclosed within the separatrix based on the model Hamiltonian (Eqs. 4.1.2-4.4).(d) Normalized geometric jumps, $\Delta S(I_0)$, for the model Hamiltonian (Eqs. 4.1.2-4.4). 117

4.3 Three types of jumps in the adiabatic invariant observed in Hamiltonian (4.1.2). Note the remarkable similarity to Fig. 2.6 from Chapter 2, obtained using the mapping in the [Tsyganenko and Sitnov, 2005] model, and to Fig. 3.3 from Chapter 3, obtained from full-dimensional guiding-center simulations. 118

4.4 Radial dependence of the maximum phase-space area enclosed within the separatrix, $S_{\max} = \max_{\varphi}(S^+ + S^-)$, and within its pockets, $S^{\pm}$, using [Tsyganenko and Sitnov, 2005] magnetic field model, as calculated in Chapter 2 (see Fig. 2.7) with IMF $B = 5$ nT, $\varphi_{\rm IMF} = 225°$, zero tilt angle and: (a) $P_{dyn} = 2$ nPa, (b) $P_{dyn} = 4$ nPa. Linear trends $S_{max} = 3.1(L - 7.1)$, $S^{\pm} = 1.55(L - 7.1)$ and $S_{max} = 3(L - 6.3)$, $S^{\pm} = 1.5(L - 6.3)$ are shown for reference. 119

4.5 Evolution of 10^5 particles with $I_0 = 1$ under Mapping (4.5) (gray) and Hamiltonian (4.1.2) (red), solved for $\varepsilon = 10^{-4}$. Panels: (1) evolution of I for one test particle (red) and five mapping trajectories (gray); (2) PDF of I; (3–5) Poincaré sections in (x, p) after different number of iterations. Black dashed lines show the initial $I = 1$ and upper boundary of the bifurcation domain, $I = S_{\max}$. 120

4.6 Evolution of $F_0 = \theta(I - I_0)$ (10^6 particles) under Mapping (4.5) for different values of I_0: (a) deviation from uniform distribution, Δ_n, with the red dashed line showing exponential decay; (b), (c), (d) evolution of the cumulative distribution, with the dashed line showing the cumulative distribution of a uniform distribution $F = I/S_{\max}$ over $I \in [0, S_{\max}]$. 121

4.7 (a) Azimuthal profile of the phase-space area enclosed within the separatrix, based on the model Hamiltonian (4.1.2). (b) Evolution of the deviation from the uniform distribution, $\Delta_n = \langle |F_n(I) - I/S_{max}| \rangle$, where F_n is the cumulative distribution in I after n iterations, under the mapping associated with the model Hamiltonian (4.1.2) for different values of the initial adiabatic invariant ($F_0 = \theta(I - I_0)$, where θ is the Heaviside step function). Exponential decay $\propto \exp(-n/19)$ is shown as the best common fit for both curves. (c) Same as in (a), but for a re-scaled Hamiltonian $x \to x/4$, resulting in a self-similar increase of the phase-space areas by a factor of 4: $S \to 4 \cdot S$ and $S^{\pm} \to 4 \cdot S^{\pm}$. (d) Same as in (b), but for the re-scaled Hamiltonian $x \to x/4$. The rate of phase-space mixing, quantified by $\mathcal{N}$, remains invariant under separatrix re-scaling. . . . 122

4.8 Effective radial diffusion coefficient, $D_{LL}[\text{days}^{-1}] = 0.08L(L - L_{min})^2(\gamma - \gamma^{-1})$, with $\mathcal{N} \approx 20$ and $\tau_d[\text{days}] \approx 0.12L(\gamma - \gamma^{-1})^{-1}$ from [Schulz and Lanzerotti, 1974]: (a) results for $L_{min} = 6$, representative of a solar wind dynamic pressure of $\gtrsim 4$ nPa; (b) results for $L_{min} = 7$, representative of a solar wind dynamic pressure of ≈ 2 nPa. In both panels, thick colored lines show D_{LL} for electron kinetic energies of 50, 500, and 5000 keV. Dashed lines show empirical values of ULF-driven D_{LL} from [Brautigam and Albert, 2000] and [Ozeke et al., 2014] for K_p-index values of 1, 2, and 3. 123

5.1 ELFIN-A and ELFIN-B observations of $\gtrsim$ 100 keV electron enhancements near the dayside magnetopause on 07-Jun-2021. (a) Precipitating electron flux from ELFIN-B (04:42–04:47 UT). (b) Equatorial field line projection: L_{IGRF} ($\sim$ dipole L-shell) and L_B (Eq. 2.1); right axis: MLT. (c) Precipitating flux from ELFIN-A (08:27–08:33 UT). (d) Same as (b) for ELFIN-A. (e) Equatorial projections of ELFIN-A/B and THEMIS-B (ARTEMIS) in IGRF and IGRF+TS04 [Tsyganenko and Sitnov, 2005] fields. (f) Solar wind magnetic field at THEMIS-B (GSM). (g) Solar wind dynamic pressure, P_{dyn}. 131

5.2 CIRBE and NOAA-19 (POES) observations of energetic electron enhancement (trapped population) near the dayside magnetopause on 25-Apr-2023. (a) integral electron number flux measured by CIRBE ($>$ 300 keV) and NOAA-19 ($>$ 130 keV), projected onto the $Z_{GSM} = 0$ plane between 19:55–20:01 and 19:19–19:43 UT, respectively. (b) The same projection of the respective spacecraft measurements between 21:30–21:55 and 21:00–21:24 UT. Grey dashed lines show the approximate magnetopause location and the drift orbits of equatorially mirroring electrons (both based on the [Tsyganenko, 1995] magnetic field model). (c) Integral flux from panel (b) shown in terms of radial profiles (as a function of L-shell); for comparison, CIRBE measurements from panel (a) are also shown. For NOAA-19, integral flux $>$ 40 and 287 keV is also shown with dashed lines. (d) Differential electron number flux from CIRBE as a function of L (measurements between 21:30–21:55 UT). (e,f) Solar wind dynamic pressure (e) and IMF B_y and B_z components (f) between 19:30 and 22:30 UT (OMNI data, [King and Papitashvili, 2005]). 132

Acknowledgments

This thesis would have been impossible without the support of many people whose help and advice along the way shaped it into its present form. First and foremost is my scientific advisor, Professor Vassilis Angelopoulos, to whom both this thesis and I are greatly indebted, as he taught me to always set the highest standards for my scientific work and to do my best to achieve them.

I also wish to express my deep gratitude to Professors Anton Vladimirovich Artemyev and Ivan Yurievich Vasko, as well as to all my friends and former colleagues at IKI, who invested an incredible amount of effort in me long before there were any signs that these efforts might not be entirely fruitless.

I am also deeply indebted to my loved ones for their support, and especially to my mother, whose encouragement at the very first steps leading to this point cannot be overstated.

This thesis is largely based on data from the NASA THEMIS mission, supported under contract NAS5-02099. I also gratefully acknowledge financial support from UCLA through the Dissertation Year Award (DYA), which allowed me to focus fully on the preparation of this thesis during the last nine months.

Vita

2017–2021	B.S. (Physics), Moscow State University
2021–2023	M.S. (Space Physics), HSE University
2023–present	Doctoral Candidate (Ph.D., Expected 2026), Geophysics and Space Physics, University of California, Los Angeles

Publications

1. Kamaletdinov, S. R., Artemyev, A. V., Angelopoulos, V. (2025). Energetic electron enhancements near the dayside magnetopause: Outward radial transport due to asymmetric drift-orbit bifurcation. Geophys. Res. Lett. doi.org/10.1029/2025GL116514

2. Kamaletdinov, S. R., Artemyev, A. V., Neishtadt, A. I., Angelopoulos, V. (2025). Charged particle cross-field transport due to geometric jumps of adiabatic invariant. Phys. Rev. Lett. doi.org/10.1103/nsg2-scpg

3. Kamaletdinov, S. R., Artemyev, A. V., Runov, A., Angelopoulos, V. (2025). Ion kinetics in thin current sheets at lunar distances. Geophys. Res. Lett. doi.org/10.1029/2024GL114522

4. Kamaletdinov, S. R., Artemyev, A. V., Angelopoulos, V., Neishtadt, A. I. (2024). Electron scattering due to asymmetric drift-orbit bifurcation: Geometric jumps of adiabatic invariant. J. Geophys. Res.: Space Phys. doi.org/10.1029/2024JA032987

5. Kamaletdinov, S. R., Artemyev, A. V., Runov, A., Angelopoulos, V. (2024). Characteristics of thin magnetotail current sheet plasmas at lunar distances. J. Geophys. Res.: Space Phys. doi.org/10.1029/2024JA032755

6. Kamaletdinov, S. R., Vasko, I. Y., Artemyev, A. V. (2024). Nonlinear electron scattering by electrostatic waves in collisionless shocks. J. Plasma Phys. doi.org/10.1017/S0022377824000217

7. Kamaletdinov, S. R., Artemyev, A. V., Runov, A., Angelopoulos, V. (2024). Thin current sheets in the magnetotail at lunar distances: Statistics of ARTEMIS observations. J. Geophys. Res.: Space Phys. doi.org/10.1029/2023JA032130

8. Kamaletdinov, S. R., Vasko, I. Y., Wang, R., Artemyev, A. V., Yushkov, E. V., Mozer, F. S. (2022). Slow electron holes in the Earth's bow shock. Phys. Plasmas doi.org/10.1063/5.0102289

9. Kamaletdinov, S. R., Vasko, I. Y., Artemyev, A. V., Wang, R., Mozer, F. S. (2022). Quantifying electron scattering by electrostatic solitary waves in the Earth's bow shock. Phys. Plasmas doi.org/10.1063/5.0097611

10. Kamaletdinov, S. R., Hutchinson, I. H., Vasko, I. Y., Artemyev, A. V., Lotekar, A., Mozer, F. S. (2022). Spacecraft observations and theoretical understanding of slow electron holes. Phys. Rev. Lett. doi.org/10.1103/physrevlett.127.165101

11. Kamaletdinov, S. R., Yushkov, E. V., Artemyev, A. V., Lukin, A. S., Vasko, I. Y. (2020). Superthin current sheets supported by anisotropic electrons. Phys. Plasmas doi.org/10.1063/5.0018063

CHAPTER 1

Introduction

On 4 October 1957, the first human-made satellite, Sputnik-1, set forth from Launch Site No. 1 (later known as Gagarin's Start) at the Baikonur Cosmodrome. Despite being essentially just a radio beacon, Sputnik-1 opened a previously unseen avenue for space exploration and was followed one month later by Sputnik-2, equipped with a set of scientific instruments, including Geiger–Müller tubes designed by Sergei Nikolaevich Vernov. With extensive experience studying galactic cosmic rays—ultrarelativistic particles originating from the Sun and deep space—using ground-based and balloon experiments, Vernov and his team quickly recognized the potential of above-atmosphere measurements. The Geiger–Müller tubes onboard Sputnik-2 provided the team with 10 days' worth of particle count-rate data. Much to the team members' surprise, the instrument registered significantly higher count rates than expected for galactic cosmic rays especially at high latitudes [Vernov et al., 1958a, Vernov et al., 1958b, Vernov and Chudakov, 1960]. The first interpretation by Vernov's team attributed this enhanced radiation to the arrival of energetic solar particles from a recent solar flare (see the historical review by [Baker and Panasyuk, 2017]).

Just a few months later, these first satellites were followed by Explorer-1 and Explorer-3, carrying scientific instruments built and designed by James Van Allen at the State University of Iowa, including Geiger–Müller tubes designed by George Harry Ludwig. The Geiger–Müller tubes onboard the Explorer spacecraft exhibited the same unexpected pattern: periods during which the count rate matched that expected for cosmic rays, other periods with much higher counts, and still other intervals when it dropped to zero. After careful laboratory calibration,

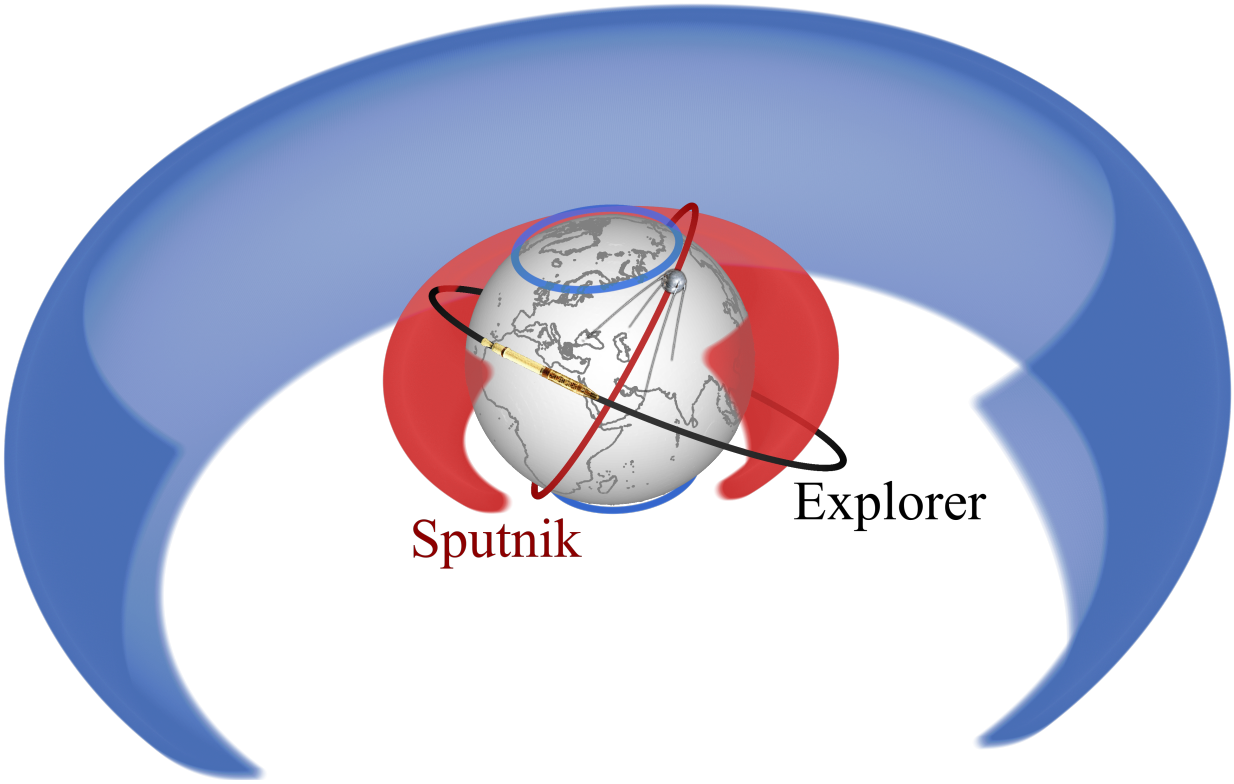

Figure 1.1: Schematic representation of the Sputnik-2 and Explorer-3 orbits. The red and blue shaded regions indicate the approximate radial locations of the inner (proton) and outer (electron) radiation belts, respectively. For the outer radiation belt, its (inner edge) polar projection along the dipole magnetic field lines is also shown.

the only reasonable explanation was that the satellites were encountering extremely high fluxes of particles near the equator—fluxes at least a thousand times higher than those expected from cosmic rays [Van Allen et al., 1958]. The discovery and its striking interpretation were presented by Van Allen at the meeting of the National Academy of Sciences and American Physical Society in May 1958 [Van Allen, 1958].

These first observations were swiftly followed and expanded upon after the launch of Sputnik-3, which carried the largest set of scientific instruments to date, including a scintillation detector proposed by Alexander Yevgenievich Chudakov, capable of detecting

>30 MeV protons and ~ 100 keV electrons. The relatively high inclination of the Sputnik orbit (65°, compared to Explorer's 33°, see Fig. 1.1) led to the important discovery that polar regions above 60° latitude were primarily populated by ~ 100 keV electrons, while equatorial regions contained ~ 100 MeV protons [Vernov et al., 1959, Vernov and Chudakov, 1960].

The double-belt structure was shortly thereafter observed by Explorer-4 and Pioneer-3 [van Allen and Frank, 1959]. By the end of 1958, the term "*radiation belt*" for describing these (as we now know, radially) confined regions of high proton and electron flux trapped on magnetic field lines was already established. These two regions of stable trapped particles would later become known as the inner and outer radiation belts. Since the first observations by the Sputnik and Explorer spacecraft, the radiation belts remain one of the central topic in geophysics, and the importance of understanding their dynamics was growing as crewed spacecraft began venturing beyond Earth and communication satellites kept occupying near-Earth orbits. Interestingly, the possibility of permanently trapped trajectories of charged particles in the terrestrial magnetic field was first pointed out by [Størmer, 1937, Störmer, 1955], nearly two decades before the observations of Vernov and Van Allen. Moreover, in the same year, 1957—just prior to the discovery of the radiation belts—Nicholas Christofilos proposed the possibility of an *artificial* stable belt of injected electrons (see [Melissinos, 1993] and references therein).

Nowadays, the physics of the radiation belts still poses many challenging questions, serving as a source of fruitful debate within the scientific community. In particular, understanding the mechanisms contributing to the large variability of electron fluxes inside the radiation belts and the acceleration of electrons from keV to MeV energies remains an active and not-yet-fully resolved problem. Predicting the fluxes and spatial distribution of $\gtrsim 1$ MeV electrons is important from a practical standpoint, as these so-called "Killer Electrons" pose significant risks to the ever-growing constellations of communication satellites in geosynchronous orbit [Horne, 2007, Horne et al., 2018]. The two most often invoked mechanisms explaining electron

energization are: (1) radial transport and (2) local acceleration [Green and Kivelson, 2004]. The first mechanism relies on electrons undergoing inward (Earthward) transport due to interactions with ultra-low-frequency (ULF, $\sim$ mHz) electric and magnetic field fluctuations (waves) [Elkington et al., 1999]. This Earthward transport into regions of stronger magnetic fields, which often takes the form of slow radial "diffusion," results in energization. The second mechanism relies on local (essentially along a single field line) acceleration of electrons interacting with various high-frequency electromagnetic waves via cyclotron resonance [Horne and Thorne, 1998]. However, the actual dynamics of the radiation belts often do not perfectly fit into these two frameworks. Observations indicate that reproducing the inferred radial transport often requires going beyond conventional diffusion-based models (see discussion in [Shprits et al., 2015, Osmane et al., 2023, Lejosne et al., 2024]). One such mechanism contributing to electron radial transport is the drift–orbit bifurcation, which has recently received renewed attention [Öztürk and Wolf, 2007, Ukhorskiy et al., 2011, Luo et al., 2024]. This mechanism relies on electrons intersecting magnetic field lines with split magnetic field minima at the outer edge of the dayside outer radiation belt. Despite a long history of studies indicating its importance for electrons in the outer radiation belt, investigations assessing its role under realistic magnetic field configurations remain severely lacking. Such realistic conditions include accounting for the effects of Earth's magnetic dipole tilt and the variable orientation of the interplanetary magnetic field, i.e., the solar magnetic field carried toward Earth by the solar wind (see discussion in 1.1). These effects result in magnetic field configurations that significantly deviate from an ideal dipole field and lack both east–west and north–south symmetry. The absence of these symmetries, in turn, profoundly alters the topology of magnetic field lines, which is the primary element determining the characteristics of the drift–orbit bifurcation mechanism.

This thesis aims to quantify the role of Drift-Orbit Bifurcation in electron radial transport, with a particular focus on realistic east–west and north–south asymmetric magnetic field configurations. The first, introductory, chapter provides the necessary background information

upon which we will build in the following chapters. Section 1.1 provides an overview of the main regions in the inner magnetosphere and the processes linking radiation belt dynamics to the overall dynamics of the magnetosphere and the solar wind as its ultimate driver. Section 1.2 establishes the main mathematical framework used to describe charged particle motion in the inner magnetosphere, introducing the concepts of the three main periodic motions and their associated adiabatic invariants. Section 1.3 provides the necessary mathematical toolkit for describing destruction (jumps) of the adiabatic invariant, which will be especially relevant in Chapters 2 and 4. Section 1.4 expands upon the concept of radial diffusion and provides a rigorous treatment of the drift-orbit bifurcation mechanism, drawing on the mathematical toolkit developed in Sections 1.2 and 1.3. Finally, Section 1.5 summarizes the premises of this thesis, states the formal questions it aims to answer, attributes the content of each chapter, and provides an overview of the thesis structure.

1.1 Inner Magnetosphere Processes

Nowadays, the radiation belts are clearly understood as an integral part of a much larger system of charged particles and magnetic fields shaped jointly by terrestrial and solar processes. All planets in the solar system reside in the ever-expanding, hot, gaseous (plasma) outflow of the solar atmosphere, the so-called solar wind. Unlike the other terrestrial planets, Earth possesses a strong intrinsic dipolar magnetic field. At the surface, its strength ranges from about 30,000 to 60,000 nanotesla (nT). With increasing distance from Earth, the field strength decays approximately as the inverse cube of the distance. The location where the magnetic pressure associated with this field falls below the ram pressure of the solar wind is called the *magnetopause*. The magnetopause demarcates the boundary between the solar wind and the *magnetosphere* [Gold, 1959], a "cavity" carved out by the Earth's magnetic field in the interplanetary medium. Under typical solar wind conditions, the magnetopause stands about 10 Earth radii (with $R_E \approx 6378$ km) sunward, the cross-section of the magnetosphere is

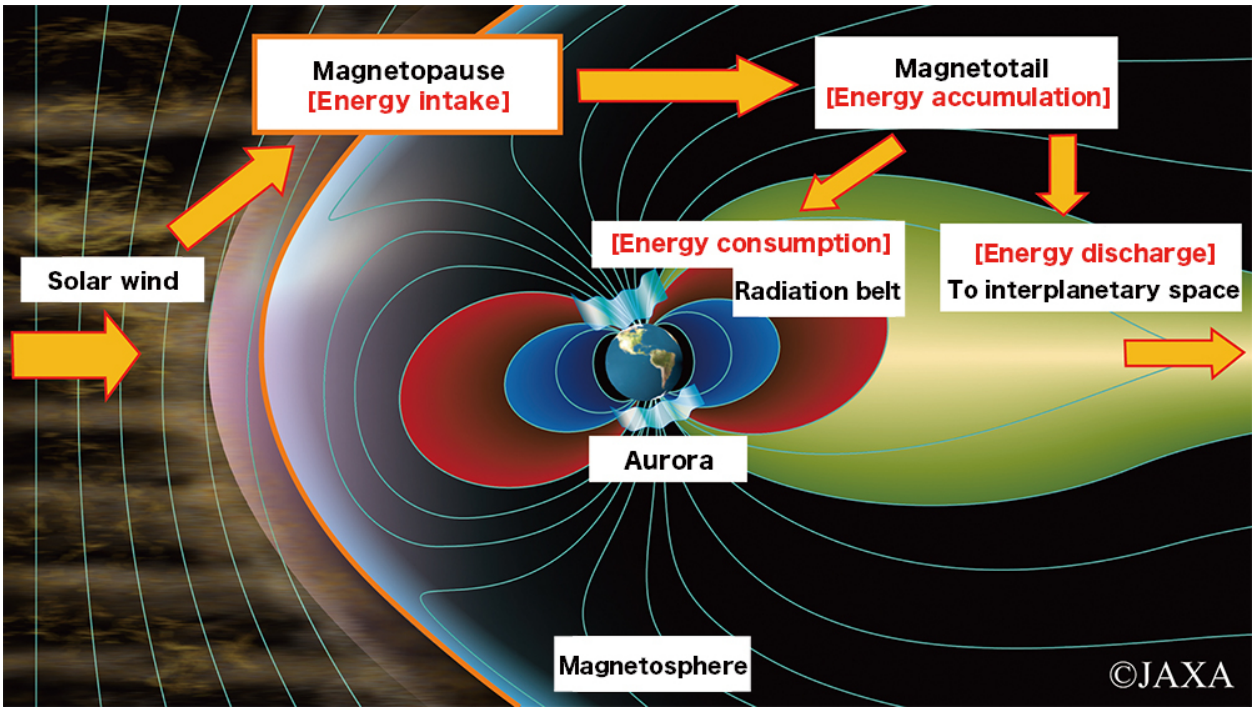

Figure 1.2: Energy flow in the magnetosphere. By Hiroshi Hasegawa, Naritoshi Kitamura, retrieved from www.isas.jaxa.jp

about 60 R_E, and the magnetosphere extends to $\gtrsim 200 R_E$ in the anti-sunward direction.

The solar wind is the ultimate driver of global magnetospheric dynamics. Besides carrying charged particles from the upper layers of the solar atmosphere, it also convects solar magnetic field lines, giving rise to the *Interplanetary Magnetic Field* (IMF). The IMF direction, although highly variable in time, is crucial for determining the energy intake from the solar wind into the magnetosphere. When its vertical component (roughly perpendicular, northward/southward to the ecliptic) is southward, the magnetic field lines carried by the solar wind can mutually annihilate (reconnect) with those connected to the Earth at the magnetopause. This process, known as *reconnection*, converts magnetic energy into particle heating and acceleration. The recently reconnected magnetic field lines are then transported anti-sunward, resulting in magnetic flux being gradually stored in the so-called *magnetotail* region. The magnetotail

extends to $\gtrsim 200 R_E$ in the anti-sunward direction and consists of a northern and a southern lobe filled with highly stretched magnetic field lines pointing in the sunward/anti-sunward direction, respectively. When the accumulated magnetic flux reaches a critical level, the oppositely directed magnetic field lines at the interface between the northern and southern lobes begin to merge, initiating magnetotail reconnection. During this process, magnetic energy is once again converted into particle heating and acceleration, and the resulting energization is partitioned between earthward injections into the inner magnetosphere and tailward-directed outflows into the distant magnetotail. This cycle—beginning with magnetopause reconnection, followed by flux storage in the lobes, and culminating in the merging of magnetic field lines on the nightside—is known as the Dungey cycle [Dungey, 1961].

The energy released in tail reconnection is injected into the inner magnetosphere in a form of fast plasma flows [Angelopoulos et al., 1992], carrying both energetic particles ($\lesssim 100$ keV) and magnetic flux. As these injections penetrate earthward, they reach the outer radiation belt and terminate near geostationary orbit ($\approx 7\ R_E$). Under the combined action of the global electric field and the non-uniform magnetic field, the injected electrons begin drifting duskward, while the ions drift dawnward, resulting in an approximately azimuthally symmetric, donut-shaped configuration of the radiation belts (see Fig. 1.1). This azimuthal drift occurs alongside the much faster particle bouncing along the field lines near the magnetic equator and the even faster (gyro-)rotations around the magnetic field lines. The relatively strong magnetic field at these radial distances produces a clear separation of the three main periodic motions in time scales, which in turn contributes to the remarkable stability of particles trapped within the radiation belts. Therefore, explaining dynamical changes inside the radiation belts requires mechanisms that can violate these periodic motions.

During active solar wind conditions [Gonzalez et al., 1999], the structure of Earth's radiation belts can exhibit strong variability and a more complex configuration, such as the formation of a "third" radiation belt (also known as a storage ring; see, e.g., [Turner et al.,

2013, Baker et al., 2013]). At such active times, the fluxes of relativistic electrons can also drop by several orders of magnitude [Turner et al., 2012, Ukhorskiy et al., 2015]. These so-called "dropouts" are usually associated with outward radial transport and subsequent particle losses through the magnetopause [Shprits et al., 2006, Turner et al., 2012]. Observations near the dayside magnetopause often show isolated enhancements of energetic electrons, indicating that outward transport can operate even at the outer radiation belt boundary [Meng and Anderson, 1970, Meng and Anderson, 1975, Williams et al., 1985, Dunlop et al., 2008]. At the same time, low-energy particles are often accelerated and transported radially (Earthward). Although particle acceleration can occur locally, i.e., without significant radial displacement [Reeves et al., 2013, Allison and Shprits, 2020], explaining the global variability of the outer radiation belt over a wide range of radial distances as a result of these often-localized particle acceleration and loss events requires an efficient mechanism for radial transport [Fälthammar, 1965, Kress et al., 2007, Desai et al., 2021]. The radial transport necessitates a significant distortion of the azimuthal motion, i.e. closed drift orbits of particles around the Earth should be destroyed (open). The mechanisms responsible for this destruction will be discussed in detail in Section 1.4. Before that, however, we must first introduce the necessary physical framework and mathematical toolkit essential for describing these processes.

1.2 Charged Particle in Electromagnetic Field

Motion of a charged particles (charge q) in electromagnetic field, given via vector and scalar potentials, $\boldsymbol{A}(\boldsymbol{r},t)$ and $\phi(\boldsymbol{r},t)$, is described by the Hamiltonian [Landau and Lifshitz, 1971]

$$H(\boldsymbol{r},\boldsymbol{P},t) = mc^2\sqrt{1+\left(\frac{\boldsymbol{P}-q\boldsymbol{A}(\boldsymbol{r},t)/c}{mc}\right)^2} + q\phi(\boldsymbol{r},t) \tag{1.1}$$

where $\boldsymbol{P} = \boldsymbol{p} + \frac{q}{c}\boldsymbol{A}$ is the momentum canonically conjugate to $\boldsymbol{r}$ and $\boldsymbol{p} = \gamma m\boldsymbol{v}$ ($\boldsymbol{v}$ -

velocity and $\gamma = 1/\sqrt{1 - \boldsymbol{v}^2/c^2}$). The electric and magnetic fields are given as

$$\begin{cases} \boldsymbol{E} = -\boldsymbol{\nabla}\phi - (1/c)(\partial \boldsymbol{A}/\partial t) \\ \boldsymbol{B} = \boldsymbol{\nabla} \times \boldsymbol{A} \end{cases} \tag{1.2}$$

Dynamics described by Hamiltonian 1.1 can be recasted in the form of standard Newton-Lorenz equations:

$$\begin{aligned} \frac{d\boldsymbol{p}}{dt} &= q\boldsymbol{E} + \frac{q}{\gamma mc}\boldsymbol{p} \times \boldsymbol{B} \\ \frac{d\boldsymbol{r}}{dt} &= \frac{\boldsymbol{p}}{\gamma m} \end{aligned} \tag{1.3}$$

In the case of a uniform and static fields, the motion parallel ($||$) and perpendicular ($\perp$) to the magnetic field completely decouple. In the reference frame where $E_\perp = 0$, the motion perpendicular to the magnetic field reduces to (gyro-)rotation with a frequency of $\omega = \omega_c = |q|B/(\gamma mc)$ (gyro-frequency) where $B = |\boldsymbol{B}|$, with $|\boldsymbol{p} \times \boldsymbol{b}| = p_\perp = \text{const}$ ($\boldsymbol{b} = \boldsymbol{B}/B$) and a constant curvature radius (gyro-radius) of $\rho = v_\perp/\omega_c$ [Landau and Lifshitz, 1971] .

1.2.1 Guiding-Center Approximation and the First Adiabatic Invariant

In realistic (non-uniform and time-dependent) electric and magnetic fields, charge particle motion becomes much more complex. However, in the context of electron motion in the inner magnetosphere, much progress can be achieved by limiting our consideration to quasi-static and weakly non-uniform electro-magnetic fields satisfying $\max\{|\boldsymbol{E}|^{-1}|\partial \boldsymbol{E}/\partial t|, |\boldsymbol{B}|^{-1}|\partial \boldsymbol{B}/\partial t|\} \sim \tau^{-1} \ll \omega_c$ and $\max\{|\boldsymbol{\nabla} B|/B, |(\boldsymbol{b} \cdot \boldsymbol{\nabla})\boldsymbol{b}|\} \sim L^{-1} \ll \rho^{-1}$. This introduces a small parameter into the system, $\epsilon = \max\{(\omega_c\tau)^{-1}, \rho/L\} \ll 1$. A small-parameter expansion with respect to ϵ allows the actual motion $\boldsymbol{r}(t)$ to be decomposed into fast ($\sim \omega_c$) rotation around the field and a slow drift of the the so-called *guiding center*, $\boldsymbol{R}$ [Sivukhin, 1965, Northrop, 1963]. Following [Morozov and Solov'ev, 1966, Bogoliubov and Mitropolski, 1961], we write

$$\begin{aligned}\boldsymbol{r}(t) &= \boldsymbol{R} + \rho\left(\boldsymbol{\tau}_1 \sin\theta - \boldsymbol{\tau}_2 \cos\theta\right)\\ \boldsymbol{v}(t) &= v_{||}\boldsymbol{b} + v_\perp\left(\boldsymbol{\tau}_1 \cos\theta + \boldsymbol{\tau}_2 \sin\theta\right)\end{aligned} \tag{1.4}$$

where θ is the gyro-phase and $\boldsymbol{\tau}_{1,2}$ are two unit vectors orthogonal to $\boldsymbol{b}$ defined via $\boldsymbol{\tau}_1 \times \boldsymbol{\tau}_2 = \boldsymbol{b}$, $\boldsymbol{\tau}_2 \times \boldsymbol{b} = \boldsymbol{\tau}_1$, and $\boldsymbol{b} \times \boldsymbol{\tau}_1 = \boldsymbol{\tau}_2$. Decomposition 1.4 is written under the assumption $|v_{\boldsymbol{E}\times\boldsymbol{B}}| \ll v_\perp$, where $v_{\boldsymbol{E}\times\boldsymbol{B}} = c(\boldsymbol{E}\times\boldsymbol{B})/B^2$. When this assumption is violated, the term $v_{\boldsymbol{E}\times\boldsymbol{B}}$ should be explicitly added to the second equation in 1.4 (see the discussion in Section 1.2.4).

To obtain the equations describing $\boldsymbol{R}$ and ρ, we substitute Eqs.1.4 into the Lorentz Eq. 1.3. It is convenient to first recast Eq. 1.3 in terms of the particle acceleration, $\dot{\boldsymbol{v}}$, and introduce $\boldsymbol{\omega} = -q\boldsymbol{B}/(\gamma mc)$ and $\boldsymbol{f} = q\boldsymbol{E}/(\gamma m)$

$$\frac{d\boldsymbol{v}}{dt} = \boldsymbol{f} - \frac{1}{c^2}(\boldsymbol{v}\cdot\boldsymbol{f})\boldsymbol{v} + \boldsymbol{\omega}\times\boldsymbol{v} \tag{1.5}$$

Substituting the velocity decomposition from Eq. 1.4 into Eq. 1.5 and taking the dot product of the resulting expression with $\boldsymbol{b}$, $(\boldsymbol{\tau}_1\cos\theta + \boldsymbol{\tau}_2\sin\theta)$, and $(-\boldsymbol{\tau}_1\sin\theta + \boldsymbol{\tau}_2\cos\theta)$, we arrive at the following system:

$$\begin{aligned}\dot{\boldsymbol{r}} &= v_{||}\boldsymbol{b} + v_\perp\left(\boldsymbol{\tau}_1\cos\theta + \boldsymbol{\tau}_2\sin\theta\right)\\ \dot{v}_{||} &= f_{||} - \frac{v_{||}}{c^2}\boldsymbol{v}\cdot\boldsymbol{f} + v_\perp\dot{\boldsymbol{b}}\cdot(\boldsymbol{\tau}_1\cos\theta + \boldsymbol{\tau}_1\sin\theta)\\ \dot{v}_\perp &= (\boldsymbol{\tau}_1\cos\theta + \boldsymbol{\tau}_2\sin\theta)\cdot\left(\boldsymbol{f} - \frac{1}{c^2}(\boldsymbol{v}\cdot\boldsymbol{f})\boldsymbol{v} - v_{||}\boldsymbol{b}\right)\\ \dot{\theta} &= \omega - \frac{1}{v_\perp}(\boldsymbol{\tau}_1\sin\theta - \boldsymbol{\tau}_2\cos\theta)\cdot\left(\boldsymbol{f} - v_{||}\dot{\boldsymbol{b}} - v_\perp(\dot{\boldsymbol{\tau}}_1\cos\theta + \dot{\boldsymbol{\tau}}_2\sin\theta)\right)\end{aligned} \tag{1.6}$$

On the right-hand-side, time-derivatives $\dot{\boldsymbol{b}}$ and $\dot{\boldsymbol{\tau}}_{1,2}$ are taken as convectional derivative along the particle trajectories:

$$\frac{d\boldsymbol{\tau}}{dt} = \frac{\partial \boldsymbol{\tau}}{\partial t} + (\boldsymbol{v}\cdot\boldsymbol{\nabla})\boldsymbol{\tau} = \frac{\partial \boldsymbol{\tau}}{\partial t} + v_{||}(\boldsymbol{b}\cdot\boldsymbol{\nabla})\boldsymbol{\tau} + v_{\perp}\{\cos\theta(\boldsymbol{\tau}_1\cdot\boldsymbol{\nabla}) + \sin\theta(\boldsymbol{\tau}_2\cdot\boldsymbol{\nabla})\}\boldsymbol{\tau} \tag{1.7}$$

where $\boldsymbol{\tau} \in \{\boldsymbol{b}, \boldsymbol{\tau}_1, \boldsymbol{\tau}_2\}$. Substituting Expression 1.7 into 1.6, we arrive at the system of equations which can be written as

$$\begin{cases} \dot{\boldsymbol{x}} = \boldsymbol{F}(\boldsymbol{x}, \theta, t) \\ \dot{\theta} = \omega(\boldsymbol{x}, t) + A(\boldsymbol{x}, \theta, t) \end{cases} \tag{1.8}$$

Here $\boldsymbol{x} = (\boldsymbol{r}, v_{||}, v_{\perp})$ and $\boldsymbol{F}, A$ and $\omega = |\boldsymbol{\omega}|$ denote the right-hand sides of Eqs. 1.6 after the substitution of 1.7. System 1.8 is written in the conventional form for the Krylov–Bogoliubov averaging method [Bogoliubov and Krylov, 1935, Bogoliubov and Mitropolski, 1961] and explicitly includes the fast phase rotation $\dot{\theta} \sim \omega$. The solution to Eqs. 1.8 accurate to first order in $\epsilon \sim \omega^{-1}$ is given by $\boldsymbol{x} = \boldsymbol{\xi} + \hat{\boldsymbol{F}}/\omega$, where $\boldsymbol{\xi} = (\boldsymbol{R}, v_{||}, v_{\perp})$ is the averaged (phase-independent) part of the solution, governed by the following equation [Morozov and Solov'ev, 1966, Bogoliubov and Mitropolski, 1961].

$$\frac{d\boldsymbol{\xi}}{dt} = \langle \boldsymbol{F} \rangle_{\theta}(\boldsymbol{\xi}, t) + \left\langle \left(\hat{\boldsymbol{F}}\cdot\boldsymbol{\nabla}\right)\frac{\boldsymbol{F}}{\omega} - \delta[A]\frac{\boldsymbol{F}}{\omega} \right\rangle_{\theta}(\boldsymbol{\xi}, t) \tag{1.9}$$

Here, $\langle \ldots \rangle_{\theta} = (2\pi)^{-1}\int_0^{2\pi} \ldots d\theta$ is the phase-averaging operator, $\delta[A] = A - \langle A \rangle_{\theta}$ and $\hat{\boldsymbol{F}} = \delta\left[\int_0^{\theta} \delta[\boldsymbol{F}](\boldsymbol{\xi}, t, \theta')d\theta'\right]$. Substituting the right-hand side from Eqs. 1.6 into Eq. 1.9 and re-arranging the terms (see [Morozov and Solov'ev, 1966, Bogoliubov and Mitropolski, 1961]), we arrive at

$$\begin{aligned}
\frac{d\boldsymbol{R}}{dt} &= v_{||}\boldsymbol{b} - \frac{\boldsymbol{b}}{|\omega|}\times\left(\boldsymbol{f} - v_{||}^2\boldsymbol{\kappa} - \frac{v_\perp^2}{2|\omega|}\boldsymbol{\nabla}|\omega|\right)\\
\frac{d(\gamma mc^2)}{dt} &= \gamma m\boldsymbol{f}\cdot\frac{d\boldsymbol{R}}{dt} - \frac{cm}{q}\mu\boldsymbol{b}\cdot(\boldsymbol{\nabla}\times\boldsymbol{f})\\
\frac{d\mu}{dt} &= \frac{\mu\boldsymbol{b}}{|\omega|}\cdot\left(\boldsymbol{\nabla}\times\boldsymbol{f} - \frac{\partial\boldsymbol{\omega}}{\partial t}\right)
\end{aligned} \tag{1.10}$$

Here, $\boldsymbol{\kappa} = (\boldsymbol{b}\cdot\boldsymbol{\nabla})\boldsymbol{b}$ and $\mu = m\gamma^2 v_\perp^2/(2B) = p_\perp^2/(2mB)$. Expressing $\boldsymbol{f}$ and $\boldsymbol{\omega}$ in terms of $\boldsymbol{E}$ and $\boldsymbol{B}$ and using Faraday's law, which is equivalent to $\boldsymbol{\nabla}\times\boldsymbol{f} = \partial\boldsymbol{\omega}/\partial t$, we rewrite 1.10 as follows:

$$\begin{aligned}
\frac{d\boldsymbol{R}}{dt} &= v_{||}\frac{\boldsymbol{B}}{B} + c\frac{\boldsymbol{E}\times\boldsymbol{B}}{B^2} + \frac{c}{q}\frac{\gamma m v_{||}^2}{B}\frac{\boldsymbol{B}\times[(\boldsymbol{B}\cdot\boldsymbol{\nabla})\boldsymbol{B}]}{B^3} + \frac{c}{q}\frac{\mu}{\gamma}\frac{\boldsymbol{B}\times\boldsymbol{\nabla}B}{B^2}\\
\frac{d(\gamma mc^2)}{dt} &= q\boldsymbol{E}\cdot\frac{d\boldsymbol{R}}{dt} + \frac{\mu}{\gamma}\frac{\partial B}{\partial t}\\
\frac{d\mu}{dt} &= 0
\end{aligned} \tag{1.11}$$

The individual terms in the first equation of 1.11 are often referred to as: (1) the parallel drift ($v_{||}$), (2) the $\boldsymbol{E}\times\boldsymbol{B}$ drift, (3) the curvature drift ($\boldsymbol{B}\times\boldsymbol{\kappa}$), and (4) the gradient drift ($\boldsymbol{B}\times\boldsymbol{\nabla}B$). The third equation in 1.11 amounts to the conservation of μ along the guiding-center trajectory. This is the so-called *first adiabatic invariant* associated with gyro-rotation. Up to a constant multiplier, μ coincides with $\oint \boldsymbol{P}\cdot d\boldsymbol{r}$ calculated along the gyro-circle using the original Hamiltonian 1.1 (see [Landau and Lifshitz, 1988]). Eqs. 1.11 are first-order in ϵ, and thus formally guarantee conservation of μ only with accuracy to order ϵ. However, detailed treatment of higher-order expansions shows that μ is in fact conserved to all orders in ϵ [Hellwig, 1955, Hertweck and Schlüter, 1957, Kruskal, 1958], thus justifying the term "adiabatic invariant" [Lenard, 1959].

1.2.2 Bounce Motion and the Second Adiabatic Invariant

Consider guiding-center motion in stationary magnetic and electric fields, when $\boldsymbol{E} = -\boldsymbol{\nabla}\phi$. In this case, the last two equations in 1.11 reduce to conservation laws: $\mu = \text{const}$ and $\gamma mc^2 + q\Phi = W = \text{const}$. This allows expressing $p_{||} = \gamma m v_{||}$ as $p_{||}(\boldsymbol{r}) = \sqrt{[W - q\phi(\boldsymbol{r})]^2/c^2 - 2m\mu B(\boldsymbol{r}) - m^2c^2}$. Using this expression, we can rewrite the first of Eqs. 1.11 as

$$\frac{d\boldsymbol{R}}{dt} = \frac{p_{||}}{\gamma m}\left\{\boldsymbol{b}\cdot\left(1 - \frac{cp_{||}}{qB}(\boldsymbol{b}\cdot(\boldsymbol{\nabla}\times\boldsymbol{b}))\right) + \frac{c}{qB}\boldsymbol{\nabla}\times(p_{||}\boldsymbol{b})\right\} \tag{1.12}$$

Now assume that the topology of the magnetic field lines is such that there is a local minimum of the magnetic-field strength along a field line (a so-called magnetic-bottle configuration). In this case, as we will see shortly, the motion along the field line (in $(s, p_{||})$ space, with s the coordinate along the field line) is quasi-periodic with a characteristic bounce period of $\sim \tau_b$. It is therefore natural to rewrite Eq. 1.12 in curvilinear coordinates in which one coordinate runs along the field line and the other two describe the cross-field drift. In particular, one can choose (α, β, s), where α and β are Euler potentials satisfying $\boldsymbol{B} = \boldsymbol{\nabla}\alpha \times \boldsymbol{\nabla}\beta$ and $(\boldsymbol{\nabla}\alpha \cdot \boldsymbol{\nabla}\beta) = 0$ [Stern, 1970]. The vector operations such as curl and divergence in Eq. 1.12 are written as $\boldsymbol{\nabla}\cdot\boldsymbol{a} = g^{-1/2}\partial_i(\sqrt{g}a^i)$ and $(\boldsymbol{\nabla}\times\boldsymbol{a})^i = g^{-1/2}\varepsilon^{ijk}\partial_j a_k$, where $g = \det[g_{ik}]$, g_{ik} is the metric tensor associated with (α, β, s), and ε^{ijk} is the Levi-Civita symbol. Note that $g = \det[J^T J] = 1/B^2$ where $J = \partial(x, y, z)/\partial(\alpha, \beta, s)$ is the Jacobian matrix associated with this coordinate transformation. The upper and lower indices indicate contravariant and covariant components, such that $a_i = g_{ik}a^k$ (Einstein summation applies). Using these curvilinear coordinates, we rewrite Eqs. 1.12 as:

$$
\begin{aligned}
\frac{d\alpha}{dt} &= \frac{cv_{||}}{qB}\frac{1}{\sqrt{g}}\left[\frac{\partial(p_{||}b_3)}{\partial\beta} - \frac{\partial(p_{||}b_2)}{\partial s}\right] \\
\frac{d\beta}{dt} &= \frac{cv_{||}}{qB}\frac{1}{\sqrt{g}}\left[\frac{\partial(p_{||}b_1)}{\partial s} - \frac{\partial(p_{||}b_3)}{\partial\alpha}\right] \\
\frac{ds}{dt} &= v_{||}\left[1 - \frac{cp_{||}}{qB}\boldsymbol{b}\cdot(\boldsymbol{\nabla}\times\boldsymbol{b})\right] + \frac{cv_{||}}{qB}\frac{1}{\sqrt{g}}\left[\frac{\partial(p_{||}b_2)}{\partial\alpha} - \frac{\partial(p_{||}b_1)}{\partial\beta}\right]
\end{aligned}
\tag{1.13}
$$

Integrating the first two equations in 1.13 over one period of the bounce motion and using the substitution $v_{||}dt = ds$ yields the cross-field displacements $\Delta\alpha$ and $\Delta\beta$:

$$
\begin{aligned}
\Delta\alpha &= \frac{c}{q}\left[\frac{\partial J_{||}}{\partial\beta} - \Delta(p_{||}b_2)\right] \\
\Delta\beta &= \frac{c}{q}\left[\Delta(p_{||}b_1) - \frac{\partial J_{||}}{\partial\alpha}\right]
\end{aligned}
\tag{1.14}
$$

Here, we introduce $J_{||} = \oint p_{||}ds$ where the integral is taken along the field line over one bounce period. Assume that the cross-field displacement within one bounce period is small and the particle remains approximately on the same field line, then $\Delta(p_{||}b_{1,2}) = 0$. The same assumption allows replacing $\Delta\alpha \approx \langle\dot{\alpha}\rangle\tau_b$, $\Delta\beta \approx \langle\dot{\beta}\rangle\tau_b$ where $\langle\dots\rangle = \tau_b^{-1}\oint\dots ds/v_{||}$ is the bounce averaging. Thus,

$$
\begin{aligned}
\langle\dot{\alpha}\rangle &= \frac{c}{q\tau_b}\frac{\partial J_{||}}{\partial\beta} \\
\langle\dot{\beta}\rangle &= -\frac{c}{q\tau_b}\frac{\partial J_{||}}{\partial\alpha}
\end{aligned}
\tag{1.15}
$$

Multiplying the first and second of Eqs. 1.15 by $d\beta/dt$ and $-d\alpha/dt$, respectively, and summing them up, we obtain

$$
\left\langle\frac{dJ_{||}}{dt}\right\rangle = \frac{q\tau_b}{c}\left\langle\dot{\beta}\langle\dot{\alpha}\rangle - \dot{\alpha}\langle\dot{\beta}\rangle\right\rangle = 0 \rightarrow \oint p_{||}ds = \text{const} \tag{1.16}
$$

Thus, a particle bouncing in a magnetic-bottle configuration, in addition to the first adiabatic invariant μ, also conserves $J_{||}$, the so-called *second adiabatic invariant*, provided that the topology of the magnetic field line does not change significantly during one bounce period.

The symmetry between α and β and the from of Eqs. 1.15 suggest α and β are related via a Hamiltonian structure. Indeed, expressing $\tau_b = \oint ds/v_{||}$ via $J_{||}$ and W we obtain

$$\begin{aligned} \frac{\partial J_{||}}{\partial W} = \oint \frac{\partial}{\partial W} \sqrt{[W - q\phi]^2/c^2 - 2m\mu B - m^2c^2} ds = \\ = \oint \frac{\gamma m}{p_{||}} ds = \oint \frac{ds}{v_{||}} = \tau_b \rightarrow \frac{1}{\tau_b} = \frac{\partial W}{\partial J_{||}} \end{aligned} \tag{1.17}$$

Thus, Eqs. 1.15 can be written as [Northrop and Teller, 1960, Northrop, 1963]

$$\begin{aligned} \langle \dot{\alpha} \rangle = \frac{c}{q} \frac{\partial W}{\partial \beta} \\ \langle \dot{\beta} \rangle = -\frac{c}{q} \frac{\partial W}{\partial \alpha} \end{aligned} \tag{1.18}$$

Indeed, α and β are canonically conjugate Hamiltonian variables, with the Hamiltonian taken to be the total energy $W(\alpha, \beta; \mu, J_{||})$ (multiplied by c/q), expressed as a function of the Euler potentials α, β and the two adiabatic invariants μ and $J_{||}$. Eqs. 1.18 describe *bounce averaged* cross-field drift motion. As shown in [Northrop, 1963], the form of Eqs. 1.18 is preserved even in time-dependent fields if ϕ is replaced with $\phi + (\alpha/c)\partial\beta/\partial t$.

In the case when the electric field is absent, $\phi = 0$, $p = \text{const}$ and $p_{||}(s) = \sqrt{p^2 - 2m\mu B(s)}$. Thus, a particle bouncing near that local minimum will move back and forth between two *mirror points*, where $p_{||} = 0$ and $p^2 - 2m\mu B_m = 0$ (B_m is the magnetic-field strength at the mirror point). Under these circumstances, the canonical expression for the second adiabatic invariant (Eq. 1.16) can be rewritten as

$$I = \frac{J_{||}}{p} = \oint \sqrt{1 - \frac{B(s)}{B_m}} ds = \text{const} \tag{1.19}$$

Where we used $p = \text{const}$. Note that I, the so-called *normalized* second adiabatic invariant, is determined solely by the magnetic field topology because $B_m = p^2/(2m\mu)$ is also a conserved quantity. This invariant is closely associated with a Hamiltonian system describing field-aligned motion $(s, p_{||})$. Indeed, the energy conservation law, $\gamma = \text{const}$, relates $p_{||}$ to B. This relation can also be expressed in the form of equations of motion in $(s, p_{||})$ space. From the second equation of 1.11,

$$\frac{dp_{||}}{dt} = -\frac{m\mu}{p_{||}} \frac{d\boldsymbol{R}}{dt} \cdot \boldsymbol{\nabla} B \tag{1.20}$$

Substituting $d\boldsymbol{R}/dt$ from the first equation of 1.11 and neglecting the second-order term $\boldsymbol{\nabla} B \times (\boldsymbol{B} \times (\boldsymbol{\nabla} \times \boldsymbol{B})) \propto (\boldsymbol{\nabla} B)^2$, we obtain

$$\begin{aligned} \frac{dp_{||}}{dt} &= -\frac{\mu}{\gamma} \frac{\partial B}{\partial s} \\ \frac{ds}{dt} &= \frac{p_{||}}{\gamma m} \end{aligned} \tag{1.21}$$

Here, $B = B(s; \alpha, \beta)$, where (α, β) are treated as frozen variables specifying the field line. Since $\gamma = \text{const}$, Eqs. 1.21 can be *heuristically* treated as the equations of motion originating from the following Hamiltonian:

$$H(s, p_{||}; \alpha, \beta) = \frac{p_{||}^2}{2m^*} + \mu^* B(s; \alpha, \beta) \tag{1.22}$$

where $m^* = \gamma m$ and $\mu^* = \mu/\gamma$ are constants.

1.2.3 Cross-Field Drift and the Third Adiabatic Invariant

A qualitative description of guiding-center motion can be obtained for magnetic-field configurations satisfying $\boldsymbol{B}\cdot(\boldsymbol{\nabla}\times\boldsymbol{B}) = 0$ (no field-aligned currents). In this case, $\boldsymbol{b}\cdot(\boldsymbol{\nabla}\times\boldsymbol{b}) = 0$, and Eq. 1.12 can be written as

$$\frac{d\boldsymbol{R}}{dt} = \frac{p_{||}}{\gamma m B}\boldsymbol{\nabla}\times\left\{\boldsymbol{A} + \frac{cp_{||}}{q}\frac{\boldsymbol{B}}{B}\right\} = \frac{p_{||}}{\gamma m}\frac{\boldsymbol{B}^*}{B} \tag{1.23}$$

Here $\boldsymbol{A}^* = \boldsymbol{A} + (cp_{||}/q)\boldsymbol{b}$, and $\boldsymbol{B}^* = \boldsymbol{\nabla}\times\boldsymbol{A}^*$ are the 'effective' vector potential and its 'effective' magnetic field. As we will see in Section 1.2.4, the notion of the 'effective' potentials, $\boldsymbol{A}^*$ and $\boldsymbol{\Phi}^*$, will prove to be very fruitful in the context of the guiding-center description. From Eq. 1.23, $\dot{\boldsymbol{R}}\times\boldsymbol{B}^* = 0$, i.e., the guiding center always moves along the field lines of the 'effective' magnetic field, $\boldsymbol{B}^*$. The guiding-center 'equation of motion' formally coincides with the equations derived from the Lagrangian of a zero-mass particle: $L^*(\boldsymbol{R},\dot{\boldsymbol{R}}) = \dot{\boldsymbol{R}}\cdot\boldsymbol{A}^*$ [Morozov and Solov'ev, 1966].

$$\frac{d}{dt}\left(\frac{\partial L^*}{\partial\dot{\boldsymbol{R}}}\right) = \frac{\partial L^*}{\partial\boldsymbol{R}} \rightarrow \dot{\boldsymbol{R}}\times\boldsymbol{B}^* = 0 \tag{1.24}$$

This analogy with Lagrangian mechanics is especially useful when the magnetic-field configuration—and thus $\boldsymbol{A}$—possesses a continuous symmetry. This includes axially symmetric (e.g., dipole) or 2D (translationally invariant) magnetic-field configurations. Both symmetries can be treated in the Eulerian framework via an appropriate choice of β as either φ (the azimuthal angle) or z (the axial Cartesian coordinate). Thus, the generic representation for the vector potential reads $\boldsymbol{A} = \alpha\boldsymbol{\nabla}\beta = (g_{\beta\beta})^{-1/2}\alpha\hat{\boldsymbol{\beta}}$. In this case, $\boldsymbol{B}\cdot\hat{\boldsymbol{\beta}} = 0$, $\dot{\boldsymbol{R}}\cdot\hat{\boldsymbol{\beta}} = \sqrt{g_{\beta\beta}}\dot{\beta}$, and thus the generalized momentum associated with β, $P^*_\beta = \partial L^*/\partial\dot{\beta}$ (where $L^* = \dot{\beta}\alpha$), is conserved:

$$\frac{\partial L^*}{\partial \dot{\beta}} = \text{const} \rightarrow \alpha(\boldsymbol{r}) = \text{const} \tag{1.25}$$

Since $\alpha = \text{const}$ along the field lines, this condition—combined with the conservation of μ and γ—confines the guiding-center motion to the surface of "revolution" created by "rotating"(in β direction) the segment of the field line satisfying $B = |\boldsymbol{\nabla}\alpha \times \boldsymbol{\nabla}\beta| \leq B_n$. In particular, for a dipole field with $\alpha(r,\theta) = -B_0 R_E^3 \sin^2(\theta)/r$ and $\beta = \varphi$, the resulting magnetic field is axially symmetric. Eq. 1.25 yields $r = L R_E \sin^2\theta$ with a constant L, which is the radial distance to the equatorial foot point in the units of Earth's radii (R_E).

Relation 1.25 is also consistent with the bounce-averaged equations for cross-field drift 1.18. If $W(\alpha; \mu, J_{||})$, then $\langle\dot{\alpha}\rangle = 0$ and thus $\langle\alpha\rangle = \text{const}$. If $\alpha(\boldsymbol{r}) = \text{const}$ describes a finite surface, the bounce-averaged cross-field drift motion should be quasi-periodic. Due to the Hamiltonian structure of Eqs. 1.25, this quasi-periodic motion possesses an adiabatic invariant, $\Phi = \oint p dq = \oint \alpha d\beta$ where the integral is taken over one drift period. This is the so-called *third adiabatic invariant*, which is conserved if the ambient fields remain quasi-stationary on time scales of the drift period, $\tau_d = (q|/c)(\partial\Phi/\partial W)$. Applying Stokes' theorem to $\alpha d\beta = \alpha \boldsymbol{\nabla}\beta \cdot d\boldsymbol{r}$, we see that this adiabatic invariant is equal to the magnetic flux enclosed within the drift orbit.

$$\Phi = \oint \alpha d\beta = \oint (\boldsymbol{\nabla} \times [\alpha \boldsymbol{\nabla}\beta]) \cdot d\boldsymbol{S} = \oint \boldsymbol{B} \cdot d\boldsymbol{S} = \text{const} \tag{1.26}$$

1.2.4 Hamiltonian Description of the Guiding-Center Motion

First-order guiding-center equations 1.11 have allowed us to establish the main properties of the motion in weakly non-homogeneous and quasi-stationary fields. However, these equations have often proved problematic for particle tracing, as they lack the second-order terms in

ϵ necessary to ensure numerical conservation of the adiabatic invariant (see the review by [Cary and Brizard, 2009]). Eqs. 1.11 also lack the polarization drift associated with $\dot{\boldsymbol{E}}$ due to the omission of the explicit $v_{\boldsymbol{E}\times\boldsymbol{B}}$ term in 1.4. Both of these shortcomings can be overcome using the Hamiltonian treatment of guiding-center motion [Cary and Brizard, 2009, Tao et al., 2007]. This results in the following Hamiltonian describing particle dynamics in the four-dimensional phase space of $(\alpha, \beta, s, p_{||})$:

$$H(\alpha,\beta,s,p_{||},t) = mc^2\sqrt{1+\frac{2\mu B(\alpha,\beta,s;t)}{m^2c^2}+\left(\frac{p_{||}}{mc}\right)^2} + q\phi(\alpha,\beta,s,t) + \frac{mv^2_{\boldsymbol{E}\times\boldsymbol{B}}}{2} \tag{1.27}$$

The associated equations of motion can be written in the standard Cartesian coordinates, replacing $(\alpha, \beta, s) \rightarrow \boldsymbol{R}$, as

$$\begin{aligned}\frac{dp_{||}}{dt} &= q\frac{\boldsymbol{E}^*\cdot\boldsymbol{B}^*}{B^*_{||}}\\ \frac{d\boldsymbol{R}}{dt} &= \frac{p_{||}}{\gamma m}\frac{\boldsymbol{B}^*}{B^*_{||}} + c\frac{\boldsymbol{E}^*\times\hat{\boldsymbol{b}}}{B^*_{||}}\end{aligned} \tag{1.28}$$

Here, $\gamma(\boldsymbol{R}, p_{||}, t) = \sqrt{1 + 2\mu B(\boldsymbol{R}, t)/(mc^2) + (p_{||}/mc)^2}$ while $\boldsymbol{E}^*$ and $\boldsymbol{B}^*$ are the 'effective' electric and magnetic fields ($B^*_{||} = \boldsymbol{B}^*\cdot\boldsymbol{b}$)

$$\begin{aligned}\boldsymbol{E}^* &= \boldsymbol{\nabla}\phi^* - \frac{1}{c}\frac{\partial \boldsymbol{A}^*}{\partial t}\\ \boldsymbol{B}^* &= \boldsymbol{\nabla}\times\boldsymbol{A}^*\end{aligned} \tag{1.29}$$

where the 'effective' potentials are defined as,

$$\begin{aligned}\phi^* &= \phi + \gamma mc^2 + \frac{mv^2_{\boldsymbol{E}\times\boldsymbol{B}}}{2}\\ \boldsymbol{A}^* &= \boldsymbol{A} + \frac{c}{q}\left(p_{||}\boldsymbol{b} + m\boldsymbol{v}_{\boldsymbol{E}\times\boldsymbol{B}}\right)\end{aligned} \tag{1.30}$$

When $|v_{\boldsymbol{E}\times\boldsymbol{B}}| \ll v_\perp$, Eqs. 1.29-1.30 can be written as

$$\begin{aligned} \boldsymbol{E}^* &= \boldsymbol{E} - \frac{1}{q}\left(mc^2\boldsymbol{\nabla}\gamma - p_{||}\frac{\partial \boldsymbol{b}}{\partial t}\right) \\ \boldsymbol{B}^* &= \boldsymbol{B} + \frac{cp_{||}}{q}\boldsymbol{\nabla}\times\boldsymbol{b} \end{aligned} \tag{1.31}$$

In this work, only static or quasi-static magnetic-field configurations are considered; thus, all numerical calculations of guiding-center motion are performed using Eqs. 1.28 with the "effective" fields given in Eq. 1.31.

1.3 Adiabatic Invariant

A mechanical system is characterized by its integrals of motion. In the Hamiltonian framework, the time evolution of the system is represented by a trajectory (a curve) in the s-dimensional phase space, $(x_1, \ldots, x_s; p_1, \ldots, p_s)$, where s is the number of degrees of freedom and (x_i, p_i) are the canonical phase-space coordinates. These coordinates are related via a Hamiltonian function $H(\boldsymbol{x}, \boldsymbol{p}, t)$ as

$$\dot{p_i} = -\frac{\partial H}{\partial x_i}\ , \dot{x_i} = \frac{\partial H}{\partial p_i} \tag{1.32}$$

An integral of motion is a function in phase space, $F(\boldsymbol{x}, \boldsymbol{p})$, whose value is conserved along phase-space trajectories, $\dot{F} = dF/dt = 0$. If parameters of a system begin to change slowly in time, the integrals of motion will no longer be conserved. Specifically, let a parameter be $\lambda = \lambda(\tau)$ with $\tau = \varepsilon t$ and $\dot{\tau} = \varepsilon \ll 1$. In this case, the slow variation of the parameter causes an integral of motion to change as $\dot{F} \sim \varepsilon$. Over a long time scale, $\tau \sim 1$, this change can become non-negligible. Fortunately, for systems whose motion is periodic when $\lambda = \text{const}$ (so-called quasi-periodic systems), there exist quantities that remain approximately constant,

that is their variation is bounded by $O(\varepsilon^n)$, with $n \geq 1$. These approximate integrals are called *adiabatic invariants*. While discussing charged particle motion in weakly non-uniform and quasi-static electromagnetic fields (see Section 1.2), we already encountered quantities that are conserved up to order $O(\varepsilon)$ (e.g., see μ in Eq. 1.11). This section provides the general framework for understanding the conservation of these dynamical quantities and discusses how it can be extended to higher orders in ε. Importantly, it also states the conditions under which this conservation can be violated and quantifies the degree of such violations. As we shall see in Sections 1.4.1 and 1.4.2, these principles play a central role in governing the dynamics of charged particles in the radiation belts.

Many fundamental properties of systems possessing an adiabatic invariant can be illustrated using the simplest *non-conservative* Hamiltonian with one degree of freedom, $H(x, p; \tau) = H(x, p; \lambda(\tau))$, or, as it is often called, with $1\frac{1}{2}$ degrees of freedom (time counts as $\frac{1}{2}$). If, under $\lambda = \text{const}$, the system undergoes periodic motion, then its trajectory in the (x, p) phase space coincides with the closed curve $\Gamma = \{(x, p) \in \mathbf{R}^2 : H(x, p; \tau) = E\}$. Consider a canonical transformation $(x, p) \to (\theta, I)$ where I is the so-called *action* variable, defined as

$$I = \frac{1}{2\pi} \oint_\Gamma p dx \tag{1.33}$$

Here $I = I(E, \tau)$ since the curve Γ is uniquely determined by E for any given value λ. The variable θ which is canonically conjugate to I is introduced via a generating function, $S_0(x, I; \tau)$

$$S_0(x, I; \tau) = \int_{x_0}^{x} p dx' \text{ , where } p = p(x, E; \tau) \tag{1.34}$$

where the integral is taken along a segment of the curve Γ from some fixed point x_0 to x. Without loss of generality, we can choose $x = x_0$ at $t = 0$. According to S, we find

$\theta = (\partial S_0/\partial I)_{\tau,E}$ which is the so-called *angle* variable. Note that the generating function 1.34 has an explicit time-dependence via $\lambda = \lambda(\varepsilon t)$. Thus, the new Hamiltonian is give by $H' = H + \partial S_0/\partial t = H + \varepsilon H_1$ where $H_1(\theta, I; \tau) = \partial S_0/\partial \tau$. Changing the notation as $H' \to H$ and $H \to H_0$ we write

$$H(\theta, I; \lambda) = H_0(I, \tau) + \varepsilon H_1(\theta, I; \tau) \tag{1.35}$$

Note that H_0 *does not* depend on θ, while H_1 and, in turn, H can be treated as *periodic* in θ. Indeed, according to 1.34, one complete period in the original (x, p) space corresponds to $S \to S + \oint p dx = S + 2\pi I$, which yields $\theta \to \theta + 2\pi$ and $H_1 = \partial S/\partial \tau \to H_1 + \partial I/\partial \tau$ which does not affect the resulting equations of motion (see 1.36) because $\partial^2_{I,\tau} I = \partial^2_{\theta,\tau} I = 0$.

According to 1.35, the Hamiltonian equations of motion in (θ, I) variables are given as

$$\begin{aligned} \dot{I} &= -\varepsilon \frac{\partial H_1}{\partial \theta} \\ \dot{\theta} &= \omega(I, \tau) + \varepsilon \frac{\partial H_1}{\partial I} \end{aligned} \tag{1.36}$$

where $\omega(I) = \partial H_0/\partial I$. This system should be supplied with initial conditions at $t = 0$, $(\theta, I) = (0, I_0)$. Applying the averaging theorem [Bogoliubov and Mitropolski, 1961, Arnold, 1989], or simply phase-averaging the right-hand side of Eq. 1.36 over θ, we obtain $\dot{I} = \varepsilon \langle \partial H_1/\partial \theta \rangle_\theta = 0$, which leads to $I = I_0 + O(\varepsilon)$ being conserved over a time interval of length $1/\varepsilon$. Moreover, if $\omega > \text{const} > 0$ and $\partial \omega/\partial I \neq 0$ everywhere in the vicinity of $I = I_0$, then V.I. Arnold's theorem on perpetual invariance applies, and $I = I_0 + O(\varepsilon)$ for all times [Arnol'd, 1963]. Because of these properties, the action variable 1.33 is often referred to as an adiabatic invariant, reflecting its conservation up to order ε under slowly varying perturbations.

1.3.1 Improved Adiabatic Invariant

For well-behaved H, conservation can be improved to higher orders in ε. Consider a canonical transformation $(\theta, I) \to (\varphi, J)$ that is ε-close to identity. Let $J\theta + \varepsilon S(\theta, J; \tau)$ be its generating function, and let $\mathcal{H}(\varphi, J)$ be the new Hamiltonian such that $\mathcal{H}(J;\tau) = H_0(J;\tau) + \varepsilon\mathcal{H}_1(J;\tau) + \varepsilon^2\mathcal{H}_n(J;\tau) + \ldots$ and $S(\theta, J;\tau) = S_1(\theta, J;\tau) + \varepsilon S_2(\theta, J;\tau) + \varepsilon^2 S_3(\theta, J;\tau) + \ldots$. The new Hamiltonian no longer depends on the angle variable, while each S_n is periodic in θ. The new and old variables are related as

$$I = J + \varepsilon\frac{\partial S}{\partial \theta};\ \varphi = \theta + \varepsilon\frac{\partial S}{\partial J} \tag{1.37}$$

and the new Hamiltonian is given as

$$\mathcal{H}(J;\tau) = H(\theta, I;\tau) + \varepsilon^2\frac{\partial S}{\partial \tau} \tag{1.38}$$

Plugging Eqs. 1.37 and the θ-expansions for $\mathcal{H}$ and S into Eq. 1.38, and equating terms of the same order in ε, allows one to determine H_n. For $n = 1$, we find

$$\mathcal{H}_1(J;\tau) = H_1(\theta, J;\tau) + \frac{\partial H_0}{\partial J}\frac{\partial S_1}{\partial \theta} \tag{1.39}$$

Since $\mathcal{H}_1$ is phase-independent, applying θ-averaging yields $\mathcal{H}_1 = \langle H_1\rangle_\theta(J;\tau)$. Substituting this expression for $\mathcal{H}_1$ back into 1.39 gives $\partial_\theta S_1 = \omega^{-1}(\langle H_1\rangle_\theta - H_1)$ where $\partial_J H_0 = \omega$. Thus, truncating the ε-expansion at $S = S_1$ and $\mathcal{H}_2$ (i.e., at n = 2), from 1.37 we obtain

$$J(I,\theta) = I + \varepsilon u(I,\theta),\ \text{with}\ \ u = \frac{H_1 - \langle H_1\rangle_\theta}{\omega} \tag{1.40}$$

Truncation results in the new Hamiltonian given by $\mathcal{H} = H_0(J;\tau)+\varepsilon\mathcal{H}_1(J;\tau)+\varepsilon^2 h(\varphi, J;\tau)$, where h is the residual term resulting from the truncation. The equations of motion read: $\dot{J} = -\partial_\varphi \mathcal{H} = -\varepsilon^2 \partial_\varphi h$ and $\dot{\varphi} = \partial_J \mathcal{H} = \tilde{\omega} + \varepsilon^2 \partial_J h$, where $\tilde{\omega} = \omega + \varepsilon \partial_J \mathcal{H}_1$. Note that this system is, in form, identical to 1.36, but with the new "small parameter" being ε^2. Applying the averaging theorem then gives $J = J_0 + O(\varepsilon^2)$, meaning that the quantity 1.40 remains constant up to ε^2. This approximate invariant, $J = I + \varepsilon u$, is called the *improved adiabatic invariant* [Neishtadt, 2000]. Truncating the ε-expansion at higher order allows constructing higher invariants that remain conserved up to ε^n, where n is the number of smooth derivatives of H [Kulsrud, 1957, Lenard, 1959, Neishtadt, 2000].

We can now derive an alternative expression for the improved adiabatic invariant, which will soon prove useful. First, H_1 can be expressed directly from Eq. 1.34 as

$$\begin{aligned} H_1 &= \frac{\partial}{\partial \tau}\int_{x_0}^{x} p dx = -\int_{x_0}^{x} \frac{(\partial_\tau H_0)}{(\partial_p H_0)} dx = \\ &= -\int_{x_0}^{x} \frac{1}{\dot{x}} \frac{\partial H_0}{\partial \tau} dx = -\int_0^t \frac{\partial H_0}{\partial \tau} dt' \end{aligned} \tag{1.41}$$

where we used $\dot{\theta} = \omega + O(\varepsilon)$ (see Eq. 1.36). Following [Neishtadt, 1986], we then use 1.41 to rewrite $u(\theta, I;\tau)$ in 1.40 as

$$\begin{aligned} u &= \frac{1}{2\pi\omega^2}\int_0^{2\pi} d\theta \int_0^{\theta} \left(\left\langle \frac{\partial H_0}{\partial \tau} \right\rangle - \frac{\partial H_0}{\partial \tau} \right) d\varphi = \\ &= \frac{1}{2\pi}\int_0^T \left(\frac{T}{2} - t \right) \frac{\partial H_0}{\partial \tau} dt, \quad \text{where } T = \frac{2\pi}{\omega} \end{aligned} \tag{1.42}$$

Here we use $\theta = \omega t + O(\varepsilon)$. We omit the $O(\varepsilon)$ correction because it contributes to J only through the term εu, which amounts to $O(\varepsilon^2)$. Since J itself is defined only up to terms of order ε, this higher-order contribution can be neglected.

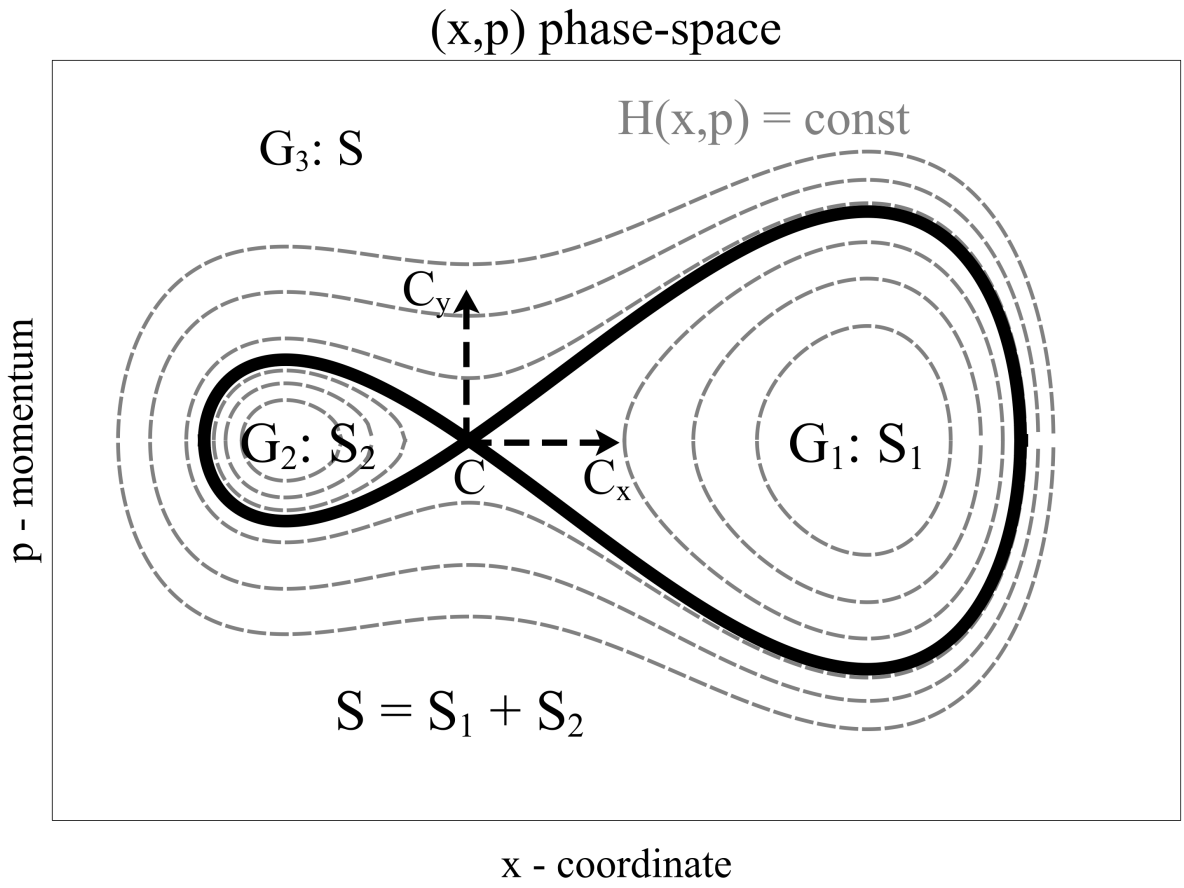

Figure 1.3: Schematic representation of a separatrix and a saddle point.

1.3.2 Jumps of Adiabatic Invariant: Separatrix Crossing

In Section 1.3.1 we emphasized that a fundamental condition for the conservation of an adiabatic invariant is that the frequency of the unperturbed motion does not vanish, $\omega \neq 0$. Thus, *violation* of adiabaticity is often associated with the condition $\omega = 0$. A natural situation arises when $\omega \neq 0$ holds almost everywhere except on a torus ($I = \text{const}$) of zero measure. In such cases, two qualitatively different regions of motion are separated by the $\omega = 0$ submanifold; this submanifold is called the *separatrix*. A well-known and historically important example is the nonlinear (Rayleigh-Lorentz) pendulum, which admits two distinct types of motion: oscillatory and rotational. Paul Ehrenfest first noted this in the context of the

old quantum theory, observing that *adiabatic* transitions between oscillations and rotations appear impossible [Ehrenfest and Breit, 1922]. This was later demonstrated by [Gamow et al., 1926], who showed that at the separatrix the adiabaticity condition is inevitably violated, even for infinitely slow transitions with arbitrarily small adiabaticity parameter ε.

Fig. 1.3 shows a generic example of a separatrix in the phase space of a Hamiltonian system with $1\frac{1}{2}$ degrees of freedom, $H(x,p;\tau) = H(x,p;\lambda(\tau))$. Two types of periodic motion are possible: (1–2) periodic motion confined to the domains G_1 or G_2, and periodic motion spanning the entire domain G_3. These three domains are separated by the separatrix. If $\lambda = \text{const}$, a particle sufficiently far from the separatrix performs periodic motion within a single domain, and its adiabatic invariant oscillates around a constant value I_0 with amplitude of order ε. However, when $d\lambda/d\tau \neq 0$, the separatrix changes its size, making transitions between G_1, G_2, and G_3 possible. Each such transition is associated with a separatrix crossing, where $\omega = 0$, and therefore produces a jump (change) in the adiabatic invariant.

Near the separatrix, $\omega \to 0$ and, consequently, $T \to \infty$. It is immediately evident that the divergence of $T = \oint \frac{dx}{\dot{x}}$ occurs near the saddle point of the separatrix at the interface between the G_1 and G_2 regions. By an appropriate coordinate transformation, the saddle point can always be placed at the origin $(0,0)$. If the saddle point is nondegenerate, a suitable coordinate rotation brings the Hamiltonian expansion near the saddle into the canonical quadratic form.

$$H(x,p;\tau) = \frac{p^2}{2}\left.\frac{\partial^2 H}{\partial p^2}\right|_{(0,0)} + \frac{x^2}{2}\left.\frac{\partial^2 H}{\partial x^2}\right|_{(0,0)} = \frac{k_p p^2 - k_x x^2}{2} \tag{1.43}$$

where $k_p = (\partial_p^2 H)(0,0) > 0$ and $k_x = -(\partial_x^2 H)_{(0,0)} > 0$. The Hamiltonian is normalized so that $H(0,0) = 0$.

Consider a particle moving close to the separatrix at energy level $H = h$, where $h < 0$ in $G_{1,2}$ and $h > 0$ in G_3. At $h = 0$, the period diverges, $T = +\infty$. To obtain the leading

asymptotic behavior of T as $h \to 0$, note that the divergence of $T = \oint dx/\dot{x}$ arises from the vicinity of the saddle point. Using Expansion 1.43, the leading-order asymptotic of T_i ($(x,p) \in G_i$) is calculated as

$$T_i(h) = \frac{\partial}{\partial h} \oint p dx = -a_i \ln|h| + b_i + O(h \ln|h|) \tag{1.44}$$

where $a_1 = a_2 = a$, $a_3 = 2a$ with $a = 1/\sqrt{k_x k_y} = 1/\sqrt{-\det[\partial^2 H]_{(0,0)}}$ and $b_3 = b_1 + b_2$ with all parameters being smooth functions of τ. Using $2\pi\partial_h I_i = T_i$ we find

$$2\pi I_i = S_i - a_i h \ln|h| + (b_i + a_i)h + O(h^2 \ln|h|) \tag{1.45}$$

where $S_i = \oint_{\partial G_i} p dx$ is the phase-space area enclosed by the separatrix in G_i. The area enclosed by the separatrix changes in time according to $2\pi\partial_\tau I = -\oint(\partial_\tau H), dt$. Introducing the rate of change $\Theta_i = dS_i/d\tau$, we can then write, using 1.44:

$$\oint_{G_i \cap \{H=h\}} \frac{\partial H}{\partial \tau} dt = -\Theta_i + O(h \ln|h|) \tag{1.46}$$

At the separatrix, i.e., in the limit $h \to 0$, we obtain

$$\frac{dS_i}{d\tau} = -\oint_{\partial G_i} \frac{\partial H}{\partial \tau} dt \tag{1.47}$$

Here, $\oint \ldots dt$ refers to the t-parametrized contour integration along the separatrix.

As we shall see, the jump of the adiabatic invariant, I, during a separatrix crossing is of order ε. It is therefore customary to use the improved invariant, $J = I + \varepsilon u$, to describe this jump, since the oscillations of J are of (higher) order ε^2 (see Section 1.3.1). Following

[Neishtadt, 1986], the function u (see Eq. 1.42) can be expressed as follows: if $(x, p) \in G_i$ lies near the saddle point along the C_x axis, then

$$2\pi u = d_i + O(\sqrt{h} \ln h) \tag{1.48}$$

where d_i are smooth functions of τ. If (x, p) lies in G_3 near the saddle point along the positive ray of C_y, we write

$$2\pi u = \frac{a}{2}(\Theta_2 - \Theta_1) \ln h + \Theta_1 \frac{b_2}{2} - \Theta_2 \frac{b_1}{2} + d_3 + O(\sqrt{h} \ln h) \tag{1.49}$$

Now consider a particle starting its motion in G_3 at $M_0 = (x_0, p_0) \in G_3$ far from the separatrix. In that case $I = I_0$ is conserved. Suppose the phase-space area enclosed by the separatrix starts increasing, $\Theta_i > 0$ $(i = 1, 2, 3)$. At some moment $\tau_{tr} = \varepsilon t_{tr}$ the separatrix area reaches $2\pi I_0 = S(\tau_{tr})$, and the particle crosses the separatrix into either G_1 or G_2. Inside G_i the adiabatic value is set to $2\pi I_i = S_i(\tau_{tr}) + O(\varepsilon)$, and this new value again remains conserved with accuracy ε. Whether a particle starting from $M_0 \in G_3$ is trapped in G_1 or G_2 depends sensitively on the initial conditions and is effectively probabilistic. The trapping probability for G_i, Π_i, is defined as the ratio of the phase-space area (or measure, mes) in the δ-neighborhood of M_0 that becomes trapped in G_i, $U_\delta^{(i)}(M_0)$, to the total measure of the δ-neighborhood, $U_\delta(M_0)$.

$$\Pi_i = \lim_{\delta \to 0} \lim_{\varepsilon \to 0} \frac{\mathrm{mes}[U_\delta^{(i)}(M_0)]}{\mathrm{mes}[U_\delta(M_0)]} \tag{1.50}$$

It was shown by [Neishtadt, 1975, Arnold et al., 2006] that for almost all initial conditions M_0, except for a set whose measure is limited by $O(\varepsilon^n)$ (with any $n \geq 1$), the probability 1.50 is given as

$$\Pi_i = \frac{\Theta_i(\tau_{tr})}{\Theta_3(\tau_{tr})} = \left(\frac{dS_i/d\tau}{dS/d\tau}\right)_{\tau=\tau_{tr}} \tag{1.51}$$

Using Eqs. 1.44–1.49, one can relate the initial value of the adiabatic invariant, I_0, to its value I_i after trapping in G_i. This relation was derived by [Neishtadt, 1986, Cary et al., 1986], and to first order in ε it takes the following form (see [Neishtadt, 1986]):

$$\begin{aligned} 2\pi I_i = {} & S_i + \varepsilon a \Theta_i \left(\xi - \frac{1}{2}\right)\left[\ln(\varepsilon\Theta_i) - \frac{2\Theta_i}{\Theta_3}\ln(\varepsilon\Theta_3)\right] - \\ & - \varepsilon a \Theta_i \ln\left[\frac{(2\pi)^{3/2}}{\Gamma(\xi)\Gamma\left(\frac{\Theta_i}{\Theta_3}(1-\xi)\right)\Gamma\left(1-\frac{\Theta_i}{\Theta_3}\xi\right)}\right] + \\ & + \varepsilon\Theta_i\left(\frac{1}{2}-\xi\right)\left(b_i - \frac{\Theta_i}{\Theta_3}b_3\right) + \varepsilon\left(d_i - \frac{\Theta_i}{\Theta_3}d_3\right) + \\ & + O(\varepsilon^{3/2}\left[|\ln\varepsilon| + (1-\xi)^{-1}\right]) \end{aligned} \tag{1.52}$$

Here, $\xi \in (0,1)$ shall be treated as a uniformly distributed random variable, and Γ denotes the Euler gamma function. All τ-dependent quantities on the right-hand side of Eq. 1.52 are to be evaluated at τ_{tr}. If the separatrix area shrinks with increasing τ, i.e., $\Theta_i < 0$ ($i \in \{1,2,3\}$), then an initially trapped particle with $M_0 \in G_i$ ($i = 1,2$) will eventually be released into G_3. In this case, the *detrapping* condition reads $2\pi I_0 = S_i$ ($i = 1,2$), and Eq. 1.52 holds if $2\pi I_i$ and S_i are replaced with $2\pi I_3$ and S_3, while $\Theta_i \to -\Theta_i$. The last condition can be regarded as a consequence of time (τ)-inversion relating trapping and detrapping.

One can rewrite Eq. 1.52 in terms of the net jump in the adiabatic invariant, $\underset{k\to i}{\Delta} I = I_i - I_k$, due to the $G_k \to G_i$ transition, where $k = 3$ and $i = 1,2$, or vice versa. Using the trapping (or detrapping) condition, $2\pi I_0 = S_k$ ($I_0 = I_k$), we write

$$2\pi \underset{k\to i}{\Delta} I = \underset{k\to i}{\Delta} S + \underset{k\to i}{\Delta} I_{st} + O(\varepsilon^{3/2}\left[|\ln\varepsilon| + (1-\xi)^{-1}\right]) \tag{1.53}$$

One can regard Eq. 1.53 as a ε-expansion of the jump of the adiabatic invariant due to a single separatrix crossing. Here, $\underset{k\to i}{\Delta} S = S_i - S_k$ is the zeroth-order term, the so-called *geometric* jump, resulting from the purely geometric change (e.g., contraction for $3 \to 1$) of the phase space area available to the particle during the separatrix crossing. The first-order term in ε, $\underset{k\to i}{\Delta} I_{st}$, is the so-called *stochastic* (or *dynamic*) jump. It results from adiabaticity violation ($\omega \approx 0$) in regions adjacent to the separatrix. This is evident from $\underset{k\to i}{\Delta} I_{st} \propto a$ (see Eq. 1.52), which reflects the logarithmic divergence of the period at the separatrix (see Eq. 1.44).

The case of a *symmetric* separatrix deserves special attention. If the Hamiltonian is $x \to -x$ symmetric, i.e., $H(x, p; \tau) = H(-x, p; \tau)$ for any p and τ, then the relation between I_0 and I_i (Eq. 1.52) can be greatly simplified. Indeed, in the symmetric case one has $S_1 = S_2 = S/2$, $\Theta_1 = \Theta_2 = \Theta = (1/2)(dS/d\tau)$, $b_1 = b_2 = b/2$, and $d_1 = -d_2 = d$. Therefore, in the symmetric case, Eq. 1.52 reduces to [Timofeev, 1978]

$$2\pi I_i = S_i \pm \varepsilon a \Theta \ln\left[2\sin(\pi\xi)\right] - (-1)^i \varepsilon d + O(\varepsilon^{3/2}\left[|\ln\varepsilon| + (1-\xi)^{-1}\right]) \tag{1.54}$$

Here, the $\sin(\pi\xi)$ term arises from the use of the well-known reflection and duplication formulas for the Gamma function [Fikhtengol'ts, 1965, Whittaker and Watson, 1996]. The '+' should be taken for $\Theta > 0$ (trapping) while '$-$' should be taken for $\Theta < 0$ (detrapping). Comparing 1.54 with 1.53, we find that geometric and dynamic jumps are given as:

$$\underset{3\to i}{\Delta} S = -\frac{S}{2}, \quad \underset{3\to i}{\Delta} I_{st} = \frac{\varepsilon a}{2}\left|\frac{dS}{d\tau}\right| \ln\left[2\sin(\pi\xi)\right] - (-1)^i \varepsilon d \tag{1.55}$$

For trapping, $G_3 \to G_i$ ($i = 1, 2$). For detrapping, $G_i \to G_3$, Eq. 1.54 reads

$$\underset{i\to 3}{\Delta} S = \frac{S}{2}, \quad \underset{i\to 3}{\Delta} I_{st} = \frac{\varepsilon a}{2}\left|\frac{dS}{d\tau}\right| \ln\left[2\sin(\pi\xi)\right] + (-1)^i \varepsilon d \tag{1.56}$$

A special note should be made about the validity of Eqs. 1.55–1.56 for *small* initial values of the adiabatic invariant. In the derivation of the original Eq. 1.52, it was implicitly assumed that before the separatrix crossing occurs, the particle resides far away from the $\sim\sqrt{\varepsilon}$ layer around the separatrix, either inside or outside. This assumption naturally excludes particles with very small adiabatic invariant, specifically $I \lesssim \varepsilon$. It turns out that such particles, during their first separatrix crossing, unlike in the standard dynamical jump, undergo a single positive jump with $\Delta I \propto \varepsilon \ln 2 > 0$ [Vainshtein et al., 1999]. This regime is often referred to as the regime of *ballistic jumps*. It is worth noting that, similar to stochastic jumps, these ballistic jumps still vanish in the limit $\varepsilon \to 0$. Thus, as we will see later (in Chapter 2), in a realistic system with an *asymmetric* separatrix, these ballistic jumps are likely overshadowed by much larger *geometric* jumps, ΔS, which do not scale with ε and can therefore be large even when $\varepsilon \to 0$.

1.4 Source and loss processes

As was discussed in Section 1.2, charged particle dynamics in weakly non-homogeneous fields can be adequately described within the guiding center approximation. The formal condition is $\epsilon = |\boldsymbol{\kappa}\rho| \ll 1$, where $\boldsymbol{\kappa} = (\boldsymbol{b}\cdot\boldsymbol{\nabla})\boldsymbol{b}$ and $\rho = p_\perp c/(|q|B)$ is the gyroradius. In the inner magnetosphere ($\lesssim 6, R_E$), the magnetic field can be approximated as dipolar. In spherical coordinates (r, θ, φ) centered at the northern magnetic pole, the (dipole) magnetic field can be written as $B = \boldsymbol{\nabla}\alpha\times\boldsymbol{\nabla}\beta$ with $\alpha = -B_0 R_E^3 \sin^2\theta/r$ ($B_0 = 31000$ nT) and $\beta = \varphi$. Therefore, the adiabaticity condition in the dipole field reads

$$\max_{\theta\in[0,\pi]} |\boldsymbol{\kappa}\rho| = 3KL^2\sqrt{\gamma^2-1} \ll 1 \tag{1.57}$$

where $K = mc^2/(|q|B_0R_E)$ and L is the equatorial distance in Earth's radii. For *electrons* with energies $\lesssim$ 10 MeV, the condition $\epsilon \ll 0.1$–1 is well satisfied for $L \lesssim 6$. At larger

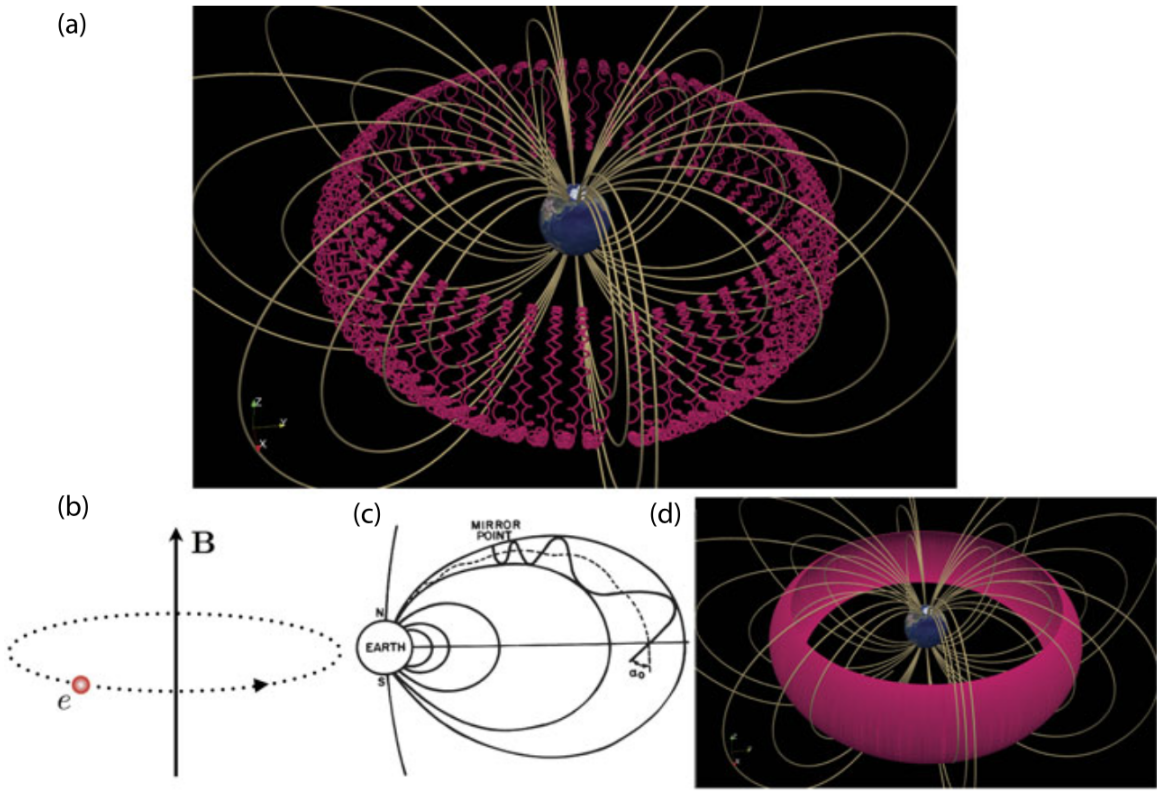

Figure 1.4: Three periodic motions in the inner magnetosphere: (a) actual motion of a 1 MeV electron with an artificial mass of 20× the electron mass (for visualization), (b) gyro-motion around the field line, (c) bounce motion along the field line between the mirror points, and (d) drift motion of the gyrocenter. From [Ukhorskiy and Sitnov, 2013]

L-values this condition is often violated due to non-dipolar features of the magnetic field topology, which result in significantly larger values of $\boldsymbol{\kappa}$ (the so-called curvature scattering, e.g., [Sergeev et al., 1993, Newell et al., 1998]). Note that the same adiabaticity condition can be written in terms of frequency as $(\omega_c\tau)^{-1} \ll 1$, where ω_c is the cyclotron frequency and τ is the characteristic period of magnetic and electric field variations. If these variations are due to waves with characteristic frequency ω, the adiabaticity condition reads $\omega \ll \omega_c$, i.e., the wave frequency should be well below the local cyclotron frequency. In reality, this condition is often violated due to the presence of various high frequency waves with $\omega \gtrsim \omega_{ce}$

[Schulz and Lanzerotti, 1974].

Condition 1.57 ensures the adiabaticity of the gyro-motion, which in turn implies conservation of the first adiabatic invariant, μ. This gyro-motion represents the fastest (high-frequency) part of the particle motion. The slower part of the motion is the bouncing between the mirror points. Its characteristic (bounce) frequency, $\omega_b = 2\pi/\tau_b$, can be estimated for nearly equatorially mirroring particles using Eq. 1.21 and expanding the magnetic field strength near the equator as (see [Schulz and Lanzerotti, 1974])

$$\gamma m\ddot{s} = -\frac{\mu}{\gamma}\frac{\partial B}{\partial s} \approx -s\frac{\mu}{\gamma}\left(\frac{\partial^2 B}{\partial s^2}\right)_{\theta=\pi/2} \tag{1.58}$$

Where $(\partial^2 B/\partial s^2)_{\theta=\pi/2} = 9B_{eq}/(LR_E)^2$. Thus, for bounce oscillations around the magnetic equator, we obtain the following linear approximation: $\ddot{s} + \omega_b^2 s = 0$ where ω_b is the *bounce-frequency* given as

$$\omega_b = \frac{3}{\sqrt{2}}\frac{c}{LR_E}\sqrt{1-1/\gamma^2} \approx \frac{0.1}{L}\sqrt{1-1/\gamma^2}\ \frac{\text{rad}}{\text{msec}} \tag{1.59}$$

The slowest (lowest-frequency) part of the charged particle motion is the azimuthal drift, arising from the curvature and gradient drifts (see Eq. 1.11). In a dipole field, this azimuthal drift is most conveniently described in terms of Euler potentials (Eqs. 1.18). For equatorially mirroring particles with $p_{||} = 0$, $\langle\alpha\rangle = \alpha(r, 0) = -B_0 R_E^2/L$, and the Hamiltonian (kinetic energy) W is only a function of α:

$$W(\alpha) = \sqrt{m^2c^4 + 2mc^2\mu B(\alpha)} \tag{1.60}$$

where we substitute $B(\alpha) = B_0/L^3 = -\alpha^3/(B_0^2 R_E^6)$. The Hamiltonian equations for (α, β) read

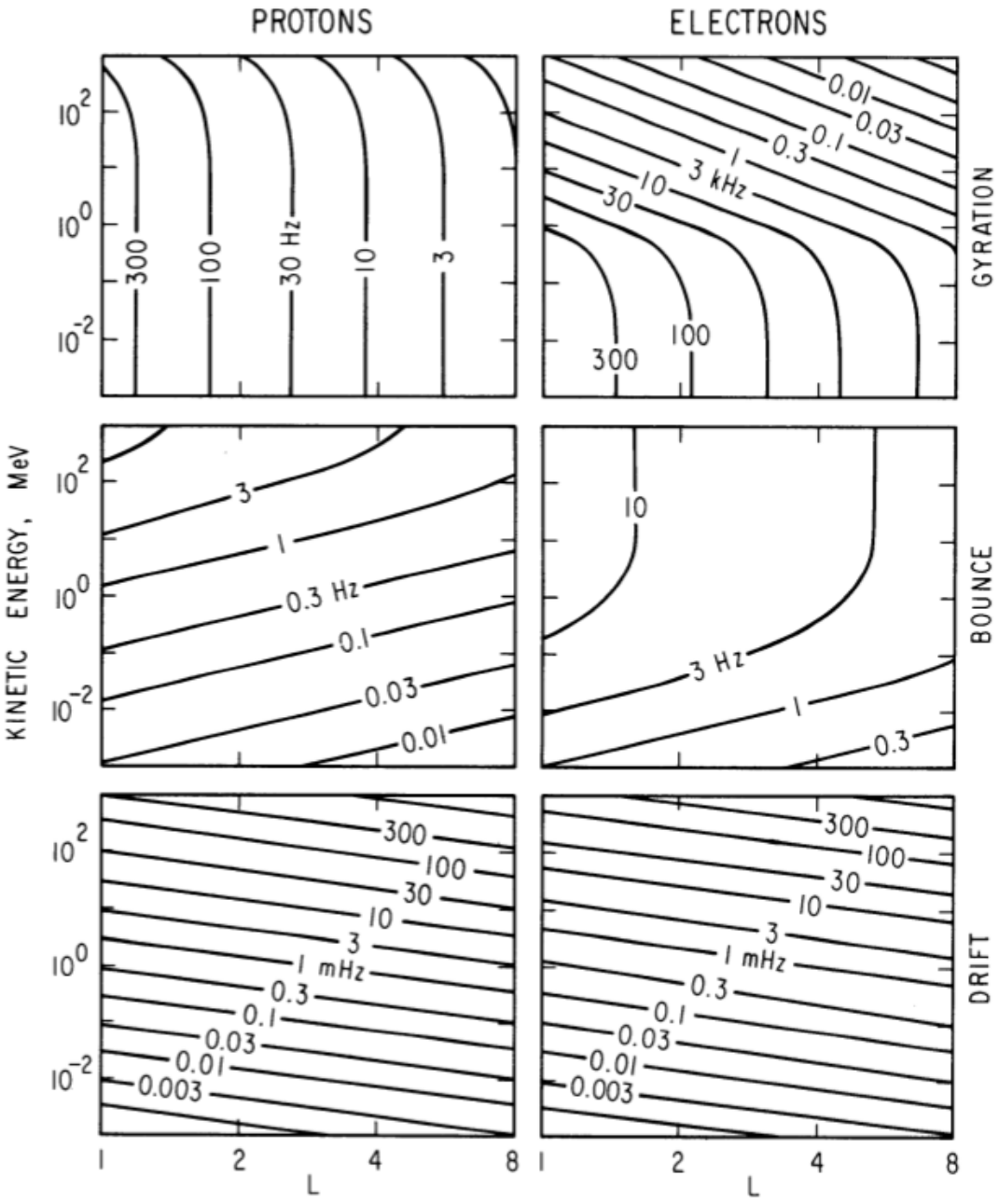

Figure 1.5: Typical time scales (frequencies) of three periodic motions in the inner magnetosphere. From [Schulz and Lanzerotti, 1974]

$$\dot{\alpha} = 0, \qquad \dot{\beta} = -\frac{c}{q}\frac{dW}{d\alpha} = \frac{3c\mu}{\gamma q}\frac{1}{(LR_E)^2} \tag{1.61}$$

Note that $\beta = \varphi$ and $\alpha = \alpha(L)$, thus, Eqs. 1.61 can be recast as

$$\dot{L} = 0, \quad \dot{\varphi} = \omega_d(L, \gamma) \tag{1.62}$$

Where $\omega_d = \omega_{0d} L(\gamma - \gamma^{-1})$ with $\omega_{0d} = 3Kc/(2R_E)$ is the *drift-frequency* [Schulz and Lanzerotti, 1974]. For electrons, $\omega_d \approx 2 \cdot 10^{-4} \cdot L(\gamma - \gamma^{-1})$ rad/sec. Eqs. 1.62 remain valid for all nearly equatorial particles. If an ensemble of particles is initiated at one field line characterized by one L value, i.e., $r(\theta) = LR_E \sin^2(\theta)$, all of them will drift azimuthally onto field lines with the same L. After one drift period $\tau_d = 2\pi/\omega_d$, they will cover a "shell" of radius L (see e.g., Fig. 1.1). This L-shell is often referred to as the drift shell or *drift orbit*.

A special note should be made regarding the applicability of the picture of closed dipole-like drift shells in the inner magnetosphere. While this picture remains remarkably accurate close to Earth, at $L \lesssim 8$, at larger radial distances the presence of the magnetopause—a sharp boundary separating the magnetosphere from the solar wind—precludes circular drift motion. Electrons injected near midnight drift dawnward and may intersect the magnetopause before reaching the dayside. This effect is commonly referred to as magnetopause shadowing and is a major source of particle losses at large radial distances (see e.g., [Shprits et al., 2006, Turner et al., 2012]).

In Section 1.2 we discussed that the cross-field drift is associated with the third adiabatic invariant, $\Phi = \oint \alpha d\beta = \oint \boldsymbol{B} \cdot d\boldsymbol{S}$, which is the magnetic flux enclosed within the drift orbit. For a dipole field, $\Phi = 2\pi\alpha = -2\pi B_0 R_E^2/L$, and thus both α and L are also adiabatically conserved. For realistic non-dipolar fields it is customary to define the so-called L^* parameter specifying the drift orbit:

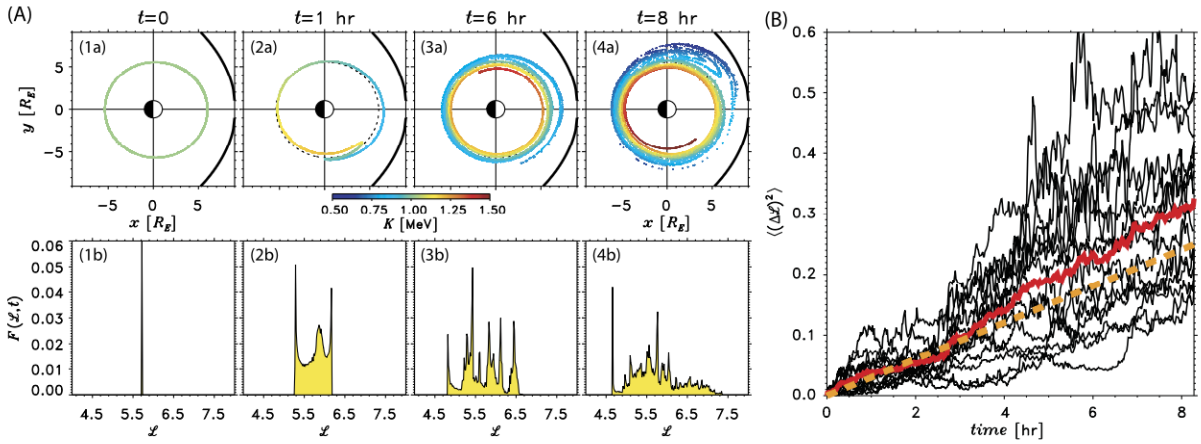

Figure 1.6: Test-particle simulation of electron radial transport driven by Ultra-Low-Frequency waves. The four upper panels show the electron radial distribution $F(L,t)$ at four moments in time. The lower panels show histograms of L at these same moments. Panel (B) shows $\langle \Delta L^2 \rangle$ calculated over an electron ensemble: a diffusive trend $\langle \Delta L^2 \rangle \propto D_{LL} t$ is observed. From [Ukhorskiy and Sitnov, 2013]

$$L^* = -\frac{2\pi B_0 R_E^2}{\Phi} \tag{1.63}$$

For a dipole field, $L^* = L$, whereas for non-dipolar fields L^* serves as a proxy for the radial extent of the drift orbit. Adiabatic conservation of Φ and L^* suggests that any *radial transport* (transport in L^*) necessitates a violation of adiabaticity (see Section 1.3). The most classical mechanism relies on interaction with Ultra-Low-Frequency (ULF) waves with frequencies close to the electron drift frequency ($\omega_d \sim$ mHz).

1.4.1 Radial Transport and Diffusion

Hamiltonian 1.60 describes the unperturbed electron dynamics in a dipole field. In the inner magnetosphere, the zeroth-order effect that violates this azimuthal symmetry is the convective

electric field in the dawn–dusk direction, $\boldsymbol{E} = E_0\hat{\boldsymbol{y}}$, as well as the corotational field. Both of these effects result in azimuthally periodic motion conserving Φ and L^* and mostly affect low-energy particles [Lyons and Williams, 1984]. In contrast, the inclusion of low-frequency oscillations allows for breaking the conservation of Φ. Consider a wave carrying an azimuthal electric field $E_w \cos\psi_n$, where $\psi_n = n\beta - \omega_n t + \psi_0$ is the wave phase and ω_n is its frequency and n is the azimuthal wavenumber; we assume that ω_n and n are related by an (unspecified) dispersion relation. The wave field can be included in Hamiltonian 1.60 via the vector-potential perturbation $A_\varphi \to A_\varphi - A_w \sin\psi_n$ with $A_w = cE_w/\omega_n$. In terms of Euler potentials, this corresponds to $\alpha = \alpha + \delta\alpha$, where $\delta\alpha = -r(\alpha_0)A_w \sin\psi_n$ and $r(\alpha) = -B_0R_E^3/\alpha$. Treating this wave field as a small perturbation on top of the dipole field and expanding $B(\alpha + \delta\alpha)$ with respect to $\varepsilon = E_w/B_0 \ll 1$ yields

$$W = mc^2\sqrt{1 + \frac{2\mu B(\alpha+\delta\alpha)}{mc^2}} \approx \gamma(\alpha)mc^2 + \frac{\mu}{\gamma(\alpha)}\frac{\partial B}{\partial\alpha}\frac{B_0R_E^3}{\alpha}A_w\sin\psi_n \tag{1.64}$$

where $\gamma(\alpha) = \sqrt{1 - 2\tilde{\mu}\alpha^3}$ with $\tilde{\mu} = \mu/(mc^2B_0^2R_E^6)$ and $\partial_\alpha B = -3\alpha^2/(B_0^2R_E^6)$. Introducing $\tilde{\phi}_n = 3c\mu/(\omega_nR_E^3)$ we rewrite 1.64 as

$$W(\alpha,\beta,t) = \gamma(\alpha)mc^2 - \varepsilon\left(\frac{\alpha\tilde{\phi}_n}{\gamma(\alpha)}\right)A_w\sin\psi_n(\beta,t) \tag{1.65}$$

If multiple wave modes with different n's and ω_n's are present, the perturbation term proportional to ε becomes a sum over all $n \in [-N_1, N_2]$, and the Hamiltonian for the (α,β) variables adheres to the following general form:

$$H(\alpha,\beta,t) = H_0(\alpha) + \varepsilon\sum_n V_n(\alpha)e^{i(n\beta-\omega_nt)} \tag{1.66}$$

Where $H = -(c/e)W$, $H_0 = -(c/e)\gamma mc^2$ and $V_n = (\alpha\tilde{\phi}_n/\gamma)\cdot cA_w/e$. The resultant equations of motion read

$$\begin{aligned}\dot{\alpha} &= -\varepsilon \sum_n n V_n e^{i(n\beta-\omega_n t)} \\ \dot{\beta} &= \omega_d + \varepsilon \sum_n \frac{dV_n}{d\alpha} e^{i(n\beta-\omega_n t)}\end{aligned} \tag{1.67}$$

Where ω_d is the drift frequency of the unperturbed motion. System 1.67 possesses two distinct time scales, a slow rotation in β due to ω_d and rapid changes in (α, β) due to resonant interactions. Consider an ensemble of particles in (α, β) with a distribution function $f(\alpha, \beta, t)$. According to Liouville's theorem [Landau and Lifshitz, 1988]

$$\frac{\partial f}{\partial t} + \dot{\beta}\frac{\partial f}{\partial \beta} + \dot{\alpha}\frac{\partial f}{\partial \alpha} = 0 \tag{1.68}$$

To find the long-term evolution of the distribution function, one can use the quasi-linear approach [Vedenov et al., 1962, Kennel and Engelmann, 1966]. Namely, one decomposes f into a slowly varying part $F(\alpha, \tau)$ with $\dot{\tau} \ll 1$, which does not depend on the phase variable (β), and a fast oscillation $\varepsilon f_1(\alpha, \beta, t) = O(\varepsilon)$. It turns out (see discussion below) that in the first non-vanishing order $\tau = \varepsilon^2 t$. With this decomposition we write $f(\alpha, \beta, t) = F(\alpha, \tau) + \varepsilon f_1(\alpha, \beta, t)$, where $f_1(\alpha, \beta, t) = \sum_n f_{1n}(\alpha) e^{i(n\beta-\omega_n t)}$. In what follows, we essentially reproduce all the steps of [Vedenov et al., 1962]. Plugging this form into Liouville's theorem 1.68 and using Eqs. 1.67, we find to first order in ε

$$f_{1n} = -\frac{n V_n}{\omega_n - n\omega_d}\frac{\partial F}{\partial \alpha} \tag{1.69}$$

Equating the terms to order ε^2 in 1.68 and applying β-averaging, $\langle \dots \rangle = (2\pi)^{-1} \int_0^{2\pi} \dots d\beta$, to the result yields the equation for $\dot{F}$:

$$\frac{\partial F}{\partial \tau} = i\frac{\partial}{\partial \alpha} \sum_n \left(n V_n f_{1n}^*\right) \tag{1.70}$$

Plugging in f_{1n} from 1.69 and expressing τ in terms of t gives us

$$\frac{\partial F}{\partial t} = \frac{\partial}{\partial \alpha}\left(D_{\alpha\alpha}\frac{\partial F}{\partial \alpha}\right) \tag{1.71}$$

where $D_{\alpha\alpha} = \pi\varepsilon^2 \sum_n n^2 |V_n|^2 \delta(\omega_n - n\omega_d)$, with $\delta(x)$ being the delta function arising from the identity $\mathrm{Im}(x - x_0)^{-1} = \pi\delta(x - x_0)$. Note that $D_{\alpha\alpha}$ is determined solely by the wave power at the integer multiples of the drift frequency, $D_{\alpha\alpha} \propto E_w^2$, as expected from the quasilinear theory [Vedenov et al., 1962, Kennel and Engelmann, 1966]. Again, note that the derivation is identical to the classical 1D velocity diffusion due to interaction with electrostatic turbulence upon replacing $(\dot{x}, x)$ with (α, β) [Vedenov et al., 1962]. A special note should be made about the form of τ. The first natural assumption for the rate of change of F would be $\tau = \varepsilon t$. This would be the case if the perturbed Hamiltonian 1.65–1.66 allowed for a nonzero drift, $\langle \varepsilon \sin\psi_n \rangle_\beta \propto \varepsilon \neq 0$. We assume that the waves are of sufficiently low amplitude ($\varepsilon \ll 1$) and that their spectrum is sufficiently broadband such that the individual resonances where $\dot{\psi}_n = 0$ strongly overlap, thereby greatly inhibiting phase-space trapping. As a result, ψ_n and β can be treated as randomly distributed in $(0, 2\pi)$. In this case, the drift term (i.e., the term first order in ε) disappears. As first demonstrated by [Landau, 1936], for equations of Hamiltonian dynamics in this specific setting, the evolution is purely diffusive (e.g., 1.71). Consequently, the first non-vanishing contribution appears only in the second order of ε, such that $\tau = \varepsilon^2 t$.

Equation 1.71 describes diffusion in the adiabatic invariant (α or Φ). In practice, it is often convenient to recast Eq. 1.71 in terms of L^*. Note that $\alpha = \Phi/(2\pi) \propto 1/L$ (here L is L^*), thus, Eq. 1.71 can be rewritten as [Fälthammar, 1965, Schulz and Lanzerotti, 1974]

$$\frac{\partial F}{\partial t} = L^2 \frac{\partial}{\partial L}\left(\frac{D_{LL}}{L^2}\frac{\partial F}{\partial L}\right) \tag{1.72}$$

This form describes *radial diffusion* due to interaction with waves at $\omega = n\omega_d$. Eq. 1.72 is solved for specified values of μ and $J_{||}$ since both are conserved quantities. It is evident that 1.72 conserves the total number of particles, $\int_{-\infty}^{0} F d\Phi = \int_{0}^{\infty} F L^{-2} dL = \text{const}$. In reality, diffusion occurs in L, in $J_{||}$, and in μ. Although including these effects significantly increases the complexity of the equation, the important consequence of μ diffusion is that particles are scattered along the field line and are lost from the system into the atmosphere. Another important loss mechanism is magnetopause shadowing, which effectively eliminates the flux above $L > L_{ex}$, where L_{ex} is often referred to as the Last-Closed-L-Shell (LCLS). To mimic these effects, a heuristic loss term, F/τ_{loss}, is often added to 1.72

$$\frac{\partial F}{\partial t} = L^2 \frac{\partial}{\partial L}\left(\frac{D_{LL}}{L^2}\frac{\partial F}{\partial L}\right) - \frac{F}{\tau_{loss}} \tag{1.73}$$

Here τ_{loss} is the effective electron e-lifetime which is a function of energy, μ and L. In practice, Eq. 1.73 is often solved using empirical approximations of D_{LL} for various driving conditions [Brautigam and Albert, 2000, Ozeke et al., 2014]. Fig. 1.6 shows the results of a numerical test-particle simulation of electron radial transport obtained by solving the guiding-center equations 1.67. The results indicate a diffusive spread in L in agreement with 1.73.

1.4.2 Drift-Orbit Bifurcation

In Section 1.4.1, we saw that radial transport arises from the violation of the third adiabatic invariant, Φ, which is driven by electron resonant interaction with ultra-low-frequency waves. It turns out that this transport can occur without any external wave driver, purely due to the topology of the (static) magnetic field. In this case, the violation of the *second* adiabatic invariant, $J_{||}$, becomes critical.

As was derived in Section 1.2, electron motion along the field line labeled by (α, β) is

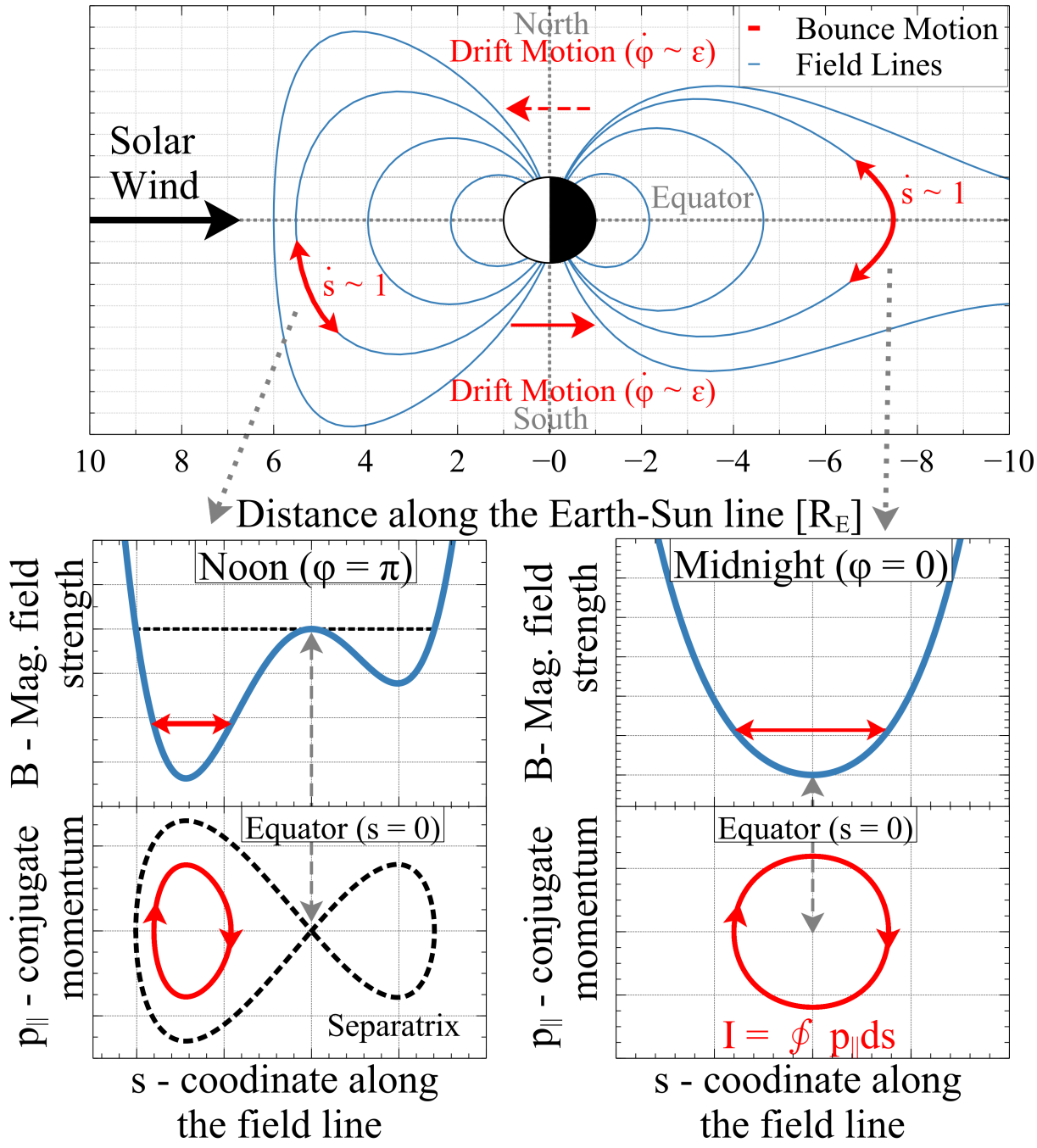

Figure 1.7: Schematic view of DOB [magnetic field lines from [Tsyganenko and Sitnov, 2005]]. From [Kamaletdinov et al., 2025b]

described by the following Hamiltonian

$$H(s, p_{||}; \alpha, \beta) = \frac{p_{||}^2}{2m^*} + \mu^* B(s; \alpha, \beta) \tag{1.74}$$

This system has two distinct intrinsic time scales: (1) fast, $\sim \omega_b$, oscillation along the field lines, and (2) slow cross-field drift in (α, β) with $\dot{\beta} \sim \omega_d$. The critical quantity is the time separation between these two motions, $\varepsilon = \omega_d/\omega_b = \tau_b/\tau_d$. Using the dipole estimates for ω_d and ω_b obtained previously, we find that the bounce and drift motions are well separated even for relativistic energies below $\lesssim$ 5–50 MeV at $L < 9$ as

$$\varepsilon \approx 10^{-6} L^2 \sqrt{\gamma^2 - 1} \lesssim 0.01 - 0.1 \tag{1.75}$$

This time separation allows us to treat changes in (α, β) as quasi-stationary from the perspective of $(s, p_{||})$ motion. Although at $L > 6$ the magnetic field lines deviate from the dipole, especially on the dayside, one may still treat (α, β) as canonical proxies for L (L^* - a proxy for the radial distance) and the azimuthal location, respectively. This is because even for arbitrary magnetic fields, both (α, β) remain constant along field lines. One can trace from the instantaneous charged-particle location onto the sphere $r = R_E$, where (α, β) take their dipolar values.

Consider a particle starting its motion on the nightside with (α, β) corresponding to L and $\varphi = 0$ (for convenience we shift $\varphi \to \varphi + \pi$ from its dipolar value). As long as $J_{||}$ is conserved, i.e., the bounce motion remains adiabatic, Eqs. 1.61–1.62 apply and $\dot{\alpha} = 0$ and $\dot{\beta} = \omega_d$. As we shall see shortly, near the dayside ($\varphi \approx \pi$) the adiabaticity is violated and $J_{||}$ undergoes a jump $\Delta J_{||}$. To estimate this jump, we draw upon the approach of unperturbed trajectories: integrate $H(s, p_{||}; \alpha, \beta)$ using unperturbed trajectories for (α, β). Note that this is completely analogous to classical quasi-linear theory, where a jump of the first adiabatic

invariant, $\Delta\mu$, and $\Delta p_{||}$ are calculated via integration along the Larmor helix (the trajectory of constant μ and $p_{||}$) [Kennel and Engelmann, 1966, Lerche, 1968]. With this rationale in mind, the unperturbed trajectories in the inner magnetosphere read: $L = \text{const}$, $J_{||} = \text{const}$ and $\varphi = \omega_d t$ and Hamiltonian 1.74 reduces to that of a dynamical system with $1\frac{1}{2}$ degrees of freedom

$$H(s, p_{||}; \varphi) = \frac{p_{||}^2}{2m^*} + \mu^* B(s, \varphi) \tag{1.76}$$

Here $\varphi = \omega_d t$ is the *slow time* since $\dot{\varphi}/\omega_b = \varepsilon \ll 1$ (see Section 1.3). In 1.76, $B(s, \varphi) = B(s, \varphi; L)$ stands for the magnetic field strength profile along the field line with corresponding to L at the azimuthal location of φ. The term $\mu^* B(s, \varphi)$ plays the role of the effective potential for $(s, p_{||})$ which slowly varies in time.

Fig. 1.7 shows the magnetic field strength profile, $B(s, \varphi)$, at midnight ($\varphi = 0$) and at the dayside ($\varphi = \pi$). Earth's magnetic field lines on the nightside resemble a (stretched) dipole, featuring a single minimum of $B(s)$ near the magnetic equator, where electrons bounce along the field lines with a typical period $\tau_b = 2\pi/\omega_b$ ($\sim$ seconds; see Eq. 1.59). In the phase plane of $(s, p_{||})$ this periodic motion is associated with the second adiabatic invariant, $J_{||} = \oint p_{||} ds$. As the electron slowly ($\sim \omega_d$) drifts from the nightside eastward, both the magnetic field profile and the instantaneous (on the bounce timescale $\sim \omega_b$) configuration slowly change, but the area inside the trajectory, i.e., $J_{||}$, only oscillates with amplitude $\sim \varepsilon$ around its constant value.

Conservation of J breaks down as the electron approaches the dayside, where field lines are compressed by the solar wind, resulting in a $B(s)$ profile with an equatorial maximum separating two local minima on either side of the equator. This leads to the formation of a separatrix in phase space $(s, p_{\|})$, demarcating trajectories of particles trapped in the two minima. As a particle crosses the separatrix, it becomes trapped in one of the minima,

resulting in a jump of the adiabatic invariant, $\Delta J_{||}$. Using the notation of Section 1.3, this jump is given by $\underset{3\to i}{\Delta} J_{||} \approx \underset{3\to i}{\Delta} S + \underset{3\to i}{\Delta} J_{st}$. Here again, subscript 3 refers to the phase-space domain outside the separatrix, while $i = 1, 2$ refers to the left ($s < 0$) and right ($s > 0$) phase-space pockets.

As the electron crosses local noon ($\varphi = \pi$) and drifts back to the nightside, the equatorial maximum of magnetic field strength diminishes and the total area inside the separatrix shrinks, $dS/d\varphi < 0$, and the particle is eventually released from the separatrix. This produces a second jump of the adiabatic invariant: $\underset{i\to 3}{\Delta} J_{||} \approx \underset{i\to 3}{\Delta} S + \underset{i\to 3}{\Delta} J_{st}$. The resultant jump over one complete drift period consists of two contributions:

$$\Delta J_{||} = \Delta S + \Delta J_{st} \tag{1.77}$$

Here, $\Delta S = \underset{3\to i}{\Delta} S + \underset{i\to 3}{\Delta} S$ is the net geometric jump, and $\Delta J_{st} = \underset{i\to 3}{\Delta} J_{st} + \underset{3\to i}{\Delta} J_{st}$ is the net stochastic jump due to $\varepsilon \neq 0$. In the generic case when the two minima and the separatrix are asymmetric (as shown in Fig. 1.7), both terms are non-negligible. Moreover, the first term, ΔS, is likely to dominate since $\Delta S = O(1)$ and depends only on the level of asymmetry, whereas $\Delta J_{st} = O(\varepsilon)$ (see Section 1.3).

It is, however, instructive to consider the symmetric case. In this case $\Delta S = 0$ (see Eqs. 1.55–1.56), and the net change of $J_{||}$ is determined solely by the stochastic jump. Using Eqs. 1.55–1.56, we write

$$\Delta J_{||} = \Delta J_{st} = \varepsilon a \left|\frac{dS}{d\varphi}\right| \ln\left[2\sin(\pi\xi)\right] \tag{1.78}$$

Here $\xi \in (0, 1)$ is determined by the initial phase and should effectively be treated as a random variable.

If an ensemble of particles with randomly distributed phases is considered, then the distribution $F(J_{||})$ evolves according to standard diffusion as

$$\begin{aligned} \langle \Delta J_{||} \rangle_\xi &= 0 \\ \langle \Delta J_{||}^2 \rangle_\xi &= \varepsilon^2 a^2 \frac{\pi^2}{12} \left(\frac{dS}{d\varphi} \right)^2 \propto \varepsilon^2 \neq 0 \end{aligned} \tag{1.79}$$

Where we used $\int_0^\pi \ln[2\sin x]dx = 0$ and $\int_0^\pi \ln^2[2\sin x]dx = \pi^3/12$ [Gradshteyn and Ryzhik, 2007]. According to 1.79, the longe-term dynamics of $J_{||}$ in the symmetric case adheres to the diffusion where the diffusion coefficient is given as $D_{JJ} = \langle \Delta J_{||}^2 \rangle_\xi / (2\tau_d)$ [Antonova et al., 2003].

The jump of $J_{||}$ during the separatrix crossings renders the third adiabatic invariant undefined, resulting in a radial displacement, ΔL. In contrast, the first adiabatic invariant, μ, remains conserved. This allows relating the radial displacement, ΔL to $\Delta J_{||}$ via $\Delta L = (\partial L/\partial J_{||})_\mu \Delta J_{||}$. For bifurcated orbits, the notion of L is ambiguous, so we choose L to be the radial extent of the drift orbit at the nightside. Coefficient $(\partial L/\partial J_{||})_\mu = 1/(\partial J_{||}/\partial L)_\mu$ should be calculated using field-line tracing in a specified magnetic field model (e.g., [Tsyganenko and Sitnov, 2005]). However, to lowest order, it can be approximated using dipole-field expressions for $J||$ and assuming nearly equatorially mirroring particles, in which case L refers to the radial extent of the drift orbit on the nightside.

The field-line motion of nearly equatorially mirroring particles reduces to that of a harmonic oscillator, $\ddot{s} + \omega_b^2 s = 0$ with bounce frequency $\omega_b = \mu B''/(m\gamma^2)$, where $B'' = 9B_{\rm eq}/(LR_E)^2$ (see Eq. 1.58). For a harmonic oscillator, the effective Hamiltonian is $h = \frac{1}{2}(\dot{s}^2 + \omega_b^2 s^2)$, and the adiabatic invariant, $\oint \dot{s} ds = J_{||}/(\gamma m)$, is given as $\oint \dot{s} ds = 2\pi h/\omega_b = \pi \omega_b s_{max}^2$ [Landau and Lifshitz, 1988]. Here s_{max} is the amplitude of oscillation along the field line. s_{max} can be found from conservation of μ and γ as $B \approx B_{eq} + \frac{1}{2}B'' s_{max}^2 = B_m$, where $B_m = p^2/(2m\mu)$ is the magnetic field strength at the mirror point (see discussion of Eq. 1.19). Thus, in the case

of near-equatorial oscillations, the second adiabatic invariant is given as

$$J_{||} = 2\pi(B_m - B_{eq})\sqrt{\frac{m\mu}{B''}} \tag{1.80}$$

Taking a derivative of 1.80 with respect to L under $\mu = \text{const}$ (and $\gamma = \text{const}$) in the limit of $B_m \to B_{eq}$, we obtain [Öztürk and Wolf, 2007]

$$\frac{\Delta J_{||}}{p} = \frac{1}{p}\left(\frac{\partial J_{||}}{\partial L}\right)_{\mu,\gamma} \Delta L \approx \frac{\pi R_E}{\sqrt{2}}\Delta L \tag{1.81}$$

Here we deliberately normalize $\Delta J_{||}$ by p, since in the absence of an electric field p is conserved, and thus the jump of $J_{||}$ is purely due to the jump of the normalized second adiabatic invariant, $\Delta J_{||} = p\Delta I$ (see Eq. 1.19).

Eqs. 1.79 and relation 1.81 suggest that under symmetric drift–orbit bifurcation the *radial* transport is also diffusive in L. This result is further supported by direct test-particle simulations [Ukhorskiy et al., 2014a]. Using 1.81 and 1.79, the radial diffusion coefficient $D_{LL} = \langle \Delta L^2 \rangle_\xi / (2\tau_d)$ can be expressed as

$$D_{LL} = \frac{2}{\pi^2 R_E^2}\frac{D_{JJ}}{p^2} = \frac{\varepsilon^2 a^2}{12\tau_d}\left(\frac{1}{pR_E}\frac{dS}{d\varphi}\right)^2 \tag{1.82}$$

Here we collected within the parentheses the term pR_E and the separatrix growth rate $dS/d\varphi$ because the separatrix area S, just like $J_{||}$, scales linearly with p and LR_E (see Chapter 2 and [Ukhorskiy et al., 2014a]). Order-of-magnitude estimates using the dipole expression for τ_d and ε (Eq. 1.75) and taking $(pR_E)^{-1}(dS/d\varphi) \approx 3L$ yield $D_{LL} \sim 0.004 \cdot \gamma^3 \cdot (L/10)^7$ days^{-1} [Öztürk and Wolf, 2007]. Compared to the radial diffusion driven by ULF waves [Brautigam and Albert, 2000], we find that radial diffusion driven by *symmetric* drift–orbit bifurcation

becomes comparable to ULF-driven transport at $L \gtrsim 7$ only at electron energies $\gtrsim 10$ MeV [Öztürk and Wolf, 2007].

The order-of-magnitude estimation above shows that the radial transport driven by symmetric drift-orbit bifurcation is inefficient for electrons with energies of $\lesssim 0.1$–1 MeV. This is easy to explain from the scaling of Eq. 1.82. Indeed, recall that in the symmetric case, the jump of the second adiabatic invariant, and thus the radial displacement, scale linearly with ε (see Eq. 1.78). For the typical plasma-sheet/outer radiation belt energies of $\lesssim 0.1 - 1$ MeV at $L < 9$, we find $\varepsilon \lesssim 10^{-4}$. The diffusion coefficient D_{LL} scales quadratically with ε, rendering radial transport under such small values of ε negligible. For particles with $I \lesssim \varepsilon$ (where I is the normalized invariant), the first bifurcation produces a non-zero drift that scales linearly with ε [Vainshtein et al., 1999, Ukhorskiy et al., 2014a]. However, subsequent crossings again follow the highly inefficient diffusion regime with $D_{LL} = O(\varepsilon^2)$.

The inefficiency of radial transport in symmetric drift-orbit bifurcation suggests that it is worth revisiting the realistic (asymmetric) case, in which the zeroth-order term in the adiabatic invariant jump—a geometric jump, $\Delta S = O(1)$—does not vanish. By definition, the geometric jump is given by the difference in the phase-space area inside the separatrix between the trapping and detrapping. Since trapping and detrapping occur when this separatrix area (or one of its pockets) reaches the current value of the adiabatic invariant, in a generic case the geometric jump is comparable in size to the adiabatic invariant itself. Indeed, numerical simulations by [Wan et al., 2010] indicate that under asymmetric solar-wind–driving conditions, i.e., IMF $B_y \neq 0$, electrons on bifurcated orbits experience large jumps in $J_{||}$. Interestingly, these results appear to conflict with later simulations by [Ukhorskiy et al., 2011], which show that the global east–west asymmetry of Earth's magnetosphere has little impact on drift-orbit bifurcation.

In this thesis, we undertake a systematic investigation of the dynamics of electrons on bifurcated drift orbits in realistic (asymmetric) magnetic field configurations. The emphasis is

placed on: (1) the typical level and relative importance of magnetic field asymmetry, quantified through jumps of the second adiabatic invariant and the associated radial displacement, ΔL; (2) the range of electron energies for which radial transport driven by drift-orbit bifurcation competes with ULF-driven diffusion; and (3) the long-term dynamics driven by such asymmetric jumps, in particular whether this dynamics is diffusive in nature. Each chapter of this thesis addresses a specific question directed toward this overarching goal.

1.5 Thesis Organization

In this chapter, we introduced the concepts of radial transport and drift-orbit bifurcation and discussed the relevant aspects of radial transport in the radiation belts. The chapter develops the necessary physical framework and mathematical toolkit that will be used throughout the thesis. The following chapters are aimed at a thorough quantification of the role that asymmetry plays in the radial transport of energetic electrons in the outer radiation belt and near the magnetopause via the drift-orbit bifurcation mechanism.

Chapter 2 is based on the results published in [Kamaletdinov et al., 2024a] and assesses the role of magnetospheric asymmetry in a realistic magnetic field configuration. Using the empirical magnetic field model of [Tsyganenko and Sitnov, 2005], we quantitatively demonstrate that global magnetospheric asymmetry, under typical solar wind conditions, makes asymmetry-driven jumps in drift-orbit bifurcation a leading-order effect and thus should be treated as the norm rather than the exception. A mapping in the adiabatic invariant is constructed, allowing the estimation of asymmetry-driven (geometric) jumps of the second adiabatic invariant. These jumps are then translated into the associated radial displacements. We show that this radial displacement can reach $\Delta L \approx \pm 1$ per drift period.

Chapter 3 focuses on a case study demonstrating the efficiency of radial transport driven by asymmetric drift-orbit bifurcation in the context of THEMIS observations of near-

magnetopause energetic electron enhancements [Kamaletdinov et al., 2025a]. A representative event of near-magnetopause energetic (> 30 keV) electron enhancement is chosen, for which an *ad hoc* magnetic field model is constructed, reflecting the concurrent solar wind conditions monitored by the ARTEMIS mission. A guiding-center simulation of an ensemble of electrons is carried out, demonstrating the formation of an (radially) isolated enhancement in the electron radial distribution at larger (bifurcated) drift orbits due to outward radial transport driven by asymmetric drift-orbit bifurcation. The results clearly demonstrate the important role that drift-orbit bifurcation may play in near-magnetopause radial transport.

Chapter 4 is based on the results published in [Kamaletdinov et al., 2025b]. The chapter quantifies the non-diffusive character of asymmetric drift-orbit bifurcation, while also exploring the fundamental properties of the long-term dynamics driven by geometric jumps in phase space. Drawing upon the framework outlined in Chapter 2, a mapping in the adiabatic invariant is constructed, allowing the long-term dynamics of large particle ensembles to be efficiently modeled. The chapter also introduces the equivalent radial diffusive rate as a natural measure of asymmetric drift-orbit bifurcation driven radial transport. This equivalent radial diffusive rate is compared with conventional radial diffusion coefficients associated with ULF waves. The results again suggest that drift-orbit bifurcation can drive effective radial transport of 0.1–1 MeV electrons, especially under low solar wind driving conditions when conventional ULF-driven diffusion may subside.

Chapter 5 concludes by summarizing the results in the context of the three key questions posed in Chapter 1. Future directions are also outlined, including not-yet-resolved problems that are likely implicated by drift-orbit bifurcation effects.

CHAPTER 2

Asymmetric Drift-Orbit Bifurcation and Geometric Jumps of Adiabatic Invariant

The Drift-orbit bifurcation mechanism under North–South and East–West symmetric magnetic field configurations has been extensively investigated, both from the perspective of the underlying theoretical framework [Roederer, 1969, Antonova et al., 2003] and by assessing its role via test-particle simulations [Öztürk and Wolf, 2007, Ukhorskiy et al., 2011]. It has recently received renewed attention as a potential driver of radial transport [Öztürk and Wolf, 2007, Ukhorskiy et al., 2011, Ukhorskiy et al., 2014a]. In particular, [Ukhorskiy et al., 2011] examined its effects on radial transport using test-particle tracing in the TS07 magnetic field model [Tsyganenko and Sitnov, 2007]. In agreement with theoretical expectations (see [Antonova et al., 2003] and Chapter 1) at large values of $J_{\|}$, the evolution of a large ensemble of particles was well-described by diffusion with $\langle \Delta J_{\|} \rangle = 0$ and $\langle (\Delta J_{\|})^2 \rangle > 0$ (here $\langle \dots \rangle$ denotes averaging over electron bounce phase for a large particle ensemble). For small $J_{\|}$, the particle dynamics is dominated by large jumps with $\langle \Delta J_{\|} \rangle > 0$ [Vainshtein et al., 1999, Zelenyi et al., 2013]. Interestingly, the results by [Ukhorskiy et al., 2011] show that the global east–west asymmetry of Earth's magnetosphere does not have a significant effect on the drift-orbit bifurcation. This contradicts the results of test-particle simulations by [Wan et al., 2010], which showed the existence of large jumps of $J_{\|}$ under strong system asymmetry due to a significant IMF B_y. The importance of a global East–West system asymmetry for creating large jumps of $J_{\|}$ independent of the bounce phase has also been discussed by [Öztürk and

Wolf, 2007], but was not studied further.

In this chapter, we aim to: (1) develop a theoretical model describing jumps in the second adiabatic invariant, $J_{\parallel}$, due to drift-orbit bifurcation in an *asymmetric* magnetic field configuration using an empirical model of the global magnetic field; (2) use this model of jumps to estimate the radial transport of particles associated with asymmetric drift-orbit bifurcation; and (3) identify solar wind conditions favorable for the radial transport due to the asymmetric drift-orbit bifurcation.

2.1 Magnetospheric Asymmetry and IMF B_y

2.1.1 Solar Wind Conditions at 1 AU: ARTEMIS dataset

The solar wind exerts strong control on the configuration of the Earth's magnetosphere via transport of particles and flux through reconnection at magnetopause and in the magnetotail [Dungey, 1961, Dungey, 1963]. Consequently, magnetospheric asymmetries are also associated with the solar wind characteristics, namely the orientation of the interplanetary magnetic field (IMF) [Liou and Mitchell, 2019, Holappa and Buzulukova, 2022]. Figure 2.1 shows the distribution of solar wind parameters collected over 12 years by the ARTEMIS mission at 1 AU [Angelopoulos, 2011]. Magnetic field data is provided by the Fluxgate Magnetometer (FGM) at a rate of 128 Samples/s with offset stability < 0.2 nT/12 hr [Auster et al., 2008]. We utilize the ion bulk velocity, $\boldsymbol{v}$, to infer solar wind ram pressure, $P_{dyn} = n_i m_i \boldsymbol{v}^2$, where n_i is ion number density and m_i is proton mass. Ion density and bulk velocity are provided by electrostatic analyzers (ESA) that measure ion (< 25 keV) distribution functions at 4s cadence [McFadden et al., 2008]. Figure 2.1c shows the distribution of the angle between the IMF vector and the y-axis (in GSM system of coordinates), defined as $\varphi_{\text{IMF}} = atan(\text{IMF } B_z/\text{IMF } B_y)$. We see that most of the time, IMF B_y is the dominant component of the IMF. This shows that the east-west asymmetric magnetospheric configuration associated with IMF $B_y \neq 0$

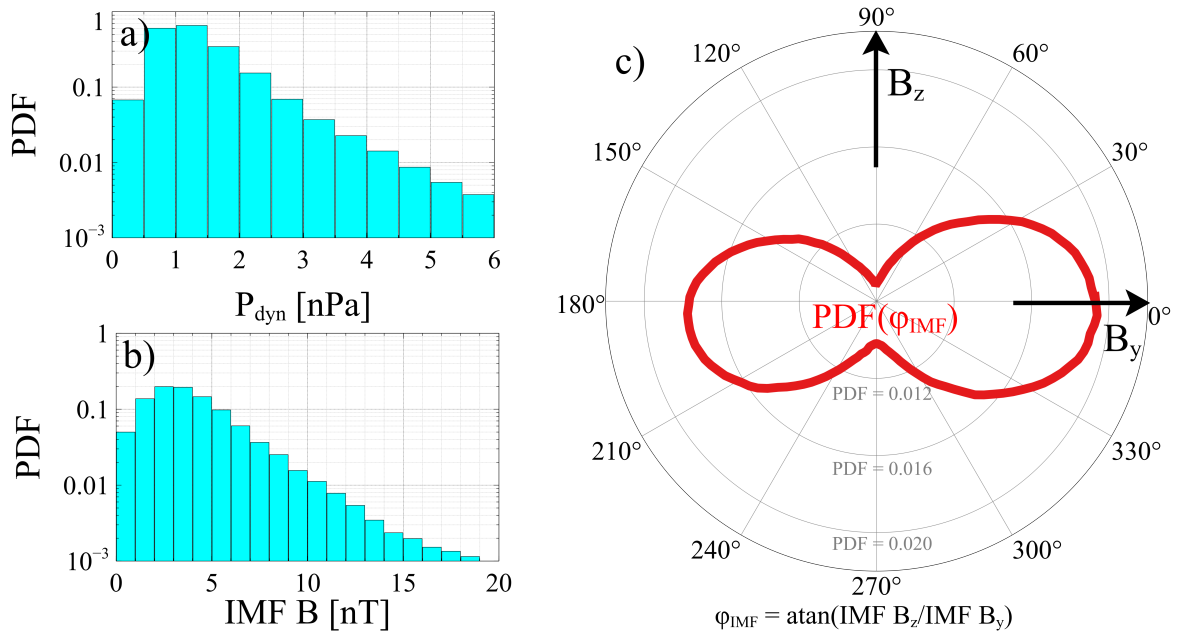

Figure 2.1: Distribution of the solar wind parameters collected during 12 years of ARTEMIS observations at 1 AU [Angelopoulos, 2011]: (a) Probability density function (PDF) of the solar wind ram pressure, P_{dyn}, (b) PDF of the magnitude of the solar wind magnetic field, IMF B, (c) PDF (angular diagram) of the angle $\varphi_{\mathrm{IMF}} = atan(\mathrm{IMF}B_z/\mathrm{IMF}B_y)$.

should be treated as the norm rather than an exception.

2.1.2 Drift Orbit

Electrons orbit the Earth from dawn to noon and then from noon to dusk due to the combination of the curvature and gradient drifts (see Chapter 1.4). The periodic motion along this drift orbit gives rise to the third adiabatic invariant, which equals the magnetic flux, $\Phi = \oint \mathbf{B}\cdot d\mathbf{S}$, enclosed within the drift orbit. For a dipole magnetic field, $\Phi = -2\pi B_0 R_E^2/L$, where L is the equatorial extent of the drift orbit. In a realistic (non-azimuthally symmetric) magnetic field configuration, drawing upon this analogy with the dipole case and using conservation of Φ allows the introduction of the generalized L^* parameter as $L^* = -2\pi B_0 R_E^2/\Phi$, which serves as a natural proxy for the radial extent of the particle drift orbit.

In the general case, determining the exact drift orbit requires numerical computation by solving the full 3D equations of motion in the guiding-center approximation (see Chapter 1). By virtue of conservation of the first adiabatic invariant, for initially equatorially mirroring particles the drift orbit coincides with the contour of constant magnetic field intensity. This is because for equatorially mirroring particles $p = p_\perp$ and, thus, the conservation of the total energy (total momentum p) and of the first adiabatic invariant $\mu = p_\perp^2/2mB(\boldsymbol{r})$ necessities $B(\mathbf{r}) = \text{const}$ everywhere along the drift orbit. If such particles start drifting at midnight with equatorial pitch-angle $\alpha_{eq} = 90°$ from the equator (at $r = r_0$), they follow the contour of $B(\mathbf{r}) = B_{eq}(r_0)$. Here, r_0 refers to the equatorial distance from Earth where the particle begins its drift at midnight. For the nearly-equatorial mirroring particles with $\alpha_{eq} \lesssim 90°$, $p_\perp^2 \gg p_{||}^2$, energy conservation inhibits significant variation in $p_\perp$, thereby restricting the particle's field-aligned motion to the vicinity of the local minimum of magnetic field strength. In other words, conservation of μ should imply $\min\limits_s B(s, \text{MLT}) \approx \text{const}$ along the drift orbit at each Magnetic Local Time (MLT) sector, where the minimum is taken along the field line (s is the coordinate along the field line). Here we assume that drift orbits of particles with $\alpha_{eq} \lesssim 90°$ approximately satisfy $\min\limits_s B(s, \text{MLT}) = B_{eq}$. Following [Ukhorskiy and Sitnov, 2008, McCollough et al., 2012], we introduce the parameter L_B, defined as

$$L_B = \left(\frac{B_0}{B_{eq}(r_0)} \right)^{1/3} \tag{2.1}$$

This parameter is analogous to L^* and L and can serve as a proxy for the equatorial cross-section of the particle drift orbit. Definition (2.1) is inspired by the fact that for a purely dipole field $B_{eq} = B_0/L^3$ and thus $L_B = L$. In a realistic magnetospheric configuration, L_B no longer has such an apparent physical meaning but is still convenient for describing the radial extent of a drift orbit.

Figure 2.2a illustrates a typical drift orbit of an equatorially mirroring electron with $L_B = 7.3$ in the X_{GSM}–Y_{GSM} plane. Figure 2.2a shows equatorial projections (along the

magnetic field lines) of the drift orbit. Here, the equator refers to the magnetic equator, where the radial component of the magnetic field vanishes, which (for zero dipole tilt) coincides with the $Z_{\mathrm{GSM}} = 0$ plane to an accuracy of ± 0.4 RE. Note that due to the deviation from the ideal dipole field, the actual radial distance to the Earth at midnight is slightly lower, $r_0 \approx 6.5$ R_E. The drift orbit was calculated by tracing field lines in the TS04 model [Tsyganenko and Sitnov, 2005]. In each MLT sector, a field line is traced from the ionosphere with a foot point in the northern hemisphere at $(r, \theta, \phi) = (1, \theta, \mathrm{MLT})$ to the conjugate foot point in the southern hemisphere. Here, (r, θ, ϕ) are the spherical system coordinates with θ measured from Earth's dipole axis. For a given L_B and MLT, the tracing is performed for different values of θ until $\theta = \theta^*$ is found, such that the local minimum along the field line satisfies $\min_s B(s, \theta^*, \mathrm{MLT}) = B_0/L_B^3$. In the case where two local minima are present on the dayside, we choose the local minimum in the same hemisphere for all $8 < \mathrm{MLT} < 16$ (see further discussion for details). It is of interest to note that this "tracing" technique used to construct an "approximate" drift orbit has a very natural explanation in terms of the Euler potentials (see Chapter 1). Recall that in the zeroth order the particle drift motion occurs with $\alpha = \mathrm{const}$ and $\beta = \omega_d t$. Since (α, β) are constant along field lines, and because at the Earth's surface the dipole expressions for $\alpha \propto 1/L$ and $\beta \propto \mathrm{MLT}$ apply, describing the drift orbit in terms of (MLT, L_B) becomes almost fully analogous to using (α, β).

Figures 2.2b-2.2d show profiles of the magnetic field strength along the field line (referred to as the B-profile) in three different MLT sectors: 0, 10, and 14. These profiles are shown for two cases: $\varphi_{\mathrm{IMF}} = 45°$ and $\varphi_{\mathrm{IMF}} = 225°$, for IMF $B_y > 0$ (westward) and IMF $B_y < 0$ (eastward), respectively. At midnight, the B-profile exhibits a U shape with a single minimum at the equator (see Fig. 2.2). On the dayside, the magnetic field strength profile acquires a W-shape with two local minima in the southern and northern hemispheres, separated by a local maximum. For reasons discussed in the following section, we assign $s = 0$ to the deepest minimum at the moment when the local maximum first appears (around $\mathrm{MLT} = 8.77$). We keep the value of this minimum fixed throughout the entire drift orbit without changing

hemispheres. Figures 2.2b-2.2d show that the W-shaped profiles of magnetic field strength exhibit two significantly asymmetric minima, with a varying degree of asymmetry across different MLT sectors. These profiles are both north-south asymmetric (at a given MLT) as well as east-west asymmetric. The latter is evident in the different shapes of the B profiles before and after local noon, such that $B(s, 12 - \delta\text{MLT}) \neq B(s, 12 + \delta\text{MLT})$. The degree of these asymmetries depends on the tilt angle and on φ_{IMF}: IMF B_z and the tilt angle primarily contribute to the north-south asymmetry, while IMF B_y is the primary source of east-west asymmetry. We note that IMF B_y can also contribute to the effective north-south asymmetry of B-profiles. This occurs because the field lines on the dayside bend either eastward or westward depending on the sign of IMF B_y. Note that the dipole field also features a non-zero B_y on either side of local noon. Specifically, in the pre-noon sector, $B_y > 0$ in the northern hemisphere while $B_y < 0$ in the southern hemisphere. Thus, in the pre-noon sector, imposing IMF $B_y > 0$ (IMF $B_y < 0$) leads to an enhancement (reduction) of the magnetic field strength in the northern hemisphere and a reduction (enhancement) in the southern hemisphere by the same amount. In the afternoon sector, the situation is reversed. At local noon, IMF $B_y \neq 0$ only results in the magnetic field bending without causing any north-south asymmetry in the B-profile. Thus, even with a zero tilt angle, IMF $B_z = 0$, and IMF $B_y \neq 0$, the magnetic field configuration still features north-south and east-west asymmetries. In this chapter, we only consider the effects of IMF B_y and IMF B_z while the tilt angle is taken as zero.

2.1.3 Separatrix

In Chapter 1, Section 1.2, we have shown that particle motion along a given field line (labeled by the two Euler potentials, α and β) is consistent with being heuristically treated as arising from the equations of motion generated by the following Hamiltonian (see Eq. 1.22).

$$H_{||}(s, p; \alpha, \beta) = \frac{p_{||}^2}{2m^*} + \mu^* B(s; \alpha, \beta) \tag{2.2}$$

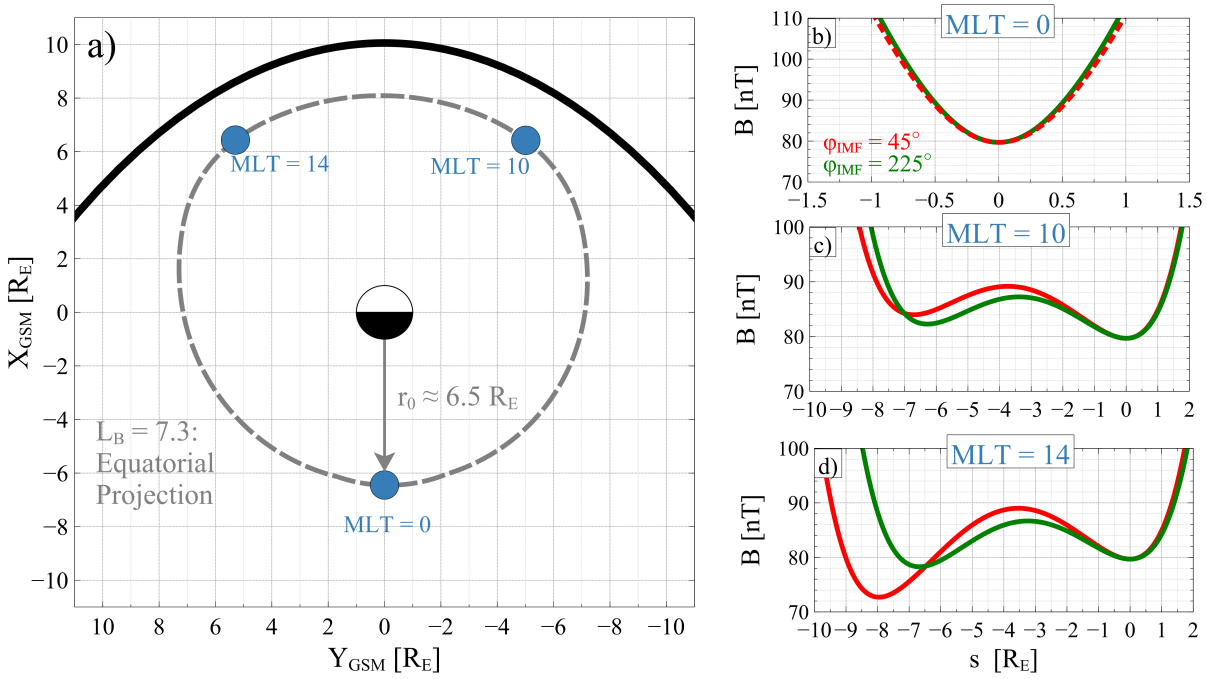

Figure 2.2: Configuration of the inner magnetosphere based on the TS04 model [Tsyganenko and Sitnov, 2005] with solar wind parameters, $P_{dyn} = 4$ nPa, IMF $B = 5$ nT and $\varphi_{\rm IMF} = 160°$: (a) drift orbit of an equatorially mirroring particle (gray) started at $r_0 \approx 6.8$ R_E at the midnight ($L_B = 7.3$), black line shows position of the magnetopause, blue dots show magnetic local time (MLT) sectors of $0, 10, 14$, (b) magnetic field strength along the field line at MLT $= 0$, red line shows $\varphi_{\rm IMF} = 20°$ and green line shows $\varphi_{\rm IMF} = 160°$, (c) magnetic field strength along the field line at MLT $= 10$, (d) magnetic field strength along the field line at MLT $= 14$.

Here $m^* = m\gamma$ is the normalized (electron) mass, $\mu^* = \mu/\gamma$ is the magnetic moment. Moreover, we only consider the case when the electric field is absent and thus the Lorentx factor γ is also constant. From Eq. 2.3, it is evident that the magnetic field strength along the field line, $B(s)$, plays the role of an effective potential for the bounce motion along the field lines. As a particle drifts in the azimuthal direction, the B-profile changes with MLT. This change s slow due to the large separation of the time scales of bounce (τ_b) and drift (τ_d) motions: $\varepsilon = \tau_b/\tau_d \sim 10^{-4}$ for $0.1 - 1$ MeV electron at $L \lesssim 8$ (see Chapter 1). As discussed

before, this MLT drift along the curve of $L_B = \text{const}$ corresponds to $\alpha = \text{const}$ and $\beta = \varepsilon t$ when time t is measured in units of the bounce period. Since the total energy (γ and p) is conserved, it is convenient to introduce the normalized momentum, $P = p_{||}/p$, and to normalize the field-aligned coordinate s by R_E. The resulting Hamiltonian reads

$$H(s, P; \varepsilon t) = \frac{1}{2}\left(P^2 + \frac{B(s, \varepsilon t)}{B_m}\right) \tag{2.3}$$

where B_m is the magnetic field strength at the mirror point (also conserved). Note that due to the normalization, the initial values of H is always 1/2. Since $B(s, \varepsilon t)$ slowly varies in time, the separation of characteristic time scales gives rise to the adiabatic invariant, $\oint P ds$.

$$I = \oint \sqrt{1 - \frac{B}{B_m}} ds \tag{2.4}$$

Non-surprisingly, this is precisely the normalized form of the second adiabatic invariant, $J_{||} = \oint p_{||} ds = pI$ (see Eqs. 1.16 and 1.19 in Chapter 1). Integration in Eq. 2.4 is performed between these two mirror points and since we only consider $p = \text{const}$, the conservation of $J_{||}$ implies that I is conserved.

On the nightside, the particle's motion along the field lines consists of 'fast' bounces between two mirror points $s_{1,2}$, where $B(s_{1,2}) = B_m$, while slowly, at a rate of $\sim \varepsilon$, drifting across MLT sectors, preserving $I = 2\int_{s_1}^{s_2} \sqrt{1 - B/B_m}, ds = I_0 = \text{const}$. On the dayside, the drifting particle encounters W-shape profile of the magnetic field strength exhibiting a local maximum, $B^* = B(s^*)$ (see Fig. 2.3a). When magnetic field strength at this maximum exceeds B_m, particle gets trapped in one of the two minima on either side of this maximum. Phase trajectories with $B_m > B^*$ and those with $B_m < B^*$ are separated by the so-called separatrix in the phase space corresponding to $B_m = B^*$. This is shown schematically in Fig. 2.3. In accordance with definition of I (see Eqs. 1.16), the phase area (apart from a factor p) enclosed by the separatrix in phase space at different MLT sectors is defined as

$$S(\mathrm{MLT}) = 2\int_{s_1^*}^{s_2^*} \sqrt{1 - \frac{B(s,\mathrm{MLT})}{B^*}}ds \tag{2.5}$$

Here, $s_{1,2}^*$ are defined as $B(s_{1,2}^*) = B^*$ (see Fig. 2.3). One also defines the phase areas (apart from a factor p) enclosed within main (m) and adjacent (a) phase pockets of the separatrix

$$\begin{aligned} S_m(\mathrm{MLT}) &= 2\int_{s^*}^{s_2^*} \sqrt{1 - \frac{B(s,\mathrm{MLT})}{B^*}}ds \\ S_a(\mathrm{MLT}) &= 2\int_{s_1^*}^{s^*} \sqrt{1 - \frac{B(s,\mathrm{MLT})}{B^*}}ds \end{aligned} \tag{2.6}$$

The distinction between main and adjacent pockets is discussed below. Note that S and $S_{m,a}$ are functions of MLT along a given drift orbit. A drifting particle becomes trapped in one of these minima when B^* exceeds B_m. This occurs in a specific MLT sector referred to as MLT_1. Just before trapping, the total area enclosed by the separatrix increases to the value of the second adiabatic invariant, $I_0 = S(\mathrm{MLT}_1)$. When trapping happens, the second adiabatic invariant undergoes a jump to $I_{tr} \approx S_i(\mathrm{MLT}_1)$ due to the reduction in the phase space area accessible to the particle, with $i \in \{m, a\}$ depending on which pocket the particle was trapped in. S and S_i reach their respective maxima near the local noon. Detrapping occurs in the afternoon MLT sector MLT_2 when S_i decreases back to the value $S_i(\mathrm{MLT}_2) = I_{tr}$. At this point, the second adiabatic invariant changes again to $I' \approx S(\mathrm{MLT}_2)$. Since the total area at the moment of detrapping (MLT_2) may not be the same as it was at the moment of trapping, the second adiabatic invariant may undergo a net change amounting to $\Delta I = I' - I_0 \approx S(\mathrm{MLT}_2) - S(\mathrm{MLT}_1)$. Note that we use $\approx$ to denote quantities that are correct in the limit of $\varepsilon \to 0$. The effects of $\varepsilon \neq 0$ will be discussed later in this chapter.

2.1.4 Magnetic Field Model

Figure 2.4a shows typical magnetic field strength profiles at three MLTs along the drift orbit (the same orbit as in Fig. 2.2a) for $\varphi_{\mathrm{IMF}} = 225°$. We observe a magnetic field profile with a single minimum of the magnetic field strength slowly evolving into a configuration with two local minima along the field line, with an adjacent pocket forming at $s < 0$. Note that $s = 0$ is defined at the position of the main pocket, representing the absolute minimum for a single B-minimum configuration. In the case of a double-well configuration, $s = 0$ corresponds to the position of the pocket that is deepest at the moment of the first bifurcation along the drift orbit. Thus, $s = 0$ represents equatorially mirroring particles, as all such particles ($I_0 = 0$) reside in the main pocket, whereas the particles with finite I_0 could be trapped in either pocket. Note that the main pocket, i.e., the deepest minimum in the pre-noon sector, is located in the northern hemisphere for IMF $B_y < 0$ and in the southern hemisphere for IMF $B_y > 0$. Consequently, for IMF $B_y < 0$, all initially equatorially mirroring electrons are trapped in the northern hemisphere, whereas for IMF $B_y > 0$, these electrons are trapped in the southern hemisphere.The observed double-well configuration allows for the trapping of particles with $I_0 > 0$ in one of two pockets. Figure 2.4c shows the MLT dependence of S and $S_{m,a}$ (see Eqs. 2.5 and 2.6). The observed S_a and S_m profiles exhibit strong asymmetry with respect to local noon. The emergence of the separatrix (the first bifurcation) at MLT ≈ 8.77 is associated with the formation of the adjacent pocket, $S_a(8.77) \gtrsim 0$, while the disappearance of the separatrix is associated with the diminishing of the main pocket at MLT ≈ 15.4, when $S_m \approx 0$, while $S_a > 0$. Similar profiles of S_a and S_m can be reproduced using a polynomial approximation of $B(s, \mathrm{MLT})$ with respect to s. Figure 2.4d shows S_a and S_m profiles yielded by the following model.

$$B(s, \mathrm{MLT}) = B_{eq}\left(1 + \frac{s^2(s - ad)^2}{a^4} + \frac{bs^3}{a^4}\right); a, b, d = f(\mathrm{MLT}) \tag{2.7}$$

Here, $B_{eq} = B_0/L_B^3$, while parameters a, b, and d depend on MLT and are chosen to best resemble the MLT profiles of S_a and S_m obtained in the TS04 model (Fig. 2.4c). Adjusting these parameters allows for a good approximation of S and $S_{m,a}$ at different values of L_B. We use this model for illustrative purposes only in this section, so we limit our analysis to the specific drift orbit with $L_B = 7.3$. The functional form of a, b, d for $L_B = 7.3$ is given as following

$$
\begin{aligned}
a(\mathrm{MLT}) &= -2.6 - 5.85\exp\left[-\left(\frac{(\mathrm{MLT}-12.5}{3.5}\right)^4\right] \\
b(\mathrm{MLT}) &= -5.08 + 5.03\exp\left[-\left|\frac{(\mathrm{MLT}-12.5}{10.1}\right|^3\right] + 1.6\exp\left[-\left(\frac{(\mathrm{MLT}-16.0}{1.2}\right)^2\right] \\
d(\mathrm{MLT}) &= 0.92 - 0.93\exp\left[-\left(\frac{(\mathrm{MLT}-16.3}{1.5}\right)^2\right] - 0.3\exp\left[-\left(\frac{(\mathrm{MLT}-8.7}{0.9}\right)^2\right] \\
&- 0.4\exp\left[-\left(\frac{(\mathrm{MLT}-16.6}{1.2}\right)^2\right]
\end{aligned}
\tag{2.8}
$$

Magnetic field strength profiles given by Eq. 2.7 at three different MLTs at $L_B = 7.3$ are shown in Fig. 2.4b. Although the magnetic field strength profiles provided by Eq. 2.7 differ somewhat in form compared to those given by TS04, our analysis indicates that the exact form of the magnetic field strength profiles has little effect on particle dynamics as long as these profiles: (1) exhibit a double-well profile on the dayside ($8 < \mathrm{MLT} < 16$) and yield S_a and S_m profiles similar to those obtained in the TS04 model, and (2) have a fixed minimum at $s = 0$.

2.2 Violation of Adiabaticity

2.2.1 Model Hamiltonian

Magnetic field model (2.7) allows for demonstrating the most salient features of the dynamics of the adiabatic invariant associated with separatrix crossing. Indeed, dynamics described by Eq. 2.3 can be simulated by approximating the particle's azimuthal (along MLT) drift as a steady increase in the azimuthal coordinate (MLT), i.e., the azimuthal drift speed is approximated by some constant value along the particle trajectory. The magnetic field, as seen by a particle along the drift orbit, can then be approximated as $B(s, \varepsilon t)$. Here, $\varepsilon t \in [0, 24]$, is the slow-time reflecting the slow change of the magnetic field strength profile due to the azimuthal drift. This dynamics can be modeled via Hamiltonian 2.3

$$H(s, P; \varepsilon t) = \frac{P^2}{2} + U(s, \varepsilon t) = \frac{1}{2}\left(P^2 + \frac{B}{B_m}\right) \tag{2.9}$$

A few technical notes on the normalization should be provided. We assume that all particles start from the equator at midnight at some given drift orbit (given L_B and B_{eq}, see Eq. 2.1). Particles differ by their initial pitch angles, α_{eq}. We can write $B_m = B_{\text{eq}}/\sin^2\alpha_{\text{eq}}$ and thus $U(s, \varepsilon t) = \sin^2\alpha_{\text{eq}} B(s, \varepsilon t)/2B_{\text{eq}}$. Thus, particles starting at the equator with different initial pitch-angles are formally described not by a single Hamiltonian but rather by a *family* of Hamiltonians parameterized by α_{eq}. This is important as otherwise all particles start with the same value of the *dimensionless* energy, $H = 1/2$. We also note that Hamiltonian (2.9) does not explicitly depend on the particle energy (on the total momentum p). Although, there is implicit energy dependence via ε parameter which will be discussed in Section 2.4.

Hamiltonian (2.9) has an intrinsic adiabatic invariant, $\mathcal{I}$, defined as

$$\mathcal{I} = \oint P ds = 2\int_{s_1}^{s_2} \sqrt{2(H - U(s, \varepsilon t))}\, ds \tag{2.10}$$

Note that the dynamics described by Hamiltonian (2.9) is not completely equivalent to that described by the full guiding-center theory (Eqs. 1.11). This is because Eqs. 1.11 describe both the actual perpendicular drift and the field-aligned motion in s and intrinsically conserve the total momentum, p, i.e., the energy. In contrast, Hamiltonian (2.9) describes a reduced (non-conservative) system with $1\frac{1}{2}$ degrees of freedom. A detailed discussion comparing the properties of the actual bounce motion as part of Eqs. 1.11 and the one modeled with Hamiltonian (2.9) is provided in Section 2.2.4. Here, we note that the non-conservative nature of Hamiltonian (2.9) only leads to *quantitative* differences while still featuring *qualitatively* the same dynamics in the adiabatic invariant. In other words, Hamiltonian (2.9) allows capturing the salient features expected of the actual bounce motion in the process of slow azimuthal drift in the asymmetric magnetic field while reducing the dynamics to that of a system with $1\frac{1}{2}$ degrees of freedom. The general theory of dynamical systems with $1\frac{1}{2}$ degrees of freedom (see Section 1.3.2 and [Neishtadt, 1986, Cary et al., 1986]) suggests that trapping/detrapping conditions and the related dynamics of the adiabatic invariant should be described in terms of the area enclosed by the separatrix, $\mathcal{S}(\varepsilon t)$, which is defined as

$$\mathcal{S}(\varepsilon t) = 2\int_{s_1^*}^{s_2^*} \sqrt{2(U^* - U(s,\varepsilon t))}ds \tag{2.11}$$

Here, $U^* = U(s^*, \varepsilon t)$ where s^* is the position of the local maximum, and $s^*_{1,2}$ are two conjugate mirror points satisfying $U(s^*_{1,2}, \varepsilon t) = U^*$ (which is $B(s^*_{1,2}, \varepsilon t) = B^*$, see Fig. 2.3). Definition (2.11) represents the area enclosed by the separatrix in the phase space of (s, P). The separatrix separates phase trajectories of the particles trapped in the main/adjacent pockets from the non-trapped trajectories (see Fig. 2.3). Note that due to the non-conservative nature of Hamiltonian (2.9), the definition of the phase area enclosed by the separatrix, $S(\varepsilon t)$, is not equivalent to $S(\mathrm{MLT})$ (see Eqs. 2.5). A detailed discussion of this is provided in Section 2.2.4. The total phase area enclosed by the separatrix, $\mathcal{S}$, consists of two phase pockets (see Fig. 2.3) with the respective phase areas defined as:

$$\mathcal{S}_m(\varepsilon t) = 2\int_{s^*}^{s_2^*} \sqrt{2(U^* - U(s,\varepsilon t))}ds$$
$$\mathcal{S}_a(\varepsilon t) = 2\int_{s_1^*}^{s^*} \sqrt{2(U^* - U(s,\varepsilon t))}ds \tag{2.12}$$

2.2.2 Evolution of the Adiabatic Invariant

Magnetic field model (2.7) allows us to demonstrate typical behaviour of the dynamical system with double-well potential exhibiting slow time variation. Combining Model (2.7) with Hamiltonian (2.9), we obtain the following Hamiltonian

$$H(s,P;\varepsilon t) = \frac{P^2}{2} + \frac{\sin^2\alpha_{eq}}{2}\left(1 + \frac{s^2(s-ad)^2}{a^4} + \frac{bs^3}{a^4}\right) \tag{2.13}$$

Here, $\sin^2\alpha_{eq}$ is determined by the initial condition, and MLT dependent parameters a, b, and d are now treated as functions of slow time, εt. Figure 2.5 shows a typical test-particle trajectory obtained with Hamiltonian (2.13). The initial conditions are those of an equatorial particle ($s = 0$) with $\alpha_{eq} = 66°$, and thus $P(0) = \cos\alpha_{eq}$. Note again that α_{eq} determines not only the initial conditions but also the Hamiltonian itself (via $\sin\alpha_{eq}$). These initial conditions set the initial value of the adiabatic invariant $\mathcal{I}_0 = 1.48$.

Figure 2.5a shows the particle trajectory as a function of slow time, εt. Figures 2.5b and 2.5c show, respectively, the particle trajectory in the phase space (s, P) and the evolution of the adiabatic invariant, $\mathcal{I}(\varepsilon t)$. Away from local noon, the particle rapidly bounces between two mirror points, $s_{1,2}$, while conserving the adiabatic invariant, $\mathcal{I}(\varepsilon t) = \mathcal{I}_0$ (see Fig. 2.5c). At $\varepsilon t_1 \approx 9.76$, the particle becomes trapped in the adjacent pocket as its right mirror point (s_2) turns negative. This results in the violation of the adiabatic invariant (see Fig. 2.5c). This trapping is evident in the phase space as a slow transition from non-trapped motion above the separatrix at $\varepsilon t \in [10, 11]$ to trapping motion in the adjacent pocket between $\varepsilon t \in [11, 12]$. Figure 2.5c shows that the separatrix appears at $\varepsilon t \approx 8.77$, and then the phase

area enclosed by it, $\mathcal{S}(\varepsilon t)$, increases. Trapping inside the separatrix occurs at εt_1 satisfying $\mathcal{S}(\varepsilon t_1) = \mathcal{I}_0$, resulting in a jump of the adiabatic invariant, $\mathcal{I}_0 \to \mathcal{I}_{tr}$, which is determined by the concurrent area inside the adjacent pocket, $\mathcal{I}_{tr} \approx \mathcal{S}_a(\varepsilon t_1)$. As the total area inside the separatrix continues increasing, the particle stays trapped ($\varepsilon t \in [\varepsilon t_1, \varepsilon t_2]$), and the new value of the adiabatic invariant is conserved, $\mathcal{I} \approx \mathcal{I}_{tr} = \text{const}$. As phase areas $\mathcal{S}(\varepsilon t)$ and $\mathcal{S}_a(\varepsilon t)$ start decreasing after local noon, the particle becomes de-trapped at εt_2 when $\mathcal{S}_a(\varepsilon t_2) = \mathcal{I}_{tr}$. This detrapping is also evident in the particle trajectory (Fig. 2.5a) when the second mirror point, s_2, turns positive again. Detrapping results in the second jump of the adiabatic invariant, $\mathcal{I}_{tr} \to \mathcal{I}^{'}$, with the resulting value of the invariant determined by the concurrent phase area inside the separatrix, $\mathcal{I} \approx \mathcal{S}(\varepsilon t_2)$. Note that in Fig. 2.5 we have $\Delta\mathcal{I} = \mathcal{I}^{'} - \mathcal{I}_0 < 0$, i.e., in this case there is a net change (jump) in the adiabatic invariant over one complete drift period. From profiles $\mathcal{S}(\varepsilon t)$ and $\mathcal{S}_a(\varepsilon t)$ (Figs. 2.4d and 2.5c), we can argue that this net change of $\Delta\mathcal{I}$ is primarily caused by the north-south and east-west *asymmetries* of the separatrix and the constituent pockets (see Fig. 2.3).

Figure 2.5c and the discussion above exemplify a process of adiabatic invariant destruction described in detail in Section 1.3. Mathematically, this process is described by Eqs. 1.53 and can be recast in the form of a *mapping* that determines the resultant value of the adiabatic invariant, $\mathcal{I}'$, over one drift period. This mapping can be expressed as follows:

$$\mathcal{I}_{tr} = \begin{cases} \mathcal{S}_i(\varepsilon t_1) + \Delta\mathcal{I}_1(\theta, \varepsilon), \text{ with } t_1 \text{ determined from } \mathcal{S}(\varepsilon t_1) = \mathcal{I}_0 \\ \mathcal{I}_0, \text{ if } t_1 \text{ does not exist} \end{cases} \tag{2.14}$$

$$\mathcal{I}' = \begin{cases} \mathcal{S}(\varepsilon t_2) + \Delta\mathcal{I}_2(\theta, \varepsilon), \text{ with } t_2 \text{ determined from } \mathcal{S}_i(\varepsilon t_2) = \mathcal{I}_{tr} \\ \mathcal{I}_{tr}, \text{ if } t_2 \text{ does not exist} \end{cases} \tag{2.15}$$

Here, $i \in \{m, a\}$ depending on if the particle was trapped in the main or adjacent pocket. Mapping (2.14-2.15) also includes jumps $\Delta\mathcal{I}_{1,2}(\theta, \varepsilon)$($\theta$ is bounce phase at the moment of the

separatrix crossing), which reflect violation of the adiabaticity of the bounce motion in the vicinity of the separatrix [Timofeev, 1978, Neishtadt, 1986, Cary et al., 1986]. The net change in the adiabatic invariant over one drift period is given by Eq. 1.77, which can be regarded as an expansion with respect to ε. Retaining the first two leading terms, the expansion reads (see Chapter 1, Section 1.3.2, and [Neishtadt, 1986]):

$$\Delta\mathcal{I}(\mathcal{I}_0;\theta,\varepsilon) = \Delta\mathcal{S}(\mathcal{I}_0) + \Delta\mathcal{I}_{st}(\mathcal{I}_0;\theta,\varepsilon) + O(\varepsilon^{3/2}\ln\varepsilon) \tag{2.16}$$

Here, $\Delta\mathcal{S}$ is a zeroth-order term in ε determined from

$$\Delta\mathcal{S} = \begin{cases} \mathcal{S}(\varepsilon t_2) - \mathcal{S}(\varepsilon t_1), \text{ if both } t_1 \text{and } t_2 \text{ exist} \\ -\mathcal{S}_m(\varepsilon t_1), \text{ if } t_1 \text{ exists but } t_2 \text{ does not} \\ \mathcal{S}_a(\varepsilon t_2), \text{ if } t_1 \text{ does not exist but } t_2 \text{ does} \\ 0 \text{ if neither } t_1 \text{ nor } t_2 \text{ exist} \end{cases} \tag{2.17}$$

where $t_{1,2}$ are also to be determined in the zeroth-order approximation from $\mathcal{S}(\varepsilon t_1) = \mathcal{I}_0$ and $\mathcal{S}_i(\varepsilon t_2) = \mathcal{S}_i(\varepsilon t_1)$ or $\mathcal{S}_m(\varepsilon t_2) = \mathcal{I}_0$ if t_1 does not exist. Note that the case when t_2 does not exist implies the particle is trapped in the adjacent pocket (see Fig. 2.6a), while the case when t_1 does not exist implies trapping in the main pocket (see Fig. 2.6b). In these cases, $\Delta\mathcal{S}$ is simply the area of the other pocket, which becomes accessible to the particle's phase trajectory after detrapping from the main pocket or becomes inaccessible due to trapping in the adjacent pocket. The zeroth-order term, $\Delta\mathcal{S}$, is the *geometric jump* (see Chapter 1 and [Neishtadt, 2019]) and is given by the difference in total separatrix area between the moments of trapping and detrapping. The second term, $\Delta\mathcal{I}_{st}(\theta,\varepsilon)$, is the first correction in ε, combining effects of $\varepsilon \neq 0$. This is the *stochastic (dynamical) jump* (see Chapter 1, Section 1.3.2) which depends on the bounce phase θ and results from violation of the adiabaticity of motion in vicinity of the separatrix. Far from the separatrix, $\mathcal{I}$ oscillates with an amplitude

of order ε about a constant value, therefore remains an approximate invariant, providing a sufficient separation of time scales associated with fast (bounce) motion and slow (drift) motion, causing the change of the potential well. In contrast, in the vicinity of the separatrix, the period of the *fast* motion diverges logarithmically (see Chapter 1 Section and 1.3.2). This results in violation of time scale separation between slow and fast motions and leads to a jump in the adiabatic invariant, $\Delta\mathcal{I}_{st}(\theta,\varepsilon)$. The first calculations of the jump caused by the separatrix crossing have been carried out by [Timofeev, 1978]. These results were later generalized into a theory of separatrix crossing by [Neishtadt, 1986, Neishtadt, 1987] and [Cary et al., 1986]. For larger initial values of the adiabatic invariant, $\mathcal{I}_0$, the leading asymptotic for the stochastic jump due to a single separatrix crossing is $\Delta\mathcal{I}_{st} \propto \varepsilon \ln \varepsilon$ (see Eq. 1.52 in Chapter 1 Section and [Neishtadt, 1986, Cary et al., 1986]). For the symmetric case this term vanishes and the leading term becomes $\varepsilon \ln(2\sin\theta)$ (see Eq. 1.54 and [Neishtadt, 1986, Arnold et al., 2006]). Both asymptotics are correct with the accuracy of $O(\varepsilon^{3/2}\ln\varepsilon)$.

After averaging over the bounce phase, in the symmetric case this results in a diffusive evolution with $\langle\Delta\mathcal{I}_{st}\rangle_\theta = 0$ and $\langle\Delta\mathcal{I}_{st}^2\rangle_\theta \sim \varepsilon^2 > 0$. In the limit of small initial values of the adiabatic invariant, $\mathcal{I}_0 \lesssim \Delta\mathcal{S}$, the evolution is dominated by ballistic jumps with non-zero average drift $\langle\Delta\mathcal{I}_{st}\rangle_\theta \sim \varepsilon > 0$. As we discussed in Section 1.3.2, for a separatrix with two symmetric pockets, $\Delta\mathcal{S}$ vanishes and the evolution of the adiabatic invariant is governed by the stochastic jump. However, in an asymmetric configuration, as the one shown in Fig. 2.3 and Fig. 2.5, the dynamics of the adiabatic invariant can become dominated by the geometric jump, $\Delta\mathcal{S}$. This is because $\Delta\mathcal{I}_{st} \sim \varepsilon$, while $\Delta\mathcal{S} = O(1)$ and remains finite even if $\varepsilon \to 0$. Figure 2.5c shows a clear example when the net change in the adiabatic invariant is primarily caused by the *geometric jump*. In this chapter, we focus on the role of the asymmetry-driven jumps of the adiabatic invariant, i.e., on the geometric jumps. Eqs. 2.16 and 2.18 show, that in the limit of $\varepsilon \to 0$, the major contribution to the net change of the adiabatic invariant, $\Delta\mathcal{I}$, comes from the geometric jump, $\Delta\mathcal{S}$. In this limit, the stochastic jump vanishes, $\Delta\mathcal{I}_{st} \to 0$, and Mapping (2.14-2.15) reduces to its zeroth-order asymptotic given by Eq. 2.17. This can

be re-written in terms of resultant value of the adiabatic invariant, $\mathcal{I}'$, after one complete drift period

$$\mathcal{I}' = \begin{cases} \mathcal{S}(\varepsilon t_2), & \text{if } t_2 \text{ exists,} \\ \mathcal{S}_a(\varepsilon t_1), & \text{if } t_2 \text{ does not exist but } t_1 \text{ exists,} \\ \mathcal{I}_0, & \text{if neither } t_2 \text{ nor } t_1 \text{ exist.} \end{cases} \tag{2.18}$$

where $t_{1,2}$ are again calculated in the zeroth-order approximation in ε from $\mathcal{S}(\varepsilon t_1) = \mathcal{I}_0$ and $\mathcal{S}_i(\varepsilon t_2) = \mathcal{S}_i(\varepsilon t_1)$ or $\mathcal{S}_m(\varepsilon t_2) = \mathcal{I}_0$ if t_1 does not exist, with $i \in \{a, m\}$ for particles trapped in the adjacent (a) and main (m) pockets respectively. It is important to note that even in the limit of $\varepsilon \to 0$, Mapping (2.18) *does not* uniquely determine the jump of the adiabatic invariant, because there is no *a priory* information on which of two pockets a particle will be trapped in, if areas of both pockets are growing. Specifically, one still needs to calculate the probabilities, Π_m and Π_a (see Section 1.3.2), of trapping in the main and adjacent pockets, respectively. These probabilities are given by the relative number of particles that will get trapped and are proportional to the *rate of increase* of the area surrounded by the separatrix, that is $\Theta \propto d\mathcal{S}/d(\varepsilon t)$ (see Section 1.3.2 and [Neishtadt, 1975, Neishtadt and Vasiliev, 2005]). Thus, the resultant jump remains a probabilistic process, although with only two possible outcomes. While this probabilistic treatment can be included under some simplified assumptions, it is beyond the scope of the present study. Here we consider trapping inside the two pockets separately. In this case, for each initial value of the adiabatic invariant, $\mathcal{I}_0$, Mapping (2.18) gives us two possible resultant jumps reflecting trapping either in the main or adjacent pocket.

2.2.3 Geometric Jumps

Figure 2.6 shows the results of test-particle simulations using Hamiltonian (2.13) and magnetic field model given by Eq. 2.7 (Figs. 2.4b and 2.4d) for different initial values of the adiabatic

invariant. To demonstrate that geometric jump does not scale with ε, test-particle simulations were performed with $\varepsilon = 10^{-4}$ so that $\Delta\mathcal{I} \approx \Delta\mathcal{S}$. Figures 2.6a-c exemplify three types of geometrical jumps typical of the system described by Hamiltonian (2.13). Figure 2.6a shows a particle experiencing trapping in the adjacent pocket without subsequent detrapping. This results in a single jump with $\Delta\mathcal{I} < 0$. Such dynamics are typical of particles with $\mathcal{I}_0 \in [0.4, 1.5]$. This is a consequence of the asymmetry of $\mathcal{S}_a$, which prevents detrapping of particles with $\mathcal{I}_{tr} \lesssim 0.4$. These particles become trapped so deeply in the adjacent pocket that, even when the separatrix and the main pocket disappear, $\mathcal{S}_m = 0$, their detrapping condition is not satisfied, $\mathcal{I}_{tr} < \mathcal{S}_a$. We will refer to such jumps as 'single inward jumps,' as $\Delta\mathcal{I} < 0$ always leads to the *earthward* radial transport of particles (see further discussion for details). Figure 2.6b shows a particle experiencing a detrapping from the main pockets without undergoing initial trapping. This results in a single positive jump with $\Delta\mathcal{I} > 0$. Such dynamics are typical of particles with $\mathcal{I}_0 < 0.4$ and reflects the fact that particles with small initial values $\mathcal{I}_0$ are trapped deep enough in the main pocket to avoid initial bifurcation, i.e., condition $\mathcal{I}_0 = \mathcal{S}(\varepsilon t_1)$ is never satisfied for $\varepsilon t_1 < 12$. However, as the main pockets shrinks in size, they become released at $\varepsilon t_2 > 12$, increasing their adiabatic invariant by $\Delta\mathcal{I} = \mathcal{S}_a(\varepsilon t_2) > 0$ due to the presence of the second pocket. We refer to such jumps as 'single outward jumps' as $\Delta\mathcal{I} > 0$ always results in *outward*(anti-earthward) radial transport of particles. Figure 2.6c illustrates the most common type of geometric jumps, characterized by subsequent asymmetric trapping and detrapping. We refer to these geometric jumps as 'double jumps', $\Delta\mathcal{I}$ resulting from double jumps can be either negative or positive, depending on the pocket in which the particle was trapped (see discussion below). Figure 2.6d shows comparison between test-particle simulation and Mapping (2.18); all particles with $\mathcal{I}_0 \lesssim 2.5$ are susceptible to bifurcation with $\Delta\mathcal{I}$ being of order of the initial value of the invariant itself exhibiting both positive and negative jumps, $\Delta\mathcal{I} \sim \pm\mathcal{I}_0$. This result suggests that geometric jump, $\Delta\mathcal{S}$, indeed dominates the total jump of the adiabatic invariant. Figure 2.6d demonstrates that particles trapped in the main pockets always undergo a *positive*

jump, $\Delta\mathcal{I} > 0$, while those trapped in the adjacent pocket always undergo a *negative* jump, $\Delta\mathcal{I} < 0$. This is an interesting salient feature of the observed asymmetric magnetic field profile (Fig. 2.4). The origin of this behavior is evident from the $\mathcal{S}$ and $\mathcal{S}_{m,a}$ profiles (e.g., Fig. 2.4d). While the total phase area enclosed by the separatrix is approximately symmetric with respect to local noon, the individual areas $\mathcal{S}_{m,a}$ are somewhat asymmetric. Specifically, the size of the main pocket in the pre-noon sector is larger compared to its size in the afternoon sector, $\mathcal{S}_m(12-\delta) \geq \mathcal{S}_m(12+\delta)$ with $\delta > 0$, while the opposite is true for the adjacent pocket, $\mathcal{S}_a(12-\delta) \leq \mathcal{S}_a(12+\delta)$. Recall that the geometric jump, $\Delta\mathcal{S}$, equals the difference in phase areas enclosed by the other pocket between the moments of trapping and detrapping. Thus, when a particle gets trapped in the main pocket in the pre-noon sector at εt_1 and then released back in the afternoon sector at εt_2, it undergoes two jumps which add up to $\Delta\mathcal{S} = \mathcal{S}(\varepsilon t_2) - \mathcal{S}(\varepsilon t_1) = \mathcal{S}_a(\varepsilon t_2) - \mathcal{S}_a(\varepsilon t_1) > 0$ due to $\mathcal{S}_a$ being larger in the afternoon sector compared to pre-noon. Conversely, for particles trapped in the adjacent pocket, the situation is reversed, with $\Delta\mathcal{S} = \mathcal{S}(\varepsilon t_2) - \mathcal{S}(\varepsilon t_1) = \mathcal{S}_m(\varepsilon t_2) - \mathcal{S}_m(\varepsilon t_1) < 0$.

2.2.4 Non-conservative Hamiltonian

In Sections 2.2.1-2.2.3, we use a simplified Hamiltonian system with slow-time dependence, εt, where $\varepsilon \ll 1$ (see Eq. 2.9), to illustrate the typical dynamics of the adiabatic invariant associated with asymmetric separatrix crossing. This system simplifies particle drift motion to slow steady motion ($\sim \varepsilon$) along the drift orbit. The drift orbit is approximated by that of an equatorially mirroring particle, such that actual $\boldsymbol{R}_\perp$ is replaced with $\boldsymbol{R}_{\perp,90^\circ}(\varepsilon t)$, where $\boldsymbol{R}_{\perp,90^\circ}(\text{MLT})$ denotes the drift orbit of an equatorially mirroring particle as obtained from TS04 in Section 2.1.4. This results in the reduction of the original phase space to just a subspace of $(s, p_{||})$ and introduces explicit time dependence, as $B(\boldsymbol{R}) = B(s, \boldsymbol{R}_\perp)$ is replaced with $B(s, \varepsilon t)$. As a result, Hamiltonian (2.9) becomes time-dependent and does not conserve the total energy. Despite that important dissimilarity, both Hamiltonian (2.9) and the original

system exhibit trapping under the separatrix and jumps of the adiabatic invariant associated with it (for both systems the adiabatic invariant is conserved far from the separatrix). Although, there are some *quantitatively* differences resulting from non-conservative nature of the model Hamiltonian system. First of all, note that energy conservation in the full guiding center system (Eqs. 1.11) allows conservation of B_m, which is the magnetic field strength at the mirror point where $p_{||} = 0$. In the model system described by Hamiltonian (2.9), this is no longer the case. Indeed, initially, the value of B_m is prescribed as an external parameter. Due to normalization, all particles start with $H = 1/2$. Thus, at $t \approx 0$, when the total energy has not changed from its initial value, mirroring indeed happens at $B(s_{1,2}, \varepsilon t) \approx B_m$, as dictated by

$$H(s_{1,2}, P; \varepsilon t \approx 0) = \frac{B(s_{1,2}, \varepsilon t)}{2B_m} \approx H(s(0), P(0); 0) = \frac{1}{2} \Leftrightarrow B(s_{1,2}, \varepsilon t) \approx B_m \tag{2.19}$$

However, due to explicit time dependence, at later times the energy will not be conserved (in fact, it decays until $\varepsilon t \lesssim 12$)

$$\frac{dH(s, P; \varepsilon t)}{dt} = \frac{\varepsilon}{2B_m} \frac{dB(s, \varepsilon t)}{d(\varepsilon t)} \neq 0 \tag{2.20}$$

Because of that, the actual mirroring happens at a lower value of magnetic field strength, $B(s_{1,2}, \varepsilon t) \lesssim B_m$. As a result of this energy non-conservation, the trapping conditions are somewhat different for the original system (Eqs. 1.11) and for the model Hamiltonian. For the original system, one has two mutually consistent trapping criteria: (1) $B_m = B^*$, where B^* is the magnetic field strength at the local maximum along a given field line (see Fig. 2.3a), and (2) $S(\mathrm{MLT}_1) = I_0$, with S being the total phase area (apart from a factor p) enclosed by the separatrix (see Eq. 2.5) and I_0 the initial value of the normalized adiabatic invariant (see Eq. 2.10). Both of these criteria are practically identical due to B_m-conservation. This is no longer the case for the model Hamiltonian (2.9); B_m no longer dictates the actual point of

particle mirroring. For Hamiltonian (2.9), one has to rely on the trapping condition relating the adiabatic invariant to the total area enclosed by the separatrix: $\mathcal{S}(\varepsilon t_1) = \mathcal{I}_0$. Due to these different trapping conditions and energy non-conservation, the MLT profile of the total area enclosed by the separatrix, although *qualitatively* similar, is *quantitatively* different in these two systems. That is, $S(\text{MLT}) \neq \mathcal{S}(\text{MLT})$, even if the same $B(s, \text{MLT})$ is used (see Eqs. 2.5 and 2.11). Indeed, using Eq. 2.11 and $U(s, \varepsilon t) = B(s, \varepsilon t)/2B_m$ we easily find

$$\begin{aligned} \mathcal{S}(\varepsilon t) &= 2\int_{s_1^*}^{s_2^*} \sqrt{2(U^* - U(s,\varepsilon t))}ds = 2\int_{s_1^*}^{s_2^*} \sqrt{\frac{B^* - B(s,\varepsilon t)}{B_m}}ds = \\ &= 2\int_{s_1^*}^{s_2^*} \sqrt{\frac{B^*}{B_m}}\sqrt{1 - \frac{B(s,\varepsilon t)}{B^*}}ds \end{aligned} \tag{2.21}$$

Comparing this with definition of $S(\text{MLT})$ (see Eq. 2.5), we see that $\mathcal{S}$ coincides with S only if trapping happens at $B^* = B_m$, that is only if the total energy is conserved (as in Eqs. 1.11). By recalling $B_m = B_{eq}/\sin^2\alpha_{eq}$, we can rewrite Eq. 2.21 as

$$\begin{aligned} \mathcal{S}(\varepsilon t) &= 2\int_{s_1^*}^{s_2^*} \sqrt{2(U^* - U(s,\varepsilon t))}ds = 2\int_{s_1^*}^{s_2^*} \sqrt{\frac{B^* - B(s,\varepsilon t)}{B_m}}ds = \\ &= 2|\sin\alpha_{eq}|\int_{s_1^*}^{s_2^*} \sqrt{\frac{B^* - B(s,\varepsilon t)}{B_{eq}}}ds \end{aligned} \tag{2.22}$$

Thus, $\mathcal{S}$ also depends on the initial pitch angle, even for particles starting on the same drift orbit (same B_{eq}). This is the reason why we see different $\mathcal{S}(\varepsilon t)$ for different α_{eq}(different $\mathcal{I}_0$) in Fig. 2.6a-c. This is unlike $S(\text{MLT})$, which is only a function of MLT along a given drift orbit. In conclusion, we note that all these limitations are inevitable in the considered Hamiltonian system, because all the features of the actual 3D motion cannot be reproduced with a reduced Hamiltonian system with $1\frac{1}{2}$ degrees of freedom. We note again that this reduced Hamiltonian system is only used in Section 2.1.4 to exemplify geometric jumps of the

adiabatic invariant resulting from asymmetric separatrix crossing. In the rest of this chapter we rely only on the mapping arising directly from Eqs. 1.11 that conserves B_m.

2.2.5 Mapping

Figure 2.6d demonstrates that the evolution of the adiabatic invariant driven by geometric jumps can be accurately reproduced using a mapping that only invokes the phase area enclosed by the separatrix and its pockets at different MLT sectors. Building on this result, one may replace the actual 3D motion of an electron experiencing drift-orbit bifurcation with a similar mapping. Specifically, a mapping identical to Mapping (2.18) can be performed directly using TS04-based profiles of phase areas (Fig. 2.4c). In this case, the MLT profiles of phase areas should be defined using Eqs. 2.5 and 2.6. Starting with an initial value of the second adiabatic invariant, I_0, the final value after one complete drift period, $I^{'}$, is calculated as

$$I^{'} = \begin{cases} S(\mathrm{MLT}_2), & \text{if } \mathrm{MLT}_2 \text{ exists,} \\ S_a(\mathrm{MLT}_1), & \text{if } \mathrm{MLT}_2 \text{ does not exist but } \mathrm{MLT}_1 \text{ exists,} \\ I_0, & \text{if neither } \mathrm{MLT}_2 \text{ nor } \mathrm{MLT}_1 \text{ exist.} \end{cases} \tag{2.23}$$

where MLT_1 is such that $S(\mathrm{MLT}_1) = I_0$ and MLT_2 is such that $S_i(\mathrm{MLT}_2) = S_i(\mathrm{MLT}_1)$ with $i \in \{m, a\}$ or $S_m(\mathrm{MLT}_2) = I_0$ if MLT_1 does not exist. Here, the case when MLT_2 does not exist implies trapping in the adjacent pocket, while the case when MLT_1 does not exist implies trapping in the main pocket. Figure 2.6e shows distribution of the geometric jumps, $\Delta I = I' - I_0$, obtained with Mapping (2.23) using the TS04-based profiles of phase-areas (Fig. 2.4c). Similarity between Figs. 2.6d and 2.6e suggests that dynamics of charged particles experiencing bifurcation should bear strong resemblance of that modeled by Hamiltonian (2.13). In particular, we expect that *geometric jumps* due the asymmetry of Earth's magnetosphere play the major role in governing the evolution of the second adiabatic invariant during dayside

bifurcation.

2.3 Radial Transport due to Geometric Jumps

During drift-orbit bifurcation, the second adiabatic invariant undergoes a jump, ΔI, while the magnetic moment is conserved, $\mu = \text{const}$. Here $I = J_{||}/p$ is the normalized adiabatic invariant whose conservation is contingent upon conservation of total energy (p). Conservation of the magnetic moment leads to conservation of the mirror field strength, B_m. Thus, in the L_B-I space, radial transport of particles can only occur along the contours of constant B_m (see discussion of Eq. 1.81 and [Öztürk and Wolf, 2007, Ukhorskiy et al., 2011])

$$B_m(I, L_B) = B_m(I + \Delta I, L_B + \Delta L) = \text{const} \tag{2.24}$$

where (I, L_B) are the initial values of the adiabatic invariant and drift-orbit L_B parameter (see Eq. 2.1). To quantify the effects of the asymmetric drift-orbit bifurcation on the radial transport of particles, we compute MLT profiles of separatrix areas in the TS04 magnetic field model at different values of L_B. We then use these profiles as inputs for Mapping (2.23) to compute $\Delta_{m,a}I(I_0)$ (see Fig. 2.6e). For a given drift orbit (given L_B), there is a unique correspondence between B_m and $I_0 = 2\int_{s_1}^{s_2}\sqrt{1 - B/B_m}ds$, where B is the magnetic field strength profile at some fixed MLT sector outside of the bifurcated region. We use MLT $= 6$ to avoid contributions from the magnetotail current sheet. Accordingly, we introduce $r_{\text{MLT}=6}$ which is the equatorial extent of the drift orbit at MLT $= 6$. Eq. 2.24 allows relating $\Delta_{m,a}I$ to the radial displacement $\Delta_{m,a}L$ for a given drift orbit. Note that $\Delta_{m,a}I$ is calculated under the assumption that $L_B = \text{const}$, which is then used to estimate ΔL. Thus, our calculations are intrinsically not self-consistent. Although this may lead to some overestimation of the actual radial displacement, we note that this approach is akin to the well-known 'unperturbed-trajectories' method, where the zeroth-order approximation ($L_B = \text{const}$) is used to estimate

the first-order correction (ΔL).

Figure 2.7a shows radial displacement, $\Delta_{m,a}L$, from the drift orbit with $L_B = 7.3$. Particles with small adiabatic invariant, $I_0 \lesssim 0.4$ ($\alpha_{eq} \gtrsim 80°$), exhibit significant *outward* jumps, $\Delta L > 0$, while no *inward* jumps occur until $I_0 \gtrsim 0.4$. This observation aligns with Mapping (2.23) and Fig. 2.6e, indicating that such particles undergo single jumps with $\Delta I > 0$ during their detrapping from the main pocket. Above $I_0 \gtrsim 0.4$, both outward and inward jumps are observed with similar magnitudes. At larger values of L_B, the upper boundary of the bifurcation region increases, enabling radial transport of particles with larger I_0 (smaller α_{eq}) due to the increased maximum area enclosed by the separatrix.

To quantify the magnitude of the outward and inward radial displacement from a given drift orbit, we consider the maximum positive and negative jumps (see Fig. 2.6e) of the adiabatic invariant

$$\begin{aligned} \Delta_+ I &= \max_{I_0}(\Delta I_m) \\ \Delta_- I &= \min_{I_0}(\Delta I_a) \end{aligned} \tag{2.25}$$

Using these typical values of ΔI-jumps, we then calculate the radial displacement, $\Delta_\pm L$, using transport characteristics (Eq. 2.24)

$$\Delta_\pm L = \Delta_\pm I \left(\frac{\partial I}{\partial L_B}\right)^{-1}\Bigg|_{B_m=\text{const}} \tag{2.26}$$

Figure 2.7b shows the range of equatorial pitch angles (at MLT = 6) affected by the drift-orbit bifurcation. Typically, bifurcation affects particles with $\alpha_{eq} \in [\tilde{\alpha}, 90°]$, where the lower boundary, $\tilde{\alpha}$, decreases with increasing L_B, reaching the range of $[40°, 90°]$ at $L_B = 8.4$. Figure 2.7c shows the inward ($\Delta_- L$) and outward ($\Delta_+ L$) radial displacements from various drift orbits (see Eq. 2.26) which we refer to as the displacement profile. The displacement profile becomes broader with with L_B increase, indicating more effective transport from

outer drift orbits. At $L_B = 8.4$ the upper bound of the displacement profile corresponds to the outward radial displacement of $\Delta_+ L \approx 1.5$, while the magnitude of the inward radial displacement seems somewhat smaller, $\Delta_- L \approx -1$. This asymmetry reflects the asymmetry of the geometric jumps of the second adiabatic invariant, $\Delta_\pm I$ (see Fig. 2.6e).

Figure 2.8 shows the amplitudes of radial displacements, $\Delta_\pm L$, for different values of $\varphi_{\rm IMF}$, IMF B, and solar wind ram pressure, $P_{\rm dyn}$. We present results for $L_B < 8$, while the last close drift orbit is situated at $L_B \gtrsim 8.0 - 8.3$, depending on the value of the ram pressure. Figure 2.8a shows radial displacement profiles for different values of $|\cos(\varphi_{\rm IMF})|$ with $\varphi_{\rm IMF} \in [0, 360°]$. We observe the most significant radial displacement for eastward and westward IMF with $\cos(\varphi_{\rm IMF}) = \pm 1$, reaching magnitudes of $\Delta_\pm L \pm 1$. Interestingly, the least effective radial displacement is observed for purely southward and northward IMF, $\cos(\varphi_{\rm IMF}) = 0$. In these cases, the magnitude of radial displacement is small ($|\Delta_\pm L| \lesssim 0.2$). This suggests that the asymmetric drift-orbit bifurcation is primarily controlled by the IMF B_y component. We argue that this is due to the role of east-west asymmetry and the associated MLT asymmetry of $S_{m,a}$ and S (see Fig. 2.4). A larger east-west asymmetry should result in a larger ΔS, thus increasing the magnitude of geometric jumps. Note that a purely southward/northward IMF leads to north-south asymmetry, i.e., $S_a \neq S_m$; the lack of east-west asymmetry results in $\Delta S \approx 0$. Figure 2.8b shows radial displacement profiles for different values of the solar wind ram pressure, $P_{\rm dyn}$. We observe larger values of ram pressure resulting in larger magnitudes of both inward and outward radial displacements. Note that an increase in ram pressure also broadens the range of drift orbits affected by the drift-orbit bifurcation; for $P_{\rm dyn} = 2$ nPa, bifurcation starts at $L_B \approx 7.1$, while for $P_{\rm dyn} = 4$ nPa, bifurcation starts at $L_B \approx 6.5$. Figure 2.8c shows radial displacement profiles for different IMF B. We observe the magnitude of radial displacement increasing with increasing IMF B. Note that this increase in the magnitude of ΔL results from stronger asymmetry associated with larger values of IMF B and cannot be simply treated as an increase in the net pressure on the magnetopause. This is because the contribution of magnetic pressure, $P_{\rm mag} = {\rm IMF}B^2/2\mu_0$, to the net pressure on

the magnetopause is negligible compared to the ram pressure. Even for IMF$B = 10$ nT, $P_{\rm mag}$ yields only 0.04 nPa, while $P_{\rm dyn} \approx 1$ nPa (see Fig. 2.1b).

2.4 Discussion and Summary

In this chapter, we combined the theoretical framework put forward by [Shabansky and Antonova, 1968], [Shabansky, 1971], [Shabansky, 1972], [Antonova et al., 2003] with the general theory of separatrix crossing in slow-fast Hamiltonian systems [Neishtadt, 1986, Neishtadt, 1987, Neishtadt, 2019, Cary et al., 1986] to describe drift-orbit bifurcation in a realistic (asymmetric) magnetospheric configuration. Our results indicate that in the presence of a significant IMF B_y component, jumps of the second adiabatic invariant are on the order of the invariant itself, reflecting the so-called geometric jumps arising due to the asymmetry of the separatrix of the corresponding Hamiltonian system. We develop a mapping technique that allows estimating these jumps for a given magnetic field configuration. Using this mapping, we estimate radial transport due to geometric jumps. Our results indicate that the radial displacement can reach values of $\Delta L \sim \pm 1$ per one drift. We show that solar wind conditions most favorable for such jumps are those with a significant IMF B_y component.

These results are consistent with those obtained by [Wan et al., 2010], who also found that global magnetospheric asymmetry induced by a non-zero IMF B_y component can significantly increase the magnitude of the jumps in the second adiabatic invariant. The role of magnetospheric asymmetry in drift-orbit bifurcation was first pointed out by [Öztürk and Wolf, 2007], who correctly concluded that asymmetric bifurcation can result in a change of the adiabatic invariant, which is of zero order in $\varepsilon = \tau_b/\tau_d$ and, thus, does not depend on particle energy. However, at first glance these results appear to contradict the conclusion by [Ukhorskiy et al., 2011], who argued that magnetospheric asymmetry does not play a significant role in the jump of the second adiabatic invariant due to drift-orbit bifurcation. Our results allow gaining insight into the source of this apparent contradiction. While test-particle

simulation in [Ukhorskiy et al., 2011] was carried out in the TS07 magnetic field model, which provides realistic global scale structure of the magnetosphere, the authors used specific solar wind conditions with IMF $B \lesssim 1$ nT and zero tilt angle (quiet time magnetospheric conditions at 05:00 UT on 8 March 2008). Our analysis shows that such types of solar wind driving conditions result in a highly east-west-symmetric magnetospheric configuration, which does not encompass large geometric jumps of the second adiabatic invariant. However, the solar wind driving conditions leading to the magnetosphere asymmetry discussed herein are actually more representative at 1 AU (see Fig. 2.1). Thus, our results support the idea of [Öztürk and Wolf, 2007] and [Wan et al., 2010] that magnetospheric asymmetry plays an essential role in particle scattering due to drift-orbit bifurcation. Figures 2.7 and 2.8 demonstrate that asymmetric drift-orbit bifurcation can produce significant radial displacement in one drift period. This radial displacement can occur in both inward (earthward) and outward directions with $\Delta L \sim \pm 1$, allowing for both particle acceleration via conservation of the magnetic moment and particle losses through the magnetopause. Importantly, this mechanism of radial transport is likely to be fast and non-diffusive due to the large amplitude and deterministic nature of the geometric jumps.

Our analysis relies on the assumption that the drift orbit of equatorial-mirroring particles ($\alpha_{eq} = 90°$) is a valid approximation for particles with other pitch angles. While it can be a good approximation for particles with $\alpha_{eq} \approx 90°$, its validity for smaller pitch angles is unclear and can only be verified via full 3D test-particle tracing in the guiding center approximation. However, our simplistic model still captures the salient features and *qualitative* characteristics associated with asymmetric drift-orbit bifurcation that should be present also for the cases of more field-aligned particles. In particular, our analysis clearly demonstrates that the large jumps of the adiabatic invariant observed by [Wan et al., 2010] are geometric jumps which are of order zero in $\varepsilon = \tau_b/\tau_d$ and do not depend on particle energy. Indeed, thus far we have not specified any energy range relevant to asymmetric drift-orbit bifurcation. This is because the jump of the adiabatic invariant per drift period is energy independent, with

only the *implicit* energy dependence coming: (1) from the drift period (τ_d) and (2) from the condition $\varepsilon \to 0$. We note that for relativistic electrons, the drift period scales linearly with particle energy, while the condition of $\varepsilon < 0.1$ is well satisfied for electrons with energies below 10 MeV. In this regime, the effects of the magnetic field asymmetry, i.e., geometric jumps, dominate the effects of a finite ε, i.e., stochastic jumps, for reasonably asymmetric magnetic field configurations. Note that the effects of the magnetic field asymmetry cannot be reproduced by the theory of stochastic jumps and are likely to result in non-diffusive radial transport of particles. This question will be the subject of Chapter 3. We also note that our result on three types of geometric jumps obtained with the mapping technique (Figs. 2.6a-c) are consistent with prior work by [Wan et al., 2010]. In particular their Figs. 4a and 4d which show particles that only exhibit one jump in the second adiabatic invariant. That behavior contradicts the conventional theory of drift-orbit bifurcation which predicts two jumps, associated with trapping and detrapping, respectively (see, e.g., Fig. 2 in [Ukhorskiy et al., 2011]). Such single jumps cannot be described as stochastic jumps and can only be geometric jumps, similar to those shown herein, in Figs. 2.6a and 2.6b. Another important cause of global magnetospheric asymmetry is the seasonal variation of Earth's tilt angle. Our preliminary analysis indicates that a non-zero tilt angle is the source of an additional, north-south asymmetry which can also affect the jumps of the second adiabatic invariant and radial displacements in the presence of a non-zero IMF B_y component, providing essentially an increased east-west asymmetry. However, we leave the detailed analysis of this effect to a later study.

In summary, we investigated the effects of magnetospheric asymmetry on drift-orbit bifurcation. Specifically, we utilized the TS04 model[Tsyganenko and Sitnov, 2005] to quantify the jumps of the second adiabatic invariant, assuming drift orbits close to those of equatorially mirroring particles. By constructing a qualitative model of the Hamiltonian system with $1\frac{1}{2}$ degrees of freedom, we demonstrated that under IMF $B_y \neq 0$ conditions, geometric jumps of the second adiabatic invariant are observed, with magnitudes comparable to the initial values

of the adiabatic invariant. We propose a mapping technique to estimate these geometric jumps for a given field configuration. These jumps necessarily result in opening of the drift orbit, allowing for radial transport. Building on this result, we identify solar wind conditions favorable for such jumps due to asymmetric drift-orbit bifurcation. These findings suggest that magnetospheric asymmetry can significantly alter the dynamics of energetic particles in the outer radiation belt and should therefore be incorporated into radiation belt models. As we shall see in Chapter 3, the framework developed here will be further validated using direct test-particle simulations in the guiding-center approximation.

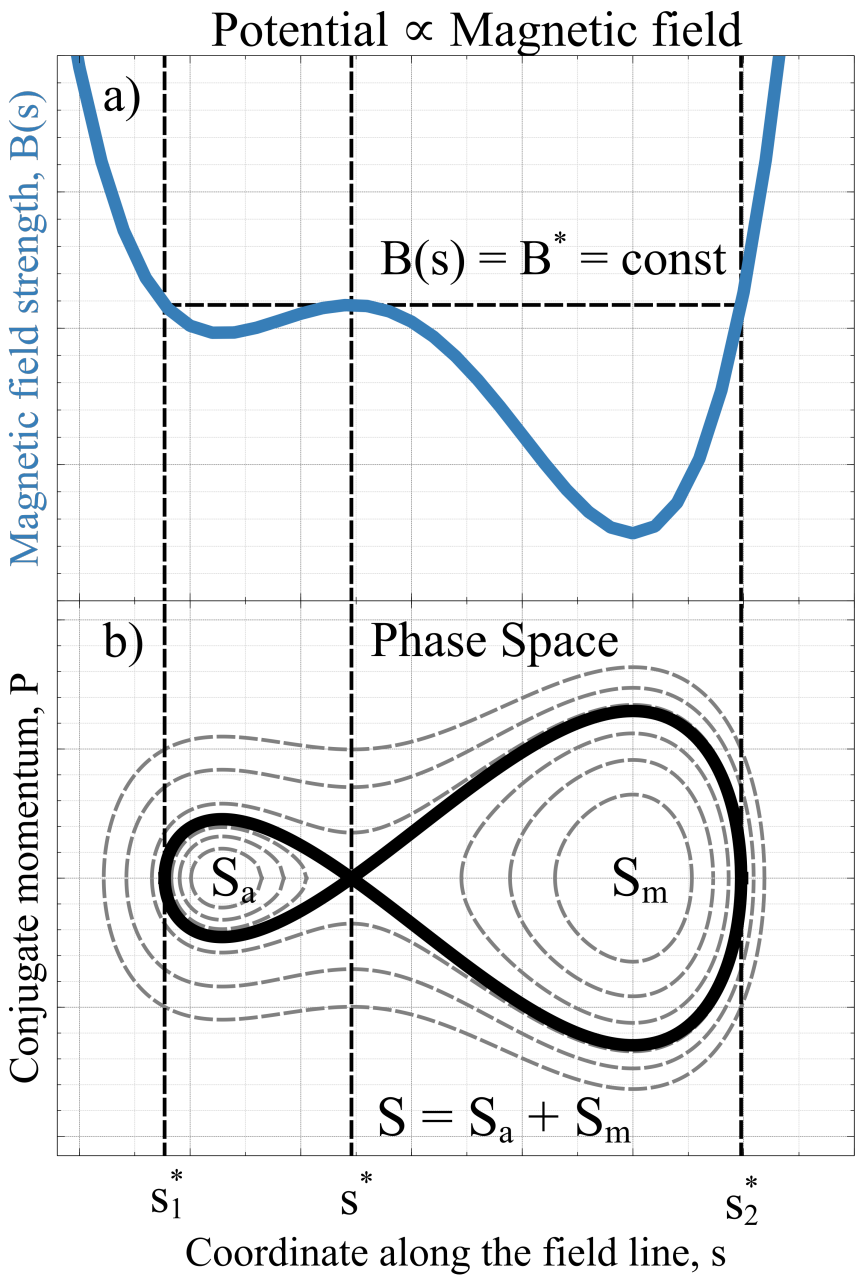

Figure 2.3: A schematic of the separatrix in a double-well potential: a) typical W-shape magnetic field strength profile $B(s)$ (effective potential, see Hamiltonian (2.9)), b) associated phase space of (s, P) with phase trajectories (gray) given by Hamiltonian (2.9).

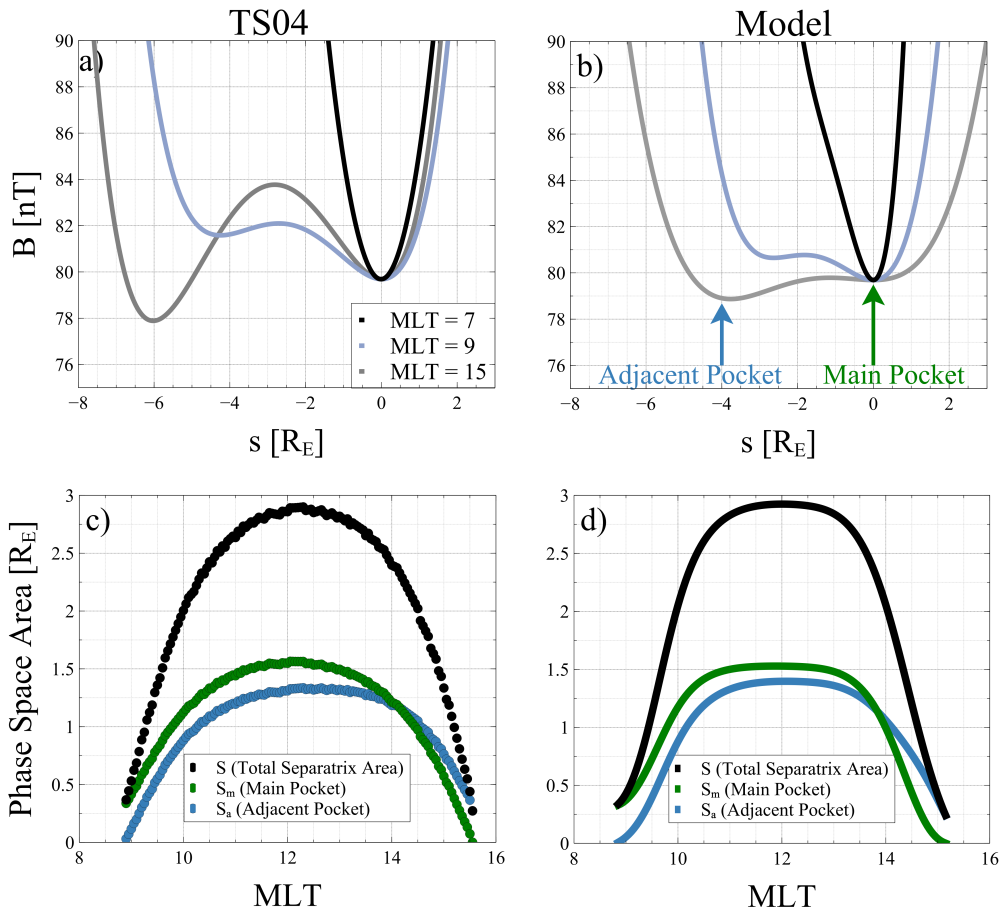

Figure 2.4: Comparison of magnetic field strength profiles along the drift orbit (Fig. 2.2 with $\phi_{\text{IMF}} = 225°$, TS04 [Tsyganenko and Sitnov, 2005]) with the model (Eq. 2.7) at $L_B = 7.3$. a) Magnetic field along the field lines at three MLTs along the the drift orbit (Fig. 2.2), b) Magnetic field along the field lines at the same MLTs yielded by Eq. 2.7, c) TS04-based MLT profiles of the phase areas (apart from a factor p) enclosed inside the main pocket (S_m), adjacent pocket (S_a), and the total area inside the separatrix $S = S_m + S_a$, d) same MLT profiles of S, S_m and S_a yielded by Eq. 2.7.

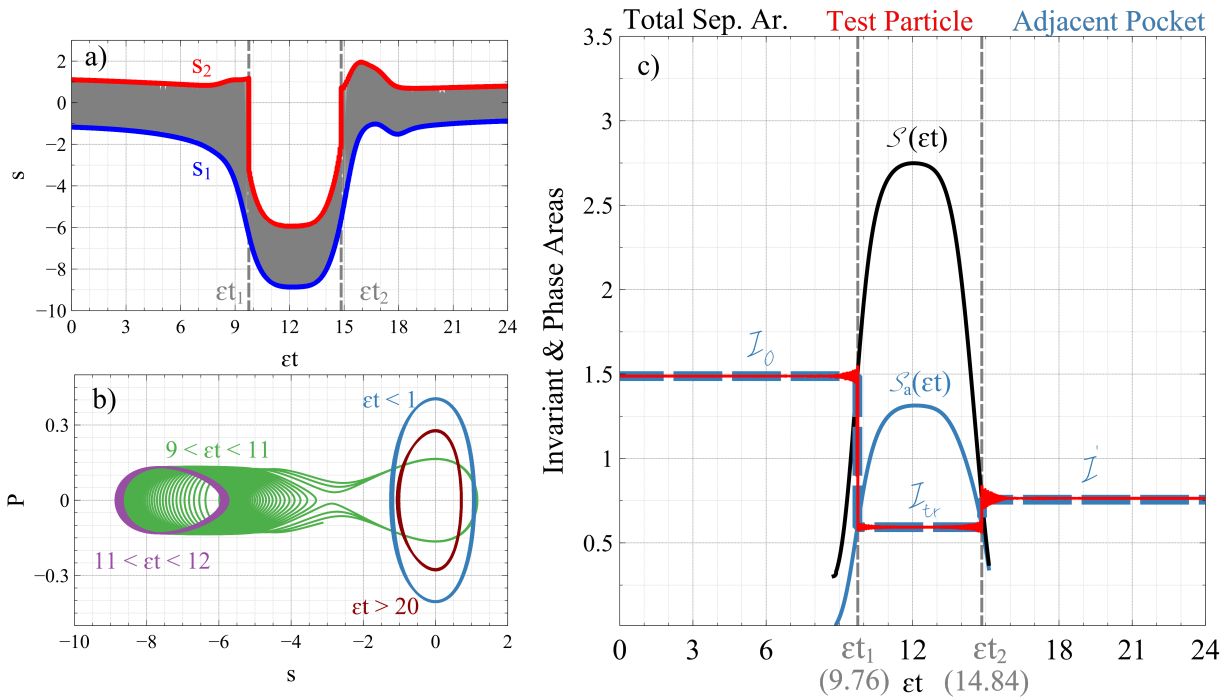

Figure 2.5: Test-particle simulation according to Hamiltonian (2.13) with $\varepsilon = 10^{-3}$ and initial conditions, $s(0) = 0$ and $P(0) = \cos\alpha_{eq}$ with $\alpha_{eq} = 66°$: a) test-particle trajectory, $\mathcal{S}(\varepsilon t)$, as a function of slow time (gray), two mirror points,$s_{1,2}$ (blue and red), computed as $H(s_{1,2}, 0; \varepsilon t) = H(s(\varepsilon t), P(\varepsilon t); \varepsilon t)$ from Hamiltonian (2.13), b) phase trajectory of the test-particle in (s, P) for 4 intervals of slow time; $\varepsilon t < 1$ (blue), $\varepsilon t \in [10, 11]$ (green), $\varepsilon t \in [11, 12]$ (violet), and $\varepsilon t > 20$ (dark red), c) adiabatic invariant as a function of slow time, $\mathcal{I}(\varepsilon t)$ (red), total area inside the separatrix, $\mathcal{S}(\varepsilon t)$ (black), phase-area inside the adjacent pocket, $\mathcal{S}_a(\varepsilon t)$ (blue), blue-dashed lines show results of Mapping (2.18), gray lines signify particle trapping and detrapping. Note that $\mathcal{S}$ and $\mathcal{S}_a$ are smaller by a factor of $\sin\alpha_{eq} \approx 0.91$ compared to S and S_a, as shown in Fig. 2.4d. See details in Section 2.2.4.

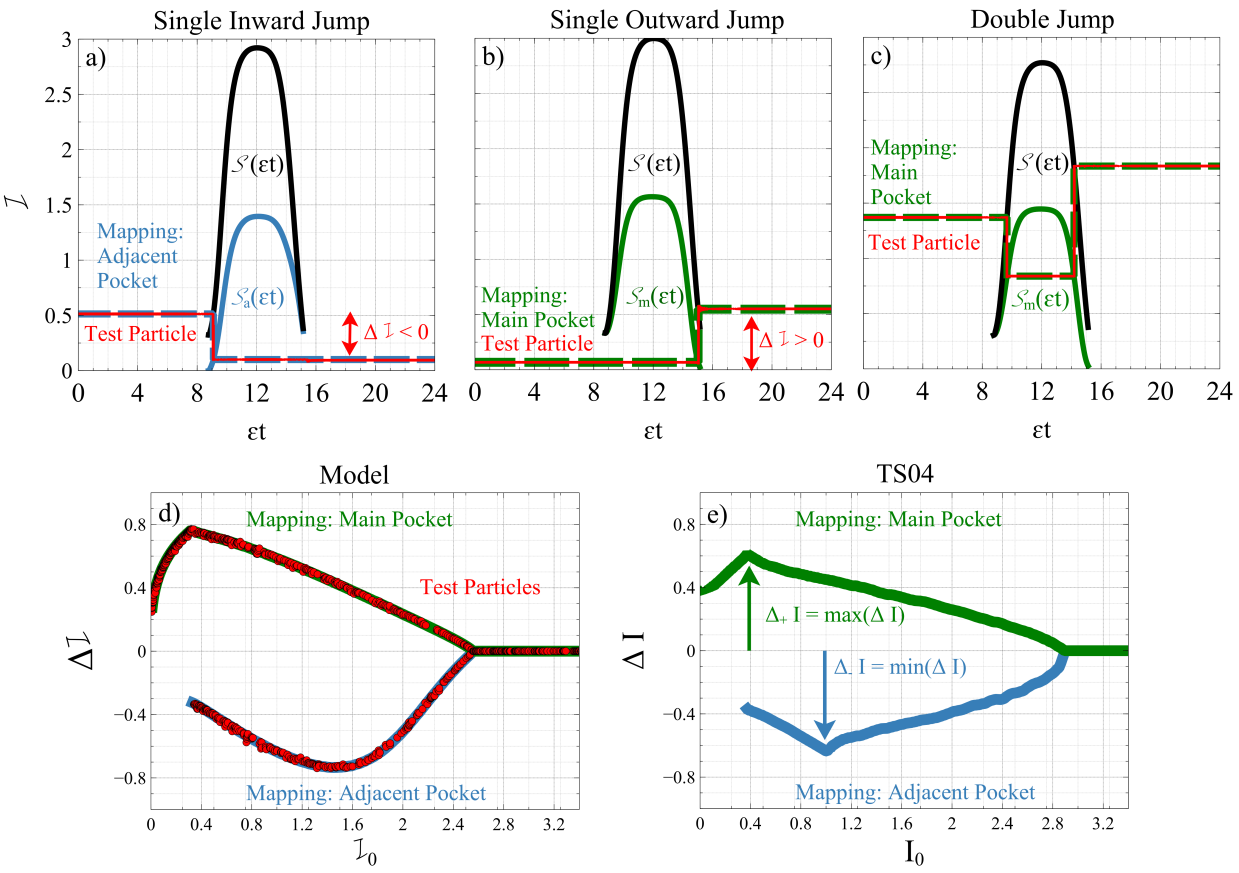

Figure 2.6: Evolution of the adiabatic invariant, comparison between test-particle simulations governed by Hamiltonian (2.13) with $\varepsilon = 10^{-4}$ and the result of Mapping (2.18) for different initial values of the adiabatic invariant ($\mathcal{I}$ defined via Eq. 2.10), a) $\mathcal{I}_0 = 0.48$, b) $\mathcal{I}_0 = 0.07$ c) $\mathcal{I}_0 = 1.37$ reflecting different equatorial pitch angles, a) $\alpha_{eq} = 76°$, b) $\alpha_{eq} = 85°$, c) $\alpha_{eq} = 66°$. Panel (d) shows distribution of $\Delta\mathcal{I}(\mathcal{I}_0)$ for $\mathcal{I}_0 \in [0, 3.4]$ from test-particle simulations (red) and results of Mapping (2.18), assuming trapping in the main (green) and adjacent (blue) pockets. Panel (e) shows geometric jumps in terms of $I = J_{||}/p$ obtained by applying Mapping (2.18) to TS04 profiles of the phase-areas shown in Fig. 2.4c.

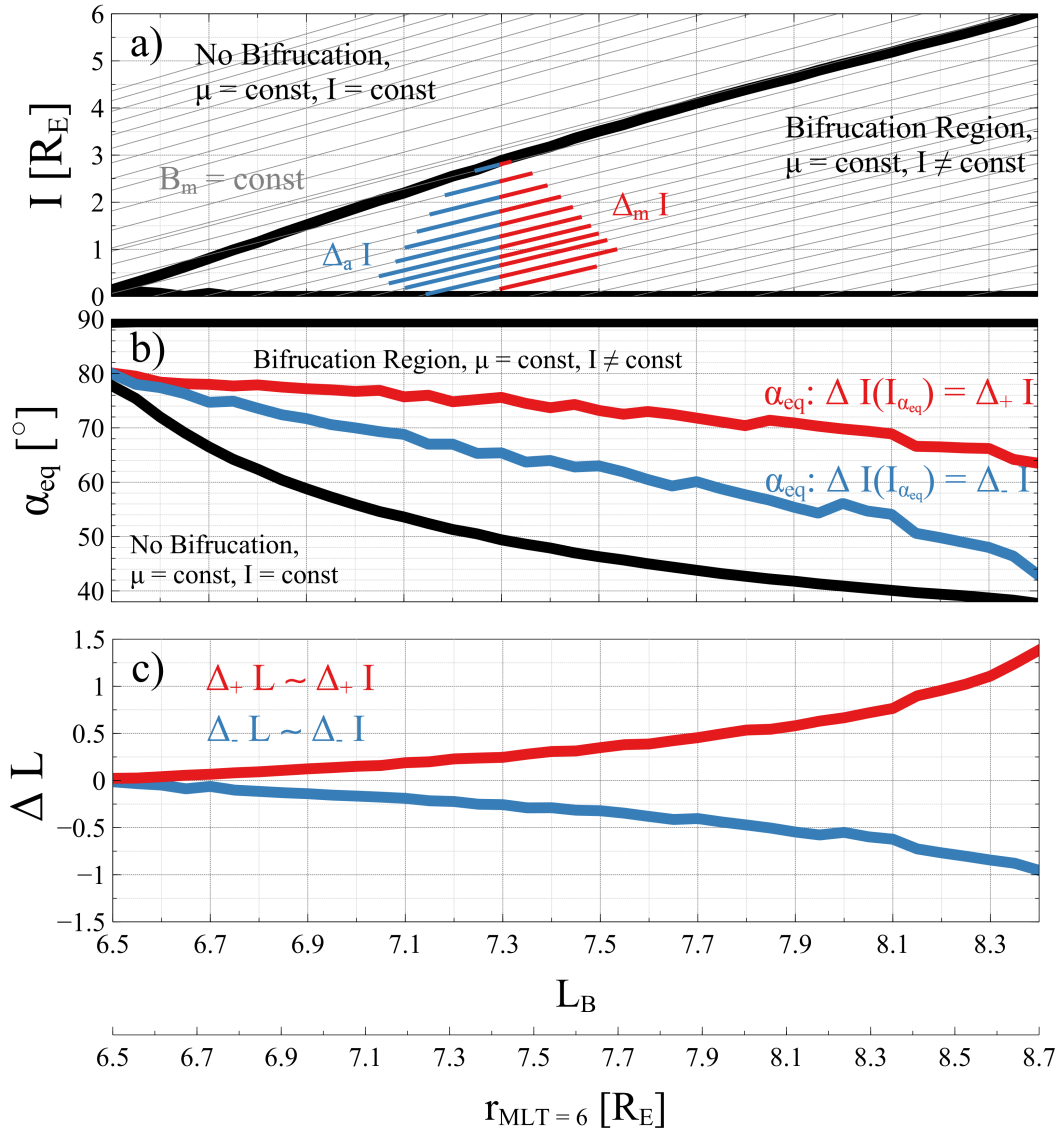

Figure 2.7: Radial transport due to asymmetric drift-orbit bifurcation as estimated in the TS04 magnetic field model ($P_{dyn} = 4$ nPa, IMF $B = 5$ nT, $\varphi_{\rm IMF} = 225°$, zero tilt). Panel (a) shows jumps (red/blue) from the drift orbit with $L_B = 7.3$ in L_B–I space. Adiabatic invariant jumps, $\Delta_{m,a}I$, are computed via Mapping (2.23) and converted to radial displacements, $\Delta_{m,a}L$, using transport characteristics (B_m = const, gray). Black lines mark bifurcation boundaries. Panel (b) shows equatorial pitch-angle ranges, α_{eq} (MLT= 6), subject to bifurcation vs. L_B. Red/blue curves correspond to maximum positive/negative jumps, $\Delta_+ I$ and $\Delta_- I < 0$. Panel (c) shows corresponding radial jumps $\Delta_\pm L$ (Eq. 2.26). The top axis gives $r_{\rm MLT=6}$.

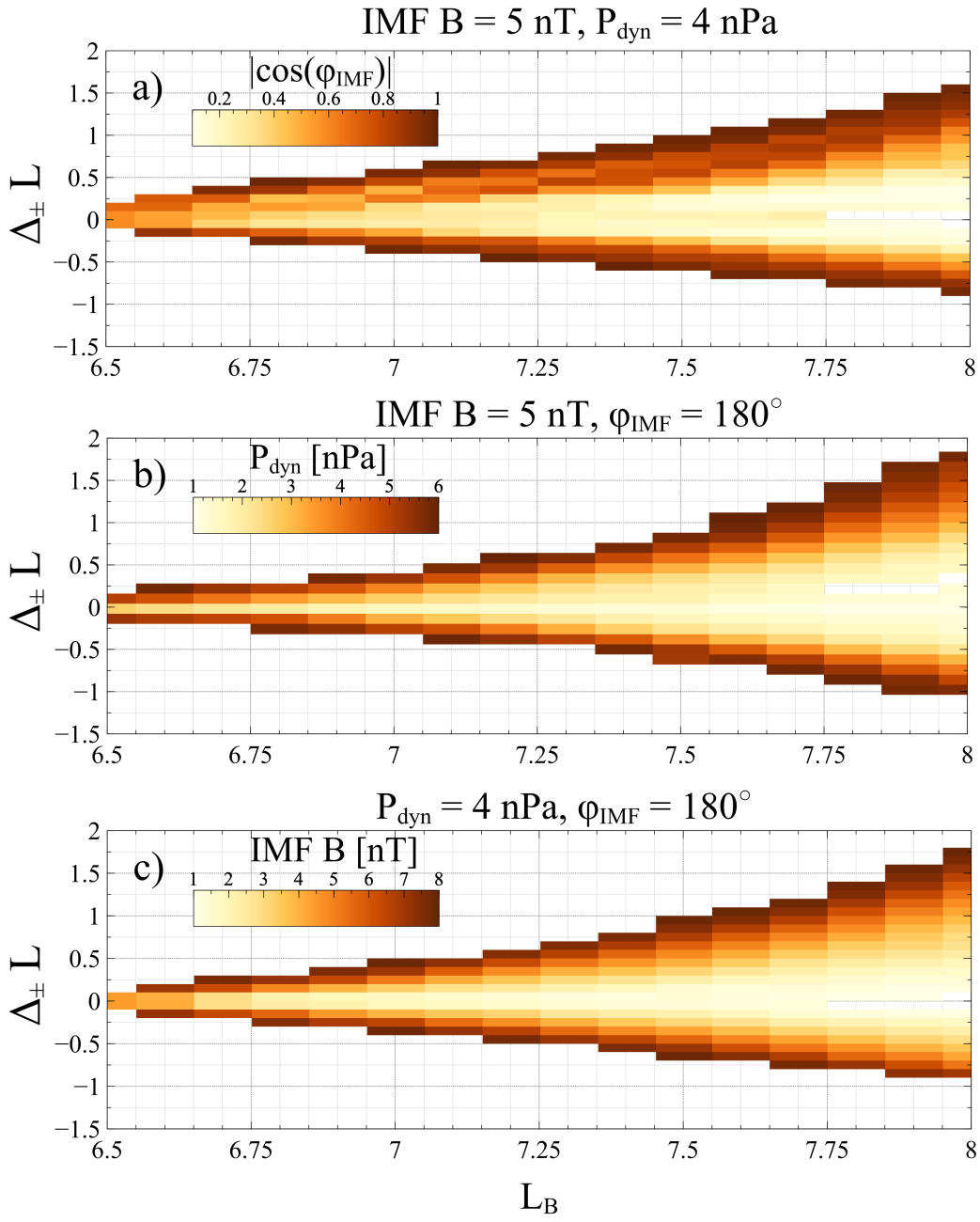

Figure 2.8: Magnitude of the radial displacement (Eqs. 2.25 and 2.26) from different drift orbits as a function of the solar wind parameters; a) IMF $B = 5$ nT, $P_{\rm dyn} = 4$ nPa, and $\varphi_{\rm IMF} \in [0, 360°]$, b) IMF $B = 5$ nT, $\varphi_{\rm IMF} = 180°$, and $P_{\rm dyn} \in [1, 6]$ nPa, c) $P_{\rm dyn} = 4$ nPa, $\varphi_{\rm IMF} = 180°$, and IMF $B \in [1, 8]$ nT

CHAPTER 3

Energetic Electron Enhancements Near the Dayside Magnetopause: Outward Radial Transport Due to Asymmetric Drift-Orbit Bifurcation

The magnetopause boundary layer is often characterized by the appearance of isolated energetic electron enhancements at energies above a few tens keV [Meng and Anderson, 1970, Meng and Anderson, 1975, Williams et al., 1985, Dunlop et al., 2008]. Their origin is elusive, as mechanisms such as dayside reconnection or wave-particle interactions often struggle to explain the acceleration of magnetosheath electrons from a few tens eV to tens of keV [Walsh et al., 2012, Phan et al., 2013, Fu et al., 2019]. At the same time, electrons with energies of tens of keV are typical of the outer radiation belt. This suggests an outward radial transport mechanism for radiation belt electrons operating near the dayside magnetopause (see discussion in, e.g., [Parks et al., 1999, Walsh et al., 2012]). The concept of outward radial transport has also been invoked to explain energetic electron leakage through the dayside magnetopause and their penetration into magnetopause-shadowed regions [Sibeck and McEntire, 1988, Cohen et al., 2016].

In this Chapter, we analyze a representative dayside magnetosphere crossing by the Time History of Events and Macroscale Interactions during Substorms (THEMIS) mission [Angelopoulos, 2008] on October 1, 2018, showing the formation of an energetic electron enhancement near the magnetopause on timescales of a few hours, comparable to the drift period of $30 - 100$ keV electrons. Concurrent observations of solar wind conditions by the

Acceleration, Reconnection, Turbulence, and Electrodynamics of Moon's Interaction with the Sun (ARTEMIS) mission [Angelopoulos, 2011] suggest that conditions are favorable for electrons to experience drift-orbit bifurcation in regions adjacent to the magnetopause. We adopt an *ad hoc* model aimed at reproducing the main characteristics of dayside bifurcation. We conduct test-particle guiding-center simulations to study the radial transport of energetic (51 keV) electrons and discuss the results in the context of the bifurcation-driven radial transport and its (non-diffusive) characteristics.

This chapter is organized as follows. Section 3.1 provides the context for the energetic electron enhancement event observed by the THEMIS spacecraft on October 1, 2018. In Section 3.2.1, we present an analytical *ad hoc* model of the magnetic field that reproduces the main characteristics of drift-orbit bifurcation under realistic (asymmetric) conditions. Section 3.2.2 discusses the results of test-particle guiding-center simulations in this magnetic field model, particularly focusing on the dynamics of 51 keV electrons (chosen as a reference) on bifurcated drift orbits. Section 4.3 discusses the implications of these simulations in the context of energetic electron transport near the dayside magnetopause.

3.1 Observations

During 2017-2019 ($\approx$ July–November), the orbital configuration of the THEMIS spacecraft enabled inbound crossings of the magnetopause in the afternoon sector (MLT $\in [12, 16]$) with delays of a few hours between different spacecraft. This configuration allows for the study of the formation of energetic electron flux enhancements on timescales of several hours, which is comparable to the drift period of 30–100 keV electrons [Schulz and Lanzerotti, 1974]. We visually examine the THEMIS dataset of energetic electrons to identify signatures of > 30 keV electron flux enhancements forming just inside the magnetopause between consecutive magnetopause crossings by the THEMIS spacecraft. In this chapter, we present a case study of one typical events from the identified energetic electron enhancements, while leaving a

more detailed statistical analysis of similar events for future work. We use magnetic field data provided by the Fluxgate Magnetometer (FGM) at a rate of 5 samples/s [Auster et al., 2008]. The energy fluxes of energetic electrons (> 30 keV) are measured by the Solid-State Telescope (SST) (see [Angelopoulos et al., 2008]) with 3 s cadence. The event is observed on October 1, 2018, and solar wind conditions during this interval were monitored by Probe 1 of the ARTEMIS mission (formerly THEMIS-C), which entered the solar wind on September 29. To infer the solar wind dynamic pressure, we use data from Electrostatic Analyzers (ESA), which measure electron (< 30 keV) and ion (< 25 keV) distribution functions at 4 s cadence [McFadden et al., 2008]. The Interplanetary Magnetic Field (IMF) is measured by the Fluxgate Magnetometer [Auster et al., 2008].

Figure 3.1 shows magnetopause and outer radiation belt crossings on October 1, 2018, first by THEMIS-A and three hours later by THEMIS-D. Concurrent measurements of solar wind conditions are provided by THEMIS-C. Figure 3.1a shows the trajectories of the three spacecraft projected onto the xy-plane of the Geocentric Solar Magnetospheric (GSM) coordinate system. THEMIS-A crosses the dayside magnetopause in the afternoon MLT sector (MLT ≈ 15) at 8 UT, while THEMIS-D crosses the magnetopause in the same MLT sector approximately three hours later, at 11 UT. Figures 3.1b, 3.1c, and 3.1d show THEMIS-A measurements of the magnetic field in GSM coordinates and energetic electron fluxes. THEMIS-A crosses the magnetopause at 8 UT and then transits into the outer magnetosphere at approximately 10 UT. To quantify the radial position of the spacecraft in the radiation belt, we use the TS04 magnetic field model [Tsyganenko and Sitnov, 2005] and use the L_B-parameter intruded in Chapter 2, which serves as a proxy for L-shell for near-equatorially mirroring particles (see Eq. 2.1 in Chapter 2 and discussion in [Ukhorskiy and Sitnov, 2008, McCollough et al., 2012]):

Figure 3.1d shows L_B alongside L_{IGRF} ($\approx$ the dipole L-shell) along the spacecraft trajectory. Figure 3.1c shows the omnidirectional electron energy flux in 10 energy channels from 30 keV

to $\sim$ 700 keV. We see fluxes steadily increasing inward from the magnetopause. The fluxes at 30–100 keV energies exhibit a plateau near the magnetopause ($L_B \in [7, 8]$), while fluxes of $>$ 100 keV electrons display a much steeper gradient (decay) toward the magnetopause.

Figures 3.1e, 3.1f, and 3.1g show THEMIS-D crossing the magnetopause and transitioning into the outer radiation belt approximately three hours after THEMIS-A. Figure 3.1f shows electron energy fluxes in 10 energy channels from 30 keV to $\sim$ 700 keV. Intriguingly, we observe a local maximum forming at energies 30–100 keV near $L_B = 8$, where THEMIS-A previously observed a plateau in the spatial distribution. Note that the electron fluxes within the local maximum (30–100 keV) exhibit a symmetric pitch-angle distribution, with equal fluxes of electrons moving parallel and anti-parallel to the magnetic field (not shown), indicating that these electrons are trapped and undergoing bounce motion along closed magnetic field lines.

Figures 3.1h and 3.1i show concurrent measurements in the solar wind between 08:00 UT and 16:00 UT. We use ESA-based ion moments from THEMIS-C to calculate the ion number density n_i and ion bulk velocity $\boldsymbol{v}_i$, which are used to infer the dynamic pressure as $P_{dyn} = n_i m_i \boldsymbol{v}_i^2$, where m_i is the proton mass. Figure 3.1h shows the solar wind dynamic pressure increasing from $P_{dyn} \approx 1$ nPa to $P_{dyn} \approx 4$ nPa between 10:00 UT and 14:00 UT. Figure 3.1i shows variations in the IMF in the GSM coordinate system. Several IMF B_z reversals are observed, between 11:00 UT and 13:00 UT, while there was a strong B_y component. Intervals of southward IMF ($B_z < 0$) occur before 11:00 UT and after 12:50 UT. The steady increase in dynamic pressure, combined with a significant IMF B_y component, provides ideal conditions for asymmetric drift-orbit bifurcation at outer drift orbits.

3.2 Simulations

3.2.1 Magnetic Field Model

Drift-orbit bifurcation arises from the compression of dayside magnetic field lines, leading to the violation of a particle's second adiabatic invariant. This results in the opening of the drift orbits, enabling radial transport. To simulate electron transport associated with drift-orbit bifurcation, we use an *ad hoc* magnetic field model that effectively emulates the effects of a solar wind compression. We formally separate the magnetic field into the 'internal' (associated with the dipole), $\boldsymbol{B}_{int}$, and 'external', $\boldsymbol{B}_{ext}$ (representing the field produced by the external current systems and IMF). For the internal magnetic field, we use a tilted dipole

$$\boldsymbol{B}_{\text{int}} = \frac{3\boldsymbol{r}(\boldsymbol{m}\cdot r) - \boldsymbol{m}r^2}{r^5} \tag{3.1}$$

Here, $\boldsymbol{r} = x\hat{\boldsymbol{x}} + y\hat{\boldsymbol{y}} + z\hat{\boldsymbol{z}}$ and $\boldsymbol{m} = -B_0 R_E^3(\cos\theta\ \hat{\boldsymbol{z}} + \sin\theta\ \hat{\boldsymbol{x}})$ where θ is the dipole tilt angle, and $\boldsymbol{r}$ is in units of R_E, Earth's radius. The origin of the coordinate system is at Earth's center; the $\hat{\boldsymbol{x}}$-axis points toward the Sun, the $\hat{\boldsymbol{z}}$-axis lies in the plain defined by $\hat{\boldsymbol{x}}$ and $\boldsymbol{m}$, i.e., $\hat{\boldsymbol{z}} = \hat{\boldsymbol{x}}\times(\hat{\boldsymbol{x}}\times\boldsymbol{m})/m$, and $\hat{\boldsymbol{y}} = \hat{\boldsymbol{z}}\times\hat{\boldsymbol{x}}$ completes the right-handed triad. To model asymmetric bifurcation, the external magnetic field, $\boldsymbol{B}_{\text{ext}}$, is introduced via Euler potentials

$$\boldsymbol{B}_{\text{ext}} = \boldsymbol{\nabla}\alpha \times \boldsymbol{\nabla}\beta \tag{3.2}$$

Here, $\boldsymbol{\nabla} = \hat{\boldsymbol{x}}\partial/\partial x + \hat{\boldsymbol{y}}\partial/\partial y + \hat{\boldsymbol{z}}\partial/\partial z$, and α and β are the Euler potentials, given as

$$\alpha(x', z') = b_0 \frac{x'^2}{(x'^2 + z'^2)^{3/2}}, \quad \beta(y') = y' \tag{3.3}$$

Here, $b_0 = 651\ \text{nT}\cdot\text{R}_\text{E}^2$, and the prime symbol indicates a coordinate system shifted by a distance D along the x-axis and rotated by an angle ϕ in the yz-plane (see Fig. 3.2a)

$$\begin{cases} x' = x - D \\ y' = y\cos\phi - z\sin\phi \\ z' = z\cos\phi + y\sin\phi \end{cases} \tag{3.4}$$

The magnetic field model given by Eqs. 3.1-3.4 allows reproducing the effects of solar wind compression via the D parameter while the asymmetry effects associated with the IMF B_y are reproduced with a non-zero ϕ-angle. We note that a similar model has previously been employed in modeling drift-echo events in [Luo et al., 2024].

Fig. 3.2 shows the magnetic field, $\boldsymbol{B}_{\text{int}} + \boldsymbol{B}_{\text{ext}}$, of the model. Fig. 3.2a shows the magnetic field lines of $\boldsymbol{B}_{\text{int}}$ and $\boldsymbol{B}_{\text{ext}}$. Note that for $\phi = 0$, the external magnetic field lines are in xz plane, while $\phi \neq 0$ introduces a nonzero B_y-component, simulating the effects of IMF B_y. We use $\phi = 4°$, $D = 12\text{R}_\text{E}$, and a dipole tilt angle of $\theta = 1°$ to reproduce the configuration of the dayside magnetic field derived from the TS04 model under solar wind conditions on 1 October 2018 (specifically at 12:40 UT, see Fig. 3.1). Fig. 3.2b shows the magnetic field lines of $\boldsymbol{B}_{\text{int}} + \boldsymbol{B}_{\text{ext}}$ in the meridional projection at $y = 0$. On the nightside, standard dipole field lines with a single equatorial minimum are preserved, while on the dayside, the magnetic field lines appear compressed, with a local maximum of the magnetic field strength emerging at the equator. Figs. 3.2e and 3.2f show the profiles of the magnetic field strength along the field line at midnight and local noon, respectively. The formation of a local maximum and two asymmetric minima is clearly observed. In Chapters 1-2 we saw that the key factor determining jumps in the second adiabatic invariant and radial transport during asymmetric drift-orbit bifurcation suggests is the total phase area enclosed by the separatrix along the drift orbit in $(s, p_{||})$ space. Its MLT-dependence is given by $S(MLT) = \oint \sqrt{1 - B(s)/B_{\text{max}}} ds$, where B_{max} is the local (equatorial) maximum of the magnetic field strength, and the integration is performed between the mirror points, $s^*_{1,2}$, satisfying $B(s^*_{1,2}) = B_{\text{max}}$ (e.g., see Fig. 3.2f and Chapter 2). Figures 3.2c and 3.2d show that the model effectively reproduces the $S(MLT)$

profile and can thus be used to realistically model asymmetric drift-orbit bifurcation, as observed in the empirical TS04 magnetic field model (see Chapter 2).

3.2.2 Guiding Center Test-Particle Simulations

The magnetic field model (Eqs. 3.1-3.3) enables the study of the bifurcation-driven electron transport while allowing easy variation of the bifurcation parameters (D and ϕ) to model different solar wind conditions. The bifurcation violates the conservation of the second adiabatic invariant, whereas the first adiabatic invariant, μ, remains constant. This allows modeling electron dynamics using the guiding-center approximation [Northrop, 1963]. The relativistic Hamiltonian guiding center equations of motion, which, under appropriate conditions, conserve energy and adiabatic invariants, are given in Section 1.2.4 as

$$\begin{aligned} \frac{dp_{||}}{dt} &= q\frac{\boldsymbol{E}^* \cdot \boldsymbol{B}^*}{B^*_{||}} \\ \frac{d\boldsymbol{r}}{dt} &= \frac{p_{||}}{\gamma m}\frac{\boldsymbol{B}^*}{B^*_{||}} + c\frac{\boldsymbol{E}^* \times \hat{\boldsymbol{b}}}{B^*_{||}} \end{aligned} \tag{3.5}$$

Here, $\boldsymbol{r}$ is the position of the guiding center, $q = -e$ is electron charge, $\gamma(\boldsymbol{r}, p_{||}, t) = \sqrt{1 + 2\mu B(\boldsymbol{r}, t)/(mc^2) + (p_{||}/mc)^2}$ is the relativistic gamma factor, the subscript '||' denotes the direction parallel to $\hat{\boldsymbol{b}} = \boldsymbol{B}/B$, and $\boldsymbol{E}^*$ and $\boldsymbol{B}^*$ represent the 'effective' electric and magnetic fields, $\boldsymbol{E}^* = \boldsymbol{E} - \left(mc^2\boldsymbol{\nabla}\gamma - p_{||}\partial\hat{\boldsymbol{b}}/\partial t\right)/q$ and $\boldsymbol{B}^* = \boldsymbol{B} + (cp_{||}/q)\boldsymbol{\nabla} \times \hat{\boldsymbol{b}}$

Figure 3.3 shows three representative guiding-center trajectories described by Eqs. 3.5 that undergo bifurcation. For visualization purposes, we used three particles of the same energy, 3 MeV, launched from the nightside at $x = -9$ but with three different values of the adiabatic invariant I. The magnetic field configuration is identical to that shown in Fig. 3.2. Interestingly, we observe the same three types of trajectories previously seen in Chapter 1, Fig. 2.6. Due to the asymmetry, particles: (a) undergo a single capture inside the adjacent pocket without subsequent release (Fig. 3.3a), which results in *inward* transport (compare to

Fig. 2.6a); (b) undergo a single release if their I is small so that they are initially trapped in the main pocket (Fig. 3.3b), in which case they are transported *outward* (compare to Fig. 2.6b); and (c) undergo a generic double asymmetric jump (Fig. 3.3c), which can result in both outward and inward transport (compare to Fig. 2.6c).

To assess the role of the bifurcation-driven radial transport, we perform test-particle simulations using Eq. 3.5 in the magnetic field given by $\boldsymbol{B}(\boldsymbol{r},t) = \boldsymbol{B}_{\text{int}}(\boldsymbol{r}) + \boldsymbol{B}_{\text{ext}}(\boldsymbol{r},t)$. We use a time-dependent external field to simulate a slow increase in dynamic pressure via $D(t) = 22\text{R}_\text{E} - 10\text{R}_\text{E}\cdot\tanh(t/\tau)$ and an increase in east-west asymmetry via $\phi(t) = 4^\circ\cdot\tanh(t/\tau)$ with $\tau = 1$ hour. The initial magnetic field configuration represents a symmetric non-bifurcated state (at $L_B < 10$), while the final state is bifurcated and asymmetric as shown in Fig. 3.2. Although there are indications that electric fields may play an important role in drift-orbit bifurcation [Desai et al., 2021], we limit our analysis to $\boldsymbol{E} = 0$. We note that under a time-dependent magnetic field, Eqs. 3.5 no longer conserve the total energy (γ) even for $\boldsymbol{E} = 0$. However, because variations in $\boldsymbol{B}$ are slow, we find that in our simulation, variations in γ do not exceed a few percent.

Figure 3.4 presents the results of test-particle simulations for an ensemble of 35,000 electrons with 51 keV energy ($\gamma = 1.1$) and an equatorial pitch angle of 85°, randomly distributed in drift and bounce phases. The initial radial distribution in L_B fits that observed by THEMIS-A (Fig. 3.1c), with a maximum at $L_B = 5$ and a plateau over $L_B \in [7, 8]$. Figure 3.4a shows the time dependence of the external field, quantified in terms of the ϕ angle and the first bifurcated orbit (L_B at which bifurcation occurs first). Initially, all drift orbits below $L_B = 10$ are not bifurcated. However, as D decreases, the range of bifurcated orbits shifts inward to $L_B \approx 6.5$, consistent with TS04 results under a solar wind dynamic pressure of 3 nPa. Figure 3.4b shows the initial distribution of electron equatorial foot points in the xy-plane, which is symmetric in MLT and decays radially outward. Figure 3.1c shows the equatorial foot points 4.5 hours into the simulation, after the electrons undergone asymmetric

drift-orbit bifurcation. A distinct 'ring' structure forms – a local maximum at larger radial distances trailing counterclockwise from the afternoon sector. Figures 3.4d and 3.4e clearly show that the distribution develops a local maximum at $L_B \in [8, 9]$ after 4 hours of simulation while before the onset of bifurcation, i.e., for times < 1 hour, the distribution remained stationary. Examination of individual electron trajectories shows that this local maximum is formed by electrons that experience several consecutive outward radial jumps due to the drift-orbit bifurcation, similar to the one shown in Fig. 3.3b. The exact radial position of this local maximum is dictated by the interplay between outward radial transport from $L_B \lesssim 7$–8 and particle losses from $L_B > 9$ via transport onto partially 'open' field lines (i.e., those connected to B_{ext}, see Fig. 3.2a). In our simulation, we find that up to $10\% - 30\%$ of electrons initially located at $L_B > 9$ are lost by the end of the simulation (5 hours). Loss is recorded when a particle reaches $L_B \geq 18$ (i.e., $B_{\text{min}} \leq 5$ nT) within at MLT $\in [6, 18]$. This indicates that drift-orbit bifurcation can also contribute to particle leakage through the dayside magnetopause.

We note that the time-dependent magnetic field has been chosen primarily for visualization purposes and for the convenience of initializing the electron ensemble in a non-bifurcated state. Fig. 3.5 shows that the formation of an isolated maximum is also reproduced when the same ensemble is initialized in the stationary but already bifurcated field (tested for $D = 12\text{R}_\text{E}$ and $\phi = 4°$. In a non-bifurcated state, any initial distribution in L_B remains stationary on timescales of simulation (≈ 6 hr for 51 keV electrons). Lastly, we note that using electrons of any energy in the range $[30, 100]$ keV results in the same radial transport and also leads to peak formation. This is due to the nature of the asymmetric drift-orbit bifurcation mechanism, in which the jump in the second adiabatic invariant—and the associated radial transport per drift period—does not depend on particle energy. This is clearly visible in Fig. 3.6. While the drift period decreases with increasing energy, electrons of different energies undergo the same radial transport, with higher-energy electrons completing it more quickly in accordance with their shorter drift periods. Thus, the presented simulation results for 51

keV electrons are representative of the general dynamics across the entire energy range of interest ($[30, 100]$ keV). This energy scaling remains valid until the electron energy is below a few MeVs, where energy-dependent effects—arising from the finite bounce-to-drift period ratio—introduce an additional source of violation of the second adiabatic invariant

3.3 Discussion and Summary

The origin of energetic (> 30 keV) electron enhancements near the magnetopause is a long-standing question in magnetospheric physics [Meng and Anderson, 1970, Walsh et al., 2012, Dunlop et al., 2008]. Using THEMIS spacecraft data from an inbound crossing on October 1, 2018, we observe the formation of such an enhancement in $30 - 100$ keV electron fluxes within a few hours. This is comparable to the timescale of these electrons' drift periods. Simultaneous solar wind observations by the ARTEMIS mission suggest that magnetospheric conditions were favorable for drift-orbit bifurcation under asymmetric IMF. Thus, in this chapter we relate the origin of observed enhancement of electron fluxes to outward radial transport via the drift-orbit bifurcation mechanism. A model magnetic field reproducing key bifurcation features, particularly its north-south and east-west asymmetric structure that enables fast radial transport, is used in test particle simulations, demonstrating that (asymmetric) drift-orbit bifurcation leads to the formation of a localized maximum in the radial distribution of 51 keV electrons, which is representative of the general dynamics of electrons in the entire $30 - 100$ keV energy range.

We note that due to the spacecraft's orbital configuration, the electron flux enhancement is observed near the equatorial plane. Specifically, THEMIS-D observed the electron energy flux enhancement at $L \approx 8$ and MLT $\gtrsim 15.4$, based on the TS04 model. Interestingly, TS04 also indicates that this MLT sector corresponds to the region where bifurcation ceases—the 'main pocket' disappears, and all electrons are released from it. Therefore, the drift orbit bifurcation framework is consistent with the observation of recently released electrons near the equatorial

plane. However, we also note that the electron population associated with this enhancement is largely isotropic (not shown), suggesting that some pitch-angle scattering process must have taken place. Electron pitch-angle scattering at larger radial distances is often attributed to magnetic field curvature effects (e.g., [Birmingham, 1984, Büchner and Zelenyi, 1989]). In regions of weak magnetic field strength and high field-line curvature, rapid scattering leads to electron isotropization along the field line. The most plausible scenario involves electron drift into the nightside region (after their transport to $L \geq 8$ on the dayside via drift orbit bifurcation), where magnetic field lines are highly stretched and curvature-driven scattering becomes effective. As a result, after a completing the drift period they return to the dayside fully isotropic. Observations support this scenario, showing that electrons with energies > 50 keV are typically isotropic at $L \geq 8$ on the nightside [Wilkins et al., 2023, Artemyev et al., 2024]. Although the observations of isotropic pitch-angle distribution does not exclude magnetopause shadowing or magnetic reconnection as possible mechanisms behind the observed isolated electron flux enhancement, we note that classical radial diffusion driven by magnetopause shadowing typically does not produce localized spatial features such as the flux peak shown in Fig. 3.1f (e.g., see Fig. 3 in [Turner et al., 2012]). However, THEMIS-D observations alone do not allow us to rule out temporal variations in the magnetopause location (driven by the IMF B_z reversal) that may have contributed to the observed depletion of energy flux near THEMIS-D after 13:00 UT. A future detailed statistical analysis, supported by global simulations (e.g., [Sorathia et al., 2017, Sorathia et al., 2018]), is needed to assess the relative importance of radial transport versus temporal changes in the magnetopause location in producing energetic electron flux enhancements.

While this chapter primarily focuses on electron radial transport driven by the drift-orbit bifurcation in a slowly varying (essentially quasi-static; see Fig. 3.5) magnetic field configuration, short-term ($\sim$ minutes) variations in solar wind conditions and diurnal variation of the Earth's dipole tilt angle can also contribute to electron transport via the same mechanism. Although inclusion of such transient variations represents a necessary next step

for a more rigorous evaluation of the role of drift-orbit bifurcation in radial transport, the results shown in this chapter are highly indicative of its significance in driving radiation belt electrons toward the magnetopause—a process previously considered mainly in the context of ULF-driven radial diffusion. These findings have important implications for modeling energetic electron transport in the outer radiation belt and electron losses via leakage through the magnetopause.

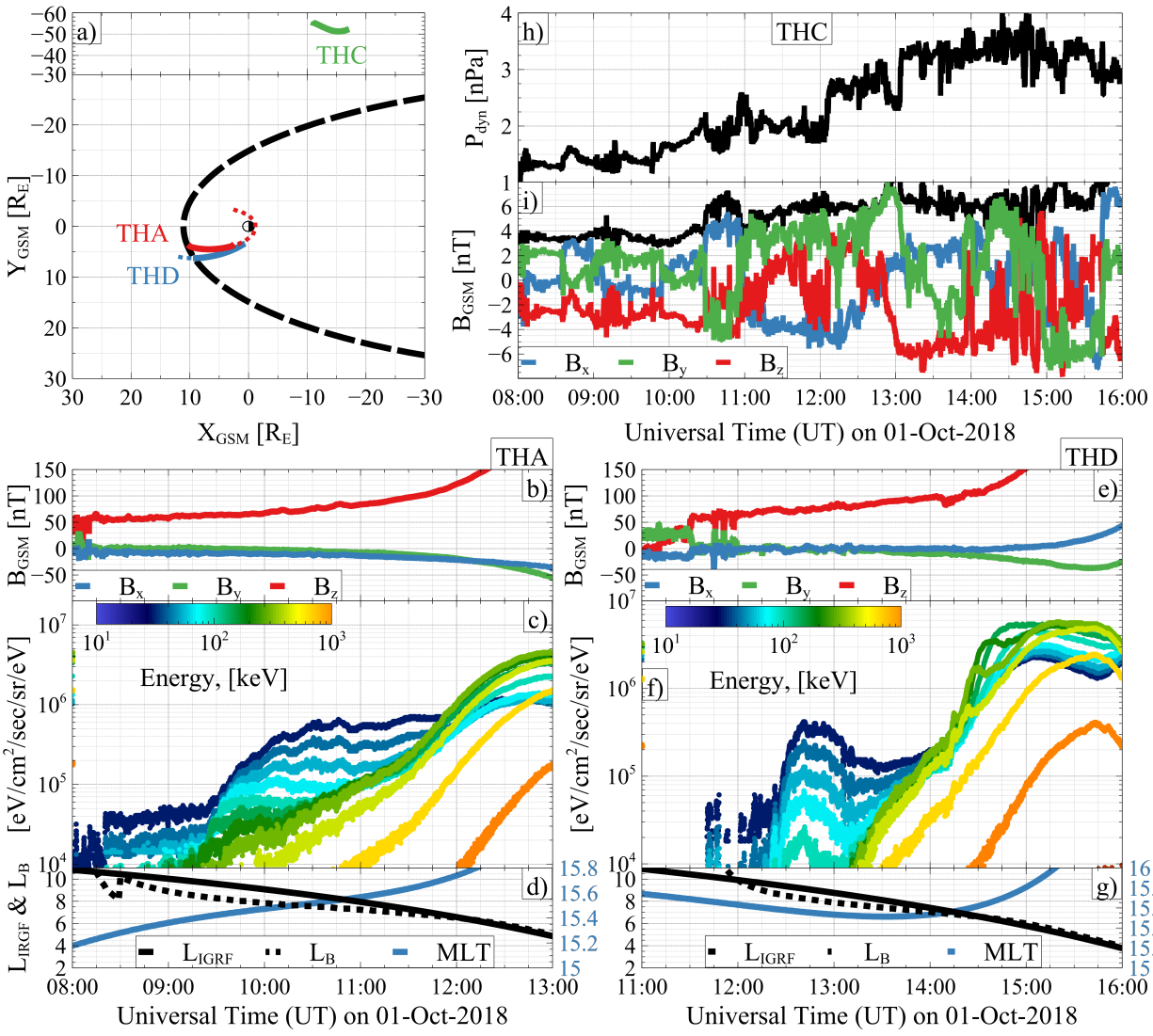

Figure 3.1: Crossings of the dayside magnetopause and the outer radiation belt by THEMIS-A and THEMIS-D spacecraft on October 1, 2018, from 8 to 16 UT. Concurrent measurements of the solar wind conditions are provided by THEMIS-C of the ARTEMIS mission. (a) Spacecraft trajectories in the GSM xy-plane. (b) Magnetic field in the GSM system of coordinates measured by THEMIS-A. (c) SST-based omnidirectional electron fluxes measured by THEMIS-A, energy channels from 30 keV to $\sim$ 700 keV. (d) spacecraft position in terms of MLT-sector, L_B (see Eq. 2.1), and L_{IGRF} ($\approx$ dipole L-shell) parameters. (e,f,g) Data in the same format obtained by THEMIS-D. (h) Solar wind dynamic pressure. (i) Interplanetary Magnetic Field in the GSM system.

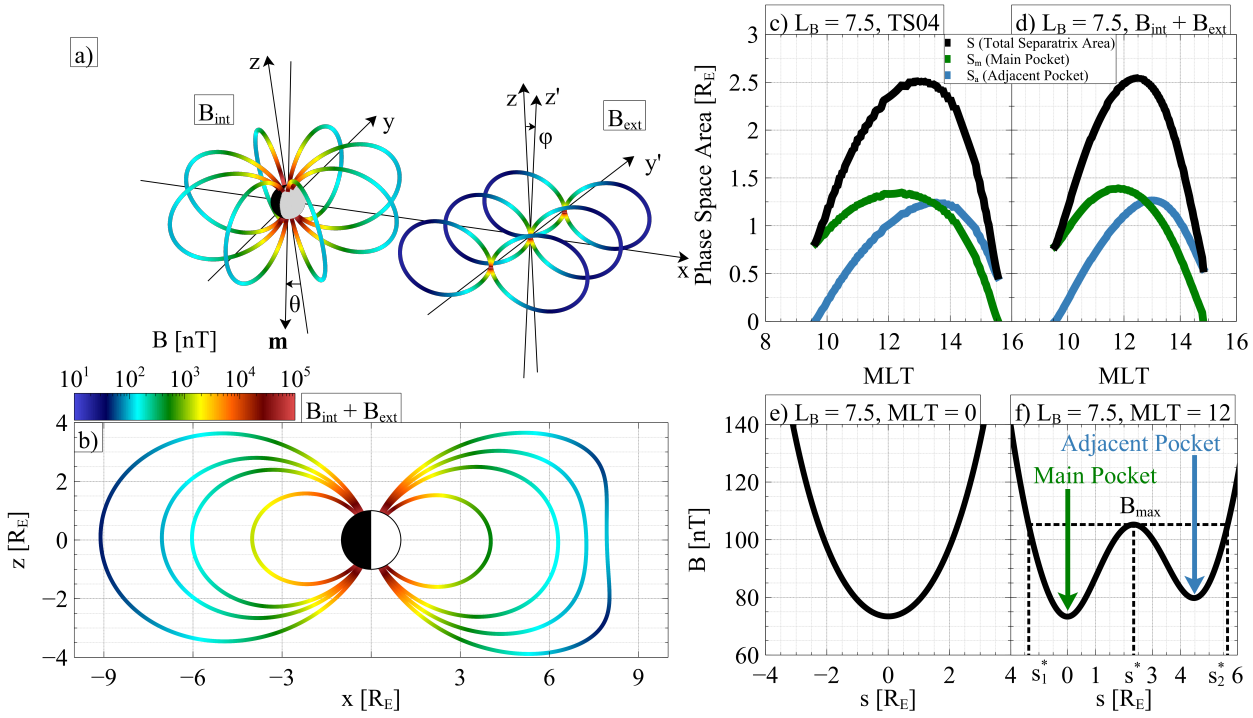

Figure 3.2: The magnetic field model, $\boldsymbol{B} = \boldsymbol{B}_{\text{int}} + \boldsymbol{B}_{\text{ext}}$. (a) Magnetic field lines of $\boldsymbol{B}_{\text{int}}$ (with $\theta = 1°$, Eq. 3.1) and $\boldsymbol{B}_{\text{ext}}$ (with $D = 12\text{R}_\text{E}$ and $\phi = 4°$, Eqs. 3.2-3.3). Color indicates the magnetic field strength in nT. (b) Magnetic field lines of $\boldsymbol{B}_{\text{int}} + \boldsymbol{B}_{\text{ext}}$ in the $y = 0$ plane, with color indicating the field strength in nT. MLT profiles of the phase space areas enclosed within the separatrix, $S = 2\int_{s_1^*}^{s_2^*} \sqrt{1 - B(s)/B_{\text{max}}} ds$, along the drift orbit with $L_B = 7.5$ (see Chapter 2): (c) using the TS04 [Tsyganenko and Sitnov, 2005] magnetic field with $P_{dyn} = 2.55$ nPa, IMF $B_z = 1.6$ nT, and $B_y = 5.1$ nT, reflecting the solar wind conditions at 12:31 UT; (d) model-based magnetic field. Magnetic field strength profile along the field line at (e) MLT = 0, (f) MLT = 12. Here, $s = 0$ is the position of the equatorially mirroring particle, $B_{\text{max}} = B(s^*)$ is the local maximum of the magnetic field strength, and $s^*_{1,2}$ satisfy $B(s_{1,2}) = B_{\text{max}}$.

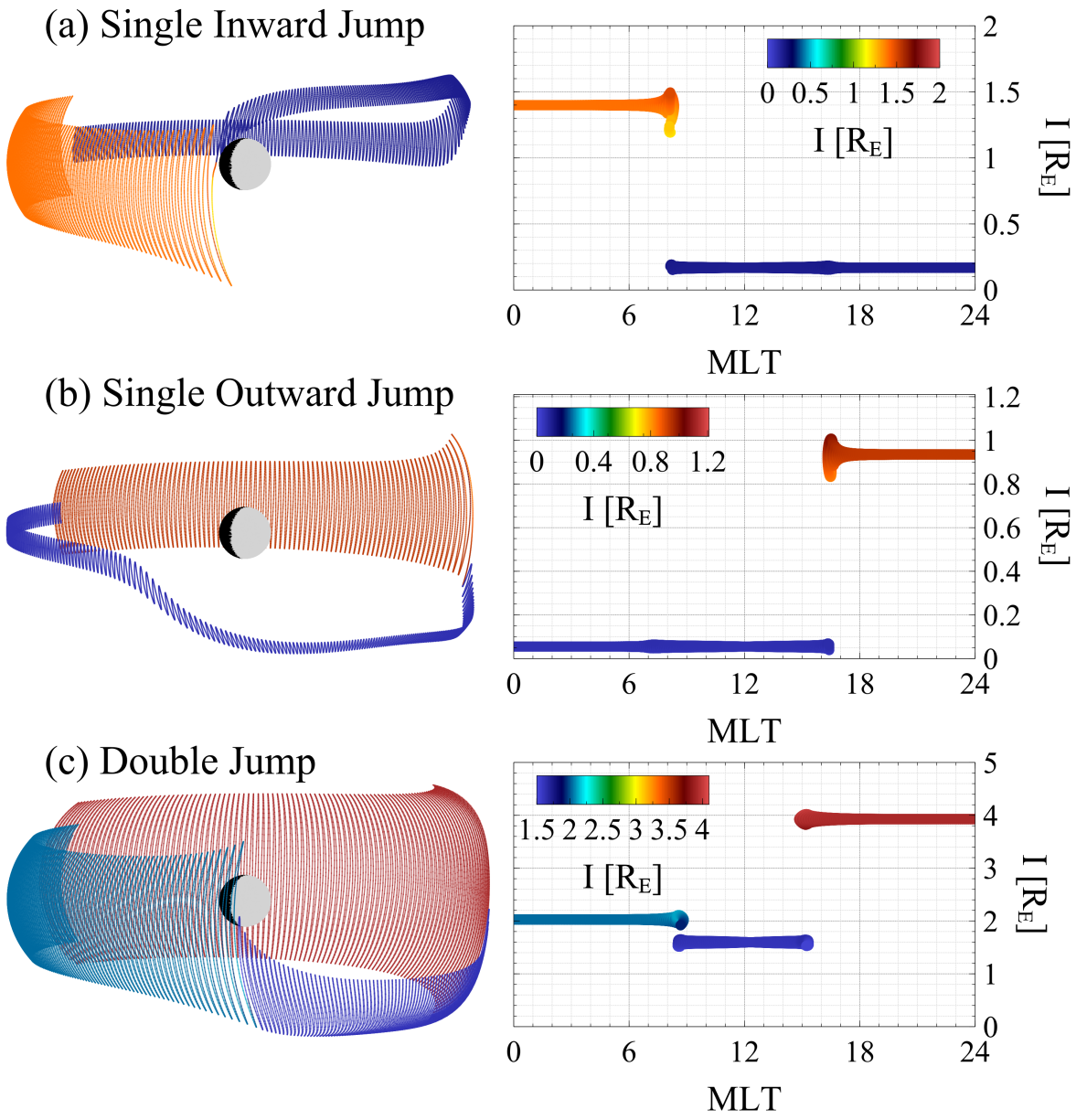

Figure 3.3: Three types of bifurcated trajectories calculated with Eqs. 3.5 in the magnetic field model $\boldsymbol{B} = \boldsymbol{B}_{\text{int}} + \boldsymbol{B}_{\text{ext}}$ with parameters from Fig. 3.2. The left column shows the guiding-center trajectory in three dimensions (Earth in the center; the dayside is shown in grey), while the right column shows the evolution of the second adiabatic invariant, $I = \oint \sqrt{1 - B(s)/B_m} ds$. In both columns, color indicates the value of I. Note the remarkable similarity to Fig. 2.6 from Chapter 2, obtained using the mapping in the [Tsyganenko and Sitnov, 2005] model.

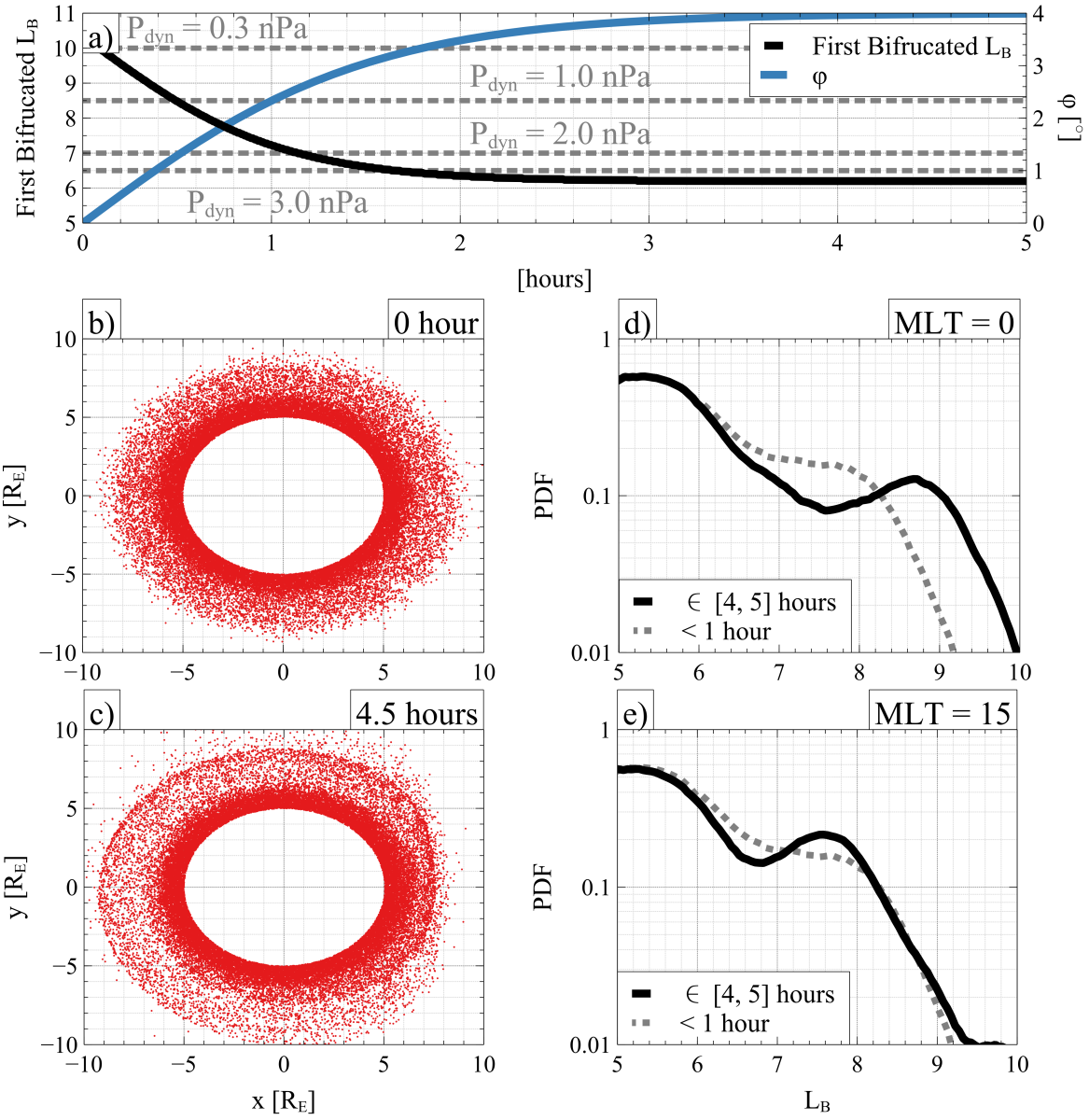

Figure 3.4: Simulation of electron transport driven by asymmetric drift-orbit bifurcation. An ensemble of $\approx 35,000$ electrons (energy: 51 keV) is used. The magnetic field is given by $\boldsymbol{B}(\boldsymbol{r},t) = \boldsymbol{B}_{\text{int}}(\boldsymbol{r}) + \boldsymbol{B}_{\text{ext}}(\boldsymbol{r},t)$, with $\phi(t) = 4^\circ \cdot \tanh(t/\tau)$ and $D(t) = 22\text{R}_\text{E} - 10\text{R}_\text{E} \cdot \tanh(t/\tau)$ with $\tau = 1$ hour (see Eqs. 3.1-3.4). (a) Change of ϕ-angle (blue) and the first bifurcated drift orbit over time. (b) Distribution of electron equatorial foot points at $t = 0$. (c) Distribution of electron equatorial foot points at $t = 4.5$ hours. (d) Radial distribution (in L_B) of electron crossings in the MLT = 0 sector. (e) Radial distribution of electron crossings in the MLT = 15 sector. The gray line shows the result accumulated at $t < 1$ hour, while the black line represents the accumulation at $t \in [4, 5]$ hours.

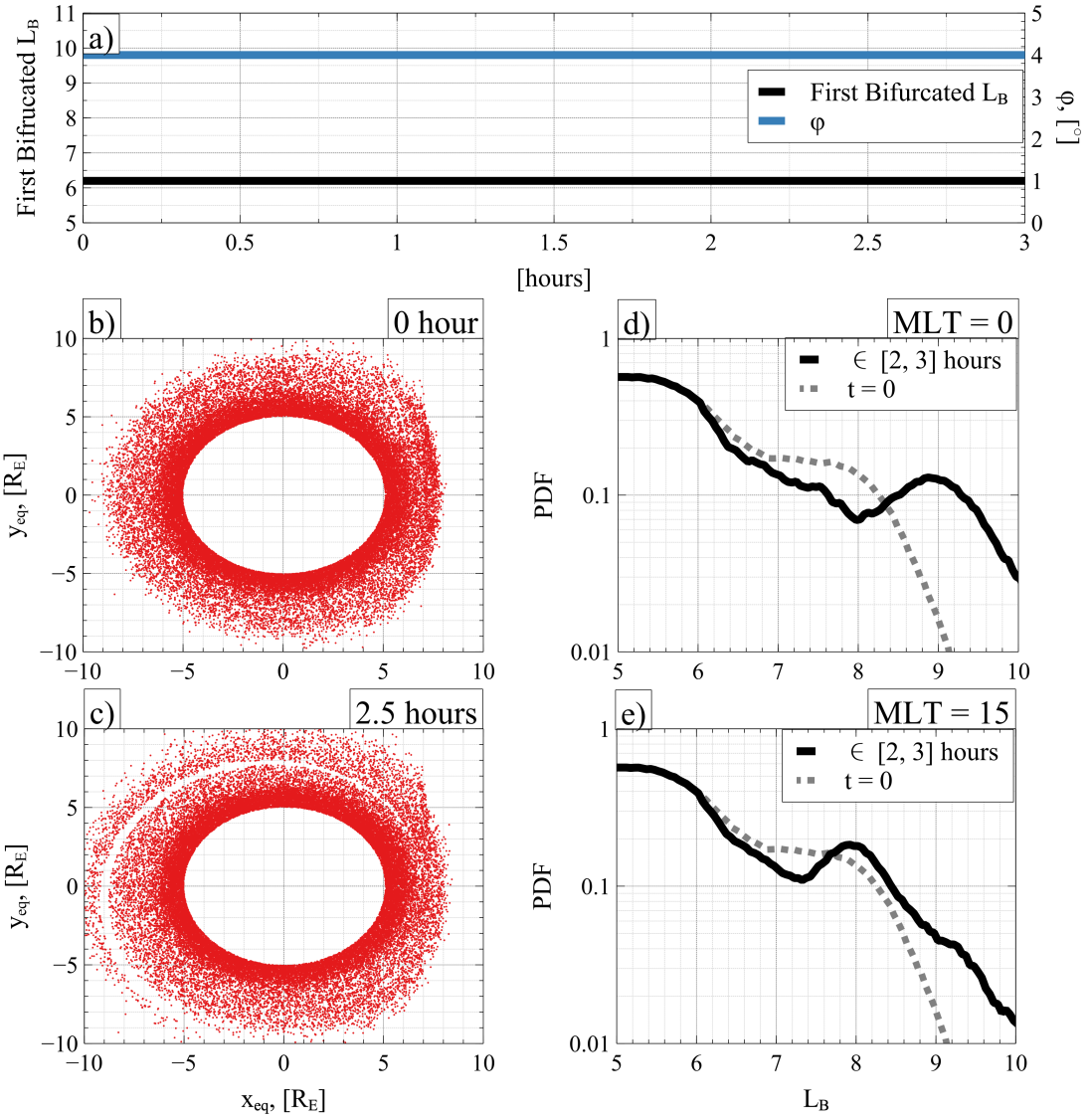

Figure 3.5: Radial transport of electrons driven by asymmetric drift-orbit bifurcation in a *static* magnetic magnetic field configuration identical to the final ($t \gg 1$ hour) configuration from Fig. 3.4: the ensemble setting: 35,000 nearly equatorially mirroring electrons (initial equatorial pitch-angle is 85° with energy of 51 keV). The magnetic field is given by $\boldsymbol{B}(\boldsymbol{r}) = \boldsymbol{B}_{\text{int}}(\boldsymbol{r}) + \boldsymbol{B}_{\text{ext}}(\boldsymbol{r})$, with $\phi = 4°$ and $D = 12\text{R}_\text{E}$. (a) ϕ-angle (blue) and the first bifurcated drift orbit. (b) Distribution of electron equatorial foot points at $t = 0$. (c) Distribution of electron equatorial foot points at $t = 2.5$ hr. (d) Radial distribution (in L_B) of electron crossings in the MLT $= 0$ sector. (e) Radial distribution of electron crossings in the MLT $= 15$ sector. The gray line shows the initial distribution, while the black line represents the accumulation of particle crossing the respective MLT-sector at $t \in [2, 3]$ hr.

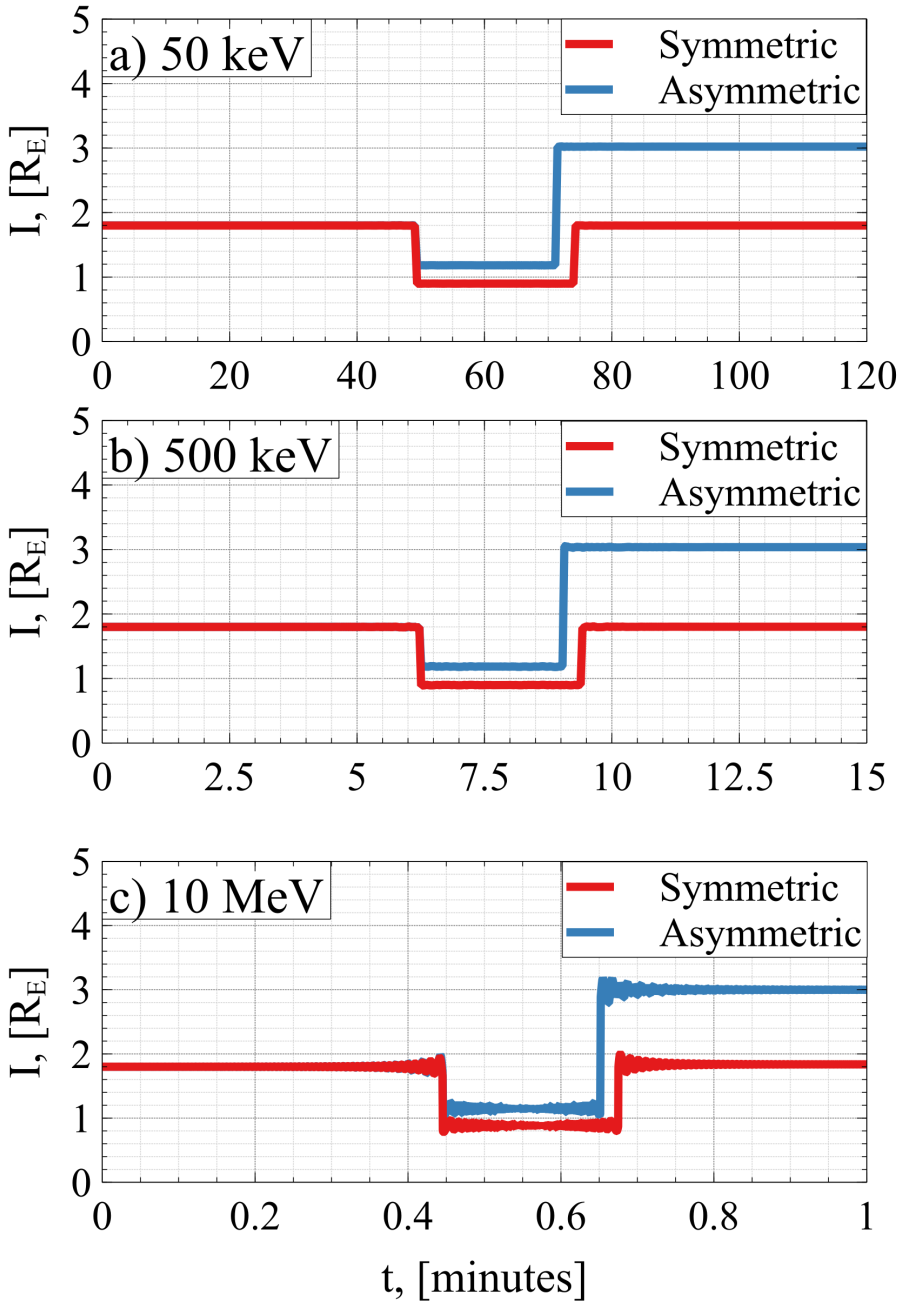

Figure 3.6: Evolution of the (normalized) second adiabatic invariant, $I = \oint \sqrt{1 - B(s)/B_m} ds$, during one complete drift period for particles of three different energies: 50, 500, and 10,000 keV. Results are shown for an East–West symmetric magnetic field configuration (red lines: $\theta = 0°$, $\phi = 0°$) and an East–West asymmetric configuration (blue lines: $\theta = 0°$, $\phi = 2°$). All particles are initialized at midnight at the radial distances of $L_B = 7.5$.

CHAPTER 4

Long-Term Dynamics and Non-Diffusive Radial Transport Driven by Geometric Jumps

The cross-field transport of charged particles in strong magnetic fields has historically been one of the central problems of plasma physics. This process is fundamental to both laboratory and space plasmas. Understanding the radial transport of energetic electrons in Earth's radiation belts is vital for describing the variability of the radiation belts' configuration [Mann et al., 2013, Ukhorskiy et al., 2014b] and electron acceleration to ultra-relativistic energies [O'Brien et al., 2003, Su et al., 2015]. As was discussed in Chapter 1, radial transport requires the violation of adiabaticity. Interaction with Ultra-Low-Frequency (ULF) waves usually results in slow radial diffusion (see in Eq. 1.72 in Chapter 1). However, recent studies have shown that radiation belts often exhibit non-diffusive dynamics that conventional diffusion-based models cannot reproduce (see discussion in [Shprits et al., 2015, Osmane et al., 2023, Lejosne et al., 2024]). This necessitates incorporating electron radial drift term (see discussion in [Shprits et al., 2015, Camporeale et al., 2022, Li and Hudson, 2019]) or unconventional off-diagonal components in the diffusion tensor [Zheng et al., 2016]. This drives the search for non-diffusive mechanisms that violate adiabaticity. In this context, the Drift-orbit bifurcation mechanism has recently been revisited using new empirical models of the Earth's magnetic field and realistic solar wind parameters. Variations in the orientation of the Interplanetary Magnetic Field (IMF) and seasonal changes in Earth's dipole tilt angle result in the global asymmetry in Earth's magnetic field, enhancing the effect of Drift-orbit

bifurcation and leading to non-diffusive transport, as demonstrated in Chapter 3. However, the exact implications of this asymmetry on the long-term evolution and radial transport of energetic electrons are not yet understood. In this chapter we aim to explain and quantify fast electron transport driven by the geometric jumps resulting from this asymmetry. Using a Hamiltonian model capturing the destruction of the adiabatic invariant, we show that asymmetry induces geometric responsible for such transport.

4.1 Model

4.1.1 Hamiltonian with $1\frac{1}{2}$ degrees of freedom

Drift-orbit bifurcation destroys adiabaticity of the particle bounce motion while still conserving μ. As such, particle motion along the field lines is described by the following Hamiltonian (see Eq. 1.22)

$$H(s, p_{||}; \varphi) = \frac{p_{||}^2}{2m} + \mu B(s, \varphi) \tag{4.1}$$

Here, $B(s, \varphi)$ is the magnetic field strength along the field line, $\varphi \in [0, 2\pi]$ denotes the particle's azimuthal location along the drift orbit [e.g., midnight ($\varphi = 0$) versus noon ($\varphi = \pi$), Fig. 1.7]. From Eq. 4.1, $\mu B(s, \varphi)$ is the effective potential for the $(s, p_{||})$ variables. $B(s, \varphi)$ slowly changes as a particle drifts around Earth [with $\dot{\varphi} \ll 1$; see Fig. 1.7]. This introduces the notion of "fast" variables $(s, p_{||})$ and a "slow" variable, φ. Accordingly, $H(s, p_{||}; \varphi)$ is often referred to as a "slow-fast" Hamiltonian system. Earth's magnetic field lines on the night side resemble a (stretched) dipole, featuring a single minimum of $B(s)$ near the magnetic equator, where electrons bounce along the field lines with a typical period of τ_b ($\sim$ seconds). This oscillatory motion defines an adiabatic invariant, $I = \oint p_{||} ds$, which is the area enclosed by the electron's orbit in the $(s, p_{||})$ space [see Fig. 1.7]. As an electron slowly drifts from the night side, I oscillates around a constant with an amplitude of $\varepsilon \ll 1$ (or smaller, for the improved invariant I, see Section. 1.3.1), where $\varepsilon = \tau_b/\tau_d$ is the ratio of the fast bounce motion period

($\tau_b \sim$ seconds) to the slow drift motion period ($\tau_d \sim$ minutes to hours). Conservation of I breaks down as the electron approaches the dayside, where field lines are compressed by the solar wind, resulting in a $B(s)$ profile with an equatorial maximum separating two local minima on either side of the equator [Fig. 1.7]. This leads to the formation of a separatrix in phase-space (s, $p_\parallel$), demarcating trajectories of particles trapped in two minima. As a particle crosses the separatrix, it becomes trapped in one minimum and is released while drifting back to the night side. Each crossing results in a jump in the adiabatic invariant (trapping and de-trapping yield two jumps), reflecting the loss and recovery of the phase area of a phase pocket. The resultant net jump in I comprises two distinct contributions [Neishtadt, 1986, Cary et al., 1986].

$$\Delta I = \Delta S(I) + \Delta I_{\rm st}(I, \theta, \varepsilon) \tag{4.2}$$

Here, ΔS is the geometric jump given by the difference in the phase-space area enclosed by the separatrix between the moments of trapping and de-trapping (see Section 1.3.2 and [Neishtadt, 2019]). For the separatrix which is Dawn-Dusk symmetric with respect to the local noon (invariant under $\varphi \to -\varphi$ transformation), one always has $\Delta S = 0$. The second term in Eq. 4.2, $\Delta I_{\rm st}(I, \theta, \varepsilon)$ - the *stochastic (dynamical) jump* (see Section 1.3.2), represents the first correction in ε due to adiabaticity violations near the separatrix (see discussion in Section 1.3.2 and [Neishtadt, 1986, Cary et al., 1986]). This jump depends on both the initial value of I and the bounce phase θ. Averaging over θ in the symmetric case yields diffusive behavior with $\langle \Delta I_{\rm st} \rangle_\theta = 0$ and $\langle \Delta I_{\rm st}^2 \rangle_\theta \propto \varepsilon^2$ for sufficiently large I. Asymmetry introduces a non-zero drift term, $\langle \Delta I_{\rm st} \rangle_\theta \propto \varepsilon$. For small I, the evolution is also dominated by ballistic stochastic jumps with $\langle \Delta I_{\rm st} \rangle_\theta \propto \varepsilon$. When $\Delta I_{\rm st}$ dominates over ΔS, the standard (symmetric) drift-orbit bifurcation dynamics are recovered, which have been widely studied both numerically and theoretically [Öztürk and Wolf, 2007, Ukhorskiy et al., 2011]. In the opposite limit of $\varepsilon \to 0$, in which $\Delta I_{\rm st} \to 0$, the dynamics are dominated by geometric jumps because $\Delta S = O(1)$ (see

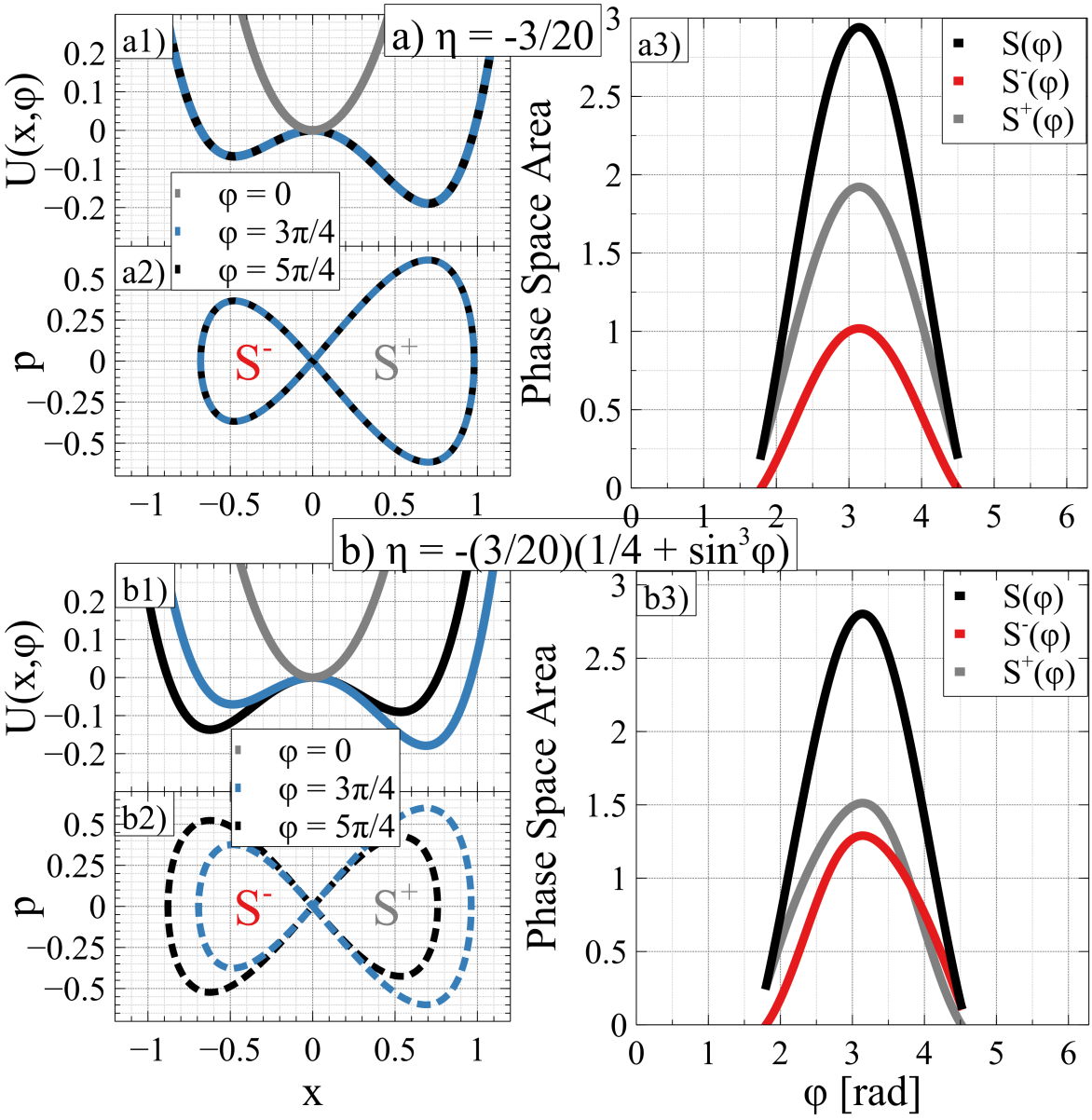

Figure 4.1: Hamiltonian (4.1.2) for (a) $\eta = -3/20$ and (b) $\eta = -(3/20)(1/4 + \sin^3\varphi)$. Panels: (1) potential $U(x, \varphi)$ at different φ, (2) separatrix in the phase-space of (x, p), (3) phase-space areas enclosed within two pockets [$S^{\pm}$, Eq. 4.4] and within the separatrix (S).

Section 1.3.2 and [Neishtadt, 2019]). In this regime the effects of magnetic field *asymmetry* dominate over those of a *finite* ε. Order-of-magnitude estimates indicate this applies to $\lesssim 10$ MeV electrons in the Earth's magnetic field. However, this regime remains largely overlooked in radiation belt models, particularly the long-term evolution driven by geometric jumps remains unknown. In this chapter, we explore the implications of geometric jumps for the long-term evolution and radial transport of energetic electrons. Using a Hamiltonian approach, we develop a mapping technique to show that even as $\varepsilon \to 0$ — where stochastic jumps are absent — geometric jumps induced by asymmetry result in rapid (exponential) phase-space mixing. We discuss how this novel effect enhances the transport of relativistic electrons ($\gtrsim 1$ MeV).

With realistic North–South and Dawn–Dusk asymmetries, the separatrix in $(s, p_{||})$ space is no longer invariant under $s \to -s$ and $\varphi \to -\varphi$ (see Chapter 1). Following Chapter 2, we use a model Hamiltonian system with $1\frac{1}{2}$ degrees of freedom, in which the polynomial potential approximates the magnetic field variation along the particle's drift orbit, as derived from the empirical model for the magnetospheric magnetic field [Tsyganenko and Sitnov, 2005]:

$$\begin{aligned} H(x, p; \varepsilon t) = \frac{p^2}{2} + U(x, \varepsilon t) = \\ = \frac{p^2}{2} + \kappa x^2 + 2\eta x^3 + x^4 \end{aligned} \tag{4.3}$$

Here, (x, p) are canonically conjugate "fast" variables [analogous to $(s, p_{||})$, see Eq. 4.1 and Fig. 1.7], defining the adiabatic invariant $I = \oint p dx$, and $U(x, \varepsilon t)$ is a potential varying with the *slow time* $\varphi = \varepsilon t$, where $\varepsilon \ll 1$ models slow azimuthal drift. We take $\kappa = (4/3)\cos\varphi$, while $\eta = \eta(\varphi)$ is chosen either as (a) $\eta = -3/20$ or (b) $\eta = -(3/20)(1/4 + \sin^3\varphi)$. In both cases, an initially single-minimum potential bifurcates to form a separatrix [see Fig. 4.1]. However, in Case (a) (shown for comparison), the separatrix remains $\varphi \to -\varphi$ symmetric, while in Case (b), it lacks any symmetry. Case (b) is designed to reproduce the realistic separatrix as obtained in Chapter 1 (see Fig. 2.4). Specifically, in Case (b), κ and η are such

that the jump $\Delta I = \Delta S(I)$ over one drift period ($\varepsilon t = 2\pi$) approximates the geometric jumps obtained in Chapter 1 Fig. 2.7.

Hamiltonian (4.1.2) is 2π-periodic in φ, which facilitates studying the long-term dynamics of the system. Its form also allows an analytical expression for the phase-space area enclosed by the separatrix, $S = S^+ + S^-$. Here, $S^\pm = \oint_{H=0, x \gtrless 0} p dx$ refers to the phase-space areas enclosed by two pockets of the separatrix, with $(+)$ denoting integration over $x > 0$ and $(-)$ denoting integration over $x < 0$:

$$\begin{aligned} S^\pm(\varphi) = \frac{1}{3}(-2\kappa)^{3/2} + \eta^2\sqrt{-2\kappa} + \\ + \sqrt{2}\eta(\eta^2 - \kappa)\left[\mp\frac{\pi}{2} + \arcsin\left(\frac{\eta}{\sqrt{\eta^2 - \kappa}}\right)\right] \end{aligned} \tag{4.4}$$

.

Figure 4.2 compares the φ-profile of the phase-space area enclosed under the separatrix from Chapter 2 with that of Hamiltonian (4.1.2), as provided by Eqs. 4.4. The numerical factors 4/3 and 3/20 were chosen so that $S_{max} = \max_{\varphi \in [0,2\pi]} S(\varphi)$ approximates the total separatrix area at $L = 7.3$. However, as we shall see in Section 4.1.3, the phase-space mixing properties of the Hamiltonian are independent of S_{max} (see the discussion of Figure 4.7). The factor of 1/4 in η for Case (b) governs the asymmetry of $S^\pm$ (see Figs. 4.2a and 4.2c). Figure 4.4 shows the radial (drift-orbit) dependence of $S_{\max}$ and $\max_{\varphi \in [0,2\pi]} S^\pm(\varphi)$ derived from the empirical magnetic field model [Tsyganenko and Sitnov, 2005] with solar wind parameters identical to Fig. 2.7 from Chapter 2 and the solar wind dynamics pressure of 2 nPa and 4 nPa. Linear trends $S_{max} = 3.1(L - 7.1)$, $S^\pm = 1.55(L - 7.1)$ and $S_{max} = 3(L - 6.3)$, $S^\pm = 1.5(L - 6.3)$ are shows for reference.

4.1.2 Mapping

Hamiltonian (4.1.2) models the evolution of the adiabatic invariant under asymmetric drift-orbit bifurcation. A particle starting with an initial value of I preserves it far from the

separatrix. In the limit of $\varepsilon \to 0$, this adiabatic invariant is preserved everywhere but undergoes a finite jump, $\Delta I = \Delta S$, during separatrix crossing. Note that separatrix crossing is only possible if $I < S_{\max}$ where $S_{\max} = \max_\varphi S(\varphi)$. For $I > \max\limits_{\varphi} S$, I is conserved. In the limit of $\varepsilon \to 0$, Eq. 4.4 allows replacing the evolution given by Hamiltonian (4.1.2) with an equivalent stochastic mapping: For a given initial value of I, the trapping occurs at $t = t_1$, satisfying $I = S(\varepsilon t_1)$ and the de-trapping condition is $S^{\pm}(\varepsilon t_2) = S^{\pm}(\varepsilon t_1)$, with $(\pm)$ chosen according to whether the particle is trapped in $x > 0$ or $x < 0$. The periodicity of Hamiltonian (4.1.2) enables iterative mapping $I_n \to I_{n+1}$, with $n = \lfloor \varphi/(2\pi) \rfloor$ ($\lfloor \dots \rfloor$ - integer part), given by:

$$I_{n+1} = \begin{cases} S(\varphi_2(I_n)), & \text{if } \varphi_2 \text{ exists,} \\ S^{\pm}(\varphi_1(I_n)), & \text{if } \varphi_2 \text{ does not exist but } \varphi_1 \text{ exists,} \\ I_n, & \text{if neither } \varphi_2 \text{ nor } \varphi_1 \text{ exist.} \end{cases} \tag{4.5}$$

where $\varphi_{1,2}$ are determined by trapping and de-trapping conditions as $S(\varphi_1) = I_n$, $S^{\pm}(\varphi_2) = S^{\pm}(\varphi_1)$ or $S^{+}(\varphi_2) = I_n$ if φ_1 does not exist. Here, $S^{\pm}$ should be taken as S^{+} or S^{-} according to the trapping probabilities, $\Pi^{\pm}$

$$S^{\pm}(\varphi_{1,2}) = \begin{cases} S^{+}(\varphi_{1,2}), \xi \in [0, \Pi^{+}(\varphi_1)] \\ S^{-}(\varphi_{1,2}), \xi \in [0, \Pi^{-}(\varphi_1)] \end{cases} \tag{4.6}$$

Here, $\xi \in [0, 1]$ is a uniformly distributed stochastic variable, $\Pi^{\pm}(\varphi)$ is the trapping probability in the respective pocket atφ, such that $\Pi^{+} + \Pi^{-} = 1$. $\Pi^{\pm}$ are proportional to the growth rate of the phase-space areas enclosed by the respective pockets, $dS^{\pm}/d\varphi$, (see discussion in Section 1.3.2). From Eq. 4.4

$$\frac{dS^{\pm}}{d\varphi} = \sqrt{-2\kappa}\frac{d}{d\varphi}\left[\frac{3\gamma^2}{2} - \kappa\right] + \sqrt{2}\left[\mp\frac{\pi}{2} + \arcsin\left(\frac{\gamma}{\sqrt{\gamma^2 - \kappa}}\right)\right]\frac{d}{d\varphi}\left[\gamma^3 - \kappa\gamma\right] \tag{4.7}$$

Taking into account normalization condition for $\Pi^{\pm}$ and $\Pi^{\pm} \propto dS^{\pm}/d\varphi$, we write

$$\Pi^{\pm} = \frac{dS^{\pm}}{d\varphi}\left(\frac{dS^{\pm}}{d\varphi} + \frac{dS^{\mp}}{d\varphi}\right)^{-1} = \frac{(dS^{\pm}/d\varphi)}{(dS/d\varphi)} \tag{4.8}$$

where $dS^{\pm}/d\varphi$ is given by Eq. 4.7 if it is positive; otherwise, it is zero.

Figure 4.2b presents an epoch analysis of normalized geometric jumps, $\Delta S/S_{max}$, across different radial distances using separatrix profiles from the TS04 model (Mapping 2.23) for various values of the normalized second adiabatic invariant, I_0/S_{max}, reproducing the results from Figs. 2.6-2.7. As shown in Figure 4.2b, the normalized mapping $\Delta S(I_0)$ remains largely invariant across radial distances when both ΔS and I_0 are normalized to the value of S_{max} at each drift orbit. Figure 4.2d shows the mapping associated with the Hamiltonian in terms of normalized geometric jumps, $\Delta S/S_{max} = (I_1 - I_0)/S_{max}$ where I_1 and I_0 are related via Eq. 4.5, for different initial values of the normalized adiabatic invariant, I_0/S_{max}. As we see, the mapping derived from Hamiltonian (4.2) is close to the empirical mapping obtained from the magnetic field model, supporting the Hamiltonian with $\kappa = (4/3)\cos\varphi$ and $\eta = -(3/20)(1/4 + \sin^3\varphi)$ (Case (b)) to model the evolution of the adiabatic invariant under geometric jumps.

4.1.3 Stationary Distribution and Convergence

Mapping (4.5) is equivalent to Hamiltonian (4.1.2) in the limit of $\varepsilon \to 0$ while $\varepsilon t \leq +\infty$. Fig. 4.5 compares the evolution given by Mapping (4.5) (gray) and Hamiltonian (4.1.2) (red). In symmetric Case (a), geometric jumps do not alter the initial distribution [Fig. 4.5a], whereas asymmetric Case (b) exhibits rapid phase-space mixing. The Poincaré sections show that, after a few periods, particles reach the outer boundary of the bifurcation domain ($I = S_{\max}$) and then gradually fill the entire domain. By $n = 60$, they uniformly cover the available phase space [Fig. 4.5(b2), (b5)]. This rapid phase-space mixing is unlike the standard diffusion where slow mixing happens due to $\langle \Delta I_{\rm st}^2 \rangle_\theta \propto \varepsilon^2 \neq 0$. Here, we observe a non-diffusive process driven by geometric jumps that result in uniform filling of the $[0, S_{\max}]$ domain. Starting with a distribution peaked around $I = I_0$, i.e., with cumulative distribution $F_0 = \theta(I - I_0)$ (θ - the Heaviside step function), we find its relaxation towards a uniform

distribution $F_n(I) \to I/S_{\max}$ as $n \to +\infty$ [Fig. 4.6]. We find that this relaxation occurs exponentially fast and is independent of I_0 [see Fig. 4.6]:

$$\Delta_n = \langle |F_n(I) - I/S_{\max}| \rangle \propto \exp\left(-n/\mathcal{N}\right) \tag{4.9}$$

where $\langle \dots \rangle = S_{\max}^{-1} \int_0^{S_{\max}} \dots dI$ denotes the averaging. Since n is a proxy for the number of drift periods (τ_d) the *e-folding* factor $\mathcal{N}$ serves as a proxy for the *e-folding* time of relaxation, $\tau_{\rm rel} = \mathcal{N}\tau_d$. We found that $\mathcal{N}$ is an intrinsic property of a given Hamiltonian reflecting its level of asymmetry, with $\mathcal{N} = \infty$ in Case (a) (no relaxation) and typically $\mathcal{N} \approx 10-50$ in Case (b) for an asymmetric Hamiltonian. Mapping (4.5) is formally known as a polymorphism - a multivalued self-map of an interval (e.g., $[0, S_{\max}]$) [Vershik, 1983, Neishtadt and Treschev, 2011]. The probability distribution transformation associated with this mapping is a multivalued analog of Perron–Frobenius operators [Lasota and Mackey, 1985]. A certain class of Perron–Frobenius operators is known to exhibit exponential relaxation towards a uniform distribution, analogous to the results shown in Fig. 4.6 [Keller, 1984].

It is wort emphasizing again that the *e-folding* factor $\mathcal{N}$ is only determined by the *asymmetry* the Hamiltonian. In other words, $\mathcal{N}$ remains unchanged under self-similar changes of the phase-space areas, $S^{\pm}$. Figure 4.7 shows a comparison of the phase-space mixing for the original Hamiltonian, $H(x, p; \varepsilon t)$ (Figs. 4.7a and 4.7b), and for the re-scaled Hamiltonian, $x \to x/4$, yielding $H(x/4, p; \varepsilon t)$ (Figs. 4.7c and 4.7d). This re-scaling amounts to an increase of all phase-space areas, i.e., S and $S^{\pm}$, by the same factor of 4. In particular, S_{max} increases from its original value of about 2.8 to $4 \cdot 2.8 \approx 11.2$. Figures 4.7a and 4.7b show that the shape and asymmetry of the separatrix phase-space profiles are preserved. Figures 4.7b and 4.7d show that the increase in S_{max} *does not* affect the exponential mixing rate; moreover, the exact e-folding time, $\mathcal{N}$, remains approximately the same, $\mathcal{N} \approx 19$ for both cases. This exemplifies an interesting property of phase-space mixing driven by geometric jumps: the mixing rate does not depend on the size (area) of the phase-space domain in which mixing

occurs. Combining these observations with the results presented in Fig. 4.4, we conclude that the entire radial range of drift orbits (e.g., $L \in [6.5, 8.0]$ in Fig. 4.4b) can be characterized by the same $\mathcal{N}$ parameter.

4.2 Comparison with Radial Diffusion

4.2.1 Equivalent Radial Diffusion

Exponential relaxation to a uniform distribution allows us to draw an interesting parallel with the classical one-dimensional diffusion. Consider the evolution of a probability density $f(I,t)$ with $I \in [0, S_{\max}]$ normalized as $\int_0^{S_{\max}} f(I,t)dI = 1$ and obeying the standard Fokker-Planck equation with a constant diffusion rate of D_{II}

$$\frac{\partial f}{\partial t} = D_{II}\frac{\partial^2 f}{\partial I^2} \tag{4.10}$$

with $(\partial f/\partial I)|_{I=0} = (\partial f/\partial I)|_{I=S_{\max}} = 0$. In this system, one also observes exponentially fast mixing, with the leading asymptotics given by (see e.g. [Tikhonov and Samarskii, 2013, Courant and Hilbert, 1989]):

$$\left\langle \left| \int_0^I f(I',t)dI' - I/S_{\max} \right| \right\rangle \propto \exp\left(-t/\tau_{\text{diff}}\right) \tag{4.11}$$

where the e-folding time, τ_{diff}, is inversely proportional to the process' diffusion rate: $\tau_{\text{diff}} = S_{\max}^2/(\pi^2 D_{II})$. Although, Fig. 4.6 clearly shows that asymmetric drift-orbit bifurcation is not diffusive in I, the existence of the e-folding time in this case allows introducing the *effective* diffusion rate, D_{II}, such that $\tau_{\text{rel}} = \tau_{\text{diff}}$, yielding $D_{II} = S_{\max}^2/(\pi^2\tau_{\text{rel}})$. We re-express D_{II} in terms of the radial diffusion rate, D_{LL}, by recalling $\Delta I = (\partial L/\partial I)_\mu \Delta L$ yielding $D_{LL} = (\partial L/\partial I)_\mu^2 D_{II}$ where $(\partial L/\partial I)_\mu \approx \sqrt{2}/\pi$ (see Eq. 1.81). Thus,

$$D_{LL} \approx \begin{cases} 18(L - L_{\min})^2 \left(\pi^4 \mathcal{N}\tau_d\right)^{-1}, \text{ if } L \geq L_{min} \\ 0, \text{ if } L < L_{min} \end{cases} \tag{4.12}$$

where the radial dependence of the drift-orbit bifurcation effect is approximated as $S_{\max} \approx 3(L - L_{\min})$ for $L > L_{\min}$ and $S_{\max} = 0$ for $L < L_{\min}$ (see Fig. 4.4). This reflects that bifurcation starts at $L = L_{\min}$ (typically $L_{\min} \approx 6 - 7$, see Fig. 4.7) and increases with $L > L_{\min}$. We again note that this increase in $S_{\max}$ does not change $\mathcal{N}$, which remains invariant under a self-similar change of $S^{\pm}$ and S, allowing us to use a fixed value of $\mathcal{N} \approx 19$ [see Fig. 4.6a] for all L [see Figs. 4.4 and 4.7]. To estimate the radial diffusion rate, we can further approximate the electron drift period as τ_d [days] $\approx 0.12 L^{-1}(\gamma - \gamma^{-1})^{-1}$, where γ is Lorentz factor (see Eq. 1.62). Thus,

$$D_{LL}[\text{days}^{-1}] = \begin{cases} 0.08L(L - L_{\min})^2(\gamma - \gamma^{-1}), \text{ if } L \geq L_{\min} \\ 0, \text{ if } L < L_{\min} \end{cases} \tag{4.13}$$

This is unlike in the standard symmetric drift-orbit bifurcation, where $D_{LL} \propto \gamma^3 L^7$ (see Eq. 1.82 and [Öztürk and Wolf, 2007]). At energies $\lesssim 10$ MeV, this new scaling *increases* the radial diffusion rate by 1-4 orders of magnitude. We should reiterate that the D_{LL} given by Eq. 4.13 is only an effective (or equivalent) diffusion rate, matching the relaxation time determined from $\mathcal{N}$, while the process *per se* is more appropriately characterized by the relaxation time τ_{rel}, without reference to an equivalent diffusive description. A description in terms of D_{LL} becomes more justifiable at times $t \gtrsim \tau_{\text{rel}}$ (after sufficient mixing).

4.2.2 Comparison with ULF-driven Diffusion

Figure 4.8 shows the radial dependence of the effective radial diffusion coefficient, D_{LL}, for different electron kinetic energies and for $L_{min} = 6$ and $L_{min} = 7$, representing different values of solar wind dynamic pressure. For reference, we also show the radial profiles of D_{LL} driven by Ultra-Low Frequency (ULF) waves, as estimated in [Brautigam and Albert, 2000, Ozeke et al., 2014] for low-driving conditions, i.e., for K_p index values less than 3. Fig. 4.8 demonstrates that drift-orbit bifurcation transport, characterized by D_{LL}, can be of comparable magnitude to classical ULF-driven transport at energies $\gtrsim 1$ MeV. We note

that ULF-driven D_{LL} provided in [Brautigam and Albert, 2000, Ozeke et al., 2014] may be overestimated when compared to the spacecraft observations (see, e.g., [Ali et al., 2016]). Note more sophisticated models of ULF-driven transport [Lejosne and Kollmann, 2020, Osmane et al., 2023] also exhibit an energy dependence absent in models from [Brautigam and Albert, 2000, Ozeke et al., 2014], but a more detailed comparison of drift-orbit bifurcation transport with ULF-driven transport is left for future study.

Note that the transport caused by drift-orbit bifurcation should still be effective, even when it does not result in larger D_{LL}. This is because drift-orbit bifurcation is, strictly speaking, non-diffusive and can cause significant radial displacement even after a single drift period [Wan et al., 2010]. However, the associated phase-space mixing can only be adequately characterized by D_{LL} after $\mathcal{N}$ drift periods, highlighting its non-diffusive nature on shorter timescales.

4.3 Summary

In this chapter, we have shown that asymmetry even in low-dimensional Hamiltonian systems (e.g., $1\frac{1}{2}$ degrees of freedom) with a separatrix can lead to rapid (non-diffusive) transport and exponentially fast mixing in phase-space. This suggests that the natural asymmetry typical of the Earth's magnetic field will significantly enhance the transport of relativistic electrons ($\gtrsim$ 1 MeV) through this mechanism. We also note that the mechanisms associated with separatrix crossings discussed in this work have broader implications for a number of physical systems, including laboratory plasma confinement [Franchi et al., 2009, Bazzani et al., 2024], Bose–Einstein condensates [Itin and Watanabe, 2007] and Hydrodynamics [Vainchtein et al., 2006, Grigoriev et al., 2006, Vainchtein et al., 2007]. In this vein, drift-orbit bifurcation in the Earth's magnetosphere exemplifies a physical system in which incorporating asymmetry significantly enhances the rate of phase-space mixing, while the underlying mechanisms remain applicable to a broad class of systems described by Hamiltonians featuring a separatrix in

phase space [Itin and Watanabe, 2007, Franchi et al., 2009, Artemyev et al., 2014].

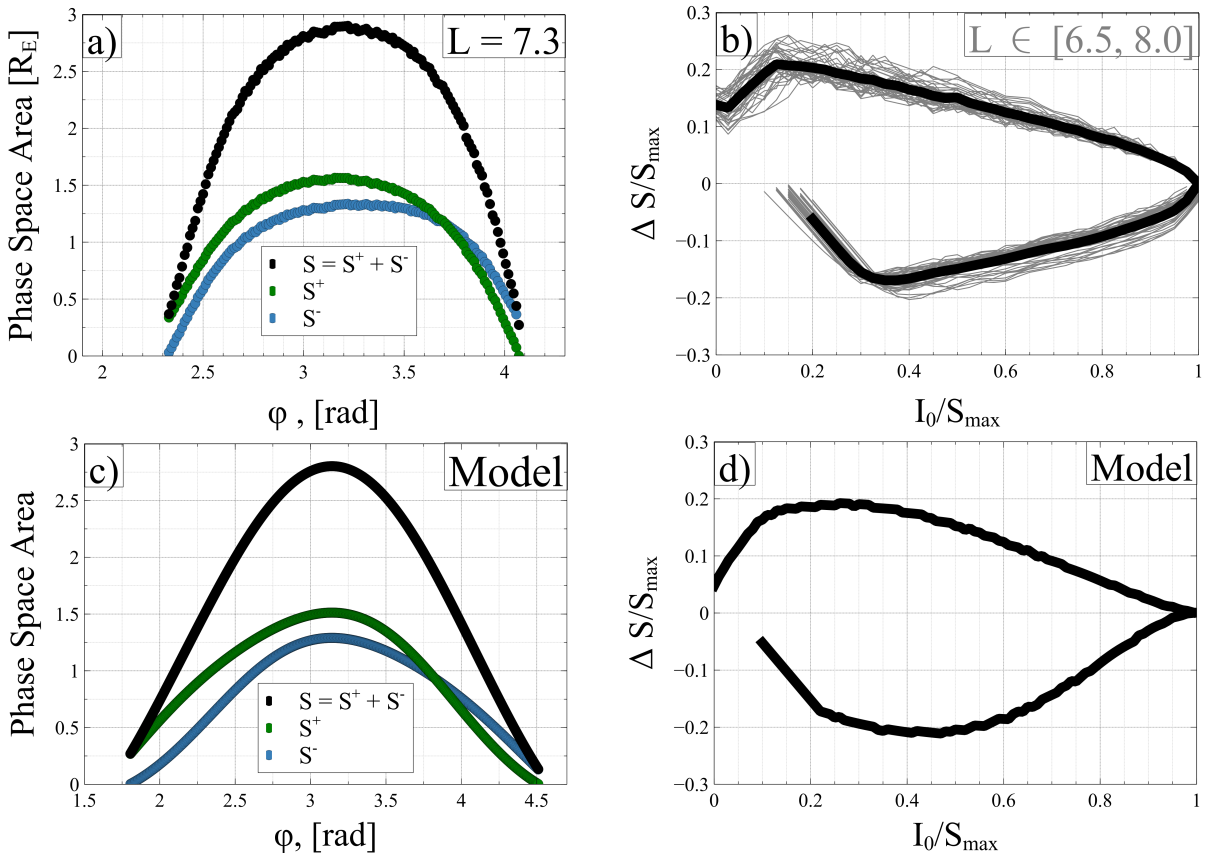

Figure 4.2: Comparison of the separatrix phase-space areas from the empirical magnetic field model [Tsyganenko and Sitnov, 2005], as calculated in Chapter 1 (see Fig. 2.4), and the separatrix phase-space areas of Hamiltonian (4.1.2) as given by Eq. 4.4. (a) Azimuthal profile of the phase-space area enclosed within the separatrix based on the empirical magnetic field model, reproduced from Fig. 2.4. (b) Epoch analysis (gray lines) of the geometric jumps $\Delta S(I_0)$ for $L \in [6.5, 8.0]$, normalized to the maximum separatrix area at each respective L; the black line shows the averaged profile. (c) Azimuthal profile of the phase-space area enclosed within the separatrix based on the model Hamiltonian (Eqs. 4.1.2-4.4).(d) Normalized geometric jumps, $\Delta S(I_0)$, for the model Hamiltonian (Eqs. 4.1.2-4.4).

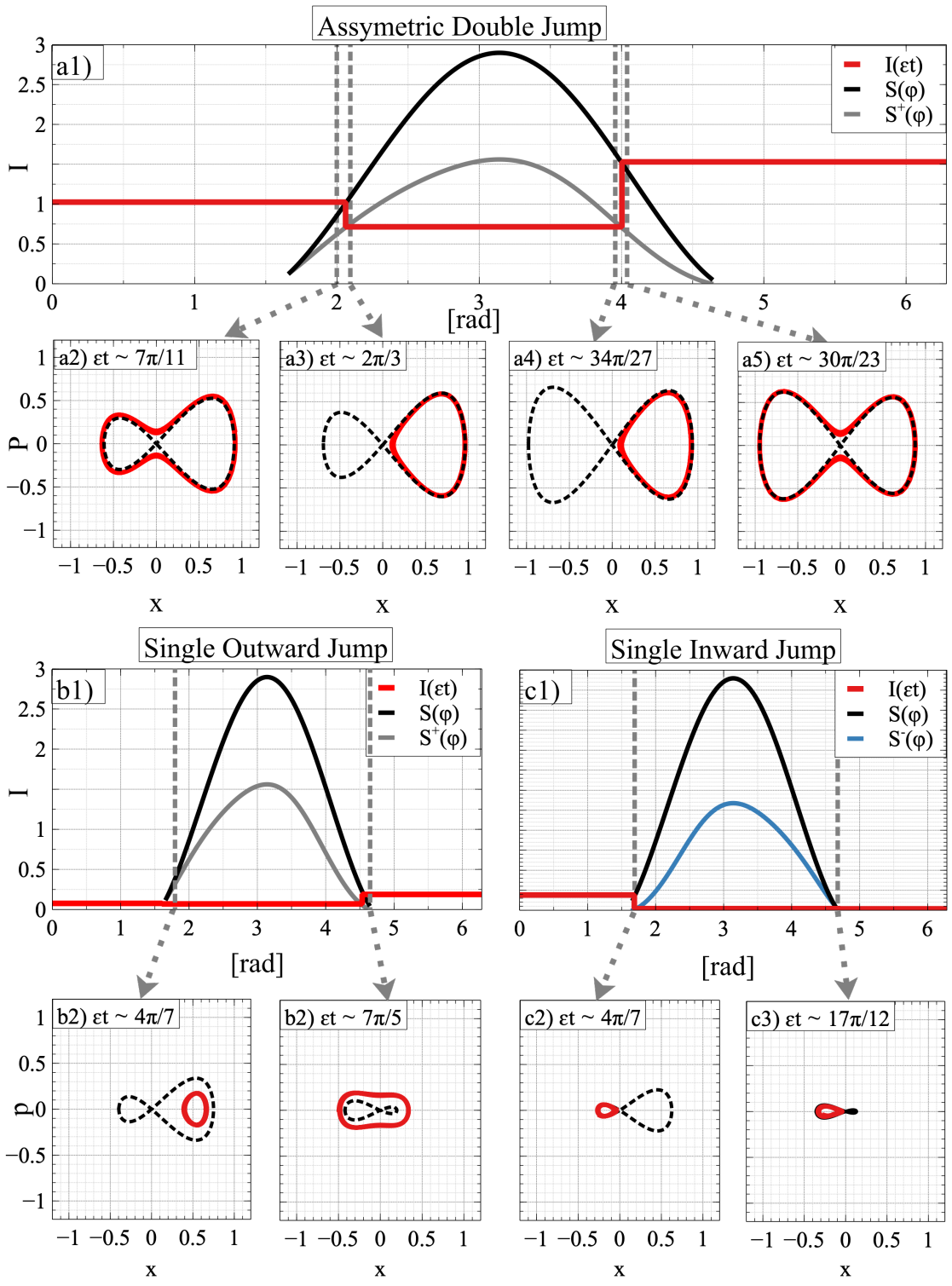

Figure 4.3: Three types of jumps in the adiabatic invariant observed in Hamiltonian (4.1.2). Note the remarkable similarity to Fig. 2.6 from Chapter 2, obtained using the mapping in the [Tsyganenko and Sitnov, 2005] model, and to Fig. 3.3 from Chapter 3, obtained from full-dimensional guiding-center simulations.

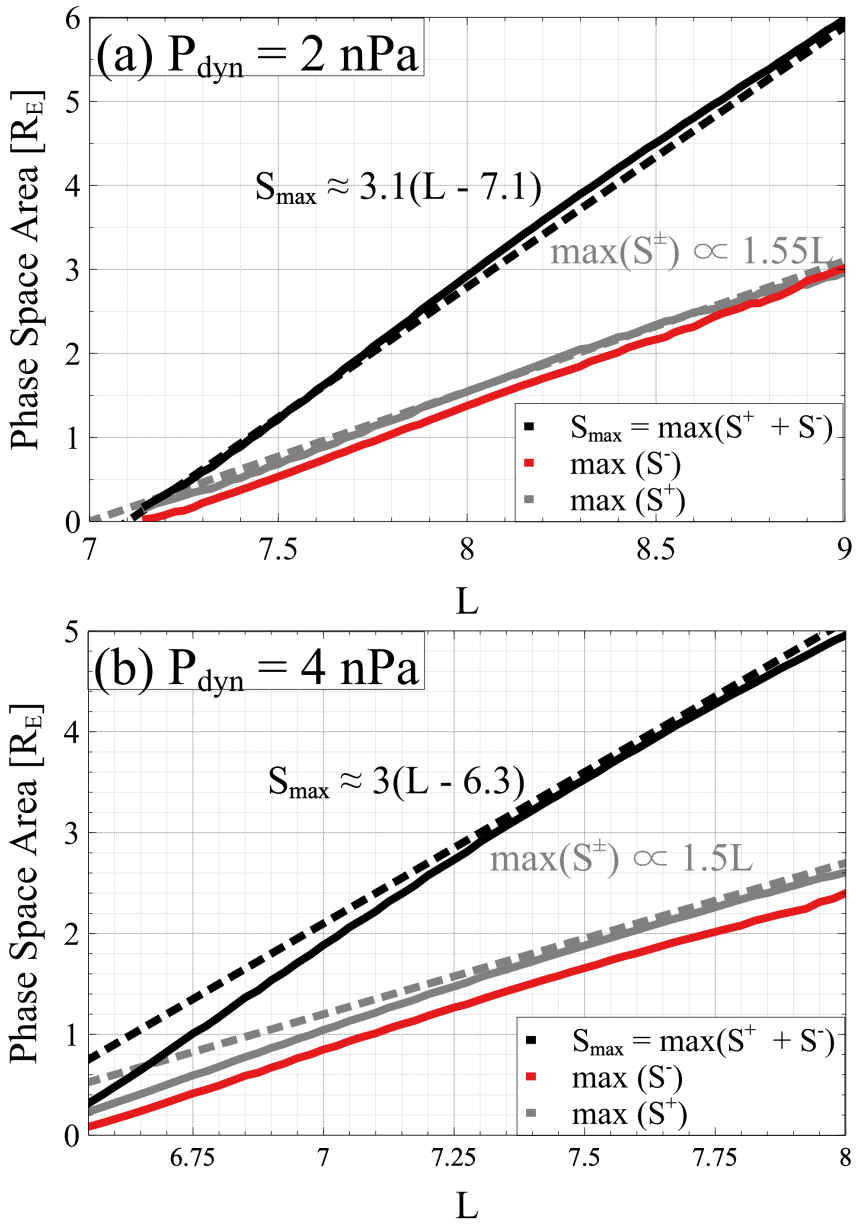

Figure 4.4: Radial dependence of the maximum phase-space area enclosed within the separatrix, $S_{\max} = \max_{\varphi}(S^+ + S^-)$, and within its pockets, $S^{\pm}$, using [Tsyganenko and Sitnov, 2005] magnetic field model, as calculated in Chapter 2 (see Fig. 2.7) with IMF $B = 5$ nT, $\varphi_{\rm IMF} = 225°$, zero tilt angle and: (a) $P_{dyn} = 2$ nPa, (b) $P_{dyn} = 4$ nPa. Linear trends $S_{max} = 3.1(L - 7.1)$, $S^{\pm} = 1.55(L - 7.1)$ and $S_{max} = 3(L - 6.3)$, $S^{\pm} = 1.5(L - 6.3)$ are shown for reference.

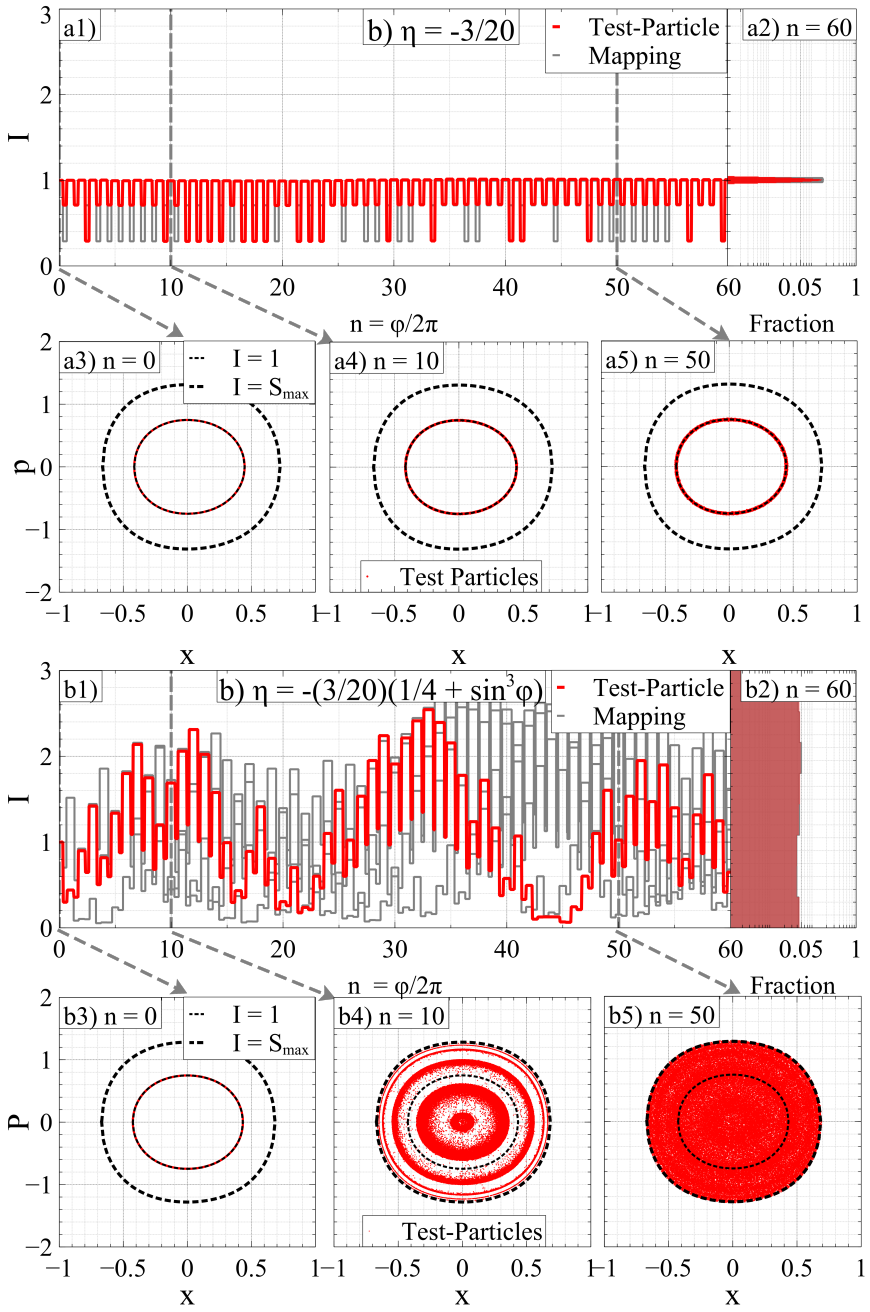

Figure 4.5: Evolution of 10^5 particles with $I_0 = 1$ under Mapping (4.5) (gray) and Hamiltonian (4.1.2) (red), solved for $\varepsilon = 10^{-4}$. Panels: (1) evolution of I for one test particle (red) and five mapping trajectories (gray); (2) PDF of I; (3–5) Poincaré sections in (x, p) after different number of iterations. Black dashed lines show the initial $I = 1$ and upper boundary of the bifurcation domain, $I = S_{\max}$.

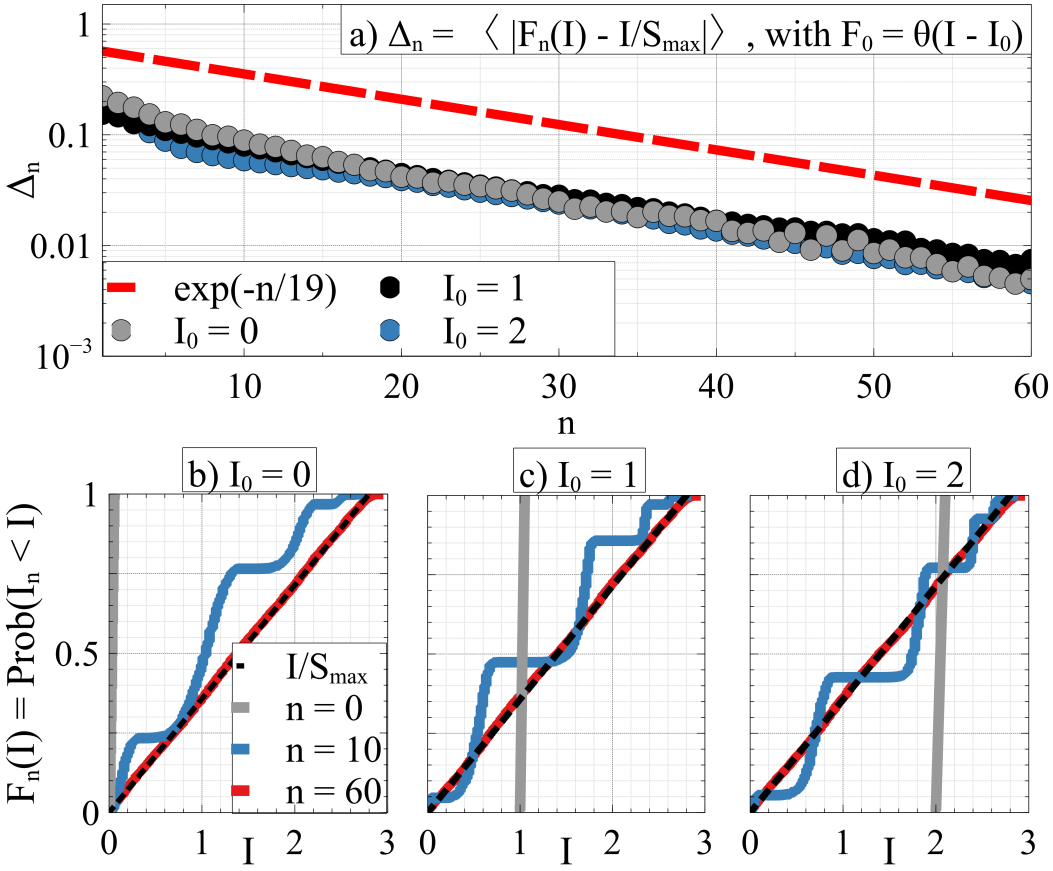

Figure 4.6: Evolution of $F_0 = \theta(I - I_0)$ (10^6 particles) under Mapping (4.5) for different values of I_0: (a) deviation from uniform distribution, Δ_n, with the red dashed line showing exponential decay; (b), (c), (d) evolution of the cumulative distribution, with the dashed line showing the cumulative distribution of a uniform distribution $F = I/S_{\max}$ over $I \in [0, S_{\max}]$.

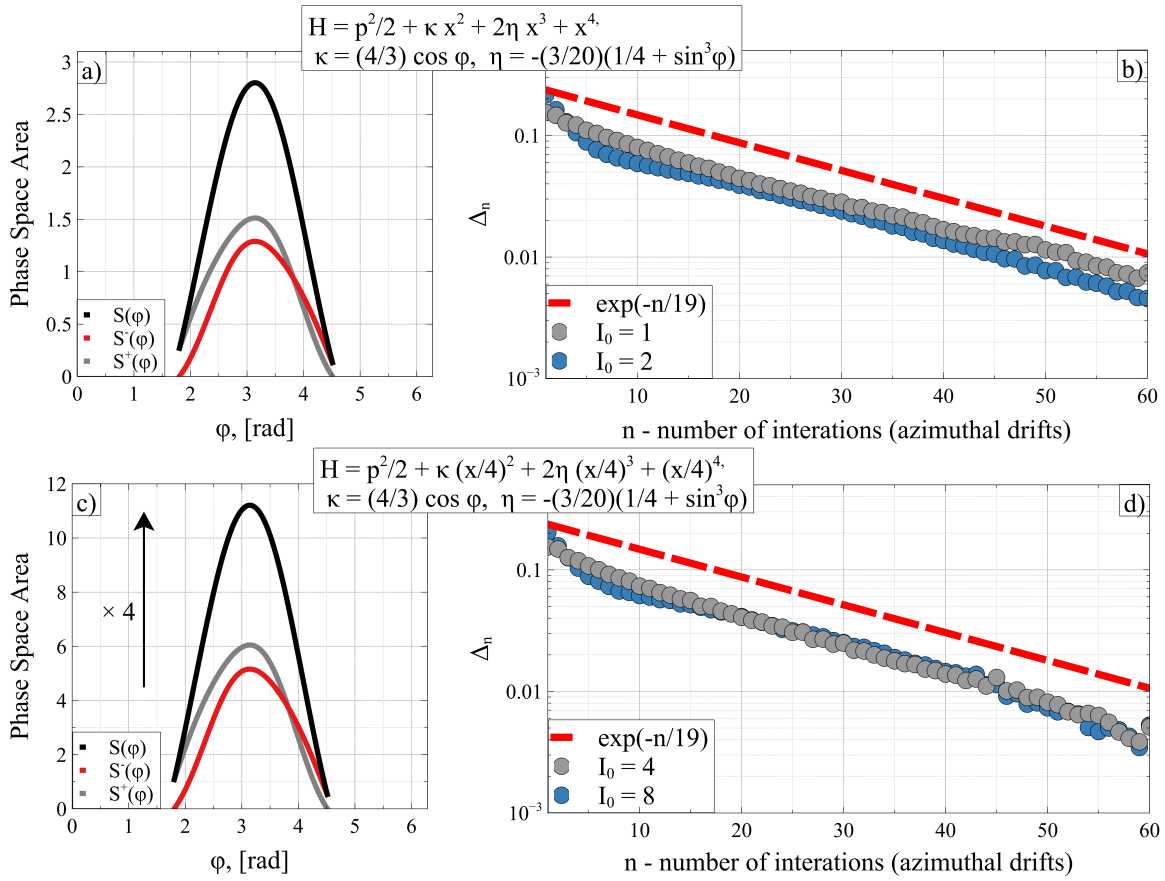

Figure 4.7: (a) Azimuthal profile of the phase-space area enclosed within the separatrix, based on the model Hamiltonian (4.1.2). (b) Evolution of the deviation from the uniform distribution, $\Delta_n = \langle |F_n(I) - I/S_{max}| \rangle$, where F_n is the cumulative distribution in I after n iterations, under the mapping associated with the model Hamiltonian (4.1.2) for different values of the initial adiabatic invariant ($F_0 = \theta(I - I_0)$, where θ is the Heaviside step function). Exponential decay $\propto \exp(-n/19)$ is shown as the best common fit for both curves. (c) Same as in (a), but for a re-scaled Hamiltonian $x \to x/4$, resulting in a self-similar increase of the phase-space areas by a factor of 4: $S \to 4 \cdot S$ and $S^{\pm} \to 4 \cdot S^{\pm}$. (d) Same as in (b), but for the re-scaled Hamiltonian $x \to x/4$. The rate of phase-space mixing, quantified by $\mathcal{N}$, remains invariant under separatrix re-scaling.

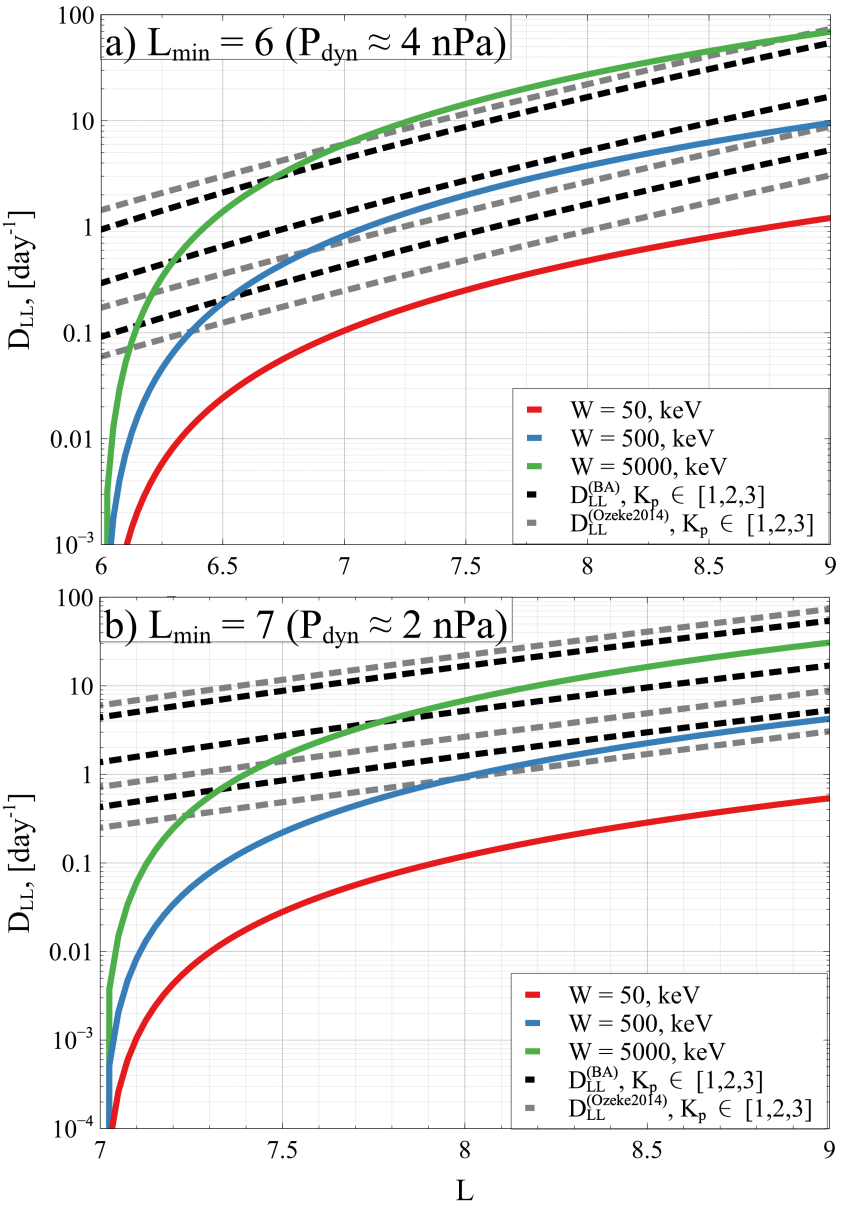

Figure 4.8: Effective radial diffusion coefficient, $D_{LL}[\text{days}^{-1}] = 0.08L(L - L_{min})^2(\gamma - \gamma^{-1})$, with $\mathcal{N} \approx 20$ and $\tau_d[\text{days}] \approx 0.12L(\gamma - \gamma^{-1})^{-1}$ from [Schulz and Lanzerotti, 1974]: (a) results for $L_{min} = 6$, representative of a solar wind dynamic pressure of $\gtrsim 4$ nPa; (b) results for $L_{min} = 7$, representative of a solar wind dynamic pressure of ≈ 2 nPa. In both panels, thick colored lines show D_{LL} for electron kinetic energies of 50, 500, and 5000 keV. Dashed lines show empirical values of ULF-driven D_{LL} from [Brautigam and Albert, 2000] and [Ozeke et al., 2014] for K_p-index values of 1, 2, and 3.

CHAPTER 5

Summary and Future Directions

I was told that this road would take me to the ocean of death, and I turned back halfway. Since then crooked, round-about, godforsaken paths stretch out before me.

-Arkady and Boris Strugatsky, «Definitely Maybe»

Сказали мне, что эта дорога меня приведёт к океану смерти, и я с полпути повернул обратно.
С тех пор всё тянутся передо мною кривые глухие окольные тропы

-Аркадий и Борис Стругацие, «За миллиард лет до конца света»

5.1 Research Summary

Cross-field transport of charged particles has historically been one of the central topics of plasma physics. It plays an important role both in plasma confinement in laboratory plasmas and in the dynamics of charged particles trapped in the Earth's radiation belts. Decades of spacecraft observations have significantly contributed to our understanding of radiation belt dynamics. Charged-particle interactions with various plasma waves form the cornerstone of modern radiation belt theory. Large-scale (across multiple drift orbits), long-term dynamics can be well described by electron interactions with ULF waves, resulting in slow radial diffusion. However, reproducing observed radiation belt dynamics on a case-by-case basis often requires the inclusion of non-canonical features, such as non-zero drift, or going beyond

this diffusive picture altogether. This is especially true in the near-magnetopause region, where isolated enhancements and outward electron leakage are often observed. It is in this context that the drift-orbit bifurcation mechanism has been invoked as a supplementary mechanism of electron radial transport. However, it was quickly recognized that under symmetric magnetospheric conditions this mechanism is mostly inefficient at transport of electron at energies $\lesssim 10$ MeV.

This thesis was aimed at a thorough investigation of radial transport driven by the drift-orbit bifurcation mechanism under realistic (asymmetric) magnetic field configurations. Specifically, it is structured around addressing the following questions: (1) what is the typical level of magnetospheric asymmetry at drift orbits with $L \gtrsim 6$–7, quantified in terms of characteristic radial displacement in one drift period; (2) what is the range of electron energies for which this displacement is comparable to or exceeds that expected from classical ULF-driven transport; and (3) is the long-term dynamics driven by such asymmetric jumps diffusive?

In Chapter 2, we used an empirical magnetic field model together with 11 years of ARTEMIS solar wind observations (see Fig. 2.1) to assess the importance of magnetospheric asymmetry under typical solar wind conditions. Using field-line tracing in the empirical magnetic field model, the drift orbits of nearly equatorially mirroring electrons were derived, and the magnetic field strength profiles along field lines at various magnetic local time (MLT) sectors were estimated. This allowed us to construct a mapping of the second adiabatic invariant, $J_{||}$, relating its initial value to the final value after one drift period. The results clearly indicate the presence of large jumps, $\left|\Delta J_{||}\right| \gtrsim J_{||}$, of the second adiabatic invariant caused by magnetic field asymmetry. Using test-particle simulations, we identify these (large) geometric jumps of the adiabatic invariant, which are well known in the theory of adiabatic invariant destruction during separatrix crossings. Translating these jumps into the associated radial displacements, $\Delta L \propto \Delta J_{||}$, shows that radial transport driven by magnetic field asymmetry

can reach $\Delta L \approx \pm 1$ per drift period. These results were published in [Kamaletdinov et al., 2024a].

Chapter 3 applied the framework developed in Chapter 2 to a case study focused on modeling a representative near-magnetopause energetic electron (> 30 keV) flux enhancement observed by the THEMIS spacecraft. Comparing observations from two THEMIS spacecraft crossing the afternoon magnetopause sector with a time delay of ~ 3 hours, together with guiding-center simulations of an electron ensemble, we showed how rapid outward radial transport driven by asymmetric drift-orbit bifurcation can transport electrons from $L \lesssim 6$–7 to near-magnetopause radial distances of $L \gtrsim 8$–9, creating a radially isolated flux enhancement within a single drift period. This result clearly demonstrated the effectiveness of outward radial transport driven by asymmetric drift-orbit bifurcation at electron energies of ~ 30–100 keV, as well as its non-diffusive nature, in stark contrast to classical symmetric drift-orbit bifurcation. This suggests that drift-orbit bifurcation is an important contributor to electron dynamics and leakage in the outer radiation belt, particularly in regions adjacent to the magnetopause. The results of this chapter are published in [Kamaletdinov et al., 2025a].

In Chapter 4, we systematically study the implications of non-diffusive transport driven by asymmetric (geometric) jumps of the adiabatic invariant. Using the Hamiltonian framework developed in Chapter 2 to model electron dynamics as a low-dimensional $1\frac{1}{2}$ degrees-of-freedom system, we apply the mapping technique to study the long-term (multiple drift-period) dynamics of electrons undergoing drift-orbit bifurcation. Intriguingly, despite the non-diffusive nature of this process, we find that its long-term behavior also results in complete phase-space mixing. Moreover, the rate of this mixing is exponential, showing an interesting similarity to classical diffusion. Using the numerically calculated e-folding time of this mixing, we estimate an equivalent ("effective") diffusion rate, allowing us to formally compare long-term transport driven by drift-orbit bifurcation with classical ULF-driven diffusion. We find that radial transport driven by drift-orbit bifurcation can be equally or even more efficient than classical

ULF-driven radial diffusion at energies $\gtrsim$ 0.1–1 MeV, particularly under low solar wind driving conditions. We also emphasize that these results have much broader relevance beyond cross-field transport in the radiation belts, as the transport driven by phase-space asymmetry have many realizations in physical systems ranging from laboratory plasma confinement to hydrodynamics. The results of these analyses have been published in [Kamaletdinov et al., 2025b].

To summarize, this thesis undertakes a thorough study of the role of dayside magnetospheric asymmetry in drift-orbit bifurcation. The specific focus is on the implications of this asymmetry for electron radial transport. Combining spacecraft observations and state-of-the-art theories of adiabatic invariant destruction, we find that the level of asymmetry *typical* of the Earth's magnetosphere, even under moderate solar wind conditions, significantly enhances the effect of drift-orbit bifurcation. The resulting radial transport can reach $\Delta L = \pm 1$ per drift period at $L \gtrsim 7$. Moreover, this mechanism is effective at transporting electrons of relatively moderate energies, $\sim$ 30–100 keV, unlike classical (symmetric) drift-orbit bifurcation. It may account for the appearance of isolated energetic electron enhancements near the magnetopause and the leakage of electrons through the magnetopause, contributing to particle losses. These findings clearly indicate that magnetospheric asymmetry must be treated as the norm rather than the exception, and firmly establish drift-orbit bifurcation as an important component of electron dynamics near the magnetopause, alongside classical ULF-driven radial diffusion.

5.2 Future Work

The work presented in this thesis can naturally be expanded upon by future studies. These include global-scale guiding-center test-particle simulations in time-dependent magnetic fields from MHD simulations, as well as more thorough statistical analyses of energetic electron enhancements near the magnetopause, using new data from the ever-growing datasets of polar-orbiting spacecraft and, most importantly, CubeSats. Below, we briefly discuss some of

the natural extensions of this work, left for the future.

5.2.1 Statistical Study of Energetic Electron Enhancements Near the Dayside Magnetopause

Figure 5.1 shows observations of energetic ($\gtrsim$ 100 keV) electron enhancement (trapped population) near the dayside magnetopause, as observed by the Electron Losses and Fields Investigation (ELFIN) CubeSat mission [Angelopoulos et al., 2020]. Figs. 5.1(a–b) show ELFIN-B observations of electron number flux from the outer radiation belt/plasma sheet in the afternoon sector (MLT $\approx$ 14) between 04:42 UT and 04:47 UT. Note that electron flux disappears after $L_B \approx 8$. Figs. 5.1(c–d) show ELFIN-A observations in the noon/afternoon sector (MLT $\approx$ 13), approximately four hours after the ELFIN-B observations, between 08:27 UT and 08:33 UT. In addition to the expected outer-radiation belt/plasma sheet electrons at $L_B \lesssim$ 6–7, we also observe an apparently isolated population from the near magnetopause region at $L_B \gtrsim 7$.

Figs. 5.1(f–g) show concurrent solar wind observations by THEMIS-B between 04:42 UT and 08:33 UT. A sudden increase in dynamic pressure is observed at approximately 07:15 UT, where P_{dyn} jumps from 2–3 nPa to $\gtrsim$ 4 nPa. This dynamic pressure enhancement can be attributed to the arrival of a solar wind discontinuity, which also results in a rotation of the magnetic field, visible in Fig. 5.1(f) at 07:15 UT, featuring large negative B_z and B_y. Comparing these observations with Fig. 3.1, one may speculate on drift-orbit bifurcation arising from the highly asymmetric IMF as the potential origin of these apparently isolated energetic electron enhancements observed very close to the magnetopause.

The event shown in Figure 5.1 is a representative example from a large dataset of events observed by ELFIN CubeSats. Similar events have also been observed by other low-orbiting spacecraft. Figure 5.2 shows combined observations of energetic electron enhancement (trapped population) near the dayside magnetopause by the Colorado Inner Radiation Belt Experiment

(CIRBE) CubeSat mission [Li et al., 2022, Li et al., 2024] and NOAA POES [Evans and Greer, 2004] spacecraft. Figures 5.2a and 5.2b show the evolution of the electron number flux in the dayside magnetosphere between 19 and 22 UT on April 25, 2023. For CIRBE and NOAA-19 measurements, integral flux > 300 keV and > 130 keV are shown, respectively, and projected from low orbit onto the $Z_{GSM} = 0$ plane. The formation of an isolated flux enhancement near the magnetopause is evident after 21 UT in both CIRBE and NOAA-19 measurements (Fig. 5.2b), in both the pre- and post-noon sectors. Indeed, Figures 5.2c and 5.2d show the flux enhancement localized near magnetopause radial distances between $L \approx 10 - 11$ and apparently occupying the entire energy range from 40 keV (NOAA-19) to $\sim$ MeV (CIRBE). Figures 5.2e and 5.2f show the concurrent solar wind conditions from 1-min OMNI data [King and Papitashvili, 2005]. Interestingly, the solar wind conditions between 19 and 21 UT show a moderate enhancement in the solar wind dynamic pressure from about 3.5 nPa to 6.5 nPa and a gradual increase (in absolute value) in the IMF B_y component. Such conditions are reminiscent of those discussed in Chapter 3 in the context of THEMIS observations of energetic electron enhancement and are favorable for drift-orbit bifurcation. Therefore, combining large datasets of such dayside measurements by CubeSats, e.g., ELFIN and CIRBE, if needed supported by NOAA POES, presents an opportunity for a thorough statistical study of the formation of such isolated energetic electron enhancements, specifically focusing on: (1) MLT extent, (2) typical solar wind conditions and dipole tilt angle (i.e., seasonal variations), and (3) L-shell range.

5.2.2 Estimation of the Equivalent Radial Diffusion Rate in a Realistic Magnetic Field Model

Building upon the framework developed in [Artemyev et al., 2021, Frantsuzov et al., 2023, Kamaletdinov et al., 2024b], guiding-center simulations (see Chapter 3) in Tsyganenko-type empirical magnetic field models can be performed for various solar wind conditions.

Alternatively, an approach similar to that in Chapter 4 can be used with a mapping $I \to I + \Delta I(L, I)$, now including a realistic radial dependence $L \to L + \Delta L(L, I)$ as calculated in Chapter 2 (see Fig. 2.7). By initializing multiple electron ensembles at different initial L-values and calculating $\langle \Delta L^2 \rangle$ over drift orbits, one can estimate the equivalent radial diffusion rate. These results can then be compared with the estimate given by Eq. 4.13 for the equivalent radial diffusion rates. Such estimates of the equivalent radial diffusion coefficients can subsequently be incorporated into a radial diffusion model to mimic the effects of drift-orbit bifurcation transport.

5.2.3 Role of Temporal Variation in Solar Wind Parameters in Asymmetric Drift-Orbit Bifurcation

Solar wind conditions at 1 AU show significant temporal variability, sometimes down to $\sim$ 5–10 minutes (as shown in Figure 5.1f). Such rapid changes in IMF orientation and solar wind dynamic pressure can thus occur on time scales comparable to the drift periods of $\gtrsim 100$ keV electrons (see Figure 3.6), providing an additional mechanism that violates electron drift motion. Although some slow (almost quasi-static) temporal evolution has been included via an *ad hoc* model in Chapter 3, a thorough study of energetic electron dynamics experiencing bifurcation under such fast ($\sim$ minutes) variations in solar wind conditions is needed to understand their impact on radial transport.

This can be done by building upon the framework of guiding center simulations used in Chapter 3, but employing realistic Tsyganenko-type empirical magnetic field models or large-scale MHD simulations (e.g., [Sorathia et al., 2017, Sorathia et al., 2018]) driven by time-dependent solar wind conditions. Particularly interesting would be a series of case studies using fast orbital scans of precipitating particles from the dayside magnetosphere with polar-orbiting satellites (e.g., ELFIN), while solar wind conditions are monitored by ARTEMIS.

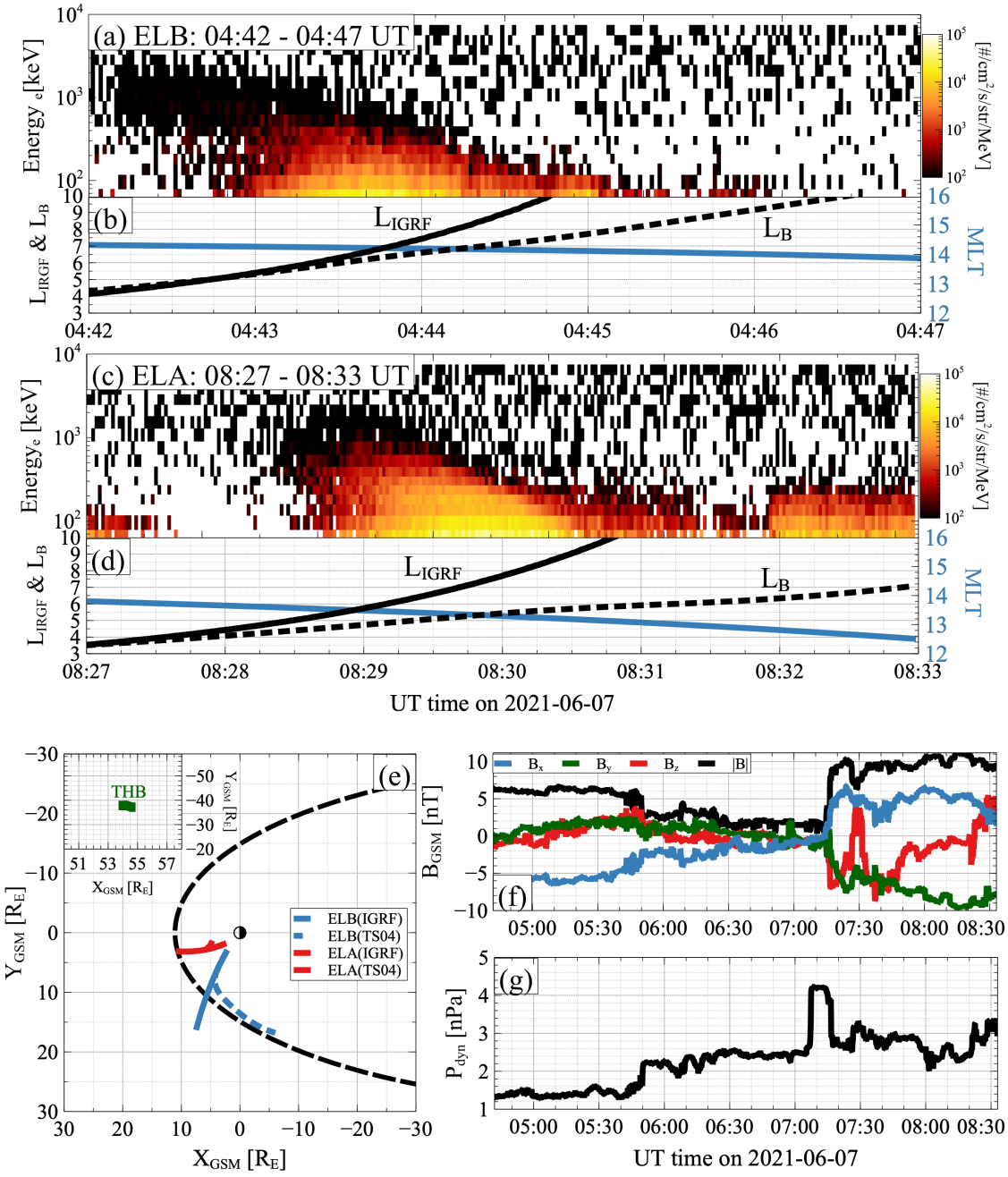

Figure 5.1: ELFIN-A and ELFIN-B observations of $\gtrsim$ 100 keV electron enhancements near the dayside magnetopause on 07-Jun-2021. (a) Precipitating electron flux from ELFIN-B (04:42–04:47 UT). (b) Equatorial field line projection: L_{IGRF} ($\sim$ dipole L-shell) and L_B (Eq. 2.1); right axis: MLT. (c) Precipitating flux from ELFIN-A (08:27–08:33 UT). (d) Same as (b) for ELFIN-A. (e) Equatorial projections of ELFIN-A/B and THEMIS-B (ARTEMIS) in IGRF and IGRF+TS04 [Tsyganenko and Sitnov, 2005] fields. (f) Solar wind magnetic field at THEMIS-B (GSM). (g) Solar wind dynamic pressure, P_{dyn}.

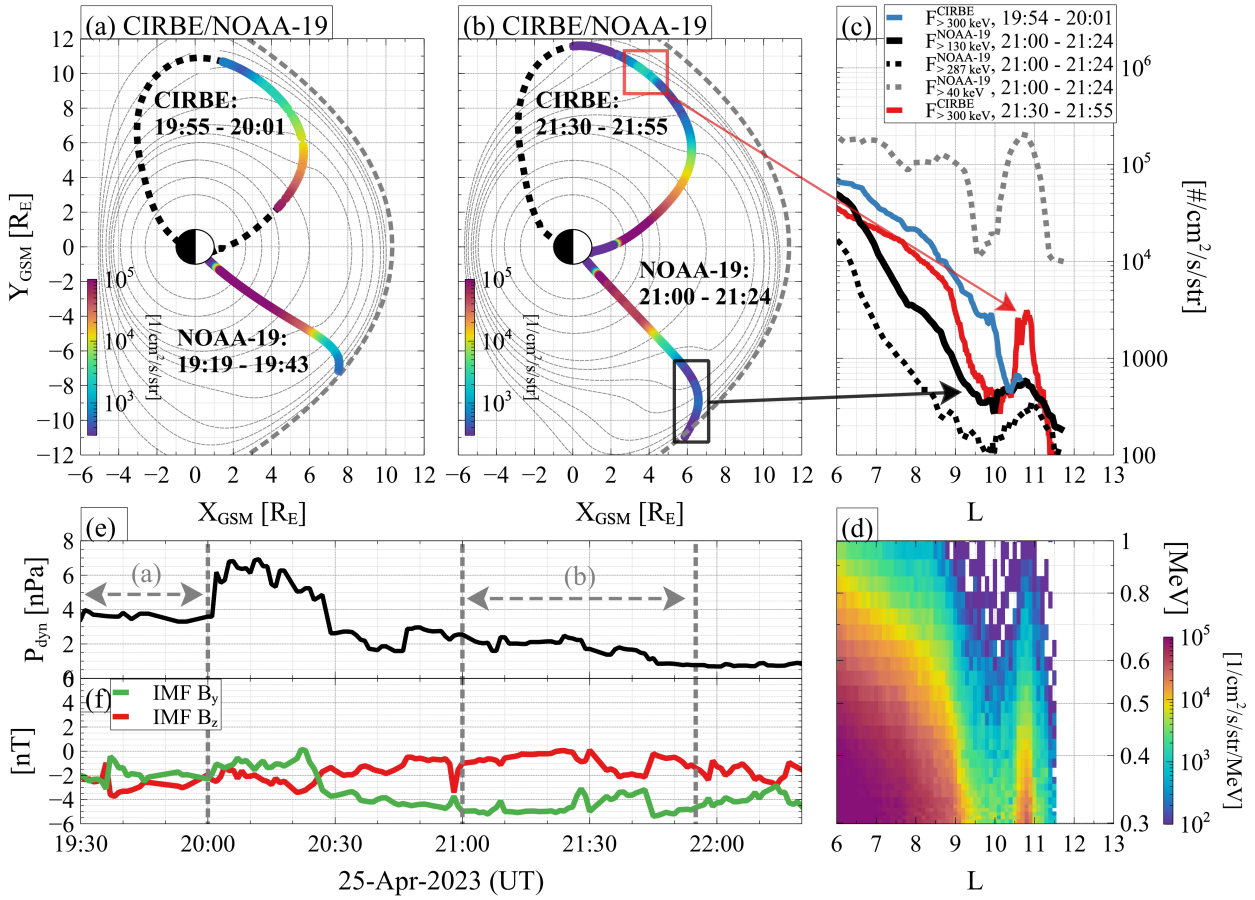

Figure 5.2: CIRBE and NOAA-19 (POES) observations of energetic electron enhancement (trapped population) near the dayside magnetopause on 25-Apr-2023. (a) integral electron number flux measured by CIRBE ($>$ 300 keV) and NOAA-19 ($>$ 130 keV), projected onto the $Z_{GSM} = 0$ plane between 19:55–20:01 and 19:19–19:43 UT, respectively. (b) The same projection of the respective spacecraft measurements between 21:30–21:55 and 21:00–21:24 UT. Grey dashed lines show the approximate magnetopause location and the drift orbits of equatorially mirroring electrons (both based on the [Tsyganenko, 1995] magnetic field model). (c) Integral flux from panel (b) shown in terms of radial profiles (as a function of L-shell); for comparison, CIRBE measurements from panel (a) are also shown. For NOAA-19, integral flux $>$ 40 and 287 keV is also shown with dashed lines. (d) Differential electron number flux from CIRBE as a function of L (measurements between 21:30–21:55 UT). (e,f) Solar wind dynamic pressure (e) and IMF B_y and B_z components (f) between 19:30 and 22:30 UT (OMNI data, [King and Papitashvili, 2005]).

References

[Ali et al., 2016] Ali, A. F., Malaspina, D. M., Elkington, S. R., Jaynes, A. N., Chan, A. A., Wygant, J., and Kletzing, C. A. (2016). Electric and magnetic radial diffusion coefficients using the van allen probes data. *Journal of Geophysical Research: Space Physics*, 121(10):9586–9607.

[Allison and Shprits, 2020] Allison, H. J. and Shprits, Y. Y. (2020). Local heating of radiation belt electrons to ultra-relativistic energies. *Nature Communications*, 11:4533.

[Angelopoulos, 2008] Angelopoulos, V. (2008). The THEMIS Mission. *Space Sci. Rev.* , 141:5–34.

[Angelopoulos, 2011] Angelopoulos, V. (2011). The ARTEMIS Mission. *Space Sci. Rev.* , 165:3–25.

[Angelopoulos et al., 1992] Angelopoulos, V., Baumjohann, W., Kennel, C. F., Coronti, F. V., Kivelson, M. G., Pellat, R., Walker, R. J., Luehr, H., and Paschmann, G. (1992). Bursty bulk flows in the inner central plasma sheet. *J. Geophys. Res.*, 97:4027–4039.

[Angelopoulos et al., 2008] Angelopoulos, V., Sibeck, D., Carlson, C. W., McFadden, J. P., Larson, D., Lin, R. P., Bonnell, J. W., Mozer, F. S., Ergun, R., Cully, C., Glassmeier, K. H., Auster, U., Roux, A., Lecontel, O., Frey, S., Phan, T., Mende, S., Frey, H., Donovan, E., Russell, C. T., Strangeway, R., Liu, J., Mann, I., Rae, J., Raeder, J., Li, X., Liu, W., Singer, H. J., Sergeev, V. A., Apatenkov, S., Parks, G., Fillingim, M., and Sigwarth, J. (2008). First Results from the THEMIS Mission. *Space Sci. Rev.* , 141:453–476.

[Angelopoulos et al., 2020] Angelopoulos, V., Tsai, E., Bingley, L., Shaffer, C., Turner, D. L., Runov, A., Li, W., Liu, J., Artemyev, A. V., Zhang, X. J., Strangeway, R. J., Wirz, R. E., Shprits, Y. Y., Sergeev, V. A., Caron, R. P., Chung, M., Cruce, P., Greer, W., Grimes, E., Hector, K., Lawson, M. J., Leneman, D., Masongsong, E. V., Russell, C. L., Wilkins, C., Hinkley, D., Blake, J. B., Adair, N., Allen, M., Anderson, M., Arreola-Zamora, M., Artinger, J., Asher, J., Branchevsky, D., Capitelli, M. R., Castro, R., Chao, G., Chung, N., Cliffe, M., Colton, K., Costello, C., Depe, D., Domae, B. W., Eldin, S., Fitzgibbon, L., Flemming, A., Fox, I., Frederick, D. M., Gilbert, A., Gildemeister, A., Gonzalez, A., Hesford, B., Jha, S., Kang, N., King, J., Krieger, R., Lian, K., Mao, J., McKinney, E., Miller, J. P., Norris, A., Nuesca, M., Palla, A., Park, E. S. Y., Pedersen, C. E., Qu, Z., Rozario, R., Rye, E., Seaton, R., Subramanian, A., Sundin, S. R., Tan, A., Turner, W., Villegas, A. J., Wasden, M., Wing, G., Wong, C., Xie, E., Yamamoto, S., Yap, R., Zarifian, A., and Zhang, G. Y. (2020). The ELFIN Mission. *Space Sci. Rev.* , 216(5):103.

[Antonova et al., 2003] Antonova, A. E., Gubar', Y. I., and Kropotkin, A. P. (2003). Effects in the radiation belts caused by the second adiabatic invariant violation in the presence of dayside off-equatorial magnetic field minima. *Advances in Space Research*, 31:1223–1228.

[Arnol'd, 1963] Arnol'd, V. I. (1963). Proof of a Theorem of A. N. KOLMOGOROV on the Invariance of Quasi-Periodic Motions Under Small Perturbations of the Hamiltonian. *Russian Mathematical Surveys*, 18:9–36.

[Arnold, 1989] Arnold, V. I. (1989). *Mathematical Methods of Classical Mechanics*. Springer-Verlag, New York, 2rd edition.

[Arnold et al., 2006] Arnold, V. I., Kozlov, V. V., and Neishtadt, A. I. (2006). *Perturbation Theory for Integrable Systems*, pages 207–349. Springer Berlin Heidelberg, Berlin, Heidelberg.

[Artemyev et al., 2021] Artemyev, A. V., Neishtadt, A. I., Vasiliev, A. A., and Mourenas, D. (2021). Transitional regime of electron resonant interaction with whistler-mode waves in inhomogeneous space plasma. *Phys Rev. E* , 104(5):055203.

[Artemyev et al., 2014] Artemyev, A. V., Neishtadt, A. I., and Zelenyi, L. M. (2014). Rapid geometrical chaotization in slow-fast Hamiltonian systems. *Phys Rev. E* , 89(6):060902.

[Artemyev et al., 2024] Artemyev, A. V., Sergeev, V. A., Angelopoulos, V., Zhang, X.-J., and Wilkins, C. (2024). Categorization of electron isotropy boundary patterns: Elfin and poes observations. *Journal of Geophysical Research: Space Physics*, 129(12):e2024JA033231. e2024JA033231 2024JA033231.

[Auster et al., 2008] Auster, H. U., Glassmeier, K. H., Magnes, W., Aydogar, O., Baumjohann, W., Constantinescu, D., Fischer, D., Fornacon, K. H., Georgescu, E., Harvey, P., Hillenmaier, O., Kroth, R., Ludlam, M., Narita, Y., Nakamura, R., Okrafka, K., Plaschke, F., Richter, I., Schwarzl, H., Stoll, B., Valavanoglou, A., and Wiedemann, M. (2008). The THEMIS Fluxgate Magnetometer. *Space Sci. Rev.* , 141:235–264.

[Baker et al., 2013] Baker, D. N., Kanekal, S. G., Hoxie, V. C., Batiste, S., Bolton, M., Li, X., Elkington, S. R., Monk, S., Reukauf, R., Steg, S., Westfall, J., Belting, C., Bolton, B., Braun, D., Cervelli, B., Hubbell, K., Kien, M., Knappmiller, S., Wade, S., Lamprecht, B., Stevens, K., Wallace, J., Yehle, A., Spence, H. E., and Friedel, R. (2013). The Relativistic Electron-Proton Telescope (REPT) Instrument on Board the Radiation Belt Storm Probes (RBSP) Spacecraft: Characterization of Earth's Radiation Belt High-Energy Particle Populations. *Space Sci. Rev.* , 179:337–381.

[Baker and Panasyuk, 2017] Baker, D. N. and Panasyuk, M. I. (2017). Discovering earth's radiation belts. *Physics Today*, 70(12):46–51.

[Bazzani et al., 2024] Bazzani, A., Capoani, F., and Giovannozzi, M. (2024). Analysis of double-resonance crossing in adiabatic trapping phenomena for quasi-integrable area-preserving maps with time-dependent exciters. *Phys. Rev. E*, 109:054212.

[Birmingham, 1984] Birmingham, T. J. (1984). Pitch angle diffusion in the Jovian magnetodisc. *J. Geophys. Res.*, 89:2699–2707.

[Bogoliubov and Krylov, 1935] Bogoliubov, N. N. and Krylov, N. (1935). *Méthodes approchées de la mécanique non linéaire dans leur application à l'étude de la perturbation des mouvements périodiques et de divers phénomènes de résonance s'y rapportant*. Académie des sciences d'Ukraine, Kiev. Available in English as: *Introduction to Nonlinear Mechanics*, Princeton University Press, Princeton, NJ (1947).

[Bogoliubov and Mitropolski, 1961] Bogoliubov, N. N. and Mitropolski, Y. A. (1961). *Asymptotic Methods in the Theory of Non-Linear Oscillations*.

[Brautigam and Albert, 2000] Brautigam, D. H. and Albert, J. M. (2000). Radial diffusion analysis of outer radiation belt electrons during the October 9, 1990, magnetic storm. *J. Geophys. Res.*, 105:291–310.

[Büchner and Zelenyi, 1989] Büchner, J. and Zelenyi, L. M. (1989). Regular and chaotic charged particle motion in magnetotaillike field reversals. I - Basic theory of trapped motion. *J. Geophys. Res.*, 94:11821–11842.

[Camporeale et al., 2022] Camporeale, E., Wilkie, G. J., Drozdov, A. Y., and Bortnik, J. (2022). Data-Driven Discovery of Fokker-Planck Equation for the Earth's Radiation Belts Electrons Using Physics-Informed Neural Networks. *Journal of Geophysical Research (Space Physics)*, 127(7):e30377.

[Cary and Brizard, 2009] Cary, J. R. and Brizard, A. J. (2009). Hamiltonian theory of guiding-center motion. *Reviews of Modern Physics*, 81:693–738.

[Cary et al., 1986] Cary, J. R., Escande, D. F., and Tennyson, J. L. (1986). Adiabatic-invariant change due to separatrix crossing. *Physical Review A*, 34(5):4256–4275.

[Cohen et al., 2016] Cohen, I. J., Mauk, B. H., Anderson, B. J., Westlake, J. H., Sibeck, D. G., Giles, B. L., Pollock, C. J., Turner, D. L., Fennell, J. F., Blake, J. B., Clemmons, J. H., Jaynes, A. N., Baker, D. N., Craft, J. V., Spence, H. E., Niehof, J. T., Reeves, G. D., Torbert, R. B., Russell, C. T., Strangeway, R. J., Magnes, W., Trattner, K. J., Fuselier, S. A., and Burch, J. L. (2016). Observations of energetic particle escape at the magnetopause: Early results from the MMS Energetic Ion Spectrometer (EIS). *Geophys. Res. Lett.*, 43(12):5960–5968.

[Courant and Hilbert, 1989] Courant, R. and Hilbert, D. (1989). *Methods of Mathematical Physics: Partial Differential Equations*. John Wiley & Sons.

[Desai et al., 2021] Desai, R. T., Eastwood, J. P., Horne, R. B., Allison, H. J., Allanson, O., Watt, C. E. J., Eggington, J. W. B., Glauert, S. A., Meredith, N. P., Archer, M. O., Staples, F. A., Mejnertsen, L., Tong, J. K., and Chittenden, J. P. (2021). Drift orbit bifurcations and cross-field transport in the outer radiation belt: Global mhd and integrated test-particle simulations. *Journal of Geophysical Research: Space Physics*, 126(10):e2021JA029802. e2021JA029802 2021JA029802.

[Dungey, 1961] Dungey, J. W. (1961). Interplanetary Magnetic Field and the Auroral Zones. *Physical Review Letters*, 6:47–48.

[Dungey, 1963] Dungey, J. W. (1963). Interactions of solar plasma with the geomagnetic field. *Planetary Space Science* , 10:233–237.

[Dunlop et al., 2008] Dunlop, M. W., Taylor, M. G. G. T., Bogdanova, Y. V., Shen, C., Pitout, F., Pu, Z., Davies, J. A., Zhang, Q.-H., Wang, J., Lavraud, B., Fazakerley, A. N., Walsh, A., Owen, C. J., Laakso, H., Zong, Q.-G., Liu, Z.-X., Escoubet, C. P., Carr, C. M., and Rème, H. (2008). Electron structure of the magnetopause boundary layer: Cluster/double star observations. *Journal of Geophysical Research: Space Physics*, 113(A7).

[Ehrenfest and Breit, 1922] Ehrenfest, P. and Breit, G. (1922). Ein bemerkenswerter fall von quantisierung. *Zeitschrift für Physik*, 9:207–210. English translation available in *Paul Ehrenfest, Collected Scientific Papers*, edited by Martin J. Klein (Amsterdam: North-Holland Publishing Company, 1959), pp. 447–450.

[Elkington et al., 1999] Elkington, S. R., Hudson, M. K., and Chan, A. A. (1999). Acceleration of relativistic electrons via drift-resonant interaction with toroidal-mode Pc-5 ULF oscillations. *Geophys. Res. Lett.*, 26(21):3273–3276.

[Evans and Greer, 2004] Evans, D. S. and Greer, M. S. (2004). Polar orbiting environmental satellite space environment monitor-2: instrument description and archive data documentation.

[Fälthammar, 1965] Fälthammar, C.-G. (1965). Effects of Time-Dependent Electric Fields on Geomagnetically Trapped Radiation. *J. Geophys. Res.*, 70:2503–2516.

[Fikhtengol'ts, 1965] Fikhtengol'ts, G. M. (1965). *The Fundamentals of Mathematical Analysis. Volume II*, volume 73 of *International Series of Monographs in Pure and Applied Mathematics*. Pergamon Press, Oxford. Translated by Ann Swinfen; translation edited by Ian N. Sneddon.

[Franchi et al., 2009] Franchi, A., Gilardoni, S., and Giovannozzi, M. (2009). Progresses in the studies of adiabatic splitting of charged particle beams by crossing nonlinear resonances. *Phys. Rev. ST Accel. Beams*, 12:014001.

[Frantsuzov et al., 2023] Frantsuzov, V. A., Artemyev, A. V., Zhang, X.-J., Allanson, O., Shustov, P. I., and Petrukovich, A. A. (2023). Diffusive scattering of energetic electrons by intense whistler-mode waves in an inhomogeneous plasma. *Journal of Plasma Physics*, 89(1):905890101.

[Fu et al., 2019] Fu, H. S., Peng, F. Z., Liu, C. M., Burch, J. L., Gershman, D. G., and Le Contel, O. (2019). Evidence of electron acceleration at a reconnecting magnetopause. *Geophysical Research Letters*, 46(11):5645–5652.

[Gamow et al., 1926] Gamow, G., Landau, L. D., and Ivanenko, D. D. (1926). On the motion of nonconservative systems with one degree of freedom. (Russian). 58(3A):477–482.

[Gold, 1959] Gold, T. (1959). Motions in the magnetosphere of the earth. *Journal of Geophysical Research (1896-1977)*, 64(9):1219–1224.

[Gonzalez et al., 1999] Gonzalez, W. D., Tsurutani, B. T., and Clúa de Gonzalez, A. L. (1999). Interplanetary origin of geomagnetic storms. *Space Sci. Rev.* , 88:529–562.

[Gradshteyn and Ryzhik, 2007] Gradshteyn, I. S. and Ryzhik, I. M. (2007). *Table of Integrals, Series, and Products*. Academic Press.

[Green and Kivelson, 2004] Green, J. C. and Kivelson, M. G. (2004). Relativistic electrons in the outer radiation belt: Differentiating between acceleration mechanisms. *Journal of Geophysical Research (Space Physics)*, 109(A3):A03213.

[Grigoriev et al., 2006] Grigoriev, R., Schatz, M., and Sharma, V. (2006). Chaotic mixing in microdroplets. *Lab Chip*, 6:1369–1372.

[Hellwig, 1955] Hellwig, G. (1955). Über die bewegung geladener teilchen in schwach veränderlichen magnetfeldern. *Zeitschrift für Naturforschung A*, 10(7):508–516. English translation of title: "On the motion of charged particles in slowly varying magnetic fields".

[Hertweck and Schlüter, 1957] Hertweck, F. and Schlüter, A. (1957). Die „adiabatische invarianz" des magnetischen bahnmomentes geladener teilchen. *Zeitschrift für Naturforschung A*, 12(10):844–849. English translation of title: "The „adiabatic invariance" of the magnetic moment of charged particles".

[Holappa and Buzulukova, 2022] Holappa, L. and Buzulukova, N. Y. (2022). Explicit IMF B_y-Dependence of Energetic Protons and the Ring Current. *Geophys. Res. Lett.*, 49(8):e98031.

[Horne, 2007] Horne, R. B. (2007). Plasma astrophysics: Acceleration of killer electrons. *Nature Physics*, 3:590–591.

[Horne et al., 2018] Horne, R. B., Phillips, M. W., Glauert, S. A., Meredith, N. P., Hands, A. D. P., Ryden, K. A., and Li, W. (2018). Realistic worst case for a severe space weather event driven by a fast solar wind stream. *Space Weather*, 16(9):1202–1215.

[Horne and Thorne, 1998] Horne, R. B. and Thorne, R. M. (1998). Potential waves for relativistic electron scattering and stochastic acceleration during magnetic storms. *Geophys. Res. Lett.*, 25:3011–3014.

[Itin and Watanabe, 2007] Itin, A. P. and Watanabe, S. (2007). Universality in nonadiabatic behavior of classical actions in nonlinear models of bose-einstein condensates. *Phys. Rev. E*, 76:026218.

[Kamaletdinov et al., 2025a] Kamaletdinov, S. R., Artemyev, A. V., and Angelopoulos, V. (2025a). Energetic electron enhancements near the dayside magnetopause: Outward radial transport due to asymmetric drift-orbit bifurcation. *Geophysical Research Letters*, 52(19):e2025GL116514. e2025GL116514 2025GL116514.

[Kamaletdinov et al., 2024a] Kamaletdinov, S. R., Artemyev, A. V., Angelopoulos, V., and Neishtadt, A. I. (2024a). Electron scattering due to asymmetric drift-orbit bifurcation: Geometric jumps of adiabatic invariant. *Journal of Geophysical Research: Space Physics*, 129(11):e2024JA032987. e2024JA032987 2024JA032987.

[Kamaletdinov et al., 2025b] Kamaletdinov, S. R., Artemyev, A. V., Neishtadt, A. I., and Angelopoulos, V. (2025b). Charged particle cross-field transport due to geometric jumps of adiabatic invariant. *Phys. Rev. Lett.*, 135:065202.

[Kamaletdinov et al., 2024b] Kamaletdinov, S. R., Vasko, I. Y., and Artemyev, A. V. (2024b). Nonlinear electron scattering by electrostatic waves in collisionless shocks. *Journal of Plasma Physics*, 90(2):905900201.

[Keller, 1984] Keller, G. (1984). On the rate of convergence to equilibrium in one-dimensional systems. *Commun.Math. Phys.*, 96:181–1932266.

[Kennel and Engelmann, 1966] Kennel, C. F. and Engelmann, F. (1966). Velocity Space Diffusion from Weak Plasma Turbulence in a Magnetic Field. *Physics of Fluids*, 9:2377–2388.

[King and Papitashvili, 2005] King, J. H. and Papitashvili, N. E. (2005). Solar wind spatial scales in and comparisons of hourly Wind and ACE plasma and magnetic field data. *J. Geophys. Res.*, 110:A02104.

[Kress et al., 2007] Kress, B. T., Hudson, M. K., Looper, M. D., Albert, J., Lyon, J. G., and Goodrich, C. C. (2007). Global mhd test particle simulations of >10 mev radiation belt electrons during storm sudden commencement. *Journal of Geophysical Research: Space Physics*, 112(A9).

[Kruskal, 1958] Kruskal, M. (1958). The gyration of a charged particle. Technical report, Princeton Univ., N.J. Project Matterhorn.

[Kulsrud, 1957] Kulsrud, R. M. (1957). Adiabatic Invariant of the Harmonic Oscillator. *Physical Review*, 106:205–207.

[Landau, 1936] Landau, L. D. (1936). Die kinetische gleichung für den fall coulombscher wechselwirkung. *Physikalische Zeitschrift der Sowjetunion*, 10:154–164. See also English translation: L. D. Landau, "The kinetic equation in the case of Coulomb interactions," in D. ter Haar (Ed.), Collected Papers of L. D. Landau, Pergamon Press, 1965.

[Landau and Lifshitz, 1971] Landau, L. D. and Lifshitz, E. M. (1971). *Vol. 2: The Classical Theory of Fields*. Course of Theoretical Physics. Pergamon Press.

[Landau and Lifshitz, 1988] Landau, L. D. and Lifshitz, E. M. (1988). *Vol. 1: Mechanics*. Course of Theoretical Physics. Oxford: Pergamon.

[Lasota and Mackey, 1985] Lasota, A. and Mackey, M. C. (1985). *Markov and Frobenius–Perron operators*, page 32–44. Cambridge University Press.

[Lejosne et al., 2024] Lejosne, S., Albert, J. M., and Ratliff, D. (2024). Characteristic times for radiation belt drift phase mixing. *Frontiers in Astronomy and Space Sciences*, 11:1385472.

[Lejosne and Kollmann, 2020] Lejosne, S. and Kollmann, P. (2020). Radiation Belt Radial Diffusion at Earth and Beyond. *Space Sci. Rev.* , 216(1):19.

[Lenard, 1959] Lenard, A. (1959). Adiabatic invariance to all orders. *Annals of Physics*, 6:261–276.

[Lerche, 1968] Lerche, I. (1968). Quasilinear Theory of Resonant Diffusion in a Magneto-Active, Relativistic Plasma. *Physics of Fluids*, 11.

[Li and Hudson, 2019] Li, W. and Hudson, M. K. (2019). Earth's Van Allen Radiation Belts: From Discovery to the Van Allen Probes Era. *Journal of Geophysical Research (Space Physics)*, 124(11):8319–8351.

[Li et al., 2022] Li, X., Kohnert, R., Palo, S., Selesnick, R., Khoo, L., Schiller, Q., Zhang, K., Cantilina, J., Bauch, E., Sims, A., Boyajian, S., Valade, T., Buedel, P., Reynolds, A., Johnson, J., Durell, A., Cervelli, B., Tate, G., Mei, Y., Chambliss, M., Flynn, S., Bryant, K., and Baringer, T. (2022). Two generations of cubesat missions (csswe and cirbe) to take on the challenges of measuring relativistic electrons in the earth's magnetosphere. In *Proceedings of the Small Satellite Conference*, Logan, Utah, USA. Utah State University.

[Li et al., 2024] Li, X., Selesnick, R., Mei, Y., O'Brien, D., Hogan, B., Xiang, Z., Khoo, L., Zhao, H., Schiller, Q., Temerin, M., and Baker, D. N. (2024). First results from reptile-2 measurements onboard cirbe. *Geophysical Research Letters*, 51(3):e2023GL107521. e2023GL107521 2023GL107521.

[Liou and Mitchell, 2019] Liou, K. and Mitchell, E. (2019). Effects of the interplanetary magnetic field y component on the dayside aurora. *Geoscience Letters*, 6(1):11.

[Luo et al., 2024] Luo, Z., Xie, L., Fu, S., Pu, Z., Zhou, X., and Zhao, X. X. (2024). Separation of electron flux in pitch angle distribution during the drift echo event and shabansky orbits effect. *Geophysical Research Letters*, 51(17):e2024GL109678. e2024GL109678 2024GL109678.

[Lyons and Williams, 1984] Lyons, L. R. and Williams, D. J. (1984). *Quantitative aspects of magnetospheric physics.*

[Mann et al., 2013] Mann, I. R., Lee, E. A., Claudepierre, S. G., Fennell, J. F., Degeling, A., Rae, I. J., Baker, D. N., Reeves, G. D., Spence, H. E., Ozeke, L. G., Rankin, R., Milling, D. K., Kale, A., Friedel, R. H. W., and Honary, F. (2013). Discovery of the action of a geophysical synchrotron in the Earth's Van Allen radiation belts. *Nature Communications*, 4:2795.

[McCollough et al., 2012] McCollough, J. P., Elkington, S. R., and Baker, D. N. (2012). The role of shabansky orbits in compression-related electromagnetic ion cyclotron wave growth. *Journal of Geophysical Research: Space Physics*, 117(A1).

[McFadden et al., 2008] McFadden, J. P., Carlson, C. W., Larson, D., Ludlam, M., Abiad, R., Elliott, B., Turin, P., Marckwordt, M., and Angelopoulos, V. (2008). The THEMIS ESA Plasma Instrument and In-flight Calibration. *Space Sci. Rev.* , 141:277–302.

[Melissinos, 1993] Melissinos, A. C. (1993). Nicholas c. christofilos: His contributions to physics. In *Proceedings, Advanced Accelerator Physics*, pages 1067–1081. PDF archived from the original on 2010-06-26, retrieved 2015-12-29.

[Meng and Anderson, 1970] Meng, C. I. and Anderson, K. A. (1970). A layer of energetic electrons (>40 kev) near the magnetopause. *Journal of Geophysical Research (1896-1977)*, 75(10):1827–1836.

[Meng and Anderson, 1975] Meng, C. I. and Anderson, K. A. (1975). Characteristics of the magnetopause energetic electron layer. *Journal of Geophysical Research (1896-1977)*, 80(31):4237–4243.

[Morozov and Solov'ev, 1966] Morozov, A. I. and Solov'ev, L. S. (1966). Motion of Charged Particles in Electromagnetic Fields. *Reviews of Plasma Physics*, 2:201.

[Neishtadt, 2019] Neishtadt, A. (2019). On mechanisms of destruction of adiabatic invariance in slow–fast hamiltonian systems. *Nonlinearity*, 32(11):R53.

[Neishtadt, 1975] Neishtadt, A. I. (1975). Passage through a separatrix in a resonance problem with a slowly-varying parameter. *Journal of Applied Mathematics and Mechanics*, 39:594–605.

[Neishtadt, 1986] Neishtadt, A. I. (1986). Change of an adiabatic invariant at a separatrix. *Soviet Journal of Plasma Physics*, 12:568–573.

[Neishtadt, 1987] Neishtadt, A. I. (1987). On the change in the adiabatic invariant on crossing a separatrix in systems with two degrees of freedom. *Journal of Applied Mathematics and Mechanics*, 51:586–592.

[Neishtadt, 2000] Neishtadt, A. I. (2000). On the accuracy of persistence of adiabatic invariant in single-frequency system. *Regular and chaotic dynamics*, 5:213–218.

[Neishtadt and Treschev, 2011] Neishtadt, A. I. and Treschev, D. (2011). Polymorphisms and adiabatic chaos. *Ergodic theory and dynamical systems*, 31(1):259–284.

[Neishtadt and Vasiliev, 2005] Neishtadt, A. I. and Vasiliev, A. A. (2005). Phase change between separatrix crossings in slow fast Hamiltonian systems. *Nonlinearity*, 18:1393–1406.

[Newell et al., 1998] Newell, P. T., Sergeev, V. A., Bikkuzina, G. R., and Wing, S. (1998). Characterizing the state of the magnetosphere: Testing the ion precipitation maxima latitude (b2i) and the ion isotropy boundary. *J. Geophys. Res.*, 103(A3):4739–4746.

[Northrop, 1963] Northrop, T. G. (1963). *The adiabatic motion of charged particles*. Interscience Publishers John Wiley and Sons, New York-London-Sydney.

[Northrop and Teller, 1960] Northrop, T. G. and Teller, E. (1960). Stability of the adiabatic motion of charged particles in the earth's field. *Phys. Rev.*, 117:215–225.

[O'Brien et al., 2003] O'Brien, T. P., Lorentzen, K. R., Mann, I. R., Meredith, N. P., Blake, J. B., Fennell, J. F., Looper, M. D., Milling, D. K., and Anderson, R. R. (2003). Energization of relativistic electrons in the presence of ulf power and mev microbursts: Evidence for dual ulf and vlf acceleration. *Journal of Geophysical Research: Space Physics*, 108(A8).

[Osmane et al., 2023] Osmane, A., Kilpua, E., George, H., Allanson, O., and Kalliokoski, M. (2023). Radial transport in the earth's radiation belts: Linear, quasi-linear, and higher-order processes. *The Astrophysical Journal Supplement Series*, 269(2):44.

[Ozeke et al., 2014] Ozeke, L. G., Mann, I. R., Murphy, K. R., Jonathan Rae, I., and Milling, D. K. (2014). Analytic expressions for ULF wave radiation belt radial diffusion coefficients. *J. Geophys. Res.*, 119:1587–1605.

[Parks et al., 1999] Parks, G. K., Datta, S., McCarthy, M., Lin, R. P., Reme, H., Sauvaud, J. A., Sanderson, T., Baumjohann, W., Haerendel, G., and Torkar, K. (1999). Magnetopause boundary structure deduced from the high-time resolution particle experiment on the equator-s spacecraft. *Annales Geophysicae*, 17(12):1574–1581.

[Phan et al., 2013] Phan, T. D., Shay, M. A., Gosling, J. T., Fujimoto, M., Drake, J. F., Paschmann, G., Oieroset, M., Eastwood, J. P., and Angelopoulos, V. (2013). Electron bulk heating in magnetic reconnection at Earth's magnetopause: Dependence on the inflow Alfvén speed and magnetic shear. *Geophys. Res. Lett.*, 40(17):4475–4480.

[Reeves et al., 2013] Reeves, G. D., Spence, H. E., Henderson, M. G., Morley, S. K., Friedel, R. H. W., Funsten, H. O., Baker, D. N., Kanekal, S. G., Blake, J. B., Fennell, J. F., Claudepierre, S. G., Thorne, R. M., Turner, D. L., Kletzing, C. A., Kurth, W. S., Larsen, B. L., and Niehof, J. T. (2013). Electron Acceleration in the Heart of the Van Allen Radiation Belts. *Science*, 341:991–994.

[Roederer, 1969] Roederer, J. G. (1969). Quantitative models of the magnetosphere. *Reviews of Geophysics and Space Physics*, 7:77–96.

[Schulz and Lanzerotti, 1974] Schulz, M. and Lanzerotti, L. J. (1974). *Particle diffusion in the radiation belts*. Springer, New York.

[Sergeev et al., 1993] Sergeev, V. A., Malkov, M., and Mursula, K. (1993). Testing the isotropic boundary algorithm method to evaluate the magnetic field configuration in the tail. *J. Geophys. Res.*, 98(A5):7609–7620.

[Shabansky, 1972] Shabansky, V. (1972). Phenomena in the near-earth space. *M. Nauka*.

[Shabansky and Antonova, 1968] Shabansky, V. and Antonova, A. E. (1968). Topology of particle drift shells in the earth's magnetosphere (english translation). *Geomagnetism and aeronomy.*, 31(3).

[Shabansky, 1971] Shabansky, V. P. (1971). Some Processes in the Magnetosphere. *Space Sci. Rev.* , 12:299–418.

[Shprits et al., 2015] Shprits, Y. Y., Kellerman, A. C., Drozdov, A. Y., Spence, H. E., Reeves, G. D., and Baker, D. N. (2015). Combined convective and diffusive simulations: VERB-4D comparison with 17 March 2013 Van Allen Probes observations. *Geophys. Res. Lett.*, 42:9600–9608.

[Shprits et al., 2006] Shprits, Y. Y., Thorne, R. M., Friedel, R., Reeves, G. D., Fennell, J., Baker, D. N., and Kanekal, S. G. (2006). Outward radial diffusion driven by losses at magnetopause. *J. Geophys. Res.*, 111:11214.

[Sibeck and McEntire, 1988] Sibeck, D. G. and McEntire, R. W. (1988). Multiple satellite observations of leakage of particles from the magnetosphere. *Advances in Space Research*, 8(9-10):201–216.

[Sivukhin, 1965] Sivukhin, D. V. (1965). *Motion of charged particles in electromagnetic fields in the drift approximation*, volume 1, pages 1–104. Consultants Bureau, New York.

[Sorathia et al., 2017] Sorathia, K. A., Merkin, V. G., Ukhorskiy, A. Y., Mauk, B. H., and Sibeck, D. G. (2017). Energetic particle loss through the magnetopause: A combined global MHD and test-particle study. *Journal of Geophysical Research (Space Physics)*, 122(9):9329–9343.

[Sorathia et al., 2018] Sorathia, K. A., Ukhorskiy, A. Y., Merkin, V. G., Fennell, J. F., and Claudepierre, S. G. (2018). Modeling the Depletion and Recovery of the Outer Radiation Belt During a Geomagnetic Storm: Combined MHD and Test Particle Simulations. *Journal of Geophysical Research (Space Physics)*, 123(7):5590–5609.

[Stern, 1970] Stern, D. P. (1970). Euler Potentials. *American Journal of Physics*, 38:494–501.

[Størmer, 1937] Størmer, C. (1937). On the Trajectories of Electric Particles in the Field of a Magnetic Dipole with Applications to the Theory of Cosmic Radiation. Sixth Communication. With 17 Figures in the Text. *Astrophysica Norvegica*, 2:193.

[Störmer, 1955] Störmer, C. (1955). *The Polar Aurora*. Clarendon press, Oxford.

[Su et al., 2015] Su, Z., Zhu, H., Xiao, F., Zong, Q. G., Zhou, X. Z., Zheng, H., Wang, Y., Wang, S., Hao, Y. X., Gao, Z., He, Z., Baker, D. N., Spence, H. E., Reeves, G. D., Blake, J. B., and Wygant, J. R. (2015). Ultra-low-frequency wave-driven diffusion of radiation belt relativistic electrons. *Nature Communications*, 6:10096.

[Tao et al., 2007] Tao, X., Chan, A. A., and Brizard, A. J. (2007). Hamiltonian theory of adiabatic motion of relativistic charged particles. *Physics of Plasmas*, 14(9):092107.

[Tikhonov and Samarskii, 2013] Tikhonov, A. and Samarskii, A. (2013). *Equations of Mathematical Physics*. Dover Books on Physics. Dover Publications.

[Timofeev, 1978] Timofeev, A. V. (1978). On the problem of constancy of the adiabatic invariant during change of the type of motion. *Sov. J. JETP*, 75:1303–1308.

[Tsyganenko, 1995] Tsyganenko, N. A. (1995). Modeling the Earth's magnetospheric magnetic field confined within a realistic magnetopause. *J. Geophys. Res.*, 100:5599–5612.

[Tsyganenko and Sitnov, 2005] Tsyganenko, N. A. and Sitnov, M. I. (2005). Modeling the dynamics of the inner magnetosphere during strong geomagnetic storms. *J. Geophys. Res.*, 110:A03208.

[Tsyganenko and Sitnov, 2007] Tsyganenko, N. A. and Sitnov, M. I. (2007). Magnetospheric configurations from a high-resolution data-based magnetic field model. *J. Geophys. Res.*, 112:A06225.

[Turner et al., 2013] Turner, D. L., Angelopoulos, V., Li, W., Hartinger, M. D., Usanova, M., Mann, I. R., Bortnik, J., and Shprits, Y. (2013). On the storm-time evolution of relativistic electron phase space density in earth's outer radiation belt. *Journal of Geophysical Research: Space Physics*, 118(5):2196–2212.

[Turner et al., 2012] Turner, D. L., Shprits, Y., Hartinger, M., and Angelopoulos, V. (2012). Explaining sudden losses of outer radiation belt electrons during geomagnetic storms. *Nature Physics*, 8:208–212.

[Ukhorskiy and Sitnov, 2008] Ukhorskiy, A. Y. and Sitnov, M. I. (2008). Radial transport in the outer radiation belt due to global magnetospheric compressions. *Journal of Atmospheric and Solar-Terrestrial Physics*, 70(14):1714–1726. Dynamic Variability of Earth's Radiation Belts.

[Ukhorskiy and Sitnov, 2013] Ukhorskiy, A. Y. and Sitnov, M. I. (2013). Dynamics of Radiation Belt Particles. *Space Sci. Rev.* , 179:545–578.

[Ukhorskiy et al., 2011] Ukhorskiy, A. Y., Sitnov, M. I., Millan, R. M., and Kress, B. T. (2011). The role of drift orbit bifurcations in energization and loss of electrons in the outer radiation belt. *J. Geophys. Res.*, 116:9208.

[Ukhorskiy et al., 2015] Ukhorskiy, A. Y., Sitnov, M. I., Millan, R. M., Kress, B. T., Fennell, J. F., Claudepierre, S. G., and Barnes, R. J. (2015). Global storm time depletion of the outer electron belt. *Journal of Geophysical Research: Space Physics*, 120(4):2543–2556.

[Ukhorskiy et al., 2014a] Ukhorskiy, A. Y., Sitnov, M. I., Millan, R. M., Kress, B. T., and Smith, D. C. (2014a). Enhanced radial transport and energization of radiation belt electrons due to drift orbit bifurcations. *Journal of Geophysical Research (Space Physics)*, 119(1):163–170.

[Ukhorskiy et al., 2014b] Ukhorskiy, A. Y., Sitnov, M. I., Mitchell, D. G., Takahashi, K., Lanzerotti, L. J., and Mauk, B. H. (2014b). Rotationally driven 'zebra stripes' in Earth's inner radiation belt. *Nature*, 507(7492):338–340.

[Vainchtein et al., 2006] Vainchtein, D. L., Neishtadt, A. I., and Mezic, I. (2006). On passage through resonances in volume-preserving systems. *Chaos: An Interdisciplinary Journal of Nonlinear Science*, 16(4):043123.

[Vainchtein et al., 2007] Vainchtein, D. L., Widloski, J., and Grigoriev, R. O. (2007). Mixing properties of steady flow in thermocapillary driven droplets. *Physics of Fluids*, 19(6):067102.

[Vainshtein et al., 1999] Vainshtein, D. L., Zelenyi, L. M., Neishtadt, A. I., and Savenkov, B. V. (1999). Jumps in an adiabatic invariant with small initial values. *Plasma Physics Reports*, 25:299–303.

[Van Allen, 1958] Van Allen, J. (1958). Special joint meeting of national academy of sciences and american physical society. *Washington, DC, May*, 1:1958.

[van Allen and Frank, 1959] van Allen, J. A. and Frank, L. A. (1959). Radiation Around the Earth to a Radial Distance of 107,400 km. *Nature*, 183:430–434.

[Van Allen et al., 1958] Van Allen, J. A., Ludwig, G. H., Ray, E. C., and McIlwain, C. E. (1958). Observation of high intensity radiation by satellites 1958 alpha and gamma. *Journal of Jet Propulsion*, 28(7):588–592.

[Vedenov et al., 1962] Vedenov, A. A., Velikhov, E., and Sagdeev, R. (1962). Quasilinear theory of plasma oscillations. *Nuclear Fusion Suppl.*, 2:465–475.

[Vernov et al., 1959] Vernov, S., Chudakov, A., Gorchakov, E., Logachev, J., and Vakulov, P. (1959). Study of the cosmic-ray soft component by the 3rd soviet earth satellite. *Planetary and Space Science*, 1(2):86–93.

[Vernov and Chudakov, 1960] Vernov, S. N. and Chudakov, A. E. (1960). Investigations of cosmic radiation and of the terrestrial corpuscular radiation by means of rockets and satellites. *Soviet Physics Uspekhi*, 3(2):230–250. Includes English translation of the results from [Vernov et al., 1958b, Vernov et al., 1958a].

[Vernov et al., 1958a] Vernov, S. N., Vakulov, P. V., Gorchakov, E. V., Logachev, I., and Chudakov, A. E. (1958a). On the primary results of the satellite measurements of cosmic rays. *Doklady Akademii Nauk SSSR*, 121(5):794–797. In Russian; partial English translation of selected results available in [Vernov and Chudakov, 1960].

[Vernov et al., 1958b] Vernov, S. N., Vakulov, P. V., Gorchakov, Y. V., Logachev, I., and Chudakov, A. Y. (1958b). *Collection of Papers on Sputnik Results*, volume 2. U.S.S.R. Academy of Sciences, Moscow. In Russian; partial English translation of selected results available in [Vernov and Chudakov, 1960].

[Vershik, 1983] Vershik, A. M. (1983). Multivalued mappings with invariant measure (polymorphisms) and markov operators. *J. Sov. Math.*, 23:2243–2266.

[Walsh et al., 2012] Walsh, B. M., Haaland, S. E., Daly, P. W., Kronberg, E. A., and Fritz, T. A. (2012). Energetic electrons along the high-latitude magnetopause. *Annales Geophysicae*, 30(6):1003–1013.

[Wan et al., 2010] Wan, Y., Sazykin, S., Wolf, R. A., and Öztürk, M. K. (2010). Drift shell bifurcation near the dayside magnetopause in realistic magnetospheric magnetic fields. *J. Geophys. Res.*, 115:10205.

[Whittaker and Watson, 1996] Whittaker, E. T. and Watson, G. N. (1996). *A Course of Modern Analysis*. Cambridge Mathematical Library. Cambridge University Press, 4 edition.

[Wilkins et al., 2023] Wilkins, C., Angelopoulos, V., Runov, A., Artemyev, A., Zhang, X. J., Liu, J., and Tsai, E. (2023). Statistical Characteristics of the Electron Isotropy Boundary. *Journal of Geophysical Research (Space Physics)*, 128(10):e2023JA031774.

[Williams et al., 1985] Williams, D. J., Mitchell, D. G., Eastman, T. E., and Frank, L. A. (1985). Energetic particle observations in the low-latitude boundary layer. *Journal of Geophysical Research: Space Physics*, 90(A6):5097–5116.

[Zelenyi et al., 2013] Zelenyi, L. M., Neishtadt, A. I., Artemyev, A. V., Vainchtein, D. L., and Malova, H. V. (2013). Quasiadiabatic dynamics of charged particles in a space plasma. *Physics Uspekhi*, 56:347–394.

[Zheng et al., 2016] Zheng, L., Chan, A. A., O'Brien, T. P., Tu, W., Cunningham, G. S., Albert, J. M., and Elkington, S. R. (2016). Effects of magnetic drift shell splitting on electron diffusion in the radiation belts. *Journal of Geophysical Research: Space Physics*, 121(12):11,985–12,000.

[Öztürk and Wolf, 2007] Öztürk, M. K. and Wolf, R. A. (2007). Bifurcation of drift shells near the dayside magnetopause. *Journal of Geophysical Research: Space Physics*, 112(A7).